BLOCK COPOLYMER DERIVED THREE-DIMENSIONAL ORDERED HYBRID MATERIALS FOR ENERGY STORAGE AND CONVERSION

Dissertation

zur Erlangung des Grades

des Doktors der Naturwissenschaften

der Naturwissenschaftlich-Technischen Fakultät

der Universität des Saarlandes

von

Tobias Sebastian Dörr

Saarbrücken
2018

Tag des Kolloquiums: 17.04.2019

Dekan: Prof. Dr. Guido Kickelbick

Berichterstatter: Prof. Dr. Tobias Kraus

                         Prof. Dr. Dominik Eder

Vorsitz: Prof. Dr. Guido Kickelbick

Akad. Mitarbeiter: Dr. Andreas Rammo

Menschen mit einer neuen Idee gelten so lange als Spinner,

bis sich die Sache durchgesetzt hat.

\- Mark Twain -

Chapter 4.1

ORDERED MESOPOROUS TITANIA/CARBON HYBRID MONOLITHS FOR LITHIUM-ION BATTERY ANODES WITH HIGH AREAL AND VOLUMETRIC CAPACITY

Dörr T. S., Fleischmann S., Zeiger M., Grobelsek I., de Oliveira P. W., Presser V., *Chem. - Eur. J.* **2018**, 24, 6358-6363

Contribution of Tobias S. Dörr

Design of the synthetic protocol: preparation and optimization of the ISO structure-directing block copolymer, preparation and optimization of the carbon/TiO_2 hybrids. Analytic methods: NMR, GPC, SEM, SAXS, and RAMAN. Conception and writing of the manuscript.

Chapter 4.2

AN AMBIENT TEMPERATURE ELECTROLYTE WITH SUPERIOR LITHIUM ION CONDUCTIVITY BASED ON A SELF-ASSEMBLED BLOCK COPOLYMER

Dörr T. S., Pelz A., Zhang P., Kraus T., Winter M., Wiemhöfer H.-D., *Chem. - Eur. J.* **2018**, 24, 8061-8065

Contribution of Tobias S. Dörr

Design of the synthetic protocol: preparation and optimization of the ISO block copolymer. Analytic methods: NMR, GPC, SAXS/WAXS, Rheology, DSC, and TGA-DSC-MS. Conception and writing of the manuscript.

The manuscript was conceived and wrote in equal contribution with Alexander Pelz.

Chapter 4.3

SELF-ASSEMBLED BLOCK COPOLYMER ELECTROLYTES: ENABLING SUPERIOR AMBIENT CATIONIC CONDUCTIVITY AND ELECTROCHEMICAL STABILITY

Pelz A., **Dörr T. S.**, Zhang P., de Oliveira P. W., Winter M., Wiemhöfer H.-D., Kraus T., *Chem. Mater.* **2018**, 31, 277-285

<u>Contribution of Tobias S. Dörr</u>

Design of the synthetic protocol: preparation and optimization of the ISO block copolymers with varied PEO block chain. Analytic methods: NMR, GPC, SAXS/WAXS, Rheology, DSC, and TGA-MS. Conception and writing of the manuscript.

The manuscript was conceived and wrote in equal contribution with Alexander Pelz.

Chapter 4.4

ORDERED MESOPOROUS TiO2 GYROIDS: EFFECTS OF PORE ARCHITECTURE AND Nb-DOPING ON PHOTOCATALYTIC HYDROGEN EVOLUTION UNDER UV AND VIS IRRADIATION

Dörr, T. S., Deilmann L., Haselmann G., Cherevan A., Zhang P., Blaha P., de Oliveira P. W., Kraus T., Eder D., *Adv. Energy Mater.* **2018**, 1802566

<u>Contribution of Tobias S. Dörr</u>

Design of the synthetic protocol: preparation and optimization of the ISO structure-directing block copolymer, preparation and optimization of the pure and doped TiO_2 gyroids. Analytic methods: NMR, GPC, SAXS, RAMAN, UV-VIS, SEM. Conception and writing of the manuscript.

ACKNOWLEDGEMENTS

Koch, Dr. Benjamin Krüner, Prof. Volker Presser, Prof. Roland Marshall, Mike Nadig, Dr. Alexander Pelz, Hwirim Shim, Pattarachai Srimuk, Prof. Hans-Dieter Wiemhöfer, Prof. Martin Winter, Dr. Marco Zeiger, and Dr. Peng Zhang.

Last, I have the best family one could imagine. Thank you for your continuous support, Mama, Papa and Alisa.

ZUSAMMENFASSUNG

Diese Doktorarbeit untersucht die Herstellung hochgeordneter, perkolierender Nanostrukturen mittels Blockcopolymeren und diskutiert deren Einfluss auf die Leistungsfähigkeit darauf basierender Materialien in Anwendungen der modernen Energiespeicherung und –umwandlung.

In einer ersten Studie wurden mesoporöse, monolithische TiO_2/C-Hybride mittels eines Triblockcopolymers hergestellt und als Lithium-Ionen-Batterieanode getestet. Die Karbonisierung des strukturgebenden Polymers ergab eine leitfähige Kohlenstoffschicht an der Grenzfläche zum Elektrolyten und erhöhte so die intrinsische Leitfähigkeit.

Einzelne Polymerblöcke wurden optimiert, um makroskopische Eigenschaften von Polymerelektrolyten unabhängig voneinander einzustellen. Eine besonders kleine, leitfähige Komponente erlaubte die Entkopplung der ionischen Leitfähigkeit von der Kettenmobilität, während kovalent gebundene, isolierenden Blöcke gleichzeitig hohe mechanische Stabilität gewährleisteten. Der verbreitete Widerspruch zwischen hoher Leitfähigkeit und Stabilität dieser Materialklasse konnte so vermieden werden.

Photokatalyse erfordert direkten Zugang der Reaktanden und der Ladungsträger zur katalytisch aktiven Oberfläche. Im letzten Teil der Arbeit wird gezeigt, dass die Entfernung des strukturgebenden Polymers zu mesoporösen, perkolierenden, anorganischen Netzwerken führte. Diese erhöhten die Effizienz der Photokatalyse, da verbesserte Porendiffusivität und hohe Ladungsträgermobilitäten kombiniert wurden.

ABSTRACT

In this thesis, block copolymers are used to rationally structure inorganic and hybrid materials into ordered, percolating nanostructures. The tunability of the microstructure, chemical composition, and porosity is explored and correlated with the materials' performance in energy storage and conversion applications.

Dense and thick mesoporous TiO_2/C hybrid monoliths were prepared by co-assembly with a triblock copolymer and characterized as potential lithium ion battery anodes. The structure-directing polymer was carbonized to retain a thin conductive carbon layer at the electrolyte|electrode interface that increases the intrinsic conductivity of the active material.

Polymer electrolytes were prepared by tailoring the individual blocks of the block copolymer. A minor conductive block decoupled ionic mobility from slow polymer relaxation, while sufficient mechanical stability was provided by covalently linked, mechanically stronger, insulating blocks. This combination overcomes a common trade-off between high conductivity and strength.

Photocatalysis requires direct access of reactants and incident photons to a catalysts' surface. The final part of the thesis shows that complete thermal removal of the template can create a mesoporous inorganic percolating network. Structuring the catalyst in this way improved the efficiency of photocatalysis as it combines high pore diffusibility with improved charge carrier transport properties.

1.   MOTIVATION

The increased demand for energy caused by population growth and enhanced lifestyle is one of the biggest challenges humanity faces over the next decades.[1] To date, almost 80% of that demand is covered by the exploitation of fossil fuels, including oil, coal, and gas. Their depletion is reflected by the rapidly increasing price and in the long-term, these limited resources need to be conserved.[2]

The exploitation of those carbon-intensive fossil fuels is not only related to its limitation but also to their impact on the environment as their consumption causes air pollution, ozone depletion, and forest destruction.[3] Anthropogenic emission of so-called global greenhouse gases (e.g. ozone, methane, carbon dioxide or nitrous oxides) results in a radiative imbalance; they absorb within the infrared spectrum which, in turn, warms the planet's atmosphere.[4] This greenhouse effect results in a change in the average weather conditions, compared to the long-term average, inter alia known as global warming. Human impact on the climate has started with the European and North American industrialization in the second half of the 19th century and was dramatically aggravated by the technological catch up of the Asian and Latin American industry during the 20th century. Increases in the average global mean temperature, the successive melting of polar caps, and the rise in sea level are only a couple of the proximately results of manmade global warming.[5]

In this context, renewable energies, considered to operate climate neutral and replenished by nature, are more relevant than ever. They are harvested either directly (such as photochemically and thermally) or indirectly (such as wind- and hydropower) from the sun. **Figure 1a** illustrates the discrepancy between solar energy production and its generalized household consumption during a sunny day. This problem is even more aggravated by the arbitrary supply of sunlight (i.e. decreased hours of sunshine in winter; cloudy days). Beside households (~25 %), the final energy consumption within the European Union (EU-28) by 2015 is mainly consumed by the

industrial (~25 %), and transportation sector (~33 %), as shown in **Figure 1b**.[6] Industry and household directly rely to proximately electrical power consumption. The transportation sector is undergoing dramatic changes: earlier dominated by combustion engines, it evolves towards electrified transport.
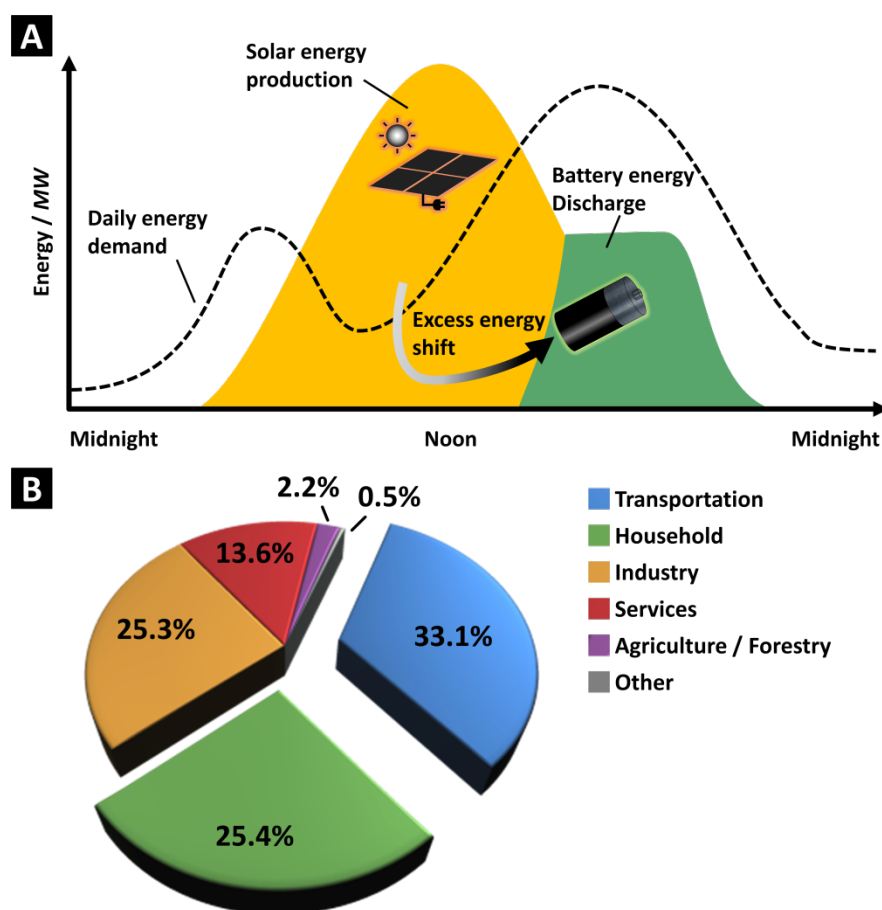
Figure 1. (**A**) Generalized schematic illustration of household energy demand versus supply from solar power: partially directly used or intermediately stored. (**B**) Percentage of final energy consumption within the EU-28 (status as of 2015, excluding energy used by power producers and energy conversation processes).Data taken from reference.[6]

In the EU-28, the market share of electric vehicles has more than quadrupled from 0.4 % (2013) to 1.7 % (2018) over the last five years, and continues to be on a rising trend.[7] The prevalent driving technology is electric, powered by large lithium ion battery arrays or H_2 fuel cells. Both

have the potential to operate climate neutral, provided that the "fuel" (current or H_2) is derived from renewable sources.

In summary, a potentially sustainable future energy economy faces two major challenges that have to be solved: (i) the climate-neutral production of energy and (ii) its efficient intermediate storage that aligns power supply and demand. The manufacturing of advanced functional materials by optimization of their (nano-)structure that improves their performance (e.g. longer battery lifetime, higher solar conversion efficiency) is consequently an important field of research along the way for "next generation" energy storage and conversion.

In this work, block copolymer (BCP) derived nanostructured materials are prepared and their performance in energy storage and energy conversion is discussed. First, general requirements and common challenges for energy materials are defined together with recent approaches and the current state of the art for electrochemical energy storage (**Chapter 2.1**) and photocatalytical conversion materials (**Chapter 2.2**). Potential strategies to apply a nanostructure on a desired material are summarized in **Chapter 2.3** and the criteria for the choice of macromolecular self-assembly are stated. To that end, the thermodynamics of BCP self-assembly and how they enable structure directing into one-dimensional (1D), two-dimensional (2D) or three-dimensional (3D) continuities are introduced in **Chapter 2.4**. With that background, the scope of this work is laid out in **Chapter 3**. The results are presented within **Chapter 4**, based on recent publications in relevant scientific journals. In closing, a summary including a critical review of the work is given in **Chapter 5** and a potential outlook for further research is depicted in **Chapter 6**.

2. THEORY AND STATE OF THE ART

2.1 Electrochemical energy storage

The enhanced human lifestyle has entailed tremendous rise in the number of (portable) electronics that usually have different requirements on their powering energy storage solution. Mobile phones and laptops, for instance, are optimized towards long lifetime and high storage capacity, while power tools require high power on demand. Energy storage systems thus are characterized based on their specific energy in Wh kg^{-1} that gives the amount of energy stored within. The rate at which the system can store and release energy is provided by the specific power in W kg^{-1}.[8] In portable devices, where space is limited, the aforementioned performance values are often normalized to the volume rather than the weight. Those two performance metrics, specific energy and specific power shown within one plot (i.e. known as Ragone plot) allows distinguishing different energy storage techniques, including capacitors, batteries, and hydro-pumped storages.

Batteries are, by far, the most popular electrochemical storage devices, mostly based on lithium (Li) ions techniques, yet, earlier solutions are still in use, such as lead acid (i.e. in cars) and alkaline batteries (i.e. in low-priced portable devices). A lithium ion battery (LIB) is typically composed of active materials (that contribute to the energy storage capacity) that are the electrodes, and inactive components, such as the electrolyte, current collectors (usually copper and aluminum), separator, (conductive) additives and cell housing (**Figure 2a**).
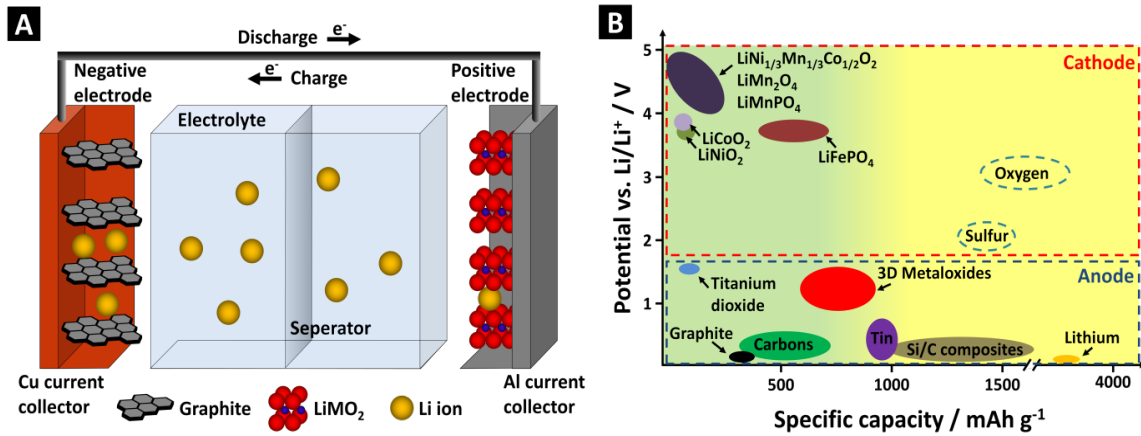
Figure 2. (**A**) Schematic model of a LIB with graphite as anode material and a Li metal oxide (here: $LiCoO_2$) as cathode. The facing electrodes are separated by an electrolyte and the separator. (**B**) Shows typical state of the art anode and cathode materials (green background) as well as promising technologies (yellow background) considered to come onto market, adapted from references.[9]

The active materials are Li intercalation materials, typically Li transition metal oxides on the cathode side, such as $LiCoO_2$,[10] $LiMn_2O_4$,[11] and $LiFePO_4$[12] that faces the anode, by default graphite.[13] A permeable membrane in-between prevents from short circuits and allows the ions to permeate within the organic or aqueous electrolyte.[14] The general mechanism for charging is given within **Equation 1 – 3** for $LiCoO_2$, a typical cathode material that has been initially proposed for its use in LIBs by the group of Goodenough in the early 1980s.[15]

$$LiCoO_2 \; \rightleftharpoons \; Li_{1-x}CoO_2 \; + \; x\,Li^+ + x\,e^- \qquad \text{Cathode} \qquad \textbf{Eq. 1}$$

$$C_6 \; + \; x\,Li^+ \; + \; x\,e^- \; \rightleftharpoons \; Li_xC_6 \qquad\qquad \text{Anode} \qquad\quad \textbf{Eq. 2}$$

$$C_6 \; + \; LiCoO_2 \; \rightleftharpoons \; Li_xC_6 \; + \; Li_{1-x}CoO_2 \qquad \text{Total cell reaction} \qquad \textbf{Eq. 3}$$
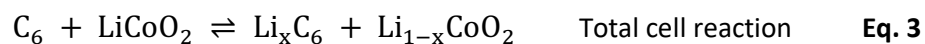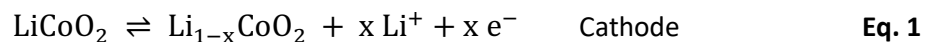
Per definition, an oxidation occurs at the anode during discharge; however, in secondary batteries also reduction takes place during charging. The rather historical designations 'anode' and 'cathode' derive from the exclusive existence of primary batteries at the beginning (that are limited to a single discharge) and are often replaced by 'negative' and 'positive' electrode,

respectively. The cell voltage of a typical LIB ranges from 2.5 V to 4.3 V (vs. Li/Li$^+$), depending on the particular choice of the electrode materials.[16] The product of the theoretical specific capacity in mAh g^{-1} of the materials and cell voltage determines how much energy can theoretically be stored. **Figure 2b** shows the specific capacity vs. the potential (vs. Li/Li$^+$) of common materials, including graphite (372 mAh g^{-1}), TiO_2 (anatase: 175 mAh g^{-1}), and $LiCoO_2$ (274 mAh g^{-1}).[9, 17] The actual specific capacity of LIBs is, however, distinctively lower, owing to a non-complete delithiation for commonly used materials, such as $Li_{1-x}CoO_2$ that is limited to x $\leq$ 0.5 (see **Eq. 1**).[10] It has been shown that manipulating the structure can increase that value towards more complete delithiation, thus offering higher capacity without changes in materials' composition.[9b] Graphite, often used on the anode side, usually completely releases intercalated ions, but suffers from slow charge/discharge rates. Solid electrolyte interface (SEI) formation on graphite limits the power performance.[17] The SEI comprises (electro-)decomposed components of the electrolyte and conductive salt that is formed during the first charge/discharge cycles.[18] To meet future demands, a combination of high capacity and fast intercalation kinetic is required. Transition metal oxides like TiO_2 and Nb_2O_5 emerged as attractive alternative anode materials owing to their superior rate capability and safer operation potential (~1.5 V vs. Li/Li$^+$) that prevents carbonate electrolyte degradation.[19] However, their semiconducting nature requires for the addition of additives that enable sufficient electronic conductivity. Conductive additives (generally ~ 5 – 20 mass %) along with current collectors, cell housing, and binder lowers the specific capacity by contributing usually more than 30 mass % of inactive material. In consequence, multiple approaches for free-standing (thus binder-free) electrodes have been followed, including electrospun inorganic fiber mats,[20] graphene and graphene composite paper electrodes,[21] and polymer derived inorganic networks.[22] Latter ones additionally allow the carbonization of the structure directing polymer to retain a thin carbon layer at the electrode|electrolyte interface. This *in-situ* carbonization in proximity of the active material enables optimized contact and high electronic conductivity that mitigates the need for conductive additives.[22-23] Such macromolecular templating (further

discussed in **Chapter 2.4**) can be tailored to obtain spatial nanostructures that provide percolating mesoporous network structures.[24] The beneficial electrolyte transport within the pores, shortened diffusion pathways, and large electrode|electrolyte interfaces allow for attractive rate handling (i.e. high capacity retention at elevated cycling currents).[25] The high and stable porosity of those network structures reduces diffusion limitations of the electrolyte within the pores and enables free-standing (i.e. binder-free), high density electrodes with superior areal and volumetric specific capacity compared to conventional admixing of nanoparticular oxides, binder, and additives casted as electrode.[22]

Another strategy in search for high performance energy storage solutions focuses on the realization of metallic lithium as anodes that offer a specific capacity far beyond the state of the art with 3862 mAh g^{-1} (**Figure 2b**).[26] Such systems are called lithium metal batteries (LMBs) and are often considered as the "next-generation" storage solution that enables, for instance, electrified transport in a range of current combustion engines. Yet, its use has been limited due to safety concerns such as its volatile reaction when exposed to air and dendrite formation; both may cause thermal runaway reactions.[26d, 27] This is even aggravated when using organic liquid electrolytes which are highly flammable, toxic, and potentially leak when the cell integrity is damaged. Polymer electrolytes, such as the most thoroughly investigated poly(ethylene oxide) (PEO), offer the potential to enable LMBs as they provide mechanical stability and flexibility that dramatically reduce a potential thermal runaway.[28] However, as of now, they suffer from insufficient ionic conductivity, especially at ambient temperature. PEO strongly coordinates Li ions at the ether oxygen, which couples ionic to polymeric mobility and leads to low conductivity.[29] Thereby, the cationic conductivity strongly correlates with the degree of crystallinity of PEO and thus, with temperature. Exceeding ~60 °C leads to an increased conductivity even for large PEO with molecular weights (M_W) of several hundred kg mol^{-1}, though common applications require an extended temperature tolerance. Electrolytes from pure PEO with lower M_W indeed have reduced crystallinity, but their mechanical performance is insufficient for battery application.[30] Recently,

block copolymers (BCPs) emerged as a promising strategy to solve this limiting trade-off.[31] They allow for a low molecular weight conductive block (i.e. PEO) embedded in a structured environment of macroscopically mechanically stable inactive blocks, i.e. poly(styrene) (PS) and poly(isoprene) (PI).[32] The microstructural order due to the self-assembling nature of particular BCPs preferentially lead to stretched PEO chains within this domain that further decreases the ionic association of Li ions and the ether oxygen and increases the mobility.[33]

To summarize, current state of the art of LIBs and LMBs offers a wide potential for a more advanced storage of energy that results in a plethora of reasonable approaches.[34] This work demonstrate (i) the potential use of a mesoporous, freestanding TiO_2/C hybrid anode[22] derived from a structure directing BCP and (ii) the direct use of tailored BCPs, exploring the critical metric for optimized trade-off between low molecular conductive block and extended macroscopic mechanical stability.[32]

2.2   Photochemical energy conversion

The concept of electrochemical energy storage as batteries has captured the market of portable electronics, electro mobility and bridging stationary energy storage. However, the current limitations in performance enable the rational consideration of promising alternatives such as the storage as chemical energy, i.e. via hydrogen (H_2). To date, the commercial production of H_2 is mostly derived from fossil resources and partially electrolysis of water.[35] Provided that the consumed energy is delivered by renewable sources electrolysis can be considered as sustainable. Yet, to mitigate energy loss due to such a multistage conversion until H_2 is obtained, photocatalysis provides a promising and green alternative.[36] Here, direct photon harvesting by a catalyst material provides the energy ($\Delta G^0 = 298 \text{ kJ mol}^{-1}$) to split water into its elements, H_2 and O_2.

The general mechanism of photocatalysis has been initially proposed for TiO_2 and is equal for all types of semiconductors (**Figure 3a**).[37] In a first step, (i) a photon at suitable energy, i.e. higher

than the band gap energy (E_G) of the semiconductor is adsorbed and creates an electron-hole pair (exciton). (ii) The hole (h^+) remains in the valence band (VB) while its counterpart electron (e^-) is excited into the conduction band (CB). After separation, (iii) the charge carriers migrate to the particle surface, usually promoted by the presence of a co-catalyst. (iv) Adsorption of reactants at the active centers allows the evolution of H_2 by combined reduction and oxidation of water.[38] Unfortunately, this depicted pathway is a competing reaction to (v) recombination that includes radiative or thermal relaxation of the created electron-hole pair instead of water decomposition.[39]

The performance metrics of a photocatalyst, such as the responsive excitation wavelength, the recombination rate, and the redox potential strongly correlates with the electronic band structure. To enable overall water splitting, a semiconductor needs to provide a flat band potential (i.e. the bottom of the CB) above the reduction potential of H^+/H_2 (*per definition* 0 V vs. SHE at pH = 0) and a VB edge that exceeds the oxidation potential of H_2O/O_2 (1.23 V vs. SHE at pH = 0). To that end, the minimum theoretical E_G required for water splitting reaction is ~ 1.23 eV, yet, distinct larger E_G are required for functional photocatalysis.[36c]
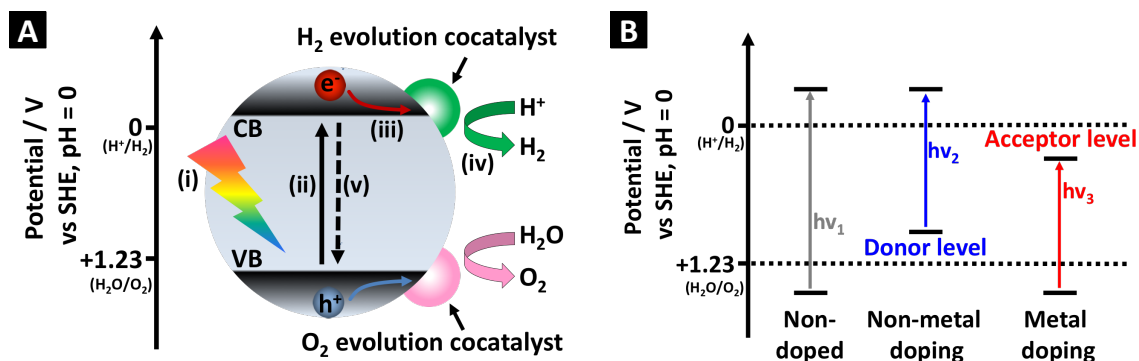
Figure 3. (**A**) Schematic representation of photocatalytic overall water splitting on a semiconductor particle: (i) the absorption of a photon creates an exciton that is (ii) excited to the conduction band. The charge carriers (iii) migrate to the active sites, usually the co-catalyst, and (iv) undergo degradation of water. Recombination (v) via thermalization or radiative relaxation is the competing reaction, generally desired to be mitigated. (**B**) Schematic modification of the original band gap (grey) via non-metal doping (blue) that forms states above the original VB and via metal heteroatoms (red) that gives rise to states below the CB.[36c]

The activity of photocatalysts is often quantified in a half-cell reaction from a model solution containing a sacrificial agent.[40] This is either an electron donor like alcohol which provides a lower oxidation potential (~0.82 eV vs. SHE) and becomes oxidized instead of water or electron acceptors such as silver nitrate (e.g. $AgNO_3$) which are alternate reduced.

Typical photocatalysts are semiconducting metal oxides; their CB and VB are composed of the oxygen's 2p-orbital and either a d^0 transition metal cation contributing an empty d-orbital or a d^{10} metal cation that has an empty s- or p-orbital.[41] The most thoroughly investigated semiconductor is TiO_2 (typically anatase - the photoctalytic most active morphology), owing to its abundance, non-toxicity, and superior performance.[42] Ongoing improvements includes its modification in terms of its shape,[21c, 43] exposed crystalline facets,[44] defect engineering,[45] and phase composition.[46]

Anatase TiO_2 has a typical E_G of $3.0 - 3.3$ eV and shows high and stable activity within the UV range ($\lambda < 400nm$).[39, 42, 46b, 47] To commercialize photocatalysis, high reactivity above 400 nm is required to exploit major parts of the solar spectrum. A prevalent approach is the introduction of

a heteroatom into TiO_2 that enables modification of E_G, including non-metal-doped TiO_2, metal doped TiO_2 and self-doped TiO_{2-x} (**Figure 3b**).[48]

The VIS response of non-metal doped TiO_2 derives from new energy levels above the valence band maximum (VBM), diverging explained as for instance in N-doped TiO_2: (i) Asahi et al.[49] claimed that the similar energy of N 2p and O 2p allows for hybrids that directly narrow the band gap. (ii) Irie et al.[50] described the partial replacement of O sites by N, giving rise to impurity energy levels above the original VBM. (iii) Ihara et al.[51] highlighted the importance of oxygen deficiency within the grain boundaries that enables VIS absorption; N-doping prevents the re-oxidation of the catalyst. These recent works demonstrate the importance of the doping mechanism distinction: N that substitutes for O forms shallow states above the VBM, in accordance to (i), while interstitial N preferentially creates isolated impurity states, as described in (ii).[52]

Metal-doped TiO_2's response in the VIS can be explained by the introduction of new energy levels, owing to the electron acceptor nature of the dopant or charge-compensating Ti^{3+}; both create states below the conduction band minimum (CBM).[53] The presence of Ti^{3+} also accounts for the bathochromic shift in absorption for self-doped TiO_{2-x}. A promising dopant is Nb that generally forms states within the original CB of (anatase) TiO_2. Charge-compensation via Ti^{3+} or surface functional peroxide groups gives rise to either bluish or yellowish samples, respectively, that show high activity under visible light.[54] High oxygen activity during calcination metal-doped TiO_2 can prevent Ti^{3+} formation, and oxygen interstitials mainly charge compensate for higher valent Nb cations and allow for visible light harvesting.[54a] Crucially, the amount of Nb introduced was found to alter its doping mechanism and thus the energetic structure: Nb substitutes isolated for Ti at low amounts and tends to cluster above 2.0 at.%.[55]

Beside the electronic structure, a morphology comprising a high surface area (e.g. small particles or porous systems) is desirable for high performance catalysis; however, such nanostructures often experience agglomeration/aggregation in heterogeneous catalysis. It was recently shown

that an ordered mesoporous $CsTaWO_6$ catalyst with 40 nm pore size outperforms those derived from a polaxamer with 5 nm average pore size – despite much lower surface area.[56] This highlights the importance of the reactants access to the active surface area that is either limited by its arbitrary decrease due to agglomeration or by potential pore diffusion limitation. An optimized morphology is thus always a trade-off between sufficiently high surface area for large catalyst|reactant interfaces and optimized porosity to mitigate pore diffusion limitation.[57]

In summary, energy conversion using solar light to produce H_2 offers a promising strategy in terms of a sustainable future energy economy. This work capitalizes on an optimized trade-off between sufficiently high surface area and suitable pore sizes that eliminate diffusion limitation via BCP derived mesoporous networked TiO_2. The model system is further developed towards response within the visible light via the introduction of Nb at different concentrations.

2.3   Nanomaterials for energy applications

Tremendous progress in the academic and technological fields has been achieved in the last decades by reducing sizes of functional solid materials to nanometers. The manipulation of the structure within the nanometer scale can thereby lead to advanced physical and chemical properties, owing to a dramatically increased surface area (along with higher surface to volume ratios),[58] extended mechanical integrity due to a reduced number of defects,[59] modified optical response owing to quantum confinement,[60] or optimized materials architecture (i.e. metamaterial-like behavior, exposed crystalline facets).[44a] This tailored preparation of nanostructures dramatically affects the performance in energy storage and conversion applications that are typically associated with physical and/or chemical reactions at the surface or interface, as depicted in **Chapter 2.1** and **2.2**. Smaller sizes can offer enhanced mass transport and a more efficient charge transfer, however, may also pose new challenges. For example, an

increased surface exposes more sites for charge recombination that lower the quantum efficiency (photocatalysis) and undersized pores may limit diffusibility of reactants or the electrolyte.

Nanomaterials are generally categorized based on the number of dimensions that are not confined to the nanoscale range (i.e. > 100 nm), e.g. fullerenes (0D - all dimensions are below 100 nm), nanotubes (1D – one dimension exceeds 100 nm), (mono-)layered structures (2D – two dimensions exceed 100 nm) and porous percolating networks (3D – all dimensions exceed 100 nm).[61]
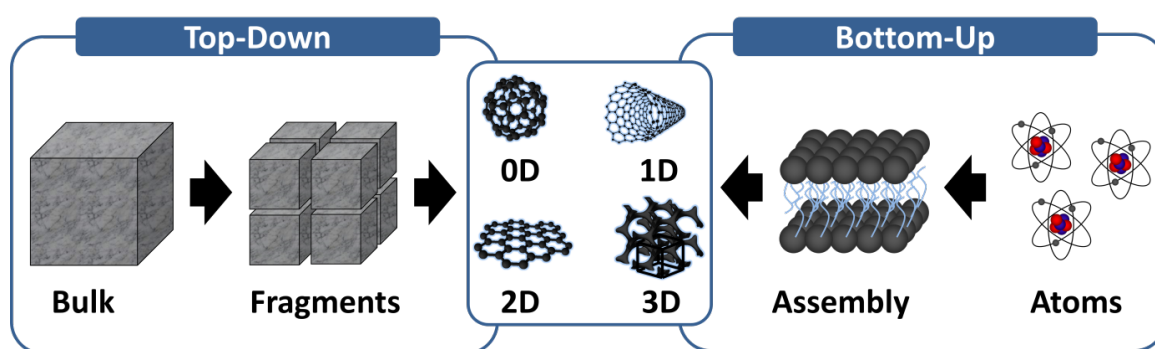
Figure 4. General illustration of nanomaterial preparation by top-down and bottom-up strategy. Nanostructures are categorized based on the number of dimensions, which are not confined to the nanoscale, including fullerenes (0D), nanotubes (1D), mono(layered) structures (2D) and percolating networks (3D).

The fabrication of such patterned nanostructures is either based on a top-down or a bottom-up approach (**Figure 4**), including (i) lithography, (ii) templated deposition, (iii) size reduction, (iv) replication against masters, and (v) self-assembly. **Table 1** summarizes representative applications for each pattern strategy and the general characteristic intrinsic limitations.

Table 1. Strategies for patterned nanostructure fabrication, exemplary applications, and their characteristic intrinsic limitation.

Pattern strategy	Examples	Limitations
Lithography UV / laser writing Stamping	Soft lithography via elastomeric masks[62] Nanoimprinting for circuits[63]	Time-consuming Defects (i.e. diffraction effects) Costly
Templated deposition Chemical vapor deposition Molecular beam epitaxy	Metal oxide nanotubes[21c, 64] Nanowire light emitting diodes[65]	Time-consuming Costly
Size reduction Exfoliation Etching	Low-defect graphene[66] Microcontact printing[67]	Reproducibility Low flexibility
Replication Mesoporous silica filling Embossing	Porous Li-ion electrodes[68] Multisegmental Nanorods[35]	Time-consuming (i.e. capillary filling) Low flexibility
Self-assembly Atomic layer deposition Macromolecular self-assembly	Porous Li-ion electrodes[23b] Nanophotonics[69] 3D battery[70] Mesoporous photocatalysts[56b, 57]	Defects (i.e. long-range order) Costly

A plethora of strategies for nanostructured materials has been reported and reviewed within the field of energy applications.[24-25, 71] My work focuses on the particular self-assembly bottom-up approach using macromolecular co-assembly with inorganic precursors that gives rise to 3D ordered porous percolating networks. The use of tailored block copolymers as structure directing agents represents a synthetic pathway that provides unique features:

(i)   A uniform porosity enables homogeneous mass transport within the (tunable) pores.[56b, 72]

(ii)   Structuring through the bulk reduces the surface area loss by agglomeration/aggregation, i.e. during electrode casting or in heterogeneous catalysis. This arbitrary decrease in active surface generally poses challenges for precise structure-property correlation.[57]

(iii) Percolating networks are desirable to enable high and homogeneous electron mobility.[70, 73]

(iv)   Different nanostructures can be prepared from the same components without dramatic changes[*] in synthesis protocol, enabling structure-performance correlation at high validity.[69, 74]

(v)   Reasonable time consumption at comparably low cost for the production of ordered nanostructures.

2.4   Macromolecular co-assembly

2.4.1 Introduction to macromolecular chemistry

Macromolecular chemistry was born in the 19th century by the successful cross-linking of natural rubber (also known as vulcanization) and the synthesis of resinous poly(styrene) (PS).[75] Important milestones in the next century towards commercialization were the launch of Bakelite, a plastic made from phenol and formaldehyde; the synthesis of poly(amide) (i.e. nylon),[76] and the organometallic catalyzed mass production of poly(ethylene).[77] Two models for polymer growth have been proposed:[78] (i) step-growth, by the inauguration of condensation of polyfunctional molecules, often under elimination of a small molecule (thermodynamically controlled),[79] and (ii) chain-growth, where initiation is required to produce reactive centers that add monomers successively (kinetically controlled).

Non-crosslinked polymers are categorized as branched or linear, dominated by the nature and number of reactive sites in the monomer unit, including dendrimers, star-shaped, comb-like and copolymers.[80] The physical behavior is usually derived from the monomer, but highly sensitive on the degree of polymerization. Usually this number varies for each polymer chain in a given sample, hence often expressed as an average. An ordinary arithmetic mean is the number average

---

[*]Usually, several microstructures are accessible from one BCP by optimization of the polymer to precursor ratio.

(M_n), determined from the individual polymer molecule masses (M_i) and the number of chains of that molecular weight (n_i), as defined in **Equation 4**. Taking into account that larger chains have a larger contribution to the properties than smaller ones, the molecular weight average (M_W) is used, given in **Equation 5**. The molecular weight distribution is further described by the dispersity index (D_P or DPI) as a ratio of M_W to M_N, see **Equation 6**.

$$M_N = \frac{\sum_i n_i M_i}{\sum_i n_i} \qquad\qquad \textbf{Eq. 4}$$

$$M_W = \frac{\sum_i n_i M_i^2}{\sum_i n_i M_i} \qquad\qquad \textbf{Eq. 5}$$

$$D_P = \frac{M_W}{M_N} \qquad\qquad \textbf{Eq. 6}$$

The closer the D_P to 1.0, the narrower the size distribution and hence the more uniform are the individual polymer chains. It can generally be influenced by synthesis parameters and polymerization techniques (i.e. radical, coordinative, and living anionic/cationic polymerization).

2.4.2 Thermodynamics of polymer mixtures

In binary mixtures of chemically different components, two phases may be formed, designated as macrophase separation. This behavior is well understood and thermodynamically described via the Gibbs free energy of mixing (ΔG_{Mix}), a temperature dependent dimension, further linked to the enthalpy of mixing (ΔH_{Mix}) and entropy of mixing (ΔS_{Mix}), given by **Equation 7**.

$$\Delta G_{\mathrm{Mix}} = \Delta H_{\mathrm{Mix}} - T\Delta S_{\mathrm{Mix}} \qquad\qquad \textbf{Eq. 7}$$

In polymer systems both, the enthalpy and entropy of mixing are described by the Flory-Huggins expression **Equation 8** and **Equation 9**.[81] This simplified model is based on the approximation that

individual polymer segments and solvent molecules occupy one particular place in a theoretical lattice.

$$\Delta S_{\text{Mix}} = -nR \left(\frac{\phi_A}{v_A N_A} ln(\phi_A) + \frac{\phi_B}{v_B N_B} ln(\phi_B) \right) \qquad \textbf{Eq. 8}$$

$$\Delta H_{\text{Mix}} = nRT \phi_A \phi_B \frac{\chi_{AB}}{v_0} \qquad \textbf{Eq. 9}$$

Here, ϕ_A and ϕ_B describe the volume fraction of polymer A and B, respectively, v_A and v_B the (molar) volume of the monomer segments, N_A and N_B the individual polymerization degrees, v_0 a reference (molar) volume (mostly $\sqrt{v_A v_B}$), n the mol of polymer, and R represents the ideal gas constant. χ_{AB} is the so called Flory-Huggins interaction parameter that describes the local interaction between both polymers A and B. Insertion of **Equation 8** and **Equation 9** into **Equation 7** results in the Flory-Huggins solution theory equation for polymer blends, given in **Equation 10**.

$$\Delta G_{\text{Mix}} = nRT \left(\frac{\phi_A}{v_A N_A} ln(\phi_A) + \frac{\phi_B}{v_B N_B} ln(\phi_B) + \phi_A \phi_B \frac{\chi_{AB}}{v_0} \right) \qquad \textbf{Eq. 10}$$

Miscibility of a binary solution requires a negative ΔG_{Mix}. Since the volume fractions ϕ_A and ϕ_B are below 1, and the polymerization degree N_A and N_B are usually large, the entropic contribution is always negative, but small and decreasing, for increasing molecular weight. In consequence, the mixing behavior of binary polymeric solutions mainly depends on the Flory-Huggins interaction parameter. It has a dimension inversely proportional to temperature and is negative for only specific attractive A-B monomer interactions (i.e. hydrogen bonding or π-π-electron interaction). Owing to that, the mixing behavior changes upon temperature increase towards miscibility (when $\chi_{AB} > 0$) or immiscibility (when $\chi_{AB} < 0$), respectively. Since both, the polymerization degree and χ_{AB} take identical effect when increasing their product, χN (segregation product) is a general dimension for the compatibility of a polymer mixture.

The high applicability of the Flory-Huggins solution theory for polymer blends has been proven by systematic investigations of deuterized and non-deuterized binary polyolefin mixtures.[82] Polymer blends that are not miscible undergo a macrophase separation, of which each phase is rich of one component. Provided that the initially homogeneous mixture was metastable, nucleation of one phase as spheres in the matrix of the other is necessary, growing over time. An instable blend spontaneously separates into two phases, with a structure originating from the originally concentration fluctuation. In contrast, compatible mixtures, such as PE and PS, typically provide new properties, for instance a new glass transition temperature (T_G), which is a threshold where a dramatic change in sequential polymer mobility is observed that lead to altered properties, e.g. an increased heat capacity.

2.4.3 Block copolymers

Copolymers are composed of at least two chemically different monomers covalently bond. Block copolymers (BCPs) contain repeating units arranged in blocks of which each block is only comprised of one component. The covalent bond impedes macroscopic phase separation. The simplest BCP is an AB diblock copolymer composed of two distinguishable blocks A and B, such as the most investigated system poly(styrene)-block-poly(isoprene) (SI).[83] Three parameters determine the separation of the two blocks into continuous microdomains, including (i) the volume fraction ϕ_A and ϕ_B, (ii) the polymerization degree N (with $N = N_A + N_B$), and (iii) the Flory-Huggins interaction parameter χ_{AB}. The latter specifies the degree of incompatibility between the blocks, dependent on the temperature (T), the Boltzmann constant (k_B), the number of nearest neighbors (z), and the interaction energies per repeating unit A-A (ε_{AA}), A-B (ε_{AB}), and B-B (ε_{BB}), as given by **Equation 11**.[83]

$$\chi_{AB} = \left(\frac{z}{k_B T}\right)\left[\varepsilon_{AB} - \frac{1}{2}(\varepsilon_{AA} + \varepsilon_{BB})\right] \qquad \textbf{Eq. 11}$$

With higher temperatures, χ_{AB} decreases and the increased compatibility leads to an order-to-disorder transition (ODT) at a temperature T_{ODT}. To minimize the unfavorable interaction between the blocks, microphase separation into continuous domains comprising exclusively one component occurs. This microphase separation leads to domains with dimension on the order of the radii of gyration. The enthalpic penalty scales with the area between the incompatible components that leads to limited freedom in arrangement. Consequently, the conformation of the chains deviates from an ideal freely-jointed chain towards elongation of the polymer chains away from the interface between the two blocks. The balance between counteracting minimization of interface area and chain stretching leads to highly ordered spatial microstructures, dominated in morphology by the particular volume fractions ϕ_A and ϕ_B, as illustrated by the cone-column model for morphological transition in **Figure 5**.[84]
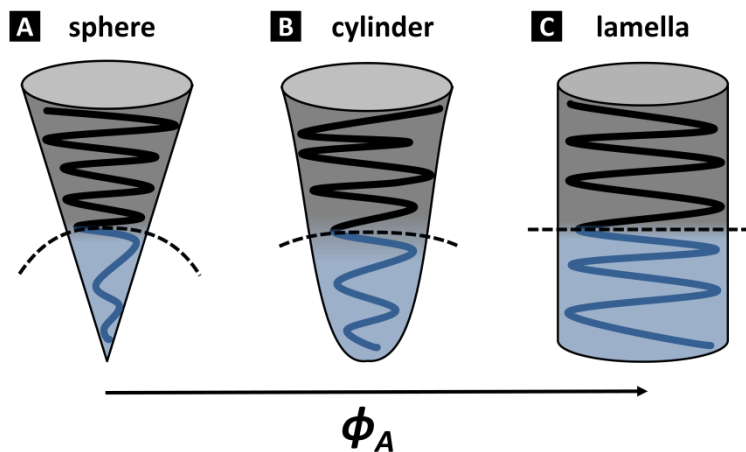
Figure 5. Cone-column model for morphological transition upon volume fraction increase of component A in an AB diblock copolymer up to ϕ_A = 0.5.[84] The dashed curve illustrates the interface between both components. Typical morphologies are (**A**) spheres, (**B**) cylinders, and as both volume fractions converge: (**C**) lamellae.

Theoretical descriptions of microphase separation define two distinguishable regimes in terms of the segregation product χN: the weak segregation limit (WSL, $\chi N \sim 10$)[85] and the strong segregation limit (SSL, $\chi N \gg 10$).[86] Within the WSL, sufficiently weak interaction leads to mostly unperturbed individual chains with a gradual phase boundary. In contrast, an interface comprising

both, A and B is negligibly thin (narrow interface approximation) in the SSL and rather sharp phase boundaries are observable. Both extremes have been connected using the "self-consistent field" (SCF) theory by Matsen and Bates, [87] revealing theoretical and experimental phase diagrams of BCP with immiscible blocks that microphase separate into different morphologies, including spheres (S), cylinders (C), bicontinious gyroidal networks (G) and lamellae (LAM) (**Figure 6**).[88] Despite high consensus between theoretical prediction and the experimentally observed equilibrium morphologies, deviation is caused by the ordinary non-uniform monomer aspect ratio and concentration fluctuations.
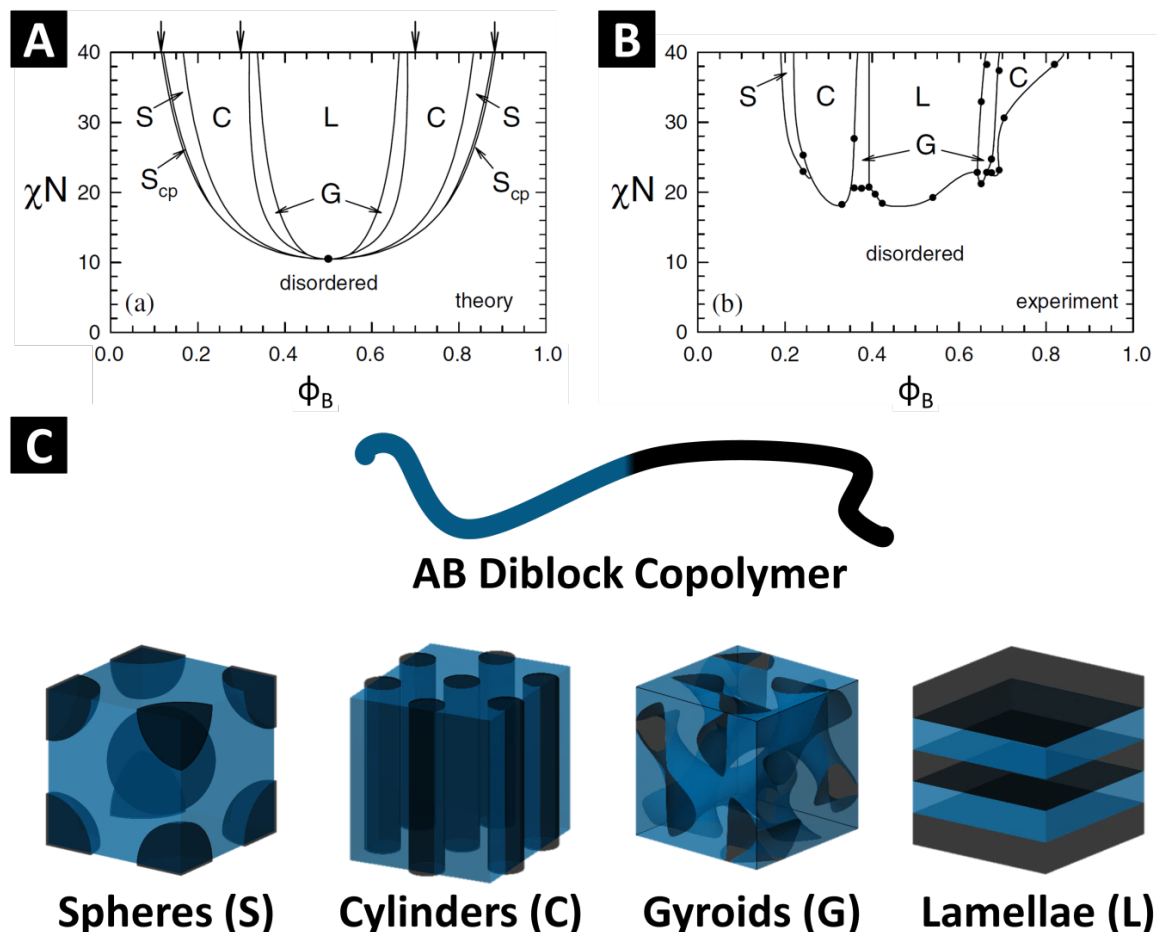
Figure 6. (**A**) Theoretical and (**B**) experimental phase diagram of poly(styrene)-block-poly(isoprene) as a typical AB diblock copolymer. Adapted with permission from reference.[88c] Copyright 2018 American Chemical Society. (**C**) Simulated equilibrium morphologies for different volume fractions ϕ_B (with $\phi_A + \phi_B = 1$). When the composition is inverted, morphological inversion takes place, where the major component forms a matrix that embeds the minor block.

With an increase in the number of blocks in linear BCPs, the variety of morphologies and their complexity is expanded.[89] The self-assembly of a linear ABC triblock copolymer, which contains three chemically distinguishable blocks A, B, and C, depends on three different interaction parameters (χ_{AB}, χ_{BC}, and χ_{AC}), the volume fractions of each block (ϕ_A, ϕ_B, and ϕ_C), as well as the total degree of polymerization N. Two categories are distinguishable for triblock copolymers: frustrated and non-frustrated ones. Non-frustrated ABC BCPs provide the highest χ for the interaction of block A and C, which are not directly covalently bonded, but separated by block B with distinctly lower χ ($\chi_{AB} \sim \chi_{BC} \ll \chi_{AC}$). Upon microphase separation, A-C interfaces are consequently avoided. In contrast, frustrated polymers are characterized by one interaction parameter of the neighboring blocks (χ_{AB} or χ_{BC}) being larger than χ_{AC}. The more favorable A-C interface allows for a broader morphological variety, including perforated lamellae.[90] This work will focus on the linear, non-frustrated BCP poly(isoprene)-block-poly(styrene)-block-poly(ethylene oxide) (ISO). Theoretical and experimental phase diagrams for an ideal ABC triblock copolymer and for this particular system have been pioneered by Bates et al., given in **Figure 7**.[91]
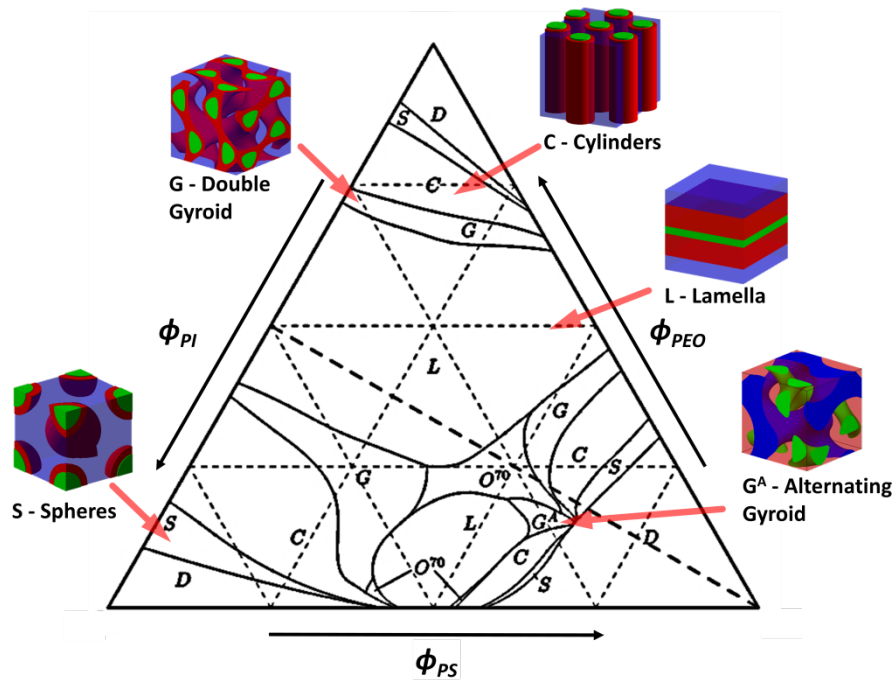
Figure 7. Theoretical, self-consistent-field theory (SCFT) derived phase diagram for a model ISO triblock copolymer with statistical segmental length (b) of b_I = 6.0 Å, b_S = 5.5 Å, and b_O = 7.8 Å and interaction parameter of $\chi_{\text{PI/PS}} N$ = 11.0, $\chi_{\text{PS/PEO}} N$ = 14.2, and $\chi_{\text{PI/PEO}} N$ = 45.8. Dashed lines show isopleth of ϕ_I and ϕ_O. Exemplary equilibrium morphologies are illustrated for ISO with poly(isoprene) in blue, poly(styrene) in red and poly(ethylene oxide) in green. Reproduced with permission of IOP Publishing in the format Thesis/Dissertation via Copyright Clearance Center.[91b]

Compared to diblock copolymers, the addition of a third block allows for core-shell arrangements, such as the core-shell double gyroid (G) or core-shell spheres (S), but alternating morphologies like for instance the alternating gyroid (G^A) are possible, too. Linear triblock copolymers, such as the ISO, offer high compatibility and tunability: three chemically different blocks can be selectively blended or selectively removed and backfilled. This offers a versatile way for templating many materials into highly ordered bicontinuous structures (further described in **Chapter 2.4.5**). The addition of a fourth or even more blocks further extends the variability of structures and opens "Pandora's box" of parameter space.[92]

2.4.4 Anionic polymerization

For its use as a template, the individual chains of a BCP have to be uniform in M_W of each block as well as overall; in other words, a low D_P is required. This is generally achieved by using sequential living (anionic) chain growth polymerization that includes cyclic ethers or vinyl functional groups on the monomer unit. In a first step, a reactive species, such as a carbanion or oxyanion, is generated by an initiator and propagates via nucleophilic addition to the monomer. To obtain molecular weight control, the initiation step must be faster or at least the same rate as the chain propagation; otherwise the first chains growth are longer than the subsequently initiated.[93] Initiation typically occurs via the nucleophile addition of organometallic compounds of alkali metals or by electron transfer from free alkali metals. Most important for the sequential living anionic polymerization of ISO is the use of lithium organic compounds in non-polar solvents that promotes an insertion mechanism via π-complex formation.[91a, 94] **Equations 12–14** summarize the mechanism of anionic polymerization, including a nucleophilic initiator (I$^-$), a monomer (M), at constant reaction rate k_{obs}, and an electrophilic, terminating species (T$^+$).

$$\mathrm{I^- + M \rightarrow IM^-} \qquad \text{Initiation (fast)} \qquad \textbf{Eq. 12}$$

$$\mathrm{IM_n^- + M \xrightarrow{k_{obs}} IM_{n+1}^-} \qquad \text{Propagation, n= 1,2,3, …} \qquad \textbf{Eq. 13}$$

$$\mathrm{IM_n^- + T^+ \rightarrow IM_nT} \qquad \text{Termination (fast)} \qquad \textbf{Eq. 14}$$
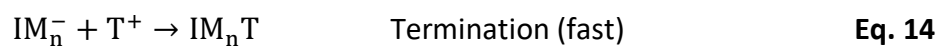
Without impurities, there is no transfer reaction or termination expected that allows for a low dispersity. The concentration of living chains thus equals the initial concentration of the initiator $[I]_0$ and the monomer concentration [M] at a time $t = \tau$ that can be derived from **Equation 15**.

$$[\mathrm{M}]_\tau = [\mathrm{M}]_0 \exp(-k_{\mathrm{obs}}[\mathrm{I}]_0\,\tau) \qquad \textbf{Eq. 15}$$

Chain-growth proceeds until all monomers are consumed and further addition of any monomer species results in propagation of chain growth that enables the synthesis of block copolymers. **Figure 8** illustrates the sequential living anionic polymerization of ISO according to the synthesis in this work.
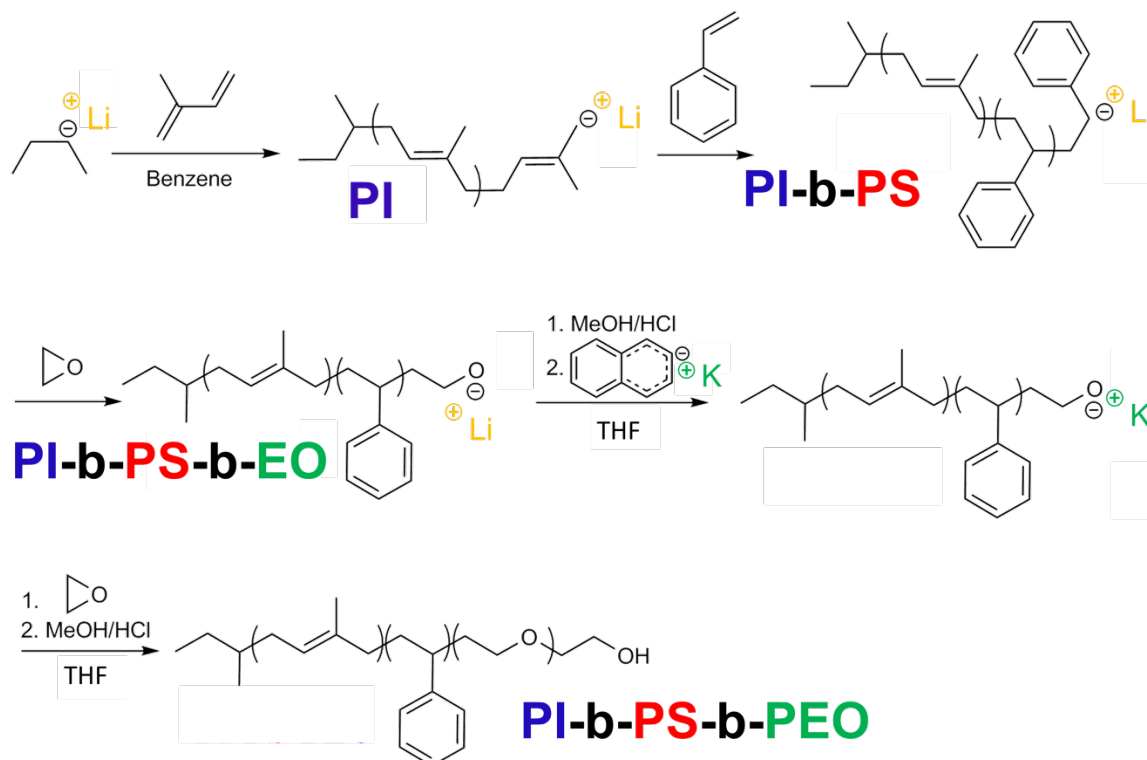
Figure 8. Reaction scheme for the preparation of ISO (PI-b-PS-b-PEO) via sequential anionic polymerization. The PI-b-PS-b-PEO triblock copolymer is prepared through reinitiating associated with a counterion exchange of the parent diblock PI-b-PS.

The parent diblock copolymer poly(isoprene)-block-poly(styrene) (*short*: PI-b-PS) is prepared in non-polar benzene using sec-butyllithium (*short*: sec-BuLi) as nucleophilic initiator and subsequent addition of isoprene and styrene monomers.[94-95] Chain growth proceeds via an insertion mechanism that favors the formation of (1,4)-isomers of PI, yet, typically a minor amount of (3,4)-isomers (~10 %) can be found. The parental PI-b-PS diblock copolymer is end-functionalized by an excess of ethylene oxide (*short:* PI-b-PS-b-EO); no further propagation is observed owing to the strong oxyanion lithium-interaction. The PI-b-PS-b-EO is terminated by methanolic hydrochloric acid and the counterion is exchanged. Washing of the precipitated

lithium chloride and reinitiation through deprotonation with potassium naphthalenide accomplishes the cation exchange. In the more polar solvent tetrahydrofuran (THF) PEO is polymerized. The living chains are end-functionalized with a hydroxyl group by methanolic hydrochloric acid that yields the final hydroxyl end-functionalized ISO (PI-b-PS-b-PEO).

2.4.5 Block copolymer co-assembly

The requirements for functionality of the materials in energy storage and conversion go far beyond those of pure polymers. To meet this advanced requirements hybrids of block copolymers and inorganic materials that comprise a well-defined structure on the scale of 10 - 100 nm have been explored.

First efforts have been made with organic molecule self-assembly[96] to produce nanostructured silicates that have been extended by the use of anionic surfactants (i.e. Pluronics[†]),[97] and non-ionic low-molecular weight BCPs.[98] Macromolecular co-assembly with large-molecular weight BCPs only soluble in organic solvents has been pioneered by Wiesner et al. for an organically modified aluminosilicate.[99] An amphiphilic diblock copolymer PI-b-PEO was used to form well-ordered mesostructures through evaporation induced self-assembly with (3-glycidyloxypropyl-)trimethoxysilane (GLYMO) and aluminum sec-butoxide. In the last two decades, the range of BCP derived mesostructured functional materials has drastically evolved, including transition metal oxides,[73, 100] carbons,[72, 101] and metals.[102]

Generally, the macromolecular co-assembly occurs via selective attractive interaction (e.g. hydrogen bonding, ionic/polar/coordination interactions) between one block of the BCP and the additive(s). Examples include organometallic precursors (e.g. for transition metals), low

---

[†] Pluronics is a trademark of BASF for their poloxamers that are nonionic triblock copolymers. The general structure is $(PEO)_a$-$(PPO)_b$-$(PEO)_a$ with a= 2-130 and b = 15-67.

molecular weight oligomers (i.e. for carbons), and (surface-modified) nanoparticles (i.e. for metals and transition metals or ceramics). It has been shown that the upper size of the additive is limited to be smaller than the radius of gyration of the attracting block to prevent segregation.[102b, 103]

Varying the amount of precursor that selectively swells one block provides a well-controllable pathway to achieve different hybrid mesostructures that would be expected along the PEO isopleth in the ABC terpolymer phase diagram,[91b] as illustrated in **Figure 9** for ISO.[104]
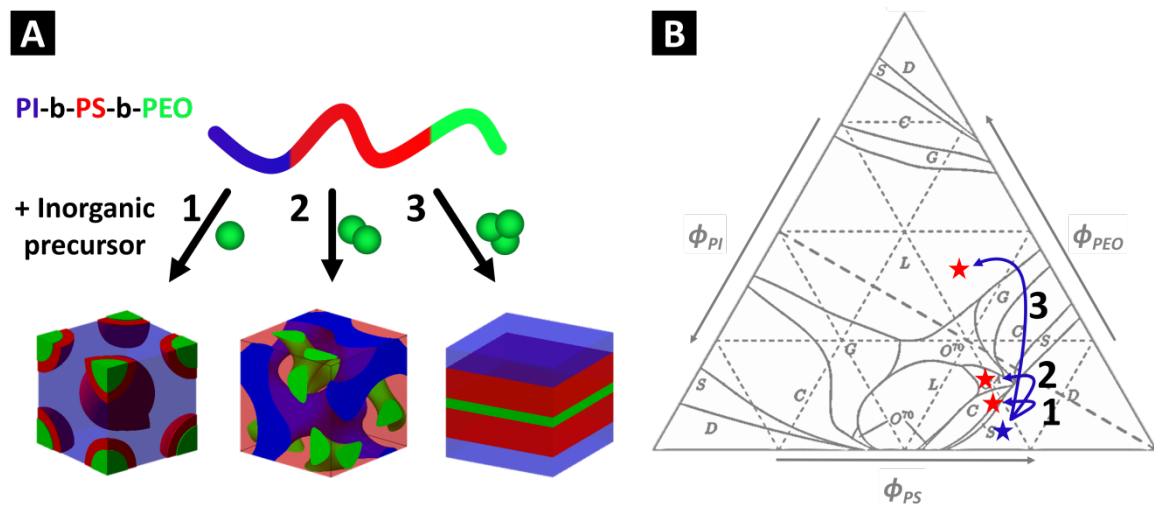
Figure 9. Illustration of the pathway for various morphologies by (**A**) varying the amount of inorganic precursor that selectively swells the PEO block (green) of an ISO. (**B**) Structures that would be expected are located along the PEO isopleth in the theoretically ISO phase diagram. Reproduced with permission of IOP Publishing in the format Thesis/Dissertation via Copyright Clearance Center.[91b]

Although multiple structure-directing BCPs are available, in this work ISO was chosen, owing to several key features that include: (i) the compatibility of the PEO block with a plethora of hydrophilic inorganic precursors for functional energy materials (i.e. organometallics, conductive lithium salts, and phenolic resins). (ii) Compared to diblock copolymers, a triblock copolymer allows for an extended accessibility of structures even with a minority volume fraction of one block (i.e. using diblock copolymer, a lamellar morphology would require at least one $\phi \geq 0.4$ as seen from **Figure 6a**). (iii) The phase diagram of ISO suggests percolating networked structures with homogeneous porosity (e.g. G^A) to be more frequent.

The BCP co-assembly results in polymer-inorganic hybrids that allow for their direct use in device applications or enable additional modifications, including carbonization of the organic template or complete removal, to obtain porosity and readily access to the inorganic materials functionality.

3. SCOPE

Nanostructured materials that combine percolating networks for enhanced transport properties and large porosities that mitigate diffusion limitations are essential for energy storage and conversion applications. This thesis highlights the use of ordered functional energy materials derived from BCP co-assembly as a powerful tool towards superior performance in device applications (**Figure 10**).
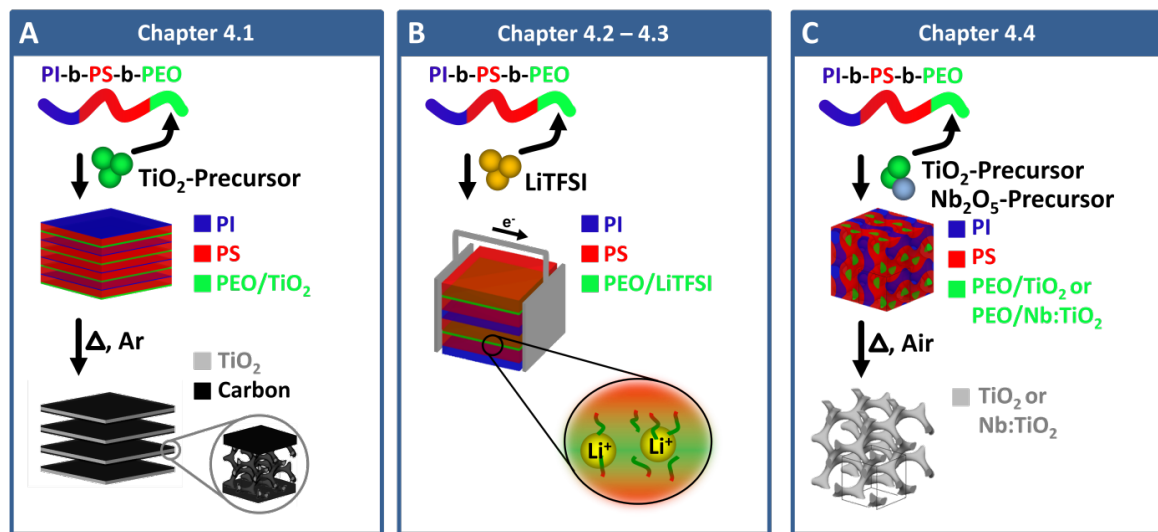
Figure 10. Summarized illustration of conducted post-treatment of self-assembled polymer-inorganic hybrids. (**A**) Strategy of **Chapter 4.1**: carbonization of the structure directing template that *in-situ* generates a conductive carbon layer on the active material. (**B**) Strategy of **Chapter 4.2–4.3**: direct use of the hybrid as BCE. (**C**) Strategy of **Chapter 4.4**: complete polymer removal after structure formation that enables photocatalysis on the active material.

Chapter 4.1 shows the BCP co-assembly of ISO with a titanium dioxide (TiO_2) precursor that yields an interesting material for LIB anode materials due to TiO_2's safe operation potential (compared to graphite) in combination with attractive intercalation kinetics. The mesoporous microstructure enables superior electrolyte transport and thus shortened ion diffusion pathways. To obtain such porosity, the polymer has to be removed after self-assembly, yet, the general insufficient electrical conductivity of an oxide can be compensated by *in-situ* carbonizing of the macromolecular template to a thin conductive carbon layer (**Figure 10a**). High mechanical integrity allows for

ultrathick (300 μm) and dense (0.88 g cm^{-3}), freestanding TiO$_2$/C monoliths that (i) benefit from reduction of inactive components, (ii) provide unprecedented high areal and volumetric capacity, and (iii) show high rate capability.

Chapter 4.2 reports on an ISO block copolymer that is selectively loaded with conductive lithium bis(trifluoromethane-sulfonyl)imidate (LiTFSI) in the PEO phase. Here, the ISO is an essential part of the functional material, and no further removal of the structure-directing agent is required (**Figure 10b**). Dissolving of an optimized amount of LiTFSI leads to an ionic conductivity within the lamellar oriented PEO domain in the self-assembled hybrid. Crucially, the $M_{W,PEO}$ is designed to be the minor component of the BCP; PI and PS provide macroscopic mechanical integrity. The combined functionality over a broad temperature range of this self-assembled BCP/LiTFSI hybrid allows for its stable use as block copolymer electrolyte (BCE), potentially in LMBs and LIBs. The beneficial stretched chain arrangement within the self-assembled PEO/LiTFSI domain and a modified coordination of Li that deviates from classical two ether oxygen coordination allowed unprecedented high ionic conductivity. This suggests the decoupling of ionic mobility from slow polymer relaxation. Conductivity that derives from Li$^+$ being transported through accounts thereby for 70% of the total conductivity (compared to < 20% in pure PEO electrolytes with additionally several decades lower conductivity). The concept of such an ultra-small block containing BCEs represents a promising strategy to enable safer LMB operation, crucially, even at low temperatures.

In **Chapter 4.3**, the focus was placed on the interplay of PEO block size and conductivity, electrochemical stability and mechanical integrity. The PEO block size was varied between 2 kg mol^{-1} and 53 kg mol^{-1}, while the PI:PS ratio was kept constant. We found that a lamellar microstructure usually depicted the highest conductivity. $M_{W,PEO}$ as high as 53 kg mol^{-1} had similar performance than commercial PEO electrolytes, however, the benefits of BCP self-assembly allowed distinct improved cationic conductivity. Decreasing to 7 kg mol^{-1} deteriorates the overall

performance, but along with increased Li^+ contribution to the overall conductivity. Most importantly, we found that below 5 kg mol^{-1}, and especially with a $M_{W,PEO}$ of 2 kg mol^{-1}, the BCEs tend to be optimized towards high and stable conductivity between -20 °C and 90 °C and superior cationic contribution as high as 70%. The chemical stability vs. lithium, high mechanical integrity, and electrochemical durability indicates the concept of an ISO based BCE with ultra-small PEO block size is highly promising to realize the "next-generation" of batteries that capitalize on the high specific capacity of lithium metal.

In applications that require direct access to the active materials surface, the structure directing polymer can be thermally removed, as for instance in photocatalysis for energy conversion that is presented in **Chapter 4.4.** Pure and Nb-doped TiO_2 catalysts with a highly ordered alternating gyroid architecture and well-controllable mesopore size were prepared (**Figure 10c**). The polymer template has to be removed to enable photon harvesting and surface redox reaction towards H_2 evolution. By optimization of the temperature protocol for calcination, a crystalline semiconductor oxide with highly preserved G^A morphology was obtained. In typical hydrogen evolution experiments under UV, our pure G^A-TiO_2 outperformed comparable TiO_2 catalysts from literature and even the benchmark P25-TiO_2 more than 5-fold. We ascribed the performance to the loss of diffusion limitation that gave access to the large surface area, while compartmentalization of the material by ~15 nm particles allowed for inter-grain charge transfer that dramatically reduced recombination rate. Visible light activity was achieved via the introduction of the metal dopant Nb that led to clustering at higher dopant amounts (i.e. 3 at. %) and created shallow trap states. Those trap states diminished dramatically the activity independent from the excitation wavelength. In contrast, at low Nb contents (i.e. 1 at. %), the VIS activity was 3-fold increased due to the discrete energy levels introduced. This model system represents the superior performance of an ordered mesostructure which (i) is an optimized trade-off between pore accessibility and high surface area, while (ii) the percolating network enables high charge mobility, and (iii) even further light-material interaction are expected.

4.   RESULTS AND DISCUSSION

Chapter 4.1

Ordered Mesoporous Titania/Carbon Hybrid Monoliths for Lithium-ion Battery Anodes with High Areal and Volumetric Capacity

Chapter 4.2

An Ambient Temperature Electrolyte with Superior Lithium Ion Conductivity based on a Self-Assembled Block Copolymer

Chapter 4.3

Self-Assembled Block Copolymer Electrolytes: Enabling Superior Ambient Cationic Conductivity and Electrochemical Stability

Chapter 4.4

Ordered Mesoporous TiO_2-gyroids: Effects of Pore Architecture and Nb-doping on Photocatalytic Hydrogen Evolution under UV and VIS irradiation

Chapter 4.1

Ordered Mesoporous Titania/Carbon Hybrid Monoliths for Lithium-ion Battery Anodes with High Areal and Volumetric Capacity

Tobias S. Dörr,[1,2] Simon Fleischmann,[1,2] Marco Zeiger,[1,2] Ingrid Grobelsek,[1] Peter W. de Oliveira,[1] and Volker Presser[1,2,*]

[1]INM - Leibniz Institute for New Materials, Campus D2 2, 66123 Saarbrücken, Germany
[2]Saarland University, Campus D2 2, 66123 Saarbrücken, Germany

Abstract

Free-standing, binder-free, and conductive additive free mesoporous titanium dioxide/carbon hybrid electrodes were prepared from co-assembly of a poly(isoprene)-block-poly(styrene)-block-poly(ethylene oxide) block copolymer and a titanium alkoxide. By tailoring an optimized morphology, we prepared macroscopic mechanically stable

300 mm thick monoliths that were directly employed as lithium-ion battery electrodes. High areal mass loading of up to 26.4 mg cm^{-2} and a high bulk density of 0.88 g cm^3 were obtained. This resulted in a highly increased volumetric capacity of 155 mAh cm^3, compared to cast thin film electrodes. Further, the areal capacity of 4.5 mAh cm^2 represented a 9-fold increase compared to conventionally cast electrodes. These attractive performance metrics are related to the superior electrolyte transport and shortened diffusion lengths provided by the interconnected mesoporous nature of the monolith material, assuring superior rate handling, even at high cycling rates.

CHEMISTRY
A European Journal
Communication

■ Energy storage | *Hot Paper* |

Ordered Mesoporous Titania/Carbon Hybrid Monoliths for Lithium-ion Battery Anodes with High Areal and Volumetric Capacity

Tobias S. Dörr,[a, b] Simon Fleischmann,[a, b] Marco Zeiger,[a, b] Ingrid Grobelsek,[a] Peter W. de Oliveira,[a] and Volker Presser*[a, b]

Abstract: Free-standing, binder-free, and conductive additive-free mesoporous titanium dioxide/carbon hybrid electrodes were prepared from co-assembly of a poly(isoprene)-block-poly(styrene)-block-poly(ethylene oxide) block copolymer and a titanium alkoxide. By tailoring an optimized morphology, we prepared macroscopic mechanically stable 300 μm thick monoliths that were directly employed as lithium-ion battery electrodes. High areal mass loading of up to 26.4 mg cm^{-2} and a high bulk density of 0.88 g cm^{-3} were obtained. This resulted in a highly increased volumetric capacity of 155 mAh cm^{-3}, compared to cast thin film electrodes. Further, the areal capacity of 4.5 mAh cm^{-2} represented a 9-fold increase compared to conventionally cast electrodes. These attractive performance metrics are related to the superior electrolyte transport and shortened diffusion lengths provided by the interconnected mesoporous nature of the monolith material, assuring superior rate handling, even at high cycling rates.

In the growing field of long-lasting and stable performing mobile electronics and electrified transportation, lithium-ion batteries (LIBs) find widespread use in rechargeable energy storage systems.[1] LIBs commonly employ a graphite anode and a lithium metal oxide cathode.[2] Energy is stored by Faradaic intercalation reactions of lithium ions into the layered structure of the graphite anode during the charging step. The relatively slow lithium ion diffusion into the host material limits the power performance of the device.[3] However, to meet future demands, a combination of high overall energy density with fast charge/discharge rates is required. To that end, transition metal oxides like TiO_2,[4] $Li_4Ti_5O_{12}$,[5] and Nb_2O_5[6] emerged

as attractive alternatives to graphite anode materials, because of their superior lithium intercalation kinetics and safer operation potential, above the lowest unoccupied molecular orbital of the carbonate electrolytes.[7] The insufficient electrical conductivity of such oxides is typically addressed by admixing of 5–20 mass % carbon conductive additive, forming an electrode with 5–10 mass % polymer binder to achieve mechanical stability. The high total amount of electrochemically inactive material, up to 30 mass %, drastically decreases the specific capacity per mass of the final electrode, which is why binder-free and free-standing electrodes can offer advantages.[8] This is even more pronounced for the volumetric and areal capacities since the mixing process with a conductive additive and polymer binder yields comparably low electrode densities. High electrode density and areal loading of active material are considered crucial for a transfer to practical electrochemical energy storage applications.[9] While many studies report outstanding gravimetric performance values for thin film electrodes with loadings often below 1 mg cm^{-2}, the mass of current collectors, separator, electrolyte, and housing are often neglected. Considering the added mass of these device components, thin and/or hollow electrodes become far less attractive since only areal mass loadings above 10 mg cm^{-2} are attractive for actual applications.[9, 10] However, increasing the thickness and mass loading of electrodes often substantially decreases the electrode performance because of limitations posed by electrolyte transport and increased overpotentials, if no well-designed 3D electrode architecture is applied.[10, 11]

Ordered mesoporous metal oxides have been shown to offer attractive rate handling characteristics due to the beneficial electrolyte transport shortened diffusion paths in their mesopore network.[12] In a study of Jiao et al., mesoporous lithium manganese oxide was synthesized by a hard-templating approach.[13] The obtained material possessed a uniform pore size distribution around 5 nm with a low wall thickness of 7–15 nm, leading to attractive rate capability as LIB cathodes when admixed with a binder and a conductive additive.[13] Lee et al. demonstrated an approach of direct hybridization of mesoporous titanium oxide with carbon by co-assembly of a diblock copolymer structure directing agent for uniform mesopores up to 7 nm and higher specific surface areas (>100 m^2 g^{-1}).[14] They further demonstrate that preservation of the polymeric template as a thin carbon shell around the electrode core material framework (e.g., TiO_2, $Li_4Ti_5O_{12}$) increases the conductivity and maintains the 3D network at the same

[a] T. S. Dörr, S. Fleischmann, Dr. M. Zeiger, Dr. I. Grobelsek, Dr. P. W. de Oliveira, Prof. Dr. V. Presser
INM–Leibniz Institute for New Materials
Campus D2 2, 66123 Saarbrücken (Germany)
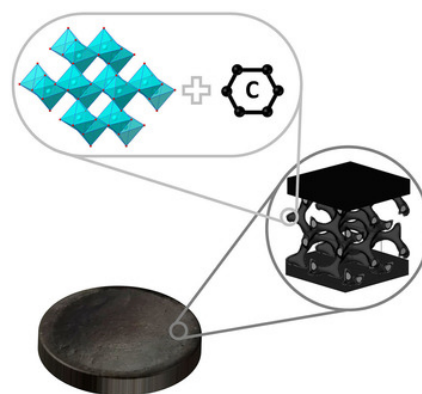E-mail: volker.presser@leibniz-inm.de

[b] T. S. Dörr, S. Fleischmann, Dr. M. Zeiger, Prof. Dr. V. Presser
Saarland University, Campus D2 2, 66123 Saarbrücken (Germany)

📄 Supporting information for the manuscript, and the ORCID identification
⬡ number(s) for the author(s) of this article can be found under https://doi.org/10.1002/chem.201801099.

time.[3, 15] Thin films of this material, cast on a current collector using a polymer binder, showed good rate handling as a LIB anode material.

Though the described materials showed attractive gravimetric performances when cast as thin film electrodes, the resulting low electrode density and limited mass loading yield low volumetric and areal capacities. In this study, we report for the first time on free-standing, binder and conductive additive-free mesoporous TiO_2/carbon hybrid monoliths (TiO_2/C) that form electrodes without further preparation processes. By creating an optimized pore structure, we obtained mechanically stable 300 µm thick electrodes with unprecedentedly high areal mass loadings of up to 26.4 mg cm^{-2}. Capitalizing on the high density, mass loading, and additive-free character of these hybrid electrodes, improved areal and volumetric capacities were obtained, compared to electrodes prepared using conventional mixing of mesoporous TiO_2 (gyroidal TiO_2), conductive additive, and binder. The synthesis can easily be adapted to other Faradaic materials, underlining the high suitability of our one-pot approach to obtain well-designed 3D electrode structures feasible for practical applications.

Our approach for the synthesis of mesoporous structured TiO_2/carbon hybrids and gyroidal TiO_2 by macromolecular co-

assembly of a poly(isoprene)-block-poly(styrene)-block-poly-(ethylene oxide) (ISO) and a titanium alkoxide is illustrated in Figure 1 A. Further details on the synthesis (including materials and methods) are found in the Supporting Information. The block copolymer (BCP) template was synthesized by living anionic polymerization and comprised 30, 60, and 10 vol% polyisoprene (PI), polystyrene (PS), and polyethylene oxide (PEO), respectively, with a narrow polydispersity of 1.09 and an overall molecular weight of 61,000 g mol^{-1}. Through evaporation-induced self-assembly (EISA), microphase separation occurs due to the internal repulsion of the unique polymer blocks into pure phase domains; of those the PEO is exclusively swelled by the hydrophilic metal oxide precursor sol.[16]

By changing the conditions during the pyrolysis, we could selectively choose to 1) preserve the organic polymer template as a carbon shell around the TiO_2 core material to obtain monoliths (500 °C/700 °C, argon atmosphere; samples TiO_2/C-500 and TiO_2/C-700) or 2) completely remove the BCP (400 °C, air, sample gyroidal TiO_2), resulting in mesoporous TiO_2 particles. Although the ISO was initially designed to preferably direct into gyroidal morphology (as it was indeed done for the gyroidal TiO_2), we found that for free-standing electrodes comprising a conductive carbon shell, a mixture of lamellar and gyroi-
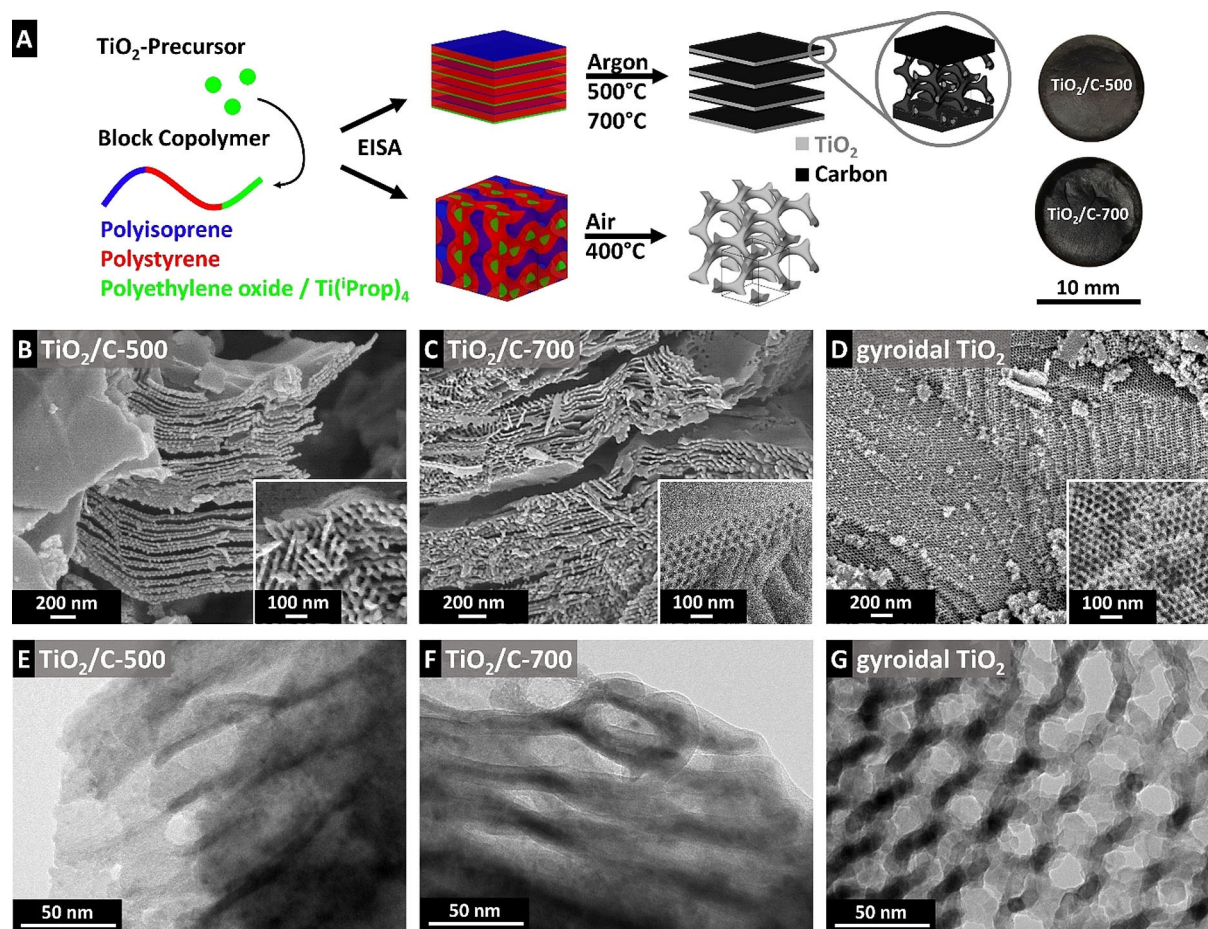
Figure 1. (A) Schematic of the TiO_2/C and gyroidal TiO_2 preparation via evaporation induced self-assembly (EISA) of the ISO BCP and Ti(iProp)$_4$. Variation of the pyrolysis atmosphere can selectively preserve a conductive carbon shell. Photographs of the freestanding TiO_2/C-500 and TiO_2/C-700 electrodes are shown. (B–D) Scanning electron micrographs and (E-G) transmission electron micrographs of TiO_2/C-500, TiO_2/C-700, and gyroidal TiO_2.

dal material provides much higher macroscopic mechanical stability. Earlier studies have highlighted the transition and the coexistence of a lamellar and a gyroidal phase, designated as hexagonally perforated lamellar (HPL).[17] We assume that the complexity and internal stress of pure gyroidal morphology, with its high amount of grain boundaries, are adverse for a free-standing electrode, although the carbon shell was expected to support the networked TiO_2. Therefore, we have adjusted the swelling of the PEO phase by adding adequate amounts of the metal organic precursor, to yield a structure combining the stability of the less complex lamellar morphology with partially mesoporous character in the individual lamella. Such a structure was not possible to synthesize without the supporting carbon shell since the carbon condensates in the deeper region of the lamellae and thus allows them to be covering the particle surface. In the case of complete thermal removal of the BCP, the TiO_2 lamellae simply collapse, ultimately leading to a powder sample. Accordingly, we used a mesoporous alternating gyroidal TiO_2 to compare the electrochemical characterization of TiO_2 with or without hybridized carbon.

Electron micrographs of the pyrolyzed material show the primary lamellae order of the free-standing TiO_2/C hybrids with partial additional secondary interlamellar porosity; the latter is very similar for TiO_2/C-500 and TiO_2/C-700 (Figure 1 B–G). The average interlamellar distance is about 40 nm, as seen from transmission electron micrographs. This value is identical for TiO_2/C-500 and TiO_2/C-700, thereby suggesting no significant difference in the carbon contents. All samples are composed of randomly oriented nanometer-sized TiO_2 domains, covered by a shell of disordered carbon in case of samples pyrolyzed in argon. We assume that the combination of the polycrystalline

character of TiO_2 in combination with the high structural stress of the gyroidal morphology causes insufficient macroscopic stability of pure gyroidal samples, independent of the presence of an additional supporting carbon shell. The elemental analysis by energy dispersive X-ray spectroscopy (EDX) is found in Supporting Information, Table S1.

Results of the small-angle X-ray scattering (SAXS) characterization for the ISO/precursor, TiO_2/C hybrids, and gyroidal TiO_2 are depicted in Figure 2 A. From the first diffraction (q^*), allowed q/q^* ratios for lamellar ($q/q^* = 1, 2, 3, \ldots$) and alternating gyroidal ($q/q^* = 1, \sqrt{3}, \sqrt{4}, \sqrt{5}, \ldots$) morphology are calculated and given above the corresponding pattern.[18] Based on our strategy, sufficient macroscopic stability is achieved for a lamellar ordered sample, preserving partial porosity inside the unique lamellae. The result is an ISO/precursor (TiO_2/C) hybrid comprising lamellar and alternating gyroidal scattering peaks in first and second order well perseverd during pyrolysis.[17a] The periodicity ($d_{spacing}$) decreases during the thermal treatment from 44.8 nm of the ISO/precursor (TiO_2/C) hybrid to 33.4 and 32.2 nm, for TiO_2/C-500 and TiO_2/C-700, respectively, evidenced by a shift of q^* towards higher q-values. Very similar behavior is observed for just gyroidal TiO_2, where the ISO/precursor hybrid exhibits a unique scattering, further identified as typical gyroidal diffractions. As expected, a smaller $d_{spacing}$ of 38.7 nm for the ISO/precursor (gyroidal TiO_2) hybrid was found, and we observed a further decrease to 29.8 nm due to the thermal shrinking during calcination.[17a]

The mesoporous morphology is additionally studied by nitrogen gas sorption (Supporting Information, Figure S1 A). Both TiO_2/C hybrids show identical hysteresis shape at high relative pressures, indicating a similar level of mesoporosity in good
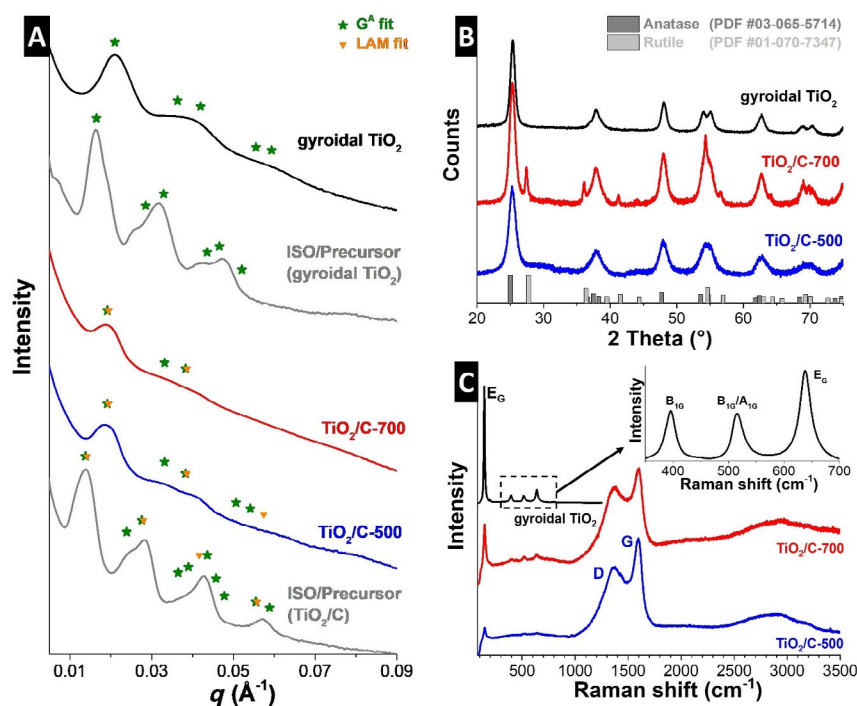
Figure 2. (A) Small-angle X-ray scattering pattern of the polymer/precursor, the pyrolyzed hybrid materials TiO_2/C-500 and TiO_2/C-700, and gyroidal TiO_2, including observable ideal peak positions for lamellar (LAM) and alternating gyroidal (G^A) morphology. (B) X-ray diffraction pattern (wide angle) and (C) Raman spectra of TiO_2/C-500, TiO_2/C-700, and gyroidal TiO_2. Inset: Typical B_{1G}, $A_{1/G}$, and E_G bands of crystalline anatase TiO_2 from the gyroidal TiO_2 sample.

agreement with SAXS, SEM, and HRTEM. We determined a total pore volume of $0.12\ cm^3 g^{-1}$ for TiO_2/C-500 and of $0.16\ cm^3 g^{-1}$ for TiO_2/C-700. Increasing pyrolysis temperature favors the formation of micropores, observed by the curve progression at low pressure for TiO_2/C-700. The BET specific surface area (SSA) was very similar for all samples: $73\ m^2 g^{-1}$ for TiO_2/C-500, $107\ m^2 g^{-1}$ for TiO_2/C-700, and $93\ m^2 g^{-1}$ for gyroidal TiO_2. The latter has a distinct higher volume of mesopores (total pore volume: $0.39\ cm^3 g^{-1}$) due to the lack of remaining carbon and the ordered nature of the pores of the gyroid morphology.

The formation of crystalline titania is evident from X-ray diffraction (Figure 2B), identified to be pure nano-crystalline anatase for the TiO_2/C-500 and gyroidal TiO_2. Higher process temperatures favor the formation of rutile in TiO_2/C-700, calculated to be 12% from Rietveld refinement (Supporting Information Table S2 and Figure S2). The lack of graphite-related reflection peaks shows the disordered nature of the carbon phase for TiO_2/C-500 and TiO_2/C-700. For such an amorphous carbon, the typical D-band (prohibited in perfectly crystalline graphite) and G-band (in-plane bond-stretching of sp^2-hybridised carbon rings) are observed in Raman spectra at 1370 and $1590\ cm^{-1}$, respectively (Figure 2C).[19] An intense and sharp signal at $144\ cm^{-1}$, assigned to the E_{1g} mode of anatase, evidences the presence of the TiO_2 core material in TiO_2/C samples. Strong fluorescence masks further modes of titania phases, such as B_{1g} ($394\ cm^{-1}$), E_g ($636\ cm^{-1}$), and the combined B_{1g}/A_{1g} (centered at $514\ cm^{-1}$). For the gyroidal TiO_2, without such a carbon shell, several anatase modes are clearly observable, as can be seen in the inset of Figure 2C.

The total amount of amorphous carbon in the TiO_2/C samples was determined by thermogravimetric analysis (TGA) conducted in synthetic air (Supporting Information, Figure S1B). Above $300\,°C$, oxidation takes place and is almost completed at $500\,°C$. Thereby, we can identify a total amount of carbon of ca. 15 mass% for TiO_2/C-500 and TiO_2/C-700. There was no noteworthy mass loss for the reference gyroidal TiO_2, since the polymer template was already completely removed during calcination in air at $400\,°C$ as part of the material synthesis.

The electrochemical performance of TiO_2/C-500 and TiO_2/C-700 free-standing monolith electrodes will be evaluated by comparison with gyroidal TiO_2 particles admixed with conductive additive and binder to form conventional electrodes. To allow for an investigation on the monolith structure on the performance, conventional electrodes will be prepared from gyroidal TiO_2 as thin films ($60\ \mu m$) and in the same thickness as the monolith electrodes ($300\ \mu m$). The electrodes' bulk densities and areal mass loadings are given in Supporting Information, Table S3.

Cyclic voltammograms of the samples are recorded at a scan rate of $0.1\ mV\,s^{-1}$ (Figure 3A) for a qualitative assessment of the electrode performances versus a lithium counter electrode in 1 M $LiClO_4$ ethylene carbonate/dimethyl carbonate electrolyte. The onset of the main lithiation peaks can be observed for all electrodes at about 1.7 V versus Li^+/Li, whereas delithiation occurs starting at around 1.9 V versus Li^+/Li. This reaction is associated with the lithiation of anatase with about 0.55 Li

per TiO_2.[20] Peak-stretching can be observed for the monolith electrodes, related to mass transport limitations in the thick electrodes.[11] Besides the main intercalation peaks, two small pairs of peaks can be observed around 1.5 V versus Li^+/Li, which are much more significant for the two monolith electrodes than for the gyroidal TiO_2 samples. These intercalation peaks represent further lithiation/delithiation of the material up to 1 Li per TiO_2, which has been previously reported for anatase TiO_2 with nanoscopic domain sizes.[20] This behavior is only found for anatase TiO_2, which is why the peak duplet is more pronounced for TiO_2/C-500 than for rutile-containing TiO_2/C-700.

Quantitative analysis of the gravimetric and volumetric electrochemical performance and rate handling was conducted by galvanostatic cycling at varying specific currents (Figure 3B–C), the charge/discharge profiles including the first cycle are found in Supporting Information, Figure S3 and Figure S4A–D. At a low rate, TiO_2/C-500 electrode showed the highest capacity of $155\ mAh\,cm^{-3}$, whereas both cast electrodes exhibited around $90\ mAh\,cm^{-3}$. This is due to the higher density of the monolith materials, since it can be expected that few limitations are posed by diffusion or mass transport at very low rates. At increasing rates, up to $1\ A\,g^{-1}$, the $300\ \mu m$ monolith hybrid electrodes still exhibit a comparable capacity to the $60\ \mu m$ gyroidal TiO_2, with a retention of about $60\ mAh\,cm^{-3}$. For comparison, the cast $300\ \mu m$ gyroidal TiO_2 electrode dropped significantly to around $15\ mAh\,cm^{-3}$ at this rate. The much higher capacity retention of the monolith electrodes is a consequence of the improved electrolyte mass transport within the interconnected mesoporous network with the carbon shell as electron pathways in the TiO_2/C. In the particle-based gyroidal TiO_2 electrode, depletion of lithium ions leads to the capacity drop; only a small part of the electrode volume partakes in the intercalation reaction. The stability of the electrodes is tested by prolonged cycling at a low rate of $0.025\ A\,g^{-1}$ (Figure 3C). It can be observed that the hybrid monolith electrodes exhibit a very stable cycling behavior over 100 charge/discharge cycles, whereas the gyroidal TiO_2 thin film electrode shows a slight drop of 9% over 100 cycles. High stability of TiO_2/C hybrid samples can be related to the interconnected network, where titania domains are engulfed in a carbon shell, effectively preventing disintegration during cycling.

The advantages of the hybrid monolith electrodes become even more apparent when considering the areal performance (Figure 4A). The maximum areal capacity of around $4.5\ mAh\,cm^{-2}$ of the TiO_2/C-500 electrode represents a 9-fold increase compared to the $60\ \mu m$ gyroidal TiO_2 electrode, and an almost two-fold increase compared to the corresponding $300\ \mu m$ gyroidal TiO_2 electrode with the same thickness. Even at a high rate of $2\ A\,g^{-1}$, the TiO_2/C-700 electrode still shows twice the area-normalized performance compared to the thin film electrode.

For better comparability with literature, galvanostatic cycling was carried out by normalizing to the cycling current to the electrode masses. However, when comparing different electrodes that are optimized for density and mass loading, normalization to the electrode area can be useful (Figure 4B). In a re-
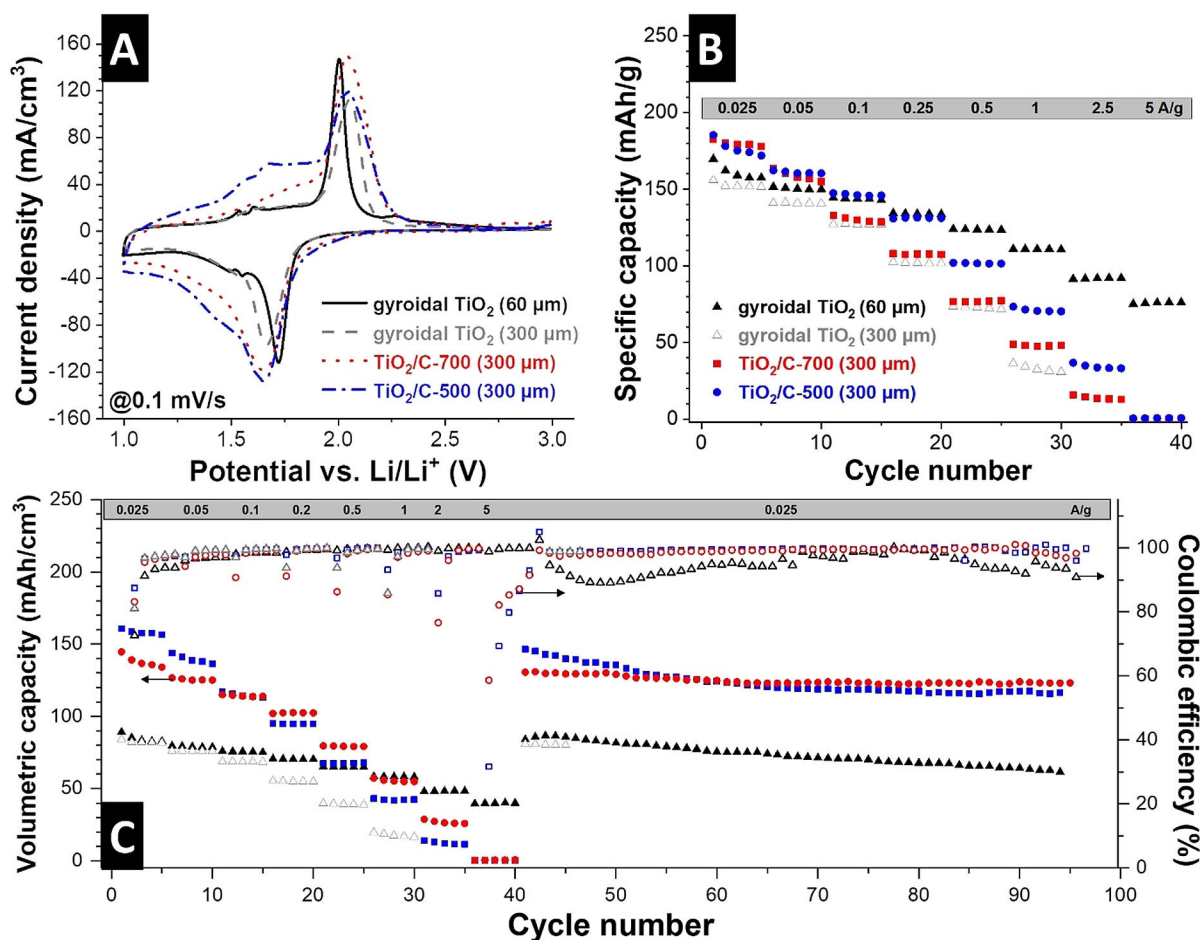
Figure 3. (A) Cyclic voltammograms of TiO$_2$/C-500, TiO$_2$/C-700, and gyroidal TiO$_2$ electrodes at 0.1 mV s^{-1} in a voltage window of 1.0–3.0 V vs. Li$^+$/Li. (B) Gravimetric discharge capacity with variable rates from 0.025 to 5 A g^{-1} and (C) volumetric discharge capacities including Coulombic efficiency values over 100 cycles.
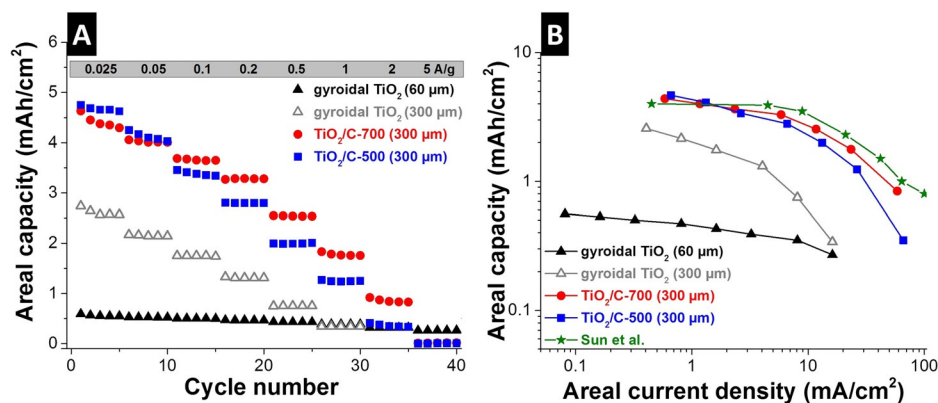
Figure 4. Areal capacity at (A) different discharge rates and (B) at different areal current densities for TiO$_2$/C-500, TiO$_2$/C-700, and gyroidal TiO$_2$ casted electrodes with 60 μm and 300 μm thickness. Data for Sun et al. are from Ref. [10].

cently reported study by Sun et al.,[10] it was demonstrated that a highly interconnected network of holey graphene, hybridized with niobia showed remarkable performance at high areal mass loadings (11 mg cm^{-2}). When comparing to the data of this material (replotted; green symbols), the TiO$_2$/C monolith electrodes exhibit similar performance. This shows that our

first report on a one-pot synthesis for free-standing electrodes with high mass loading shows attractive performance, comparable to the state-of-the-art in thick electrodes.

In conclusion, mesoporous, free-standing, binder-free, and conductive additive-free TiO$_2$/C hybrid monolith electrodes were prepared for the first time by a one-pot synthesis

method and studied with a focus on their areal and volumetric electrochemical capacity. It was found that the carbon shell supported, lamellar TiO_2 microstructure is required for sufficient macroscopic stability, concurrently ensuring sufficient conductivity. The use of TiO_2/C hybrid monolith electrodes as LIB anodes allowed the operation of ultrathick (300 µm) and dense (0.88 g cm^{-3}) electrode discs at high rates. This mass loading is at least an order of magnitude above commonly investigated LIB electrode materials. The increased electrode density and mass loading show up to 60 % higher volumetric and areal capacities than cast, mesoporous TiO_2 particle-based electrodes, while still exhibiting high rate handling performance. We believe that our results are highly interesting for industrial applications, where dense materials are required for downsizing, and high mass loadings are desired to compensate for the additional mass of cell components. The model system comprising TiO_2 as intercalation material can easily be exchanged in future studies to synthesize other metal oxide-based high-performance electrode materials.

Acknowledgements

Conflict of interest

The authors declare no conflict of interest.

[1] a) G. E. Blomgren, *J. Electrochem. Soc.* **2017**, *164*, A5019–A5025; b) B. Scrosati, J. Hassoun, Y. K. Sun, *Energy Environmental Sci.* **2011**, *4*, 3287–3295; c) M. S. Whittingham, *Chem. Rev.* **2004**, *104*, 4271–4302.

[2] a) K. Mizushima, P. C. Jones, P. J. Wiseman, J. B. Goodenough, *Mater. Res. Bull.* **1980**, *15*, 783–789; b) J. B. Goodenough, K. S. Park, *J. Am. Chem. Soc.* **2013**, *135*, 1167–1176.

[3] E. Kang, Y. S. Jung, G.-H. Kim, J. Chun, U. Wiesner, A. C. Dillon, J. K. Kim, J. Lee, *Adv. Funct. Mater.* **2011**, *21*, 4349–4357.

[4] S. Y. Huang, L. Kavan, I. Exnar, M. Gratzel, *J. Electrochem. Soc.* **1995**, *142*, L142–L144.

[5] M. Widmaier, N. Jäckel, M. Zeiger, M. Abuzarli, C. Engel, L. Bommer, V. Presser, *Electrochim. Acta* **2017**, *247*, 1006–1018.

[6] A. Tolosa, B. Krüner, S. Fleischmann, N. Jäckel, M. Zeiger, M. Aslan, I. Grobelsek, V. Presser, *J. Mater. Chem. A* **2016**, *4*, 16003–16016.

[7] A. Tolosa, S. Fleischmann, I. Grobelsek, A. Quade, E. Lim, V. Presser, *ChemSusChem* **2018**, *11*, 159–170.

[8] a) L. David, G. Singh, *J. Phys. Chem. C* **2014**, *118*, 28401–28408; b) L. David, R. Bhandavat, U. Barrera, G. Singh, *Nat. Commun.* **2016**, *7*, 10998; c) X. Zhao, C. M. Hayner, M. C. Kung, H. H. Kung, *ACS Nano* **2011**, *5*, 8739–8749.

[9] Y. Gogotsi, P. Simon, *Science* **2011**, *334*, 917–918.

[10] H. Sun, L. Mei, J. Liang, Z. Zhao, C. Lee, H. Fei, M. Ding, J. Lau, M. Li, C. Wang, X. Xu, G. Hao, B. Papandrea, I. Shakir, B. Dunn, Y. Huang, X. Duan, *Science* **2017**, *356*, 599.

[11] M. Singh, J. Kaiser, H. Hahn, *J. Electrochem. Soc.* **2015**, *162*, A1196–A1201.

[12] a) M. G. Fischer, X. Hua, B. D. Wilts, I. Gunkel, T. M. Bennett, U. Steiner, *ACS Appl. Mater. Interfaces* **2017**, *9*, 22388–22397; b) N. Li, G. Liu, C. Zhen, F. Li, L. Zhang, H.-M. Cheng, *Adv. Funct. Mater.* **2011**, *21*, 1717–1722; c) S. Fleischmann, D. Leistenschneider, V. Lemkova, B. Krüner, M. Zeiger, L. Borchardt, V. Presser, *Chem. Mater.* **2017**, *29*, 8653–8662; d) E. Lim, C. Jo, J. Lee, *Nanoscale* **2016**, *8*, 7827–7833.

[13] F. Jiao, J. L. Bao, A. H. Hill, P. G. Bruce, *Angew. Chem. Int. Ed.* **2008**, *47*, 9711–9716; *Angew. Chem.* **2008**, *120*, 9857–9862.

[14] M. Stefik, J. Lee, U. Wiesner, *Chem. Commun.* **2009**, 2532–2534.

[15] J. Lee, Y. S. Jung, S. C. Warren, M. Kamperman, S. M. Oh, F. J. DiSalvo, U. Wiesner, *Macromol. Chem. Phys.* **2011**, *212*, 383–390.

[16] M. Stefik, S. Guldin, S. Vignolini, U. Wiesner, U. Steiner, *Chem. Soc. Rev.* **2015**, *44*, 5076–5091.

[17] a) I. W. Hamley, V. Castelletto, O. O. Mykhaylyk, Z. Yang, R. P. May, K. S. Lyakhova, G. J. A. Sevink, A. V. Zvelindovsky, *Langmuir* **2004**, *20*, 10785–10790; b) J. H. Ahn, W. C. Zin, *Macromol. Res.* **2003**, *11*, 152–156.

[18] T. H. Epps, E. W. Cochran, C. M. Hardy, T. S. Bailey, R. S. Waletzko, F. S. Bates, *Macromolecules* **2004**, *37*, 7085–7088.

[19] J. G. Werner, T. N. Hoheisel, U. Wiesner, *ACS Nano* **2014**, *8*, 731–743.

[20] M. Wagemaker, W. J. H. Borghols, F. M. Mulder, *J. Am. Chem. Soc.* **2007**, *129*, 4323–4327.

CHEMISTRY

A European Journal

Supporting Information

Ordered Mesoporous Titania/Carbon Hybrid Monoliths for Lithium-ion Battery Anodes with High Areal and Volumetric Capacity

Tobias S. Dörr,[a, b] Simon Fleischmann,[a, b] Marco Zeiger,[a, b] Ingrid Grobelsek,[a] Peter W. de Oliveira,[a] and Volker Presser*[a, b]

Materials and Methods

Materials

We used the following chemicals: Benzene (99 %, Alfa Aesar), n-buthyllithium (nBuLi, 2.5 M in hexane, Alfa Aesar), 1,1-diphenylethylene (DPE, 98 %, Alfa Aesar), isoprene (99 %, <1000 ppm p-tert-butylcatechol, Sigma Aldrich), sec-buthyllithium (secBuLi, 1.4 M in cyclohexane, Sigma Aldrich), styrene (ReagentPlus, stabilized, Sigma Aldrich), calcium hydride (CaH$_2$, 1-20 mm granules, 88-98 %, Alfa Aesar), ethylene oxid (EO, 99.8 %, Praxair), potassium (98 %, pieces in mineral oil, Fisher Scientific), naphthalene (99 %, Fisher Scientific), deuterochloroform (CDCl$_3$, 99.8 atom% D, Sigma Aldrich), methanol (MeOH, 99 %, AlfaAesar), tetrahydrofuran (THF, 99 %, <1000 ppm stabilizer, Alfa Aesar), chloroform (CHCl$_3$, <99.8 %, ACS, Alfa Aesar), titan(IV)isopropoxide (Ti(^{i}Prop)$_4$, 99.999 %, Sigma Aldrich), hydrochloric acid (HCl, reagent grade, 37%, Sigma Aldrich), and absolute tetrahydrofuran (THF$_{abs}$, 99.85 %, extra dry, non-stabilized, Acros Organics) were used as received or purified as described.

Polymer synthesis

Poly(isoprene)-block-poly(styrene)-block-poly(ethylene oxide) (ISO) terpolymer was synthesized via sequential living anionic polymerization as described elsewhere.[1] Briefly, all chemicals were treated with either nBuLi or CaH$_2$ followed by distillation under reduced atmosphere. The first two blocks were sequential synthesized in benzene using sec-BuLi as the initiator. The living poly(isoprene)-block-poly(styrene) was endcapped with purified EO and deactivated by MeOH/HCl. The lithium counter ion was exchanged by potassium, washed several times with MilliQ water, dried, dissolved in THF, and reactivated by potassium naphthalenide. An appropriate amount of purified EO was added and the living ISO was then hydrated by MeOH/HCl, dried, and dissolved in CHCl$_3$. After multiple washing in MilliQ water, the polymer/CHCl$_3$ solution was finally precipitated in an aliquot of MeOH, filtrated, dried, and stored at 6 °C to slow down cross-linking or degradation.

Synthesis of mesoporous TiO$_2$/C hybrids and gyroidal TiO$_2$

Mesoporous TiO$_2$ was synthesized through an evaporation induced self-assembly (EISA) as described in literature for related inorganic materials.[2] Briefly, a 4.5 mass% ISO polymer/THF$_{abs}$ solution was blended with pre-hydrolyzed precursor sol containing HCl, THF$_{abs}$, and Ti(^{i}Prop)$_4$. The one of the important points for the preparation of our ordered mesoporous samples is a tailored sol-gel reaction to generate a hydrophilic titania containing sol. The controlled sol-gel reaction leads to TiO$_2$ seeds (ranging from discrete particles to continuous networks), small enough to favorably interact with the PEO block of our ISO BCP via hydrogen bonding.

By adding different amount of our pre-hydrolyzed sol, we alter the degree of swelling of the hydrophilic PEO and thus changing the predominating most energetic stable morphology archived by the subsequent evaporation induced microphase separation. A rough idea of the possible accessible structures using ISO, based on its relative volume fraction of each block, could get by the idealized ISO phase map from Tyler et al. (Ref. [3]). The combined BCP/precursor sol was stirred for 3 h and the solvent was evaporated on a hotplate at 35 °C, covered by a glass dome.

The samples were further aged in vacuum at 90 °C and the polymer was either removed during calcination in air at 400 °C to achieve the reference gyroidal TiO_2 particles or, to preserve a conductive carbon shell, for the mesoporous TiO_2/C hybrids, performed in argon at 500 °C or 700 °C for 3 h and a heating rate of 1 °C/min. For the latter two, the samples are consistently labelled TiO_2/C-500 and TiO_2/C-700.

Material characterization

Transmission electron microscopy (TEM) was carried out using a JEOL 2100F microscope with an acceleration voltage of 200 kV. Free-standing composite samples were dispersed in isopropanol, tip sonicated for 30 s and drop casted on a copper grid with a lacey carbon film from Gatan.

The material microstructure was investigated by use of a high-resolution field emission scanning electron microscope (SEM) JEOL JSM 7500F. Electron micrographs were recorded with an acceleration voltage of 1.5-5 kV dependent on the sample and the measurement spot. Additionally, the composition of the samples was measured using energy dispersive X-ray analysis (EDX) with a X-MAX-150 detector from Oxford Instruments in a JSM-7500F from JEOL. The free-standing and binder-free electrodes were placed on a copper substrate, the reference gyroidal TiO_2 on carbon tape, and spectra were taken at 40 different positions using 12 kV acceleration voltage.

The ISO composition and polydispersity (PDI) were characterized using a combination of nuclear magnetic resonance spectroscopy (NMR) and gel permeation chromatography (GPC) analysis. ^{1}H-NMR was performed on a Bruker Avance III HD Nanobay equipped with a SampleXpress auto sampler and a BBFO probe for 5 mm tubes. The polymer sample was dissolved in $CDCl_3$ and measured at 300 MHz. We used GPC to determine the PDI and the molecular weight (M_W) of the synthesized ISO polymer. Polymeric samples were dissolved in THF (1 mg/mL) and filtered through a polytetrafluoroethylene (PTFE) syringe filter. The GPC measurements were performed on a Waters ambient-temperature GPC system equipped with a Waters 2410 differential refractive index (RI) detector. From the analysis of the terminated polyisoprene (PI), taken after the first step of the sequential anionic polymerization, the exact $M_{w,PI}$ was determined using commercial PI standards. The integrated NMR signal was further normalized to the $M_{w,PI}$ for the final analysis.

The carbon content in the TiO_2/C hybrids was evaluated using thermogravimetric analysis (TGA). A TG 209 F1 Libra system from Netzsch with an automatic sample changer and alumina crucibles was used. Samples of ca. 10 mg were heated to 700 °C in synthetic air with a rate of 20 °C/min. The amount of titanium oxide was measured by calculating the remaining sample mass when carbon was completely oxidized.

Raman spectra were measured with a Renishaw inVia Raman microscope equipped with an excitation wavelength of 532 nm (Nd-YAG laser), a grating with 2400 lines/mm, a 50x objective (numeric aperture: 0.9), and a spectral resolution of ~1.2 cm^{-1}. Using an output power of 0.2 mW, the spot size in the focal plane of the sample was about 2 μm. The acquisition time was 20 s and 10 accumulations were used to achieve a high signal-to-noise ratio.

Powder X-ray diffraction (XRD) patterns were collected with a Bruker Discover D8 powder diffractometer unit, operating in reflection mode at 40 kV and 40 mA, with Cu-Kα (0.154 nm) as incident radiation. Measurements were performed with point focus. The data were acquired using the area detector VANTEC 500 from Bruker AXS with a resolution of 2048 pixel. In the applied configuration, the angle subtended by the detector was 33°. The integration has been applied in a 2θ angle range between 16° and 100° with a step size of 0.02°. Powder samples were analyzed by use of a sapphire single crystal sample holder. The structural refinement of the obtained phases and profile analysis of related powder diffraction patterns were carried out with the Bruker AXS program TOPAS. The line profile shapes were described by determination of an instrument function. Therefore, LaB_6 powder was chosen as standard material. The microstructural contributions were modeled including a physical broadening function in the refinement. The integral breadth-based volume weighted calculation assuming intermediate crystallite size broadening was modelled by a Voigt function.

Small-angle X-ray scattering (SAXS) pattern were recorded on a Xenocs XEUSS 2.0, equipped with a Dectris Pilatus 1M detector, a Cu Kα source (0.154 nm) and a sample to detector distance of 250 cm (calibrated by silver behenate). The samples were directly placed on a small square of polyimide tape and measured without further modifications. The primary beam was masked, and a total radial integration was performed for 1-D pattern.

A Quantachrome Autosorb iQ system was used to measure the nitrogen gas sorption. The samples were degassed at 300 °C for 20 h to remove volatile components form the surface. The relative pressure for the measurement varied between $2 \cdot 10^{-6}$ and 1. A total of 53 points were measured for the adsorption curve and 23 points for the desorption curve. The Brunauer-Emmett-Teller (BET; Ref. [4]) equation was applied with the ASiQwin software in the regime from 0.12 to 0.27 to calculate the specific surface area.

Electrochemical characterization

For electrochemical characterization, discs with a diameter of 6 mm were punched out of the free-standing and binder-free titania/carbon hybrid monoliths. Thereby, electrodes TiO_2/C-500 and TiO_2/C-700 had a thickness of 300 μm (±30 μm) and were used without further treatment.

For comparison, polymer-bound electrodes with gyroidal titania were used (labelled "gyroidal TiO_2" throughout this work). The TiO_2 powder was mixed with 20 mass% carbon black (Super C65, Imerys Graphite & Carbon) as the conductive additive, dispersed in ethanol and stirred in a mortar until a carbon slurry was obtained. To achieve a free-standing electrode, 10 mass% PTFE (60 mass% aqueous solution, Sigma Aldrich) were added and mixed in a mortar until a dough-like paste was formed. This results in 70 mass% TiO_2, 20 mass% carbon black, and 10 mass% PTFE. Using a rolling machine (MTI HR01), electrodes with a thickness of 60 μm (±10 μm) and 300 μm (±10 μm) were fabricated and dried over night at 90 °C and 2 kPa.

Cyclic voltammetry (CV) characterization was performed in custom-built cells with a polyether ether ketone body and spring-loaded titanium pistons. The layout and specification of our cells can be found in Ref. [5]. For galvanostatic measurements, we employed 2032-type coin cells. Half-cell characterization was conducted with metallic lithium as reference and counter electrode. Working and counter electrodes were separated with a glass fiber separator (Whatman Grade GF/D from GE Healthcare Life Sciences) and 12 mm copper and aluminum foil were used as current collectors on the negative and positive side, respectively. The cells were assembled in an argon filled glovebox (MBraun Labmaster 130, O_2 and H_2O <1 ppm) and filled with 1 M $LiClO_4$ in a mixture of ethylene carbonate and dimethyl carbonate electrolyte (EC/DMC, volume ratio 1:1) from BASF (battery grade). Galvanostatic charge/discharge cycling was carried out with an Arbin battery analyzer at a constant current density of 25 mA/g for charging and discharging in the potential window of 1-3 V vs. Li^+/Li. To quantify the power handling ability, we increased the specific current from 25 mA/g to 5 A/g in several steps for the first 40 cycles and then decreased again to the initial current of 25 mA/g. Finally, the stability was tested at 25 mA/g until 95 cycles were completed.

References

[1]   aM. A. Hillmyer, F. S. Bates, *Macromolecules* **1996**, *29*, 6994-7002; bJ. Chatterjee, S. Jain, F. S. Bates, *Macromolecules* **2007**, *40*, 2882-2896.
[2]   S. W. Robbins, H. Sai, F. J. DiSalvo, S. M. Gruner, U. Wiesner, *Acs Nano* **2014**, *8*, 8217-8223.
[3]   C. A. Tyler, J. Qin, F. S. Bates, D. C. Morse, *Macromolecules* **2007**, *40*, 4654-4668.
[4]   S. Brunauer, P. H. Emmett, E. Teller, *Journal of the American Chemical Society* **1938**, *60*, 309-319.
[5]   D. Weingarth, M. Zeiger, N. Jäckel, M. Aslan, G. Feng, V. Presser, *Advanced Energy Materials* **2014**, *4*, 1400316.

Supporting Figures
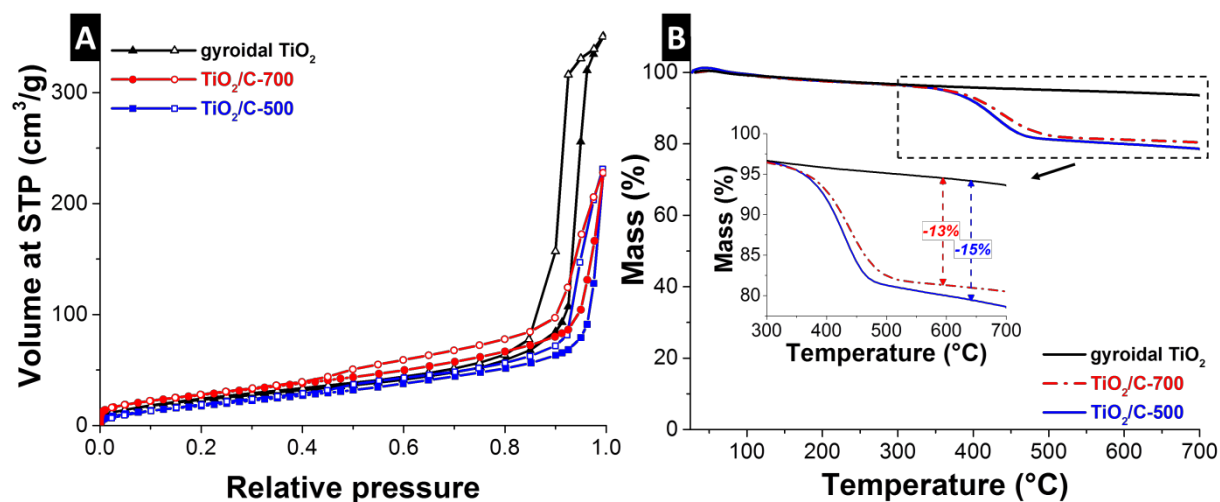
Figure S1. (A) Nitrogen gas sorption isotherms recorded at -196°C of TiO₂/C-500, TiO₂/C-700, and gyroidal TiO₂ (STP = standard temperature and pressure). (B) Thermogravimetric analysis of TiO₂/C-500, TiO₂/C-700, and gyroidal TiO₂ with carbon content determination from the data region shown in the inset.
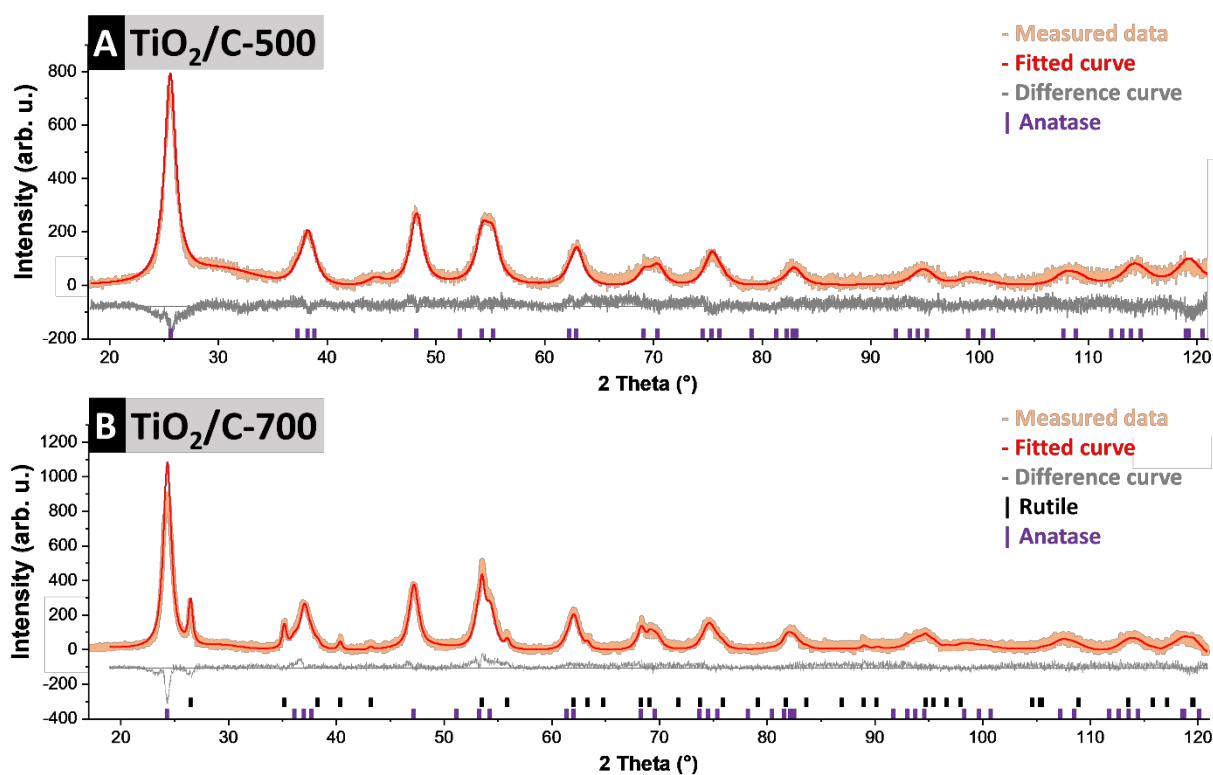
Figure S2. Rietveld refinement for (A) TiO₂/C-500 and (B) TiO₂/C-700. Lines on the bottom of each diffractogram represent anatase (PDF #03-065-5714) and rutile (PDF #01-070-7347).
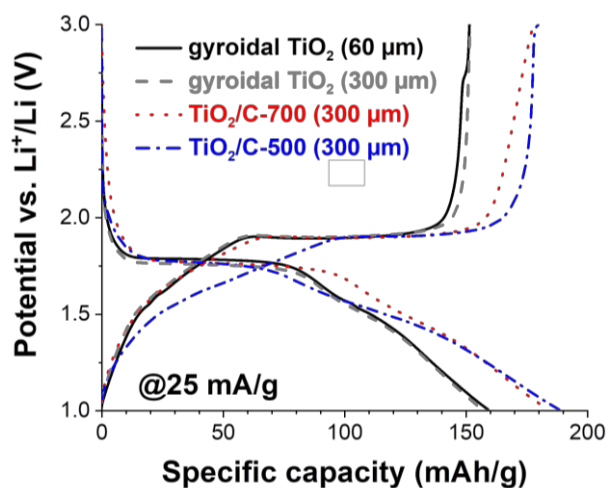
Figure S3. Galvanostatic charge/discharge profiles of all samples at 25 mA/g.
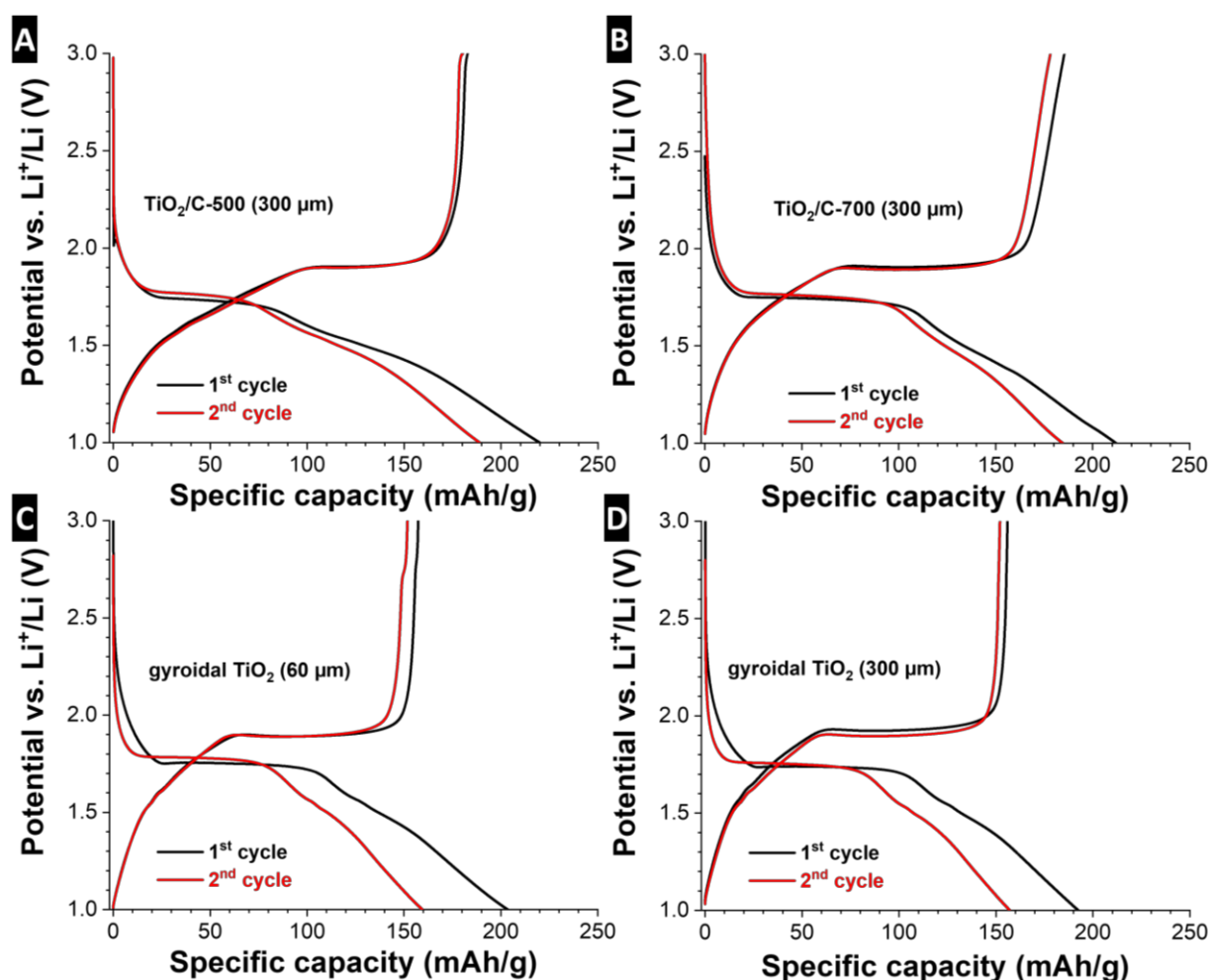
Figure S4. Comparison of first and second galvanostatic charge/discharge cycles of all samples recorded at a rate of 25 mA/g.

Supporting Tables

Table S1. EDX data.

Sample	Element in atomic% (average±standard deviation)			
	C	O	Ti	Cl
TiO_2/C-500	25.0±3.3	50.9±3.9	24.1±5.2	-
TiO_2/C-700	25.2±3.9	49.3±5.2	25.4±7.5	~0.1
Gyroidal TiO_2	3.7±0.8	63.4±10.1	32.9±10.6	-

Table S2. Rietveld refinement data.

	Sample			
	TiO_2/C-500		TiO_2/C-700	
Phase	anatase	rutile	anatase	rutile
	100 %	-	88 %	12 %
Lattice constant	a = 3.7930 Å c = 9.4812 Å	-	a = 3.7893 Å c = 9.4851 Å	a = 4.5973 Å c = 2.9626 Å
Crystallite size	6 nm	-	8 nm	33 nm
Strain (ϵ_0)	0.0029	-	0.0022	0.0000

Table S3. Characteristic electrode data.

	Electrode thickness (µm)	Electrode density (g/cm³)	Areal mass loading (mg/cm²)
TiO_2/C-500	300	0.88	26.4
TiO_2/C-700	300	0.78	23.4
Gyroidal TiO_2	60	0.54	3.2
Gyroidal TiO_2	300	0.54	16.2

Chapter 4.2

An Ambient Temperature Electrolyte with Superior Lithium Ion Conductivity based on a Self-Assembled Block Copolymer

Tobias S. Dörr,[1,2,a] Alexander Pelz,[3,4,a] Peng Zhang,[1] Tobias Kraus,[1,5] Martin Winter[3,6], Hans-Dieter Wiemhöfer,[3,4]*

[1]INM – Leibniz Institute for New Materials, Campus D2 2, 66123 Saarbrücken, Germany
[2]Department of Materials Science and Engineering, Saarland University, Campus D2 2, 66123 Saarbrücken, Germany
[3]Helmholtz-Institute Münster, Forschungszentrum Jülich GmbH, Corrensstraße 46, 48149 Münster, Germany
[4]Institute of Inorganic and Analytical Chemistry, University of Münster, Corrensstraße 28/30, 48149 Münster, Germany
[5]Colloid and Interface Chemistry, Saarland University, Campus D2 2, 66123 Saarbrücken, Germany
[6]MEET Battery Research Center, University of Münster, Corrensstraße 46, 48149 Münster, Germany
[a]These authors contributed equally to this work.

Abstract

In searching for polymer based electrolytes with improved performance for lithium ion and lithium metal batteries, we studied block copolymer electrolytes with high amounts of bis(trifluoromethane)sulfonimide lithium obtained by macromolecular co-assembly of a poly(isoprene)-block-poly(styrene)-block-poly(ethylene oxide) and

the salt from tetrahydrofuran. Particularly, an ultra-short poly(ethylene oxide) block of 2100 g mol^{-1} was applied, giving rise to 2D continuous lamellar microstructures. The macroscopic stability was ensured with major blocks from poly(isoprene) and poly(styrene) which separated

the ionic conductive PEO/lithium lamellae. Thermal annealing lead to high ionic conductivities of 1.4 mS cm at 20 °C with low activation energy and a superior lithium ion transference number of 0.7, accompanied by an improved mechanical stability (storage modulus of up to 10^7 Pa). With high Li:O ratios >1, we show a viable concept to achieve fast Li^+ transport in BCP, decoupled from slow polymer relaxation.
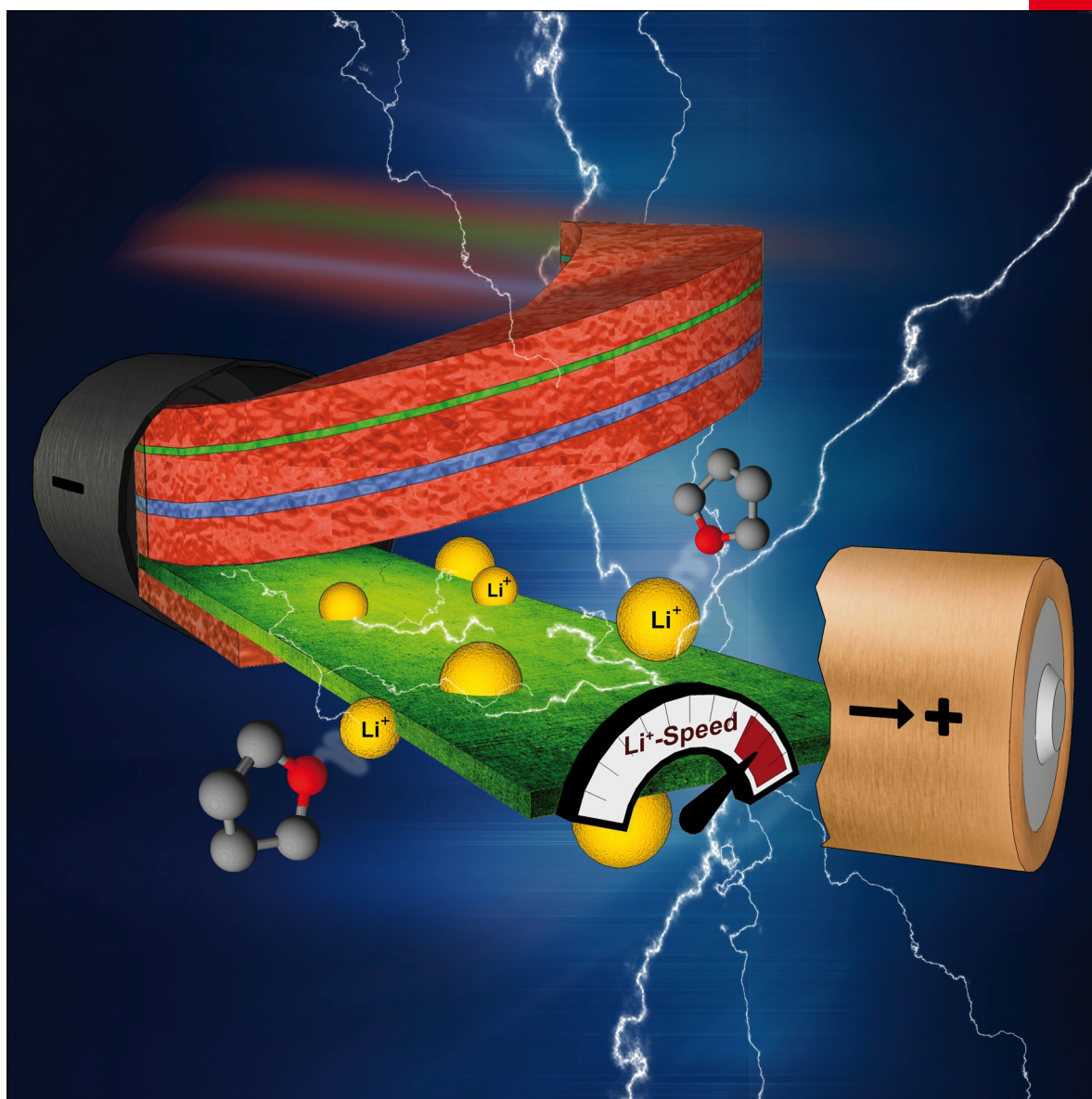
Cover Feature:

H.-D. Wiemhöfer et al.

An Ambient Temperature Electrolyte with Superior Lithium Ion Conductivity based on a Self-Assembled Block Copolymer

■ Batteries │*Hot Paper*│

An Ambient Temperature Electrolyte with Superior Lithium Ion Conductivity based on a Self-Assembled Block Copolymer

Tobias S. Dörr+,[a, b] Alexander Pelz+,[c, d] Peng Zhang,[a] Tobias Kraus,[a, e] Martin Winter,[c, f] and Hans-Dieter Wiemhöfer*[c, d]

Abstract: In searching for polymer-based electrolytes with improved performance for lithium ion and lithium metal batteries, we studied block copolymer electrolytes with high amounts of bis(trifluoromethane)sulfonimide lithium obtained by macromolecular co-assembly of a poly(iso-prene)-block-poly(styrene)-block-poly(ethylene oxide) and the salt from tetrahydrofuran. Particularly, an ultra-short poly(ethylene oxide) block of 2100 g mol^{-1} was applied, giving rise to 2D continuous lamellar microstructures. The macroscopic stability was ensured with major blocks from poly(isoprene) and poly(styrene), which separated the ionic conductive PEO/salt lamellae. Thermal annealing led to high ionic conductivities of 1.4 mS cm^{-1} at 20°C with low activation energy and a superior lithium ion transference number of 0.7, accompanied by an improved mechanical stability (storage modulus of up to 10^7 Pa). With high Li:O ratios > 1, we show a viable concept to achieve fast Li$^+$ transport in block copolymers (BCP), decoupled from slow polymer relaxation.

Lithium (Li) metal anodes are considered as key technology for novel cell chemistries, for example, lithium/sulfur, lithium/air, or solid state batteries.[1] For such cell chemistries, and specifically for Li metal anodes, the electrolyte plays a crucial role in performance, and needs to fulfill a list of criteria for long, stable, and safe cycle performance.[2] Current liquid electrolytes cannot offer the mechanical resistance required to reliably suppress Li dendrite formation that can eventually lead to short-circuits and thermal runaway reactions.[3]

A common route to improved electrolytes is to exchange liquid by polymer electrolytes. Poly(ethylene oxide) (PEO) is the most thoroughly investigated polymer for electrolyte application; however, it suffers from poor ionic conductivity σ at ambient temperature of 10^{-6} S cm^{-1}, caused by its high crystallinity.[4] Moreover, the Li$^+$ transference numbers () for common PEO electrolytes do not exceed 0.3, which indicates a rather low cationic contribution to the overall conductivity.[5] This is due to strong Li$^+$ coordination to ether oxygen in the polymer backbone.[6] Decreasing the molecular weight of PEO indeed reduces its crystallinity, but limits the mechanical stability required in a broad temperature range.[7]

Block copolymer (BCP) electrolytes enable independent tuning of mechanical, chemical, and electrochemical properties by variation of the block materials and sizes.[8] Previous work has shown that the addition of a second block, such as poly(styrene) (PS) or poly(oxybutylene) dramatically affects the crystallization behavior of PEO.[9] The incompatibility of the covalently linked blocks potentially allows microphase separation into 1D, 2D, or 3D continuity.[10] Structural investigations by Bates et al. showed the considerable potential as electrolyte by dissolution of lithium salt in a structure directing BCP.[11] We focused on tuning the individual and separated blocks to independently optimize mechanical and transport properties,[12] that is, a high elastic modulus to prevent Li dendrite growth,[13] and short PEO chains for superior ion mobility in a broad temperature range.[7]

We prepared a poly(isoprene)-block-poly(styrene)-block-poly(ethylene oxide) (ISO) BCP ($D_P = 1.09$, $M_{W,tot} = 57\,200$ g mol^{-1}) with an ultra-small PEO block of 2100 g mol^{-1}. Electrolyte membranes with high salt concentration were prepared from a solution of lithium bis(trifluoromethane)sulfonimide (LiTFSI) and the BCP in THF through an evaporation induced self-assembly (EISA) as schematically shown in Figure 1A (for further details of the synthesis, see the Supporting

[a] T. S. Dörr,+ Dr. P. Zhang, Prof. Dr. T. Kraus
INM—Leibniz Institute for New Materials
Campus D2 2, 66123 Saarbrücken (Germany)

[b] T. S. Dörr+
Department of Materials Science and Engineering, Saarland University
Campus D2 2, 66123 Saarbrücken (Germany)

[c] A. Pelz,+ Prof. Dr. M. Winter, Prof. Dr. H.-D. Wiemhöfer
Helmholtz-Institute Münster, Forschungszentrum Jülich GmbH
Corrensstraße 46, 48149 Münster (Germany)
E-mail: hdw@uni-muenster.de

[d] A. Pelz,+ Prof. Dr. H.-D. Wiemhöfer
Institute of Inorganic and Analytical Chemistry, University of Münster
Corrensstraße 28/30, 48149 Münster (Germany)

[e] Prof. Dr. T. Kraus
Colloid and Interface Chemistry, Saarland University
Campus D2 2, 66123 Saarbrücken (Germany)

[f] Prof. Dr. M. Winter
MEET Battery Research Center, University of Münster
Corrensstraße 46, 48149 Münster (Germany)

[+] These authors contributed equally to this work.

🖥 Supporting information and the ORCID identification numbers for the
ⓘ authors of this article can be found under:
https://doi.org/10.1002/chem.201801521.
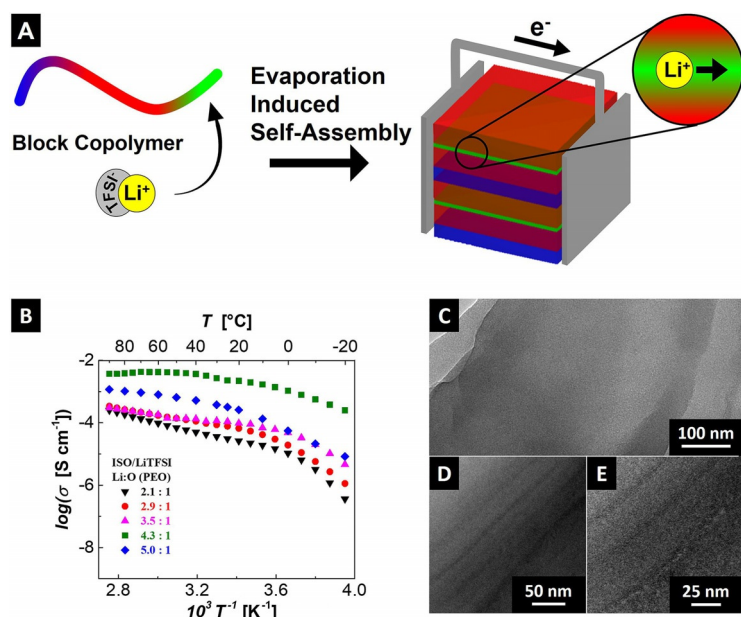
Figure 1. A) Simplified preparation scheme for ISO/LiTFSI electrolytes. The BCP comprises PI (blue), PS (red), and PEO (green), the latter blended selectively with LiTFSI. B) Arrhenius plot from electrochemical impedance spectroscopy (EIS) of different Li:O (PEO) ratios. C–E) HRTEM image of a lamellar ordered electrolyte membrane, with a Li:O (PEO) ratio of 4.3:1 / Li:O (PEO+THF) ratio of 1.4:1.

Information). The molar ratio Li:O has been varied up to 5:1 referring to O from PEO or rather up to 1.4:1 (if referring to O from PEO + non-removable THF from membrane preparation). The amount of LiTFSI dissolved in the ISO BCP crucially affects the ionic conductivity and an optimum was reached at a Li:O (PEO) ratio of 4.3:1 (Figure 1 B), simply denoted as ISO/LiTFSI. Note that the amount of LiTFSI did selectively swell the PEO block and thus altered the overall relative volume fractions, subsequently giving rise to several microstructures. However, a lamellar orientation was clearly detectable using small-angle X-ray scattering (SAXS) from Li:O (PEO) ratios of 3.5:1 and higher (Figure S2).[14] A commercial PEO-based electrolyte (400 000 Da, Li:O 1:28, sample: PEO/LiTFSI) was used as reference material.

High resolution transmission electron microscopy (HRTEM) in Figure 1 C indicated that LiTFSI dissolved in the BCP. Higher magnification in Figure 1 D,E showed that the selectively swelled lamellar oriented PEO domain produces higher contrast.[15] Insulating poly(isoprene) (PI) and PS domains were indistinguishable and separated the ion conducting PEO lamellae, which is in line with previous works on the ion distribution in BCPs.[15]

SAXS revealed long-range order in our microphase separated solid electrolyte (Figure 2 A). The neat ISO polymer exhibited long-range internal order with a periodicity (d_{100}) of 28 nm that caused sharp SAXS peaks. The selective swelling of the PEO domain with LiTFSI changed the overall relative volume fractions and led to a larger periodicity of 52 nm, as indicated by the shift of the first diffraction (q^*) towards lower q-values. It also changed the energetically favored microstructure during the EISA process towards a 2D lamellar (LAM) alignment, as already seen from HRTEM (Figure 1 C–E). As expected, there was

no detectable microstructural order found for either the neat or the LiTFSI blended PEO reference.

Wide-angle X-ray scattering (WAXS) patterns at room temperature (Figure 2 B) indicated crystalline PEO in the reference material both with and without LiTFSI through typical Bragg reflections at 14.6° (021), 15.1° (110), 19.1° (120), 22.1° (112), and 23.4° (032).[16] The absence of any reflexes from crystalline LiTFSI in the PEO/LiTFSI reference sample proved complete dissolution of the salt. The results for the ISO-based system with its ultra-small PEO blocks were quite different with only weak reflections for the neat polymer most likely from nano-crystalline PEO domains. Dissolving LiTFSI caused stronger reflexes that were clearly different from either crystalline PEO or neat LiTFSI, indicating a crystalline surrounding for Li+, which varies from non-dissociated LiTFSI (Figure S3 A).

Simultaneous thermal analysis coupled with mass spectroscopy (TGA-DSC-MS) showed a nearly stable content of 9±3 wt% of remaining THF, which could not be removed by vacuum drying (Figure S4). We conclude that the non-removable THF takes part in the aforementioned Li+ coordination, stabilizing the high salt content with molar ratios Li:O (PEO+THF) in the range 1.0:1 to 1.4:1 for all membranes and plays, in combination with the resulting high Li:O ratios, a crucial role for the high ionic conductivity. This result deviates from the common assumption that dissolved Li+ in PEO is coordinated by at least two oxygen atoms.[17] Earlier studies already proposed altered coordination of lithium in the PEO domains of a BCP, even without a lithium excess, due to stretched chains through microphase separation.[15, 18]

The total conductivity σ of the optimized ISO/LiTFSI electrolyte was monitored by electrochemical impedance spectrosco-
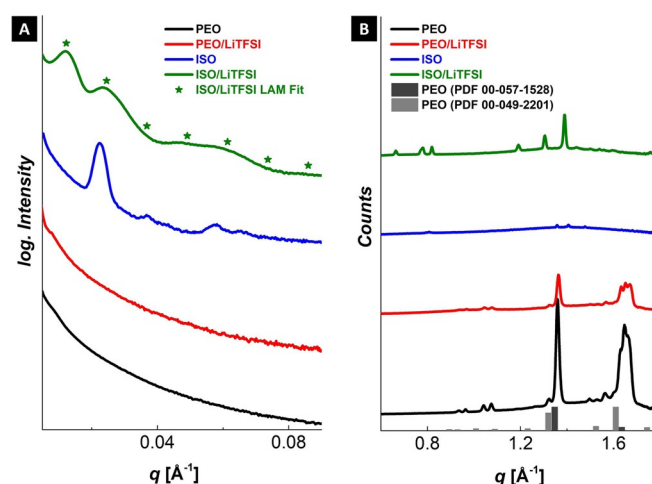
Figure 2. A) Radially integrated 1D SAXS pattern at 20°C of the neat and LiTFSI containing ISO BCP and PEO reference. Theoretically predicted q/q^* ratios for a lamellar microstructure are indicated as stars above the ISO/LiTFSI curve. B) Corresponding radially integrated 1D WAXS pattern at 20°C and the bibliographic reference peak for crystalline PEO.

py (EIS) in consecutive heating cycles from −20 to 90 °C. At 20 °C, the conductivity of the best ISO/LiTFSI electrolyte was 2.0 mS cm^{-1}, almost four orders of magnitude above that of our standard PEO/LiTFSI electrolyte (3.5×10^{-4} mS cm^{-1}) (Figure 3 A). Even down to −20 °C, ISO/LiTFSI showed high conductivity still above 0.1 mS cm^{-1}. Note that the reproducibly measured conductivity for ISO/LiTFSI proved a preferential orientation of the conductive lamellae perpendicular to the electrodes and thus to the membrane surfaces.

These are amongst the highest values reported so far for BCP-based electrolytes.[19] A high conductivity of 0.35 mS cm^{-1} was reported for a robust microphase separated PEO-PS at 30 °C,[20] whereas our best membrane reached 2.7 mS cm^{-1}. Typical gel type polymer electrolytes usually need significantly higher amounts of liquid components to reach similar conductivities, accompanied by loss of mechanical stability.[21] Taking into account that ion transport only occurs in the PEO lamellae, the effective local ionic conduction in these domains has to be even higher, as the measured values are averages over the entire electrolyte area between the electrodes, including non-conducting PI and PS domains. The HRTEM images shown in Figure 1 C–E allowed the estimation that around ten percent of the total membrane surface area consists of conductive PEO lamellae, which results in an effective local ionic conductivity in the range of 10 mS cm^{-1}.

Repeated heating cycles strongly increased the total conductivity of a pristine membrane and reached a stable, reproducible value in subsequent heating cycles after the 3rd one (Figure 3 A). This transition was reproducible for different samples and in every case irreversible, so that it can be interpreted as a thermally induced aging, resulting in a stable structured ISO/

LiTFSI electrolyte. After the second heating cycle, a reduced temperature dependence of the conductivities can be found in the Arrhenius plots reasoned by a low activation barrier of 0.14 eV in the range of 30 to 90 °C for the ion transport.

Temperature-dependent SAXS on a pristine ISO/LiTFSI membrane was performed in consecutive cycles to observe structural changes in situ; results of the first and second heating cycle are shown in Figure 3 B,C. Distinct changes in SAXS during the first heating indicated slight structural modification; when 90 °C was first reached, the reflexes shifted towards lower q-values, and higher order peaks appeared more clearly but remained consistent with the lamellar morphology. The decreased q* value implies a slightly increased periodicity from $d_{100} = 52$ to 54 nm, which is probably due to thermal-induced segregation of the lamellae. We believe that a metastable structure was initially formed by solvent evaporation, where the lamellar signal was due to the ordered PEO + LiTFSI domain, initially blurred with PS at the phase boundary. As the melting temperature of PS was reached, there was sufficient mobility to complete the PS-PEO phase separation and the thermodynamically stable lamellar structure was reached, additionally supported by differential scanning calorimetry (Figure S3 B). The q*-shifting was irreversible, only slight sharpening of the peaks in additional cycles were observed.

Thermal annealing also affected the mechanical stability as shown using rheological measurements (Figure 3 D). The storage modulus (G′) was measured from oscillatory shear experiments at constant frequency of 1 Hz between 35 and 90 °C. Not surprisingly, the PEO/LiTFSI reference exhibited a G′ of 4× 10^6 Pa up to the expected phase transition. Subsequently G′ dropped below 10^5 Pa, but restored again while cooling. In contrast, ISO/LiTFSI shows upon heating below the transition (i.e., up to 70 °C) a reproducible G′ of 3× 10^6 Pa. Once annealed up to 90 °C, G′ rapidly increased to 10^7 Pa and remained at this value in additional cycles, which is consistent with the fact that formation of a long-range ordered lamellar structure increased the storage modulus, compared to the initially formed metastable structure (Figure S5).[22] In contrast to the assumption by Newman and Monroe that for sufficient suppression of dendrite growth the storage modulus of electrolytes is required to be at least twice that of Li metal (4 GPa),[13b] other publications state distinctly lower G′ values as safe.[23]

Strong lithium cation coordination in PEO electrolytes is responsible for its low (0.1–0.2 at 60 to 90 °C).[24] Short PEO chains are known to increase the ion mobility, due to the higher segmental and molecular mobility.[7,25] Also "polymer-in-salt" like ratios of lithium per oxygen that we could introduce here without loss of mechanical stability, have been reported to favor the Li$^+$ mobility.[26] We determined t_{Li^+} for ISO/LiTFSI electrolytes and the PEO/LiTFSI reference material using the BRUCE method in symmetric Li|electrolyte|Li cells (for details, see the Supporting Information),[27] with t_{Li^+} of 0.70±0.03 for ISO/LiTFSI in the temperature range 40 to 60 °C, whereas
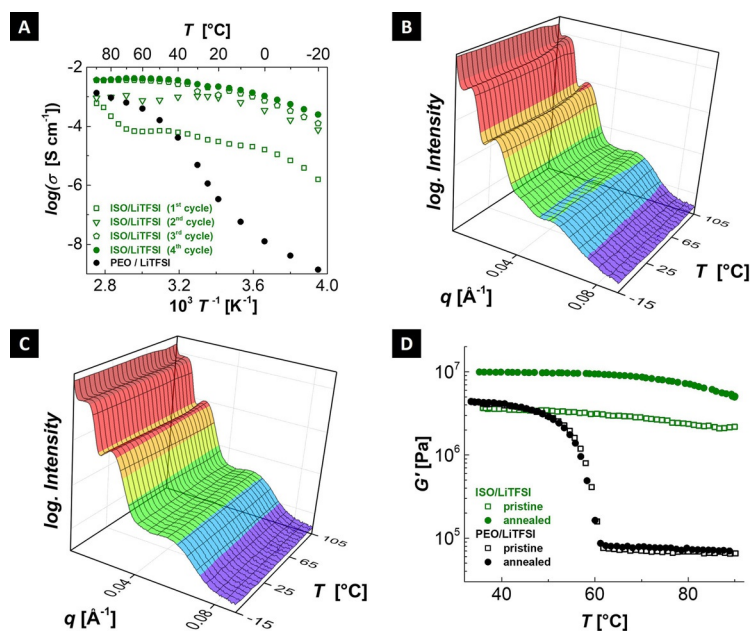
Figure 3. A) Multiple, consecutive EIS measurements for pristine ISO/LiTFSI and PEO/LiTFSI reference. Temperature-dependent SAXS measurement of ISO/LiTFSI given for a 1st B) and a 2nd C) heating cycle from −15 to 105 °C. D) Rheology measurement (ν = 1 Hz) for a pristine ISO/LiTFSI and PEO/LiTFSI before and after thermal annealing at 90 °C. The Li:O (PEO) ratio for ISO/LiTFSI is always 4.3:1.

our PEO reference yielded $t_{Li+} = 0.12 \pm 0.04$, consistent with the literature.[5,24,28] t_{Li+} as high as 0.7 have so far only been found for PEO electrolytes with an Li:O ratio of 0.5:1 at 70 °C, which suffer from distinct lower conductivities than common PEO electrolytes.[28a]

With the total conductivity and t_{Li+} measured for ISO/LiTFSI, the partial lithium ion conductivity is 1.4 mS cm^{-1} at room temperature. The effective local in the PEO lamellae will be even ten times higher, as argued above, and becomes comparable to that of inorganic solid Li$^+$ conductors[29] and even classical liquid electrolytes in lithium batteries.[2d] The results of the transference number measurements were also relevant regarding the stability, as the electrolyte surface was exposed to lithium metal electrodes. A long-term steady-state current during chronoamperometric measurement (Figure S5), indicated that the electrolyte was stable versus lithium under the applied conditions (10 mV, 40 to 60 °C), as degrading redox reactions would have resulted in a current increase and a thicker solid electrolyte interface (SEI) in a current decrease.[30]

The high ionic conductivities together with an extremely low activation energy of 0.14 eV in the range of 30 to 90 °C (Figure 3 A) in the area of superionic sulfidic solid-state conductors[31] and high in our ISO/LiTFSI electrolytes suggests that the lithium ion coordination of ether oxygen is drastically reduced and point at a conduction mechanism that is based on ordered lithium ion pathways, stabilized by THF ether oxygen and the TFSI$^-$ anion. This conduction mechanism, promoted by small PEO blocks and high Li:O ratios, seems to be decoupled from the polymer backbone movement, as σ clearly surpasses existing BCP-based electrolytes with lower Li:O ratios.[32] There, the Li$^+$ transport is still limited by strong interactions with ether oxygen of the locally bounded PEO chain.

It became clear already before 2000 that the ionic conductivities of amorphous salt in polymer electrolytes are strictly limited by the slow chain relaxations of the polymer network. It was soon evident that a further improvement of ionic conductivities relied on an effective decoupling of ion transport from the polymer relaxations.[33] Extended order or even ordered quasi-crystalline packing instead of the amorphous state was realized as a possible approach to decouple the polymer lattice from the ion transport with the chance of higher ionic mobility.[34] The work of Bruce et al. has shown that crystalline polymer domains in PEO indeed deliver channel structures and enhance the ion mobility, which becomes decoupled from the polymer mobility as predicted.[35] We think that the observations in our work are strongly connected to these earlier concepts and show another promising route towards ordered hybrid structures stabilized by ordered BCP membranes.

In conclusion, ISO/LiTFSI electrolytes with an ultra-small PEO block of 2100 g mol^{-1} and high Li:O (PEO) ratios of up to 5:1, or rather Li:O (PEO + THF) ratios of up to 1.4:1, were prepared from THF solution by evaporation induced self-assembly and studied with focus on their microstructure and lithium ion conductivity. The largest σ was found for electrolytes with a Li:O (PEO) ratio of 4.3:1, comprised a 2D lamellar orientation. In combination with the determined, we achieved of 1.4 mS cm^{-1} at 20 °C, which could possibly be enhanced by increasing the number of conductive PEO lamellae by simply tuning the BCP composition. Temperature dependent SAXS correlated thermally activated regular lamellar structure with an increased conductivity and a higher mechanical stability up to $G' = 10^7$ Pa. High Li:O ratios, low activation barriers of 0.14 eV in the range of 30 to 90 °C, and superior t_{Li+} of 0.7 indicated that the classical inter- and intrachain hopping was probably enhanced by an additional mechanism, most likely based on Li$^+$ conductive channels. The unprecedented high cationic conductivity with its low temperature dependence suggested that the Li$^+$ ion mobility in the PEO domain has been decoupled from slow polymer relaxation. Further work will now concentrate on elucidation of the fast transfer mechanisms and optimization of the BCP composition.

Acknowledgements

Conflict of interest

The authors declare no conflict of interest.

[1] a) P. Meister, H. P. Jia, J. Li, R. Kloepsch, M. Winter, T. Placke, *Chem. Mater.* **2016**, *28*, 7203 – 7217; b) R. Wagner, N. Preschitschek, S. Passerini, J. Leker, M. Winter, *J. Appl. Electrochem.* **2013**, *43*, 481 – 496; c) G. Bieker, M. Winter, P. Bieker, *Phys. Chem. Chem. Phys.* **2015**, *17*, 8670 – 8679; d) T. Placke, R. Kloepsch, S. Duhnen, M. Winter, *J. Solid State Electrochem.* **2017**, *21*, 1939 – 1964.

[2] a) J. M. Tarascon, M. Armand, *Nature* **2001**, *414*, 359 – 367; b) K. Xu, *Chem. Rev.* **2004**, *104*, 4303 – 4417; c) M. Amereller, T. Schedlbauer, D. Moosbauer, C. Schreiner, C. Stock, F. Wudy, S. Zugmann, H. Hammer, A. Maurer, R. M. Gschwind, H.-D. Wiemhöfer, M. Winter, J. H. Gores, *Prog. Solid State Chem.* **2014**, *42*, 39 – 56; d) I. Cekic-Laskovic, N. von Aspern, L. Imholt, S. Kaymaksiz, K. Oldiges, B. R. Rad, M. Winter, *Top. Curr. Chem.* **2017**, *375*, 37.

[3] a) D. Aurbach, E. Zinigrad, Y. Cohen, H. Teller, *Solid State Ionics* **2002**, *148*, 405 – 416; b) R. W. Schmitz, P. Murmann, R. Schmitz, R. Müller, L. Krämer, J. Kasnatscheew, P. Isken, P. Niehoff, S. Nowak, G.-V. Röschenthaler, N. Ignatiev, A. Lex-Balducci, C. Schreiner, I. Cekic-Laskovic, M. Winter, *Prog. Solid State Chem.* **2014**, *42*, 65 – 84.

[4] M. B. Armand, *Annu. Rev. Mater. Sci.* **1986**, *16*, 245 – 261.

[5] E. Kang, Y. S. Jung, G. H. Kim, J. Chun, U. Wiesner, A. C. Dillon, J. K. Kim, J. Lee, *Adv. Funct. Mater.* **2011**, *21*, 4349 – 4357.

[6] a) J. E. Weston, B. C. H. Steele, *Solid State Ionics* **1981**, *2*, 347 – 354; b) D. Bamford, A. Reiche, G. Dlubek, F. Alloin, J. Y. Sanchez, M. A. Alam, *J. Chem. Phys.* **2003**, *118*, 9420 – 9432; c) C. Berthier, W. Gorecki, M. Minier, M. B. Armand, J. M. Chabagno, P. Rigaud, *Solid State Ionics* **1983**, *11*, 91 – 95.

[7] A. A. Teran, M. H. Tang, S. A. Mullin, N. P. Balsara, *Solid State Ionics* **2011**, *203*, 18 – 21.

[8] W. S. Young, W. F. Kuan, T. H. Epps, *J. Polym. Sci. Part B* **2014**, *52*, 1 – 16.

[9] a) I. W. Hamley, V. Castelletto, G. Floudas, F. Schipper, *Macromolecules* **2002**, *35*, 8839 – 8845; b) P. A. Weimann, D. A. Hajduk, C. Chu, K. A. Chaffin, J. C. Brodil, F. S. Bates, *J. Polym. Sci. Part B* **1999**, *37*, 2053 – 2068; c) H. Schmalz, A. Knoll, A. J. Muller, V. Abetz, *Macromolecules* **2002**, *35*, 10004 – 10013.

[10] P. Docampo, M. Stefik, S. Guldin, R. Gunning, N. A. Yufa, N. Cai, P. Wang, U. Steiner, U. Wiesner, H. J. Snaith, *Adv. Energy Mater.* **2012**, *2*, 676 – 682.

[11] a) T. H. Epps, T. S. Bailey, R. Waletzko, F. S. Bates, *Macromolecules* **2003**, *36*, 2873 – 2881; b) T. H. Epps, T. S. Bailey, H. D. Pham, F. S. Bates, *Chem. Mater.* **2002**, *14*, 1706 – 1714.

[12] A. J. Meuler, M. A. Hillmyer, F. S. Bates, *Macromolecules* **2009**, *42*, 7221 – 7250.

[13] a) C. X. Wang, T. Sakai, O. Watanabe, K. Hirahara, T. Nakanishi, *J. Electrochem. Soc.* **2003**, *150*, A1166 – A1170; b) C. Monroe, J. Newman, *J. Electrochem. Soc.* **2005**, *152*, A396 – A404.

[14] a) J. Chatterjee, S. Jain, F. S. Bates, *Macromolecules* **2007**, *40*, 2882 – 2896; b) M. Stefik, S. Guldin, S. Vignolini, U. Wiesner, U. Steiner, *Chem. Soc. Rev.* **2015**, *44*, 5076 – 5091.

[15] E. D. Gomez, A. Panday, E. H. Feng, V. Chen, G. M. Stone, A. M. Minor, C. Kisielowski, K. H. Downing, O. Borodin, G. D. Smith, N. P. Balsara, *Nano Lett.* **2009**, *9*, 1212 – 1216.

[16] G. Zardalidis, J. Mars, J. Allgaier, M. Mezger, D. Richter, G. Floudas, *Soft Matter* **2016**, *12*, 8124 – 8134.

[17] D. Diddens, A. Heuer, O. Borodin, *Macromolecules* **2010**, *43*, 2028 – 2036.

[18] M. Singh, O. Odusanya, G. M. Wilmes, H. B. Eitouni, E. D. Gomez, A. J. Patel, V. L. Chen, M. J. Park, P. Fragouli, H. Iatrou, N. Hadjichristidis, D. Cookson, N. P. Balsara, *Macromolecules* **2007**, *40*, 4578 – 4585.

[19] a) D. T. Hallinan, S. A. Mullin, G. M. Stone, N. P. Balsara, *J. Electrochem. Soc.* **2013**, *160*, A464 – A470; b) A. Lassagne, E. Beaudoin, A. Ferrand, T. N. T. Phan, P. Davidson, C. Iojoiu, R. Bouchet, *Electrochim. Acta* **2017**, *238*, 21 – 29.

[20] S. A. Chopade, J. G. Au, Z. Li, P. W. Schmidt, M. A. Hillmyer, T. P. Lodge, *ACS Appl. Mater. Interfaces* **2017**, *9*, 14561 – 14565.

[21] A. M. Stephan, *Eur. Polym. J.* **2006**, *42*, 21 – 42.

[22] D. Rauber, P. Zhang, V. Huch, T. Kraus, R. Hempelmann, *Phys. Chem. Chem. Phys.* **2017**, *19*, 27251 – 27258.

[23] a) R. Khurana, J. L. Schaefer, L. A. Archer, G. W. Coates, *J. Am. Chem. Soc.* **2014**, *136*, 7395 – 7402; b) G. M. Stone, S. A. Mullin, A. A. Teran, D. T. Hallinan, A. M. Minor, A. Hexemer, N. P. Balsara, *J. Electrochem. Soc.* **2012**, *159*, A222 – A227.

[24] S. Lascaud, M. Perrier, M. Armand, J. Prud'homme, B. Kapfer, A. Vallee, M. Gauthier, *Electrochim. Acta* **1998**, *43*, 1407 – 1414.

[25] J. Shi, C. A. Vincent, *Solid State Ionics* **1993**, *60*, 11 – 17.

[26] R. Mishra, N. Baskaran, P. A. Ramakrishnan, K. J. Rao, *Solid State Ionics* **1998**, *112*, 261 – 273.

[27] a) P. G. Bruce, C. A. Vincent, *J. Electroanal. Chem.* **1987**, *225*, 1 – 17; b) P. G. Bruce, M. T. Hardgrave, C. A. Vincent, *J. Electroanal. Chem.* **1989**, *271*, 27 – 34.

[28] a) K. Pozyczka, M. Marzantowicz, J. R. Dygas, F. Krok, *Electrochim. Acta* **2017**, *227*, 127 – 135; b) M. Watanabe, A. Nishimoto, *Solid State Ionics* **1995**, *79*, 306 – 312; c) F. Lemaitre-Auger, J. Prud'homme, *Electrochim. Acta* **2001**, *46*, 1359 – 1367.

[29] a) A. Manthiram, X. W. Yu, S. F. Wang, *Nat. Rev. Mater.* **2017**, *2*, 16103; b) P. Knauth, *Solid State Ionics* **2009**, *180*, 911 – 916.

[30] M. Winter, *Z. Phys. Chem.* **2009**, *223*, 1395 – 1406.

[31] D. A. Weber, A. Senyshyn, K. S. Weldert, S. Wenzel, W. B. Zhang, R. Kaiser, S. Berendts, J. Janek, W. G. Zeier, *Chem. Mater.* **2016**, *28*, 5905 – 5915.

[32] W. S. Young, J. N. L. Albert, A. B. Schantz, T. H. Epps, *Macromolecules* **2011**, *44*, 8116 – 8123.

[33] C. A. Angell, C. T. Imrie, M. D. Ingram, *Polym. Int.* **1998**, *47*, 9 – 15.

[34] a) Y. Zheng, F. B. Dias, P. V. Wright, G. Ungar, D. Bhatt, S. V. Batty, T. Richardson, *Electrochim. Acta* **1998**, *43*, 1633 – 1637; b) S. H. Chung, Y. Wang, S. G. Greenbaum, D. Golodnitsky, E. Peled, *Electrochem. Solid-State Lett.* **1999**, *2*, 553 – 555; c) D. Golodnitsky, E. Livshits, Y. Rosenberg, E. Peled, S. H. Chung, Y. Wang, S. Bajue, S. G. Greenbaum, *J. Electroanal. Chem.* **2000**, *491*, 203 – 210; d) D. Golodnitsky, E. Livshits, R. Kovarsky, E. Peled, S. H. Chung, S. Suarez, S. G. Greenbaum, *Electrochem. Solid-State Lett.* **2004**, *7*, A412 – A415.

[35] a) Z. Gadjourova, Y. G. Andreev, D. P. Tunstall, P. G. Bruce, *Nature* **2001**, *412*, 520 – 523; b) E. Staunton, Y. G. Andreev, P. G. Bruce, *Faraday Discuss.* **2007**, *134*, 143 – 156; c) C. H. Zhang, S. Gamble, D. Ainsworth, A. M. Z. Slawin, Y. G. Andreev, P. G. Bruce, *Nat. Mater.* **2009**, *8*, 580 – 584.

CHEMISTRY
A European Journal

Supporting Information

An Ambient Temperature Electrolyte with Superior Lithium Ion Conductivity based on a Self-Assembled Block Copolymer

Tobias S. Dörr+,[a, b] Alexander Pelz+,[c, d] Peng Zhang,[a] Tobias Kraus,[a, e] Martin Winter,[c, f] and Hans-Dieter Wiemhöfer*[c, d]

Supporting Information

Experimental

Materials. Benzene (99 %, Alfa Aesar), bis(trifluoromethane)sulfonimide lithium (LiTFSI, 99.95 %, Sigma Aldrich), *n*-buthyllithium (*n*BuLi, 2.5 M in hexan, Alfa Aesar), 1,1-dipehnylethylene (DPE, 98 %, Alfa Aesar), isoprene (99 %, < 1000 ppm *p-tert*-Butylcatechol, Sigma Aldrich), *sec*-butyllithium (*s*BuLi, 1.4 M in cyclohexane, Sigma Aldrich), n-butyllithium (1.6 M in hexane, Acros Organics), styrene (ReagentPlus©, stabilized, Sigma Aldrich), calcium hydride (CaH2, 1-20 mm granules, 88-98 %, Alfa Aesar), ethylene oxid (EO, 99.8 %, Praxair), potassium (98%, pieces in mineral oil, Fisher Scientific), hydrochloric acid (HCl, reagent grade, 37 %, Sigma Aldrich), methanol (MeOH, 99 %, Alfa Aesar) naphthalene (99 %, Fisher Scientific), poly(ethylene oxide) (PEO, 400000 g/mol, Sigma Aldrich), tetrahydrofuran (THF, 99 %, < 1000 ppm stabilizer, Alfa Aesar) and chloroform (CHCl3, 99.8+ %, ACS, Alfa Aesar) were either purified as described or if not further mentioned used as received.

Polymersynthesis. Poly(isoprene)-block-poly(styrene)-block-poly(ethylene oxide) (ISO) terpolymer was synthesized in a living sequential anionic polymerization as previously reported.[1-2] In summary, all chemicals were additionally cleaned with either *n*BuLi or CaH2 followed by distillation under reduced atmosphere. Poly(isoprene)-block-poly(styrene) was prepared in benzene using *s*BuLi as initiator, endcapped with purified EO and deactivated by MeOH/HCl. The lithium counter ion was exchanged by potassium, and the solvent by THF. The final poly(ethylene oxide) block was synthesized and the final ISO was then hydrated by MeOH/HCl, dried and dissolved in CHCl3. The ISO/CHCl3 mixture was slowly dropped in an aliquot of MeOH and the precipitated ISO was dried and further stored at 6 °C. The polymer contained 31.3 vol% of poly(isoprene) (PI), 65.1 vol% of poly(styrene) (PS), and 3.6 vol% of PEO (Fig. S1).

ISO/LiTFSI electrolyte membrane. A 4 wt% solution of ISO in THF and a 12.5 wt% solution of LiTFSI (vacuum dried at 140 °C for 48 h) in THF were mixed in the desired ratios and stirred for 48 h. The mixture was transferred into a 5 mL PTFE beaker and stored at 35 °C in a THF saturated atmosphere to allow a slow evaporation induced self-assembly (EISA) over approximately 48 h. The resulting membranes were dried in reduced atmosphere at 80 °C over-night. Note that the exchange of the casting solvent might resulted in a brittle and non-homogeneous membrane, as for instance using CHCl3.

PEO/LiTFSI electrolyte membrane. To prepare a PEO/LiTFSI membrane, PEO (vacuum dried at 100 °C for 48 h) and LiTFSI (vacuum dried at 140 °C for 48 h) were homogenized in an agate mortar. A chewy mass was received, which was stored at 120 °C in an oven in a vacuum sealed pouch bag over night. The result is a transparent, colorless rubber. The rubber was hot-pressed to a membrane with a thickness of about 300 μm at 80 °C and 100 bar.

¹H-NMR. A Bruker Avance III HD Nanobay equipped with a SampleXpress autosampler and a BBFO probe for 5 mm tubes was used for ¹H-Nuclear magnetic resonance spectroscopy (¹H-NMR). The ISO sample was dissolved in $CDCl_3$ and measured at 300 MHz.

GPC. Polydispersity and molecular weight (M_W) of the ISO was determined by gel permeation chromatography (GPC) using a Water ambient-temperature GPC system equipped with a Waters 2410 differential refractive index (RI) detector. The sample was dissolved in THF (1 mg/mL) and filtered through a PTFE-filter.

WAXS. For wide-angle X-ray scattering (WAXS) the prepared membrane were cute and placed in a glass-capillary, sealed and the sample stage was set under vacuum. The diffraction pattern were recorded on a Xenocs XEUSS 2.0, equipped with a Cu k-alpha source (λ = 154 pm) and a Dectris Pilatus 1M detector, calibrated by Ag-behenate. For 1-D pattern, the primary beam was masked and a total radial integration was performed.

SAXS. Small-angle X-ray scattering (SAXS) pattern were recorded on a Xenocs XEUSS 2.0, equipped with a Dectris Pilatus 1M detector and a Cu k-alpha source (λ = 154 pm). The sample to detector distance was 2500 mm. Sample preparation, setup calibration and 1-D conversation were similar to the WAXS measurement.

Electrochemical impedance spectroscopy (EIS). All spectra were recorded using a Metrohm Autolab Potentiostat PG-STAT302N. The frequency range investigated was 1 Hz to 2 GHz. To investigate the ionic conductivity, the sample was measured in a symmetric steel | sample | steel cell with a square shaped contact area of 1 cm². The temperature was controlled by a Julabo temperature unit FP 45-He.

Lithium ion transference number. Also for this measurements, we used a Metrohm Autolab Potentiostat PG-STAT302N. The sample was measured in a cylindrical symmetric lithium | sample | lithium cell with a diameter of 12 mm. To determine I_0 and I_s, a constant potential of 10 mV was applied until a steady state was reached. This application was framed by two EIS measurements to determine the required resistances. Equation 1 calculates t_{Li+} from the ratio of the steady state current I_s to the initial current I_0, generated by a constant potentiostatic polarization at a potential $\Delta\varphi$ of 10 mV. Equation 2 additionally uses $R_{ct,0}$ and $R_{ct,s}$, the charge transfer resistances in the initial and the steady state. This equation takes the influences of the charge transfer processes from electrolyte to electrode into account that may change during polarization, as for example the solid electrolyte interphase may change.

$$t_{Li+} = \frac{I_s}{I_0} \tag{1}$$

$$t_{Li+} = \frac{I_s(\Delta\varphi - R_{ct,0}I_0)}{I_0(\Delta\varphi - R_{ct,s}I_s)} \tag{2}$$

Rheology measurement. The storage moduli have been determined using an Anton Paar Rheometer MCR 501 equipped with a convective temperature device (-160 °C – 600 °C). The pristine samples were measured without further modification with a D-PP25-SN0 single-use system at 1 Hz, Oscillation amplitude 0.1 % and a constant pressure of 5 N, with respect to the exact sample diameter of 20 mm.

DSC. Differential scanning calorimetry (DSC) has been performed on a Mettler Toledo GmbH HP-DSC 827. The samples have been sealed in inert atmosphere to a 40 µL aluminum crucible and measured under argon.

Simultaneous thermal analysis (TGA/DSC) coupled with mass spectroscopy (MS). Simultaneous TGA/DSC has been performed on a Netzsch STA 449 F3 coupled with a mass spectrometer from Netzsch QMS 403 C. The sample has been sealed in a stainless steel crucible under inert argon atmosphere. Measurement was carried out using a ramp of 10 °C/min from 35 °C to 600 °C.

Full references from main manuscript

[2 c)] M. Amereller, T. Schedlbauer, D. Moosbauer, C. Schreiner, C. Stock, F. Wudy, S. Zugmann, H. Hammer, A. Maurer, R. M. Gschwind, H. D. Wiemhofer, M. Winter, H. J. Gores, *Prog. Solid State Chem.* **2014**, *42*, 39-56.
[3b] W. Schmitz, P. Murmann, R. Schmitz, R. Muller, L. Kramer, J. Kasnatscheew, P. Isken, P. Niehoff, S. Nowak, G. V. Roschenthaler, N. Ignatiev, P. Sartori, S. Passerini, M. Kunze, A. Lex-Balducci, C. Schreiner, I. Cekic-Laskovic, M. Winter, *Prog. Solid State Chem.* **2014**, *42*, 65-84.
[15] E. D. Gomez, A. Panday, E. H. Feng, V. Chen, G. M. Stone, A. M. Minor, C. Kisielowski, K. H. Downing, O. Borodin, G. D. Smith, N. P. Balsara, *Nano Lett.* **2009**, *9*, 1212-1216.
[18] M. Singh, O. Odusanya, G. M. Wilmes, H. B. Eitouni, E. D. Gomez, A. J. Patel, V. L. Chen, M. J. Park, P. Fragouli, H. Iatrou, N. Hadjichristidis, D. Cookson, N. P. Balsara, *Macromolecules* **2007**, *40*, 4578-4585.

References in Supporting Information

[1] J. Chatterjee, S. Jain, F. S. Bates, *Macromolecules* **2007**, *40*, 2882-2896.
[2] M. A. Hillmyer, F. S. Bates, *Macromolecules* **1996**, *29*, 6994-7002.
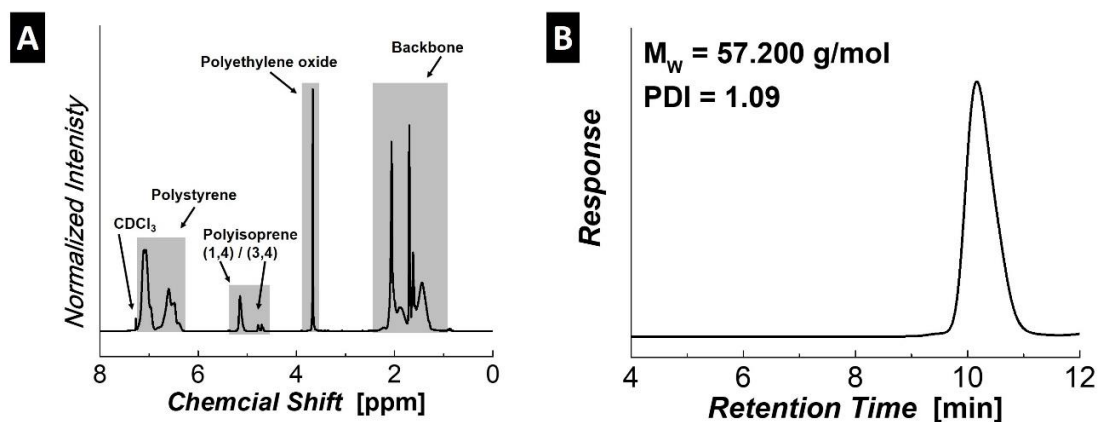
Figure S1. (A) ^{1}H-NMR spectra of neat ISO block copolymer. Impurities due to precipitation in an aliquot of methanol, eliminated by further drying in reduced atmosphere. (B) GPC of corresponding sample.
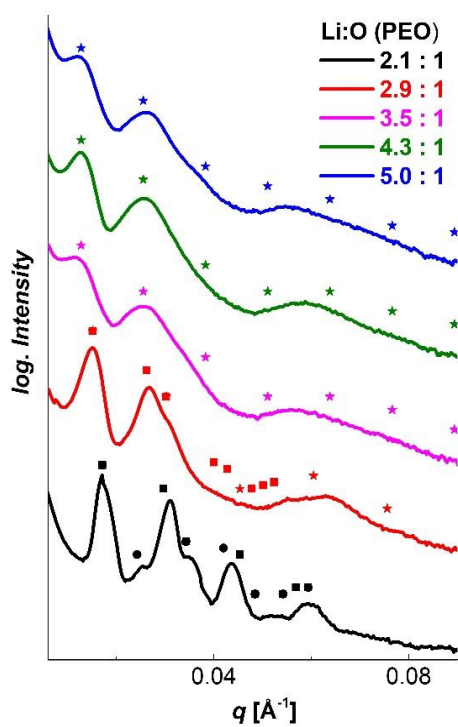
Figure S2. Radially integrated 1D SAXS pattern at 20 °C of pristine ISO/LiTFSI electrolytes at different Li:O (PEO) ratios. Theoretically predicted q/q^* ratios are indicated with dots (spherical micelle packing, BCC), squares (alternating gyroid G^A) and stars (lamellar, LAM).
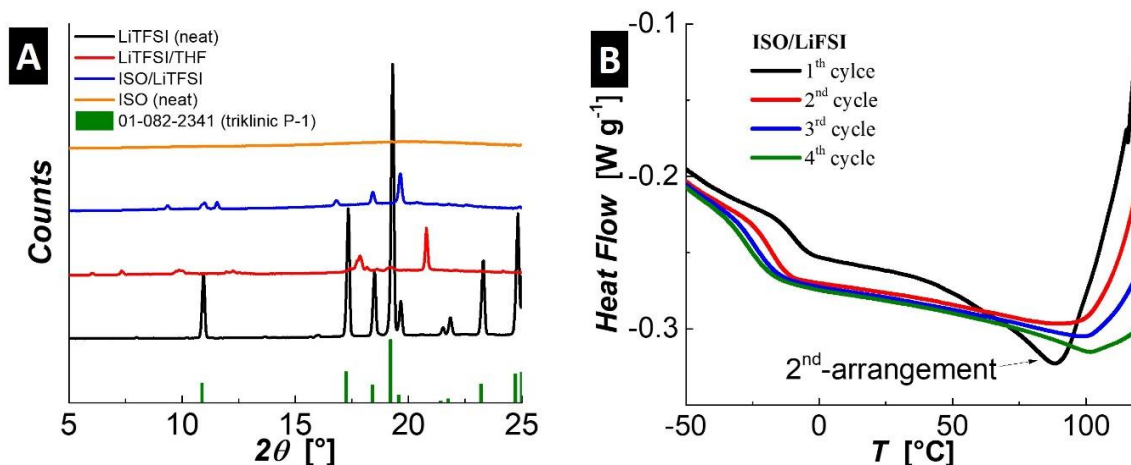
Figure S3. (A) Radial integrated 1-D WAXS pattern (@ 20 °C) of the neat and LiTFSI blended ISO BCP (Li:O (PEO) 4.3:1), neat LiTFSI and a from THF evaporated LiTFSI sample. Triklinic P-1 LiTFSI (PDF 01-082-2341) as bibliographic reference. (B) High-resolution DSC of a pristine ISO/LiTFSI (Li:O (PEO) 4.3:1) sample in consecutive temperature loops.
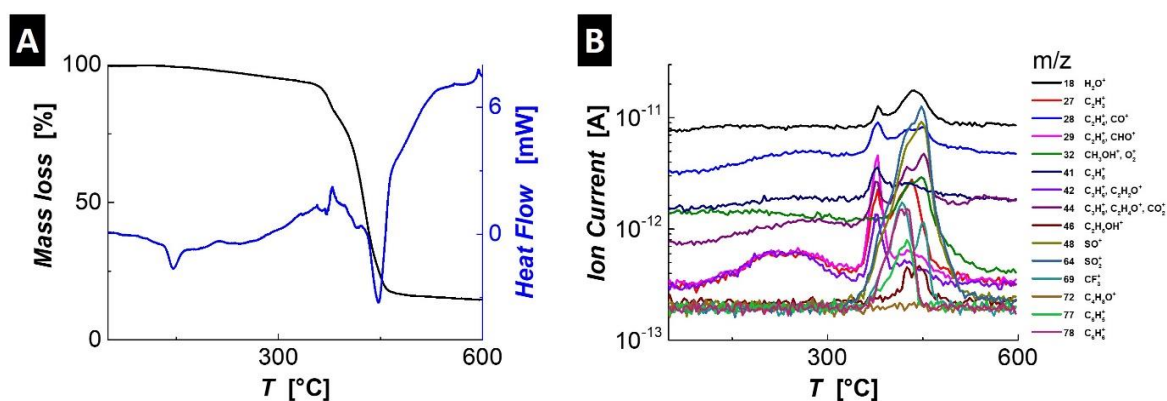
Figure S4. (A) Simultaneous thermal analysis (TGA (black)/DSC (blue)) coupled with (B) mass spectroscopy (MS) or ISO013/LiTFSI with an Li:O (PEO) ratio of 4.3:1. Mass-to-charge ratios (m/z) for expected species are referred to H_2O^+ (18), $C_2H_3^+$ (27), $C_2H_4^+/CO^+$ (28), $C_2H_5^+/CHO^+$ (29), CH_3OH^+, O_2^+ (32), $C_3H_5^+$ (41), $C_3H_6^+/C_2H_2O^+$ (42), $C_3H_8^+/C_2H_4O^+/CO_2^+$ (44), $C_2H_5OH^+$ (46), SO^+ (48), SO_2^+ (64), CF_3^+ (69), $C_4H_8O^+$ (72), $C_6H_5^+$ (77) and $C_6H_6^+$ (78).
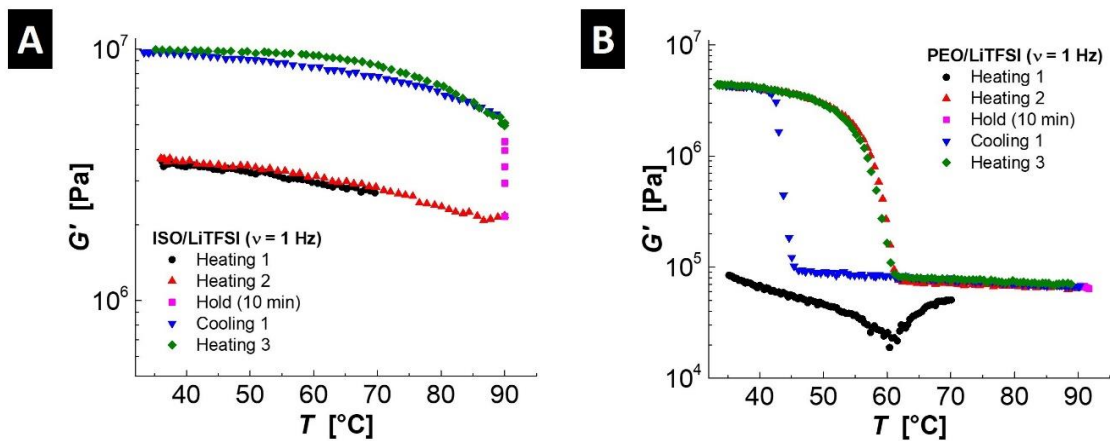
Figure S5. Rheology measurement in consecutive heating cylces of (A) a pristine ISO/LiTFSI (Li:O (PEO) 4.3:1) and (B) a pristine PEO/LiTFSI electrolyte.
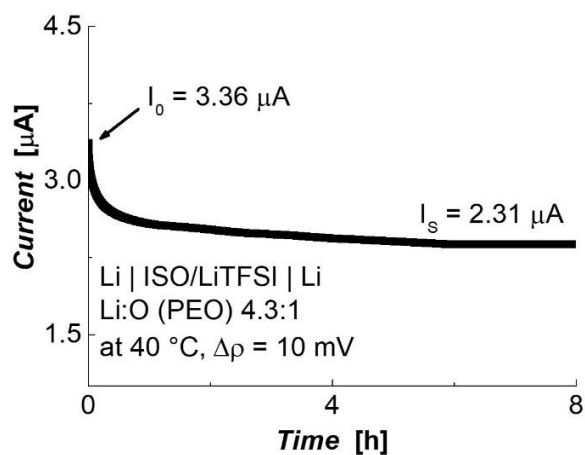
Figure S5. Chronoamperometric measurement for lithium ion transference number (t_{Li+}) determination at 40 °C with an applied potential of 10 mV in a symmetric Li|Polymer electrolyte|Li cell for ISO/LiTFSI with an Li:O (PEO) ratio of 4.3:1.

Chapter 4.3

Self-Assembled Block Copolymer Electrolytes: Enabling Superior Ambient Cationic Conductivity and Electrochemical Stability

Alexander Pelz,[a,b,+] Tobias Sebastian Dörr,[c,+] Peng Zhang,[c] Peter W. de Oliveira,[c] Martin Winter,[a,d] Hans-Dieter Wiemhöfer,[a,b] Tobias Kraus[c,e,*]

[a]Helmholtz-Institute Münster, IEK-12, Forschungszentrum Jülich GmbH, Corrensstraße 46, 48149 Münster, Germany
[b]Institute of Inorganic and Analytical Chemistry, University of Münster, Corrensstraße 28/30, 48149 Münster, Germany
[c]INM - Leibniz Institute for New Materials, Campus D2 2, 66123 Saarbrücken, Germany
[d]MEET Battery Research Center, University of Münster, Corrensstraße 46, 48149 Münster, Germany
[e]Colloid and Interface Chemistry, Saarland University, Campus D2 2, 66123 Saarbrücken, Germany

[+]These authors contributed equally to this work.

Abstract

Block copolymers are promising materials for electrolytes in lithium metal batteries that can be tuned by changing the individual blocks to

independently optimize ion transport as well as electrochemical and mechanical stability. We explored the performance of electrolytes based on modified triblock copolymers poly(isoprene)-block-poly(styrene)-block-poly(ethylene oxide). Large polyethylene oxide (PEO) blocks with a molecular mass of 53 kg mol^{-1} allowed only for low lithium salt loadings and led to poor ionic conductivity below 60 °C. However, we found that unusually small molecular weight of the ion solvating PEO blocks down to 2 kg mol^{-1} enabled polymer-in-salt loadings of up to 5:1 Li:EO. A

superior total ionic conductivity greater than 1 mS cm^{-1} was found for optimized compositions above 0 °C with remarkably low temperature dependence in a wide range from -20 °C to 90 °C. We believe that highly ordered 2D lamellae from controlled self-assembly established a beneficial environment for ionic transport with ionic mobility decoupled from segmental polymer motion. This also explains lithium ion transference numbers as high as 0.7 were obtained for the high conductivity samples.

Self-Assembled Block Copolymer Electrolytes: Enabling Superior Ambient Cationic Conductivity and Electrochemical Stability

Alexander Pelz,[†,‡,#] Tobias Sebastian Dörr,[§,#] Peng Zhang,[§] Peter William de Oliveira,[§] Martin Winter,[†,‖] Hans-Dieter Wiemhöfer,[†,‡] and Tobias Kraus*[,§,⊥]

[†]Helmholtz-Institute Münster, IEK-12, Forschungszentrum Jülich GmbH, Corrensstraße 46, 48149 Münster, Germany
[‡]Institute of Inorganic and Analytical Chemistry, University of Münster, Corrensstraße 28/30, 48149 Münster, Germany
[§]INM—Leibniz Institute for New Materials, Campus D2 2, 66123 Saarbrücken, Germany
[‖]MEET Battery Research Center, University of Münster, Corrensstraße 46, 48149 Münster, Germany
[⊥]Colloid and Interface Chemistry, Saarland University, Campus D2 2, 66123 Saarbrücken, Germany
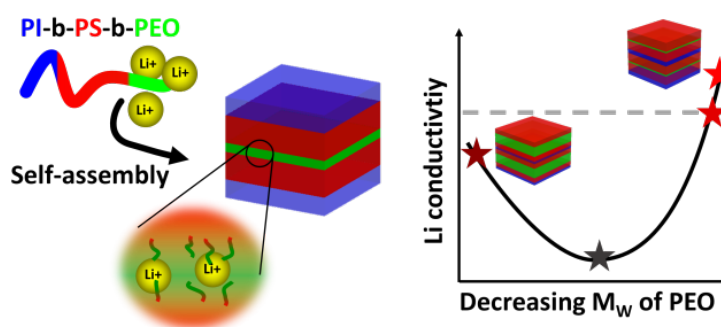
Ⓢ *Supporting Information*

ABSTRACT: Block copolymers are promising materials for electrolytes in lithium metal batteries that can be tuned by changing the individual blocks to independently optimize ion transport as well as electrochemical and mechanical stability. We explored the performance of electrolytes based on modified triblock copolymers, poly(isoprene)-*block*-poly-(styrene)-*block*-poly(ethylene oxide). Large polyethylene oxide (PEO) blocks with a molecular mass of 53 kg mol^{-1} allowed only for low lithium salt loadings and led to poor ionic conductivity below 60 °C. However, we found that unusually small molecular weight of the ion solvating PEO blocks down to 2 kg mol^{-1} enabled polymer-in-salt loadings of up to 5:1 Li/EO. A superior total ionic conductivity greater than 1 mS cm^{-1} was found for optimized compositions above 0 °C with remarkably low temperature dependence in a wide range from −20 to 90 °C. We believe that highly ordered two-dimensional lamellae from the controlled self-assembly established a beneficial environment for ionic transport with ionic mobility decoupled from segmental polymer motion. This also explains lithium ion transference numbers as high as 0.7 that were obtained for the high conductivity samples.
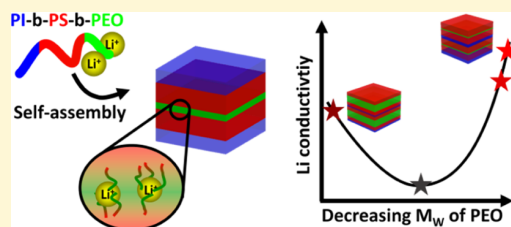
1. INTRODUCTION

Lithium (Li) metal anodes offer significantly higher specific capacities than graphite anodes in rechargeable Li-ion batteries (LIBs) and are thus considered as the "next generation" technology.[1−3] They substantially increase the specific energy of such batteries,[4−6] but their practical use is limited by the risk of inhomogeneous Li plating on the electrode surface that can lead to "dendritic" Li (HSAL)[7] morphologies with large specific areas that increase the risk for short circuits and thermal runaway reactions.[8] Polymer electrolytes and, in particular, the widely modifiable block copolymer (BCP)-based electrolytes could reduce this problem if they fulfilled the following requirements:

(i) Sufficient cationic mobility to reduce the concentration gradients that arise during (dis-)/charging[9] and prevent local electrolyte depletion.[10]

(ii) Formation of uniform and conformal solid electrode| electrolyte interfaces.

(iii) Electrochemical and chemical (kinetic) stability, in particular versus Li metal,[11,12] the cathode material,[13] and the current collectors (commonly, aluminum and copper).[14]

(iv) Sufficient mechanical storage modulus, (G'), of at least 10^5 Pa for polymeric electrolytes to suppress the dendritic Li growth in Li-metal batteries (LMB).[15−17]

No simple salt-in-polymer electrolyte is available that would meet all of the above criteria. Poly(ethylene oxide) (PEO), the most commonly investigated polymer for electrolyte application, is either too soft or not conductive enough, depending on the molecular weight (M_W). PEO strongly coordinates Li ions at the ether oxygen, which couples ionic to polymeric mobility and leads to low cationic mobility.[18−23] The cationic conductivity correlates with the degree of crystallinity of PEO and thus, with temperature. Higher mobility at temperatures exceeding ~60 °C leads to an increased conductivity even for large PEO with M_W of several hundred kg mol^{-1}. Electrolytes from PEO with lower M_W have reduced crystallinities and provide greater mobility, but their mechanical performance is insufficient for battery application.

This trade-off between macroscopic rigidity and microscopic mobility can be elegantly resolved using BCPs. The soft PEO blocks can be combined with stronger polymer blocks such as poly(styrene) (PS) to create block copolymer electrolytes (BCEs) that are suitable for Li metal anodes in rechargeable batteries.[24−27] Self-assembled, ordered BCP structures, especially such with lamellar microstructure, have been reported to

Table 1. Total M_W, Polydispersity ($Đ_P$), Volume Fractions (f), $M_{W,PEO}$, and the Estimated Corresponding Number of EO-Units of the Four ISO Compositions Prepared and Used in This Study

sample	$M_W{}^b$/kg mol^{-1}	$Đ_P{}^b$	$f_{PI}{}^a$/%	$f_{PS}{}^a$/%	$f_{PEO}{}^a$/%	$M_{W,PEO}{}^a$/kg mol^{-1}	est. number of EO units
ISO-2k	57	1.09	31	65	4	2.1	50
ISO-5k	52	1.03	32	60	8	4.6	100
ISO-7k	61	1.12	30	60	10	6.9	160
ISO-53k	88	1.32	15	28	57	52.6	1200

^{a}From combined ^{1}H NMR and GPC. ^{b}From GPC.

improve charge transport in between the electrodes.[28−30] The addition of a third block, for instance, poly(isoprene) (PI) in addition to PS and PEO, gives access to a wider range of accessible microstructures and allows for more freedom in choosing the PEO block size.[31,32] A diblock copolymer with a favorable lamellar morphology would imply a volume fraction ratio of the two types of blocks in the range ∼0.4−0.6.[33] This limits the lowest feasible block size, as the overall molecular weight of the BCP should reach several tens of kg mol^{-1} for sufficient mechanical stability at elevated temperatures.

We have recently reported first results on an electrolyte based on poly(isoprene)-*block*-poly(styrene)-*block*-poly(ethylene oxide) (PI-*b*-PS-*b*-PEO; acronymized as ISO hereafter) with an ultrashort PEO block that enables high "polymer-in-salt" Li/EO (EO = ethylene oxide repeating unit) ratios up to 5:1 within a macroscopically stable, rubberlike membrane that has a periodic lamellar microstructure.[29] These electrolytes showed high ionic mobility that was decoupled from the segmental movement of the polymer. Large amounts of salt in the lamellar PEO domains were stabilized by nonremovable residual tetrahydrofuran (THF) from the membrane preparation process. The aim of the current work was to exploit this promising principle and create electrolytes that retain the large salt loadings but meet all criteria required for deployment that are mentioned above.

To create a practically applicable electrolyte material, we tuned the molecular structure of the self-assembled, ISO-derived BCEs by successively decreasing the PEO block size at a constant PI/PS block size ratio to find the optimum in Li$^+$ mobility and stability. In Section 3.1, we correlate the overall and effective cationic conductivity as a function of the PEO block size. Conductivities were interpreted with respect to the obtained microstructures via wide- and small-angle X-ray scattering (WAXS and SAXS) in Section 3.2. We found small PEO blocks with high lithium salt concentrations to be indispensable for a distinctly increased ionic mobility. The final Section 3.3 provides data on the remaining critical parameters: thermal properties, the electrochemical stability window (ESW), and mechanical stability.

2. EXPERIMENTAL SECTION

2.1. Materials. Bis(trifluoromethane)sulfonimide lithium (LiTFSI, 99.95%, Sigma-Aldrich), 1,1-diphenylethylene (98%, Alfa Aesar), *sec*-butyllithium (*sec*BuLi, 1.4 M in cyclohexane, Sigma-Aldrich), *n*-butyllithium (1.6 M in hexane, Acros Organics), potassium (98%, pieces in mineral oil, Fisher Scientific), calcium hydride (CaH$_2$, 1−20 mm granules, 88−98%, Alfa Aesar), hydrochloric acid (HCl, reagent grade, 37%, Sigma-Aldrich), methanol (MeOH, 99%, Alfa Aesar), naphthalene (99%, Fisher Scientific), PEO (400 000 g/mol, Sigma-Aldrich), and chloroform (CHCl$_3$, 99.8+%, ACS, Alfa Aesar) were used as received. Benzene (99%, Alfa Aesar), THF (anhydrous, ≥99.9%, inhibitor-free, Sigma-Aldrich), isoprene (99%, <1000 ppm *p-tert*-butylcatechol, Sigma-Aldrich), and EO (99.8%, Praxair) were treated

with *n*BuLi and styrene (ReagentPlus, stabilized, Sigma-Aldrich) with CaH$_2$, followed by distillation under reduced pressure.

2.2. Polymer Synthesis. ISO BCP templates were synthesized using living sequential anionic polymerization, as previously reported.[34,35] Poly(isoprene)-*block*-poly(styrene) was prepared in benzene using stoichiometric amounts of *sec*BuLi as the initiator and endcapped with an excess of EO. The lithium counter ion was exchanged by potassium after deactivation of the living polymer chain. The final PEO block was synthesized in THF, and the resulting ISO was then terminated by a reaction with MeOH/HCl, dried, and dissolved in chloroform. The resulting mixture was slowly precipitated in an aliquot of MeOH, and the final ISO was dried and stored at 6 °C. Table 1 summarizes the composition of the prepared BCPs.

2.3. ISO/LiTFSI Electrolyte Membrane. Membrane preparation was conducted in a dry environment (dry room, dew point below −55 °C). A 4 wt % solution of ISO in anhydrous THF and a 12.5 wt % solution of LiTFSI (vacuum-dried at 140 °C for 2 d) in anhydrous THF were mixed in the ratios given in Table 2 and stirred for 2 d. The mixture

Table 2. Potentiostatic Determination of the Lithium Ion Transference Numbers (t_{Li^+}) with the Bruce−Vincent Method[46,47] and Partial Lithium Ion Conductivities ($σ_{Li^+}$) at 40 °C for the Four ISO Samples with Salt Concentrations which Showed the Best Conductivities

	Li/EO	$σ_{total}$/mS cm^{-1}	t_{Li^+} (eq 1)	$σ_{Li+}$/mS cm^{-1}
ISO-53k (0.04:1)	0.04:1	0.04	0.38 ± 0.08	0.02
ISO-7k (0.22:1)	0.22:1	10^{-4}	0.52 ± 0.04	5 × 10^{-5}
ISO-5k (1.33:1)	1.33:1	0.05	0.58 ± 0.04	0.03
ISO-2k (4.30:1)	4.30:1	3.66	0.70 ± 0.02	2.56

was transferred into a 5 mL PTFE beaker, and the polymer was allowed to self-assemble during slow solvent evaporation at 35 °C in a solvent-saturated atmosphere. The resulting membranes were vacuum-dried (<10^{-3} bar) at 90 °C overnight. Using other solvents than anhydrous THF (e.g., chloroform) resulted in dry, brittle, and inhomogeneous membranes that were not suitable for further investigation, which is a first indication of the importance of THF.

2.4. ^{1}H Nuclear Magnetic Resonance. ^{1}H nuclear magnetic resonance spectroscopy (^{1}H NMR) was performed on a Bruker AVANCE III HD NanoBay equipped with a SampleXpress autosampler and a BBFO probe for 5 mm tubes. Samples were dissolved in deuterated chloroform and measured at 300 MHz.

2.5. Gel Permeation Chromatography. Gel permeation chromatography (GPC) determined the polydispersity ($Đ_P$) and the molecular weight (M_W). We used a Waters ambient-temperature GPC system equipped with a Waters 2410 differential refractive index detector. For analysis, samples were dissolved in THF (1 mg mL^{-1}). For poly(isoprene) analysis, the following standards from Polymer Standards Service (Mainz, Germany) have been used for calibration: poly(isoprene-1.4) PSS-pio7.5k, PSS-pio10k, PSS-pio13k, PSS-pio21k, and PSS-pio47k.

2.6. Wide- and Small-Angle X-ray Scattering. WAXS and SAXS measurements were performed on a Xenocs Xeuss 2.0 setup, equipped with a Cu Kα source ($λ$ = 154 pm) and a DECTRIS PILATUS 1M detector. We cut pieces of the electrolyte membranes and sealed them in fused silica capillaries with epoxy resin. All samples were measured in the vacuum chamber attached to the X-ray setup. The sample to
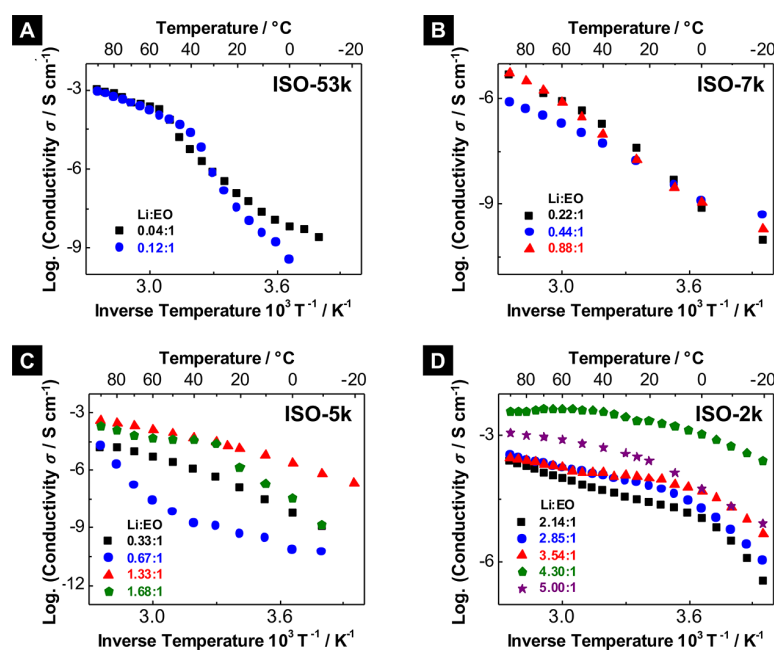
Figure 1. Arrhenius plots of the EIS results for all evaluable BCEs made from (A) ISO-53k, (B) ISO-7k, (C) ISO-5k, and (D) ISO-2k. The indicated average Li/EO ratios are based on polymer composition, and they do not account for the residual THF (more details on the preparation can be found in Table S1).

detector distances were calibrated with silver behenate to 312 ± 1 and 2506 ± 1 mm for WAXS and SAXS, respectively. The primary data analysis was done with the Foxtrot software (version 3.2.7, SOLEIL, France).

2.7. Electrochemical Impedance Spectroscopy. All spectra were recorded using a Metrohm Autolab Potentiostat PG-STAT302N in a frequency range from 1 Hz to 2 MHz with temperature controlled by a Julabo temperature unit FP 45-He. To investigate the ionic conductivity, the sample was measured in the symmetric cell setup steel|BCE|steel with a square contact area of 1 cm².

2.8. Cyclic Voltammetry. The measurements were performed by a Metrohm Autolab Potentiostat PG-STAT302N at a temperature of 60 °C in an UNE200 oven from Memmert GmbH. The scan rate was 0.5 mV s⁻¹, and the potential range observed was from −0.6 to 7.0 V versus Li/Li⁺. All samples were contacted with a stable spring-loaded metal working electrode (thickness 1 mm). Pt was used as the working electrode for the high potential range (above 3.3 V vs Li/Li⁺) and Cu for the lower potentials (below 3.3 V). Lithium metal foil (thickness 1 mm, attached on top of a Ni plate) was used as the reference electrode, and a stainless steel counter electrode with a diameter of 12 mm was used.

2.9. Lithium Ion Transference Number (t_{Li^+}). The sample was measured in the symmetric cell setup Li|BCE|Li (cylindrical geometry with diameter 12 mm) using a potentiostat (Metrohm Autolab PG STAT302N). Two electrochemical impedance spectroscopy (EIS) measurements were used to determine the required intermediate and final impedance spectra. Equation 1 provides t_{Li^+} from the ratio of the steady state current, I_S, to the initial current, I_0, generated by a constant potentiostatic polarization at a potential $\Delta\varphi$ of 10 mV. It additionally takes $R_{ct,0}$ and $R_{ct,S}$ into account, which are the charge transfer resistances in the initial and the steady state, respectively, to model the charge transfer from the electrolyte to electrode that may change during polarization, for example, when the solid electrolyte interphase changes.

$$t_{Li^+} = \frac{I_s(\Delta\varphi - R_{ct,0}I_0)}{I_0(\Delta\varphi - R_{ct,S}I_S)} \qquad (1)$$

2.10. Rheometry. An Anton Paar Rheometer MCR 501 equipped with convection heating (160−600 °C) was used to measure the storage and loss moduli, G' and G''. Pristine samples were measured

without further preparation on a D-PP25-SN0 single-use system at 1 Hz, an oscillation amplitude of 0.1%, and a constant force of 5 N with respect to the exact sample diameter (20 mm).

2.11. Differential Scanning Calorimetry. A METTLER TOLEDO HP-DSC 827 was used for differential scanning calorimetry (DSC). The samples were sealed in a 40 μL aluminum crucible under inert atmosphere and measured under argon.

2.12. Thermogravimetric Analysis−Mass Spectrometry. Thermogravimetric analysis coupled with mass spectroscopy (TGA−MS) was performed on a NETZSCH STA 449 F3 coupled with a mass spectrometer from NETZSCH QMS 403 C. Measurements were carried out using a 10 °C min⁻¹ ramp from 35 to 600 °C.

3. RESULTS AND DISCUSSION

3.1. Correlation of PEO Block Size and Cationic Conductivity. Four ISO samples with constant main block size ratios (PI/PS ratio 1:2) and decreasing PEO block sizes were prepared by sequential anionic polymerization. Three of the four ISO samples contained PEO blocks with relatively low molecular weights ($M_{W,PEO}$) of 2 kg mol⁻¹ (denoted as ISO-2k), 5 kg mol⁻¹ (denoted as ISO-5k), and 7 kg mol⁻¹ (denoted as ISO-7k), respectively. The fourth ISO composition provided a much higher value $M_{W,PEO}$ of 53 kg mol⁻¹ (denoted as ISO-53k) at the identical PI/PS ratio. Table 1 summarizes the characteristics of the four ISO compositions as obtained from combined GPC and ¹H NMR spectroscopy. The individual blocks were identified using ¹H NMR, and the particular volume fractions were determined by normalizing using the M_W of the synthesized parental PI block, as initially determined by GPC (using commercial PI standards).

BCE membranes were prepared in a dry environment (dry room, dew point below −55 °C) by mixing a constant volume of a solution containing 4.0 wt % ISO in anhydrous THF with different volumes of a solution containing 12.5 wt % vacuum-dried lithium bis(trifluoromethane)sulfonamide (LiTFSI) in anhydrous THF, as previously reported.[29] The mixture was

slowly dried to allow for evaporation-induced self-assembly (EISA) during the membrane formation. The freestanding, rubberlike membranes were dried in vacuum ($<10^{-3}$ bar) at 60 °C overnight and aged for 0.5 h at 90 °C and subsequently used as BCE. We carried out our membrane preparation in a dry-room, using only anhydrous and purified chemicals, we further determined the amount of water in the electrolytes to always be far below 100 ppm by using Karl Fischer titration. Another sufficient evidence for negligible water content is the stability of the lithium metal|electrolyte interface during polarization experiments (as controlled by the intermediate impedance measurements).

We expect two predominant effects when changing the Li salt concentration which selectively swells the PEO phase:[36,37] (i) the morphology with the lowest free energy (that forms during solvent evaporation) changes depending on the relative volume fraction of the blocks. A rough idea of the favored microstructure follows from the individual ISO compositions with respect to the phase diagram.[34,38] (ii) increasing the salt concentration first increases the overall conductivity, usually until a maximum is reached. A subsequent decrease of the total conductivity is usually attributed to the increasing ion association.[39]

Table S1 (cf. Supporting Information) summarizes the overall BCE formulation. In this work, all Li/EO ratios were calculated as referred to the PEO block size. Note that a small amount of nonvolatile THF was observed which very probably contributes to the coordination of lithium ions too (vide infra). In all samples, however, the amount of PEO predominated.

We successively increased the salt content. Salt segregation was observed when the saturation limit was exceeded yielding macroscopically inhomogeneous membranes which were not considered further. The homogeneous membranes were characterized using EIS between −20 and 90 °C. The total ionic conductivities (σ) as deduced from the impedance are shown in Figure 1. Some of the apparently homogeneous membranes turned out to be too brittle for these measurements or did not provide consistent impedance spectra; they were excluded from the EIS analysis.

Not surprisingly, the conductivities of the BCE samples as prepared from ISO-53k and containing a high PEO volume fraction of 57 vol % showed a steep increase with temperature (cf. Figure 1A) as normally observed in conventional salt-in-PEO electrolytes;[40] the very low values below the transition range 40−60 °C are due to partial crystallization. In agreement with that, we detected the crystalline-amorphous phase transition in our ISO-53K sample by DSC (Figure S1a) above 40 °C, which correlates well with the strong increase around that temperature.

Electrolytes made from the BCP samples with a lower PEO block size ($M_{W,PEO}$) did not show any detectable endothermic phase transition nor a correlated steep change of the conductivity (Figure S1b−d). The BCE samples made from ISO-7k exhibited rather small conductivities below 10^{-5} S cm^{-1} virtually independent of the Li/EO ratio and clearly not useful as battery electrolytes. This result is in agreement with earlier studies on BCP electrolytes which reported decreasing conductivities with the decreasing PEO block sizes.[41] We found, however, that this correlation only holds above $M_{w,PEO} \approx$ 7 kg mol^{-1}. Smaller PEO blocks, as used in ISO-5k, exhibited low activation energies with moderate total conductivities of 10^{-6} S cm^{-1} (−20 °C) up to 10^{-4} S cm^{-1} (90 °C). Sufficiently short PEO blocks probably increased the conductivity in two ways: (i) the reduced number of ether oxygens led to higher Li/

EO ratios that reduced the cation coordination; (ii) low $M_{W,PEO}$ values provided a higher segmental mobility and thus, increased ionic mobility of the interacting ions. Ultra-small PEO blocks exhibited the highest total conductivities with a very small dependence on the temperature, consistent with our preliminary results on ISO-2k with its "polymer-in-salt" lithium salt loadings.[29] In such materials, the ether oxygen of residual nonvolatile THF may partially compensate for the coordinative deficiency with regard to the lithium cations. The surprisingly high total conductivity strongly hints to ionic mobilities that are more or less decoupled from the slow segmental polymer relaxation. The best performing electrolyte exhibited a total conductivity of 2.2 mS cm^{-1} (20 °C) at a Li/EO ratio of 4.3:1 (referred to ether oxygen of PEO), which clearly exceeds the previously reported conductivities for other BCP-based electrolytes[42,43] and becomes similar to values for polymer gel-type electrolytes.[44,45]

We selected the most conductive Li/EO ratio for each ISO composition (further denoted as "ISO-53k (0.04:1)", "ISO-7k (0.22:1)", "ISO-5k (1.33:1)", and "ISO-2k (4.30:1)") and performed additional experiments on them with a focus on their qualification for direct current charging/discharging in lithium cells. In this context, the contribution of the partial conductivity of lithium ions is of the greatest interest as this characterizes the steady state charging/discharging rate capability of the binary electrolyte. Hence, the lithium transference number t_{Li^+} is needed. Together with the total conductivity, σ_{total}, it allows to calculate the value for partial conductivity of lithium ions according to $\sigma_{Li^+} = t_{Li^+}\sigma_{total}$.[9] In this study, we used the Bruce−Vincent method[46,47] (potentiostatic polarization, cf. Experimental Section). Table 2 summarizes the resulting values of t_{Li^+} and σ_{Li^+}. We also carried out preliminary tests of the long-term steady-state current in the symmetric Li|BCE|Li cell as used for the transference number determination. We found long-time stability against Li metal at 40 °C and 10 mV for all investigated ISO compositions; no indications were observed for instabilities such as current oscillations, short circuits, or loss of contact.

In all samples, t_{Li^+} increased with the decreasing PEO block size (cf. $M_{W,PEO}$ of the various ISO compositions in Table 1) and, as column 2 in Table 2 shows, with the increasing Li/EO, too. The value t_{Li^+} of 0.38 for ISO-53k (with a low Li/EO of 0.04:1) indicated a distinctly higher overall cationic contribution to the total conductivity. For comparison, the total conductivity was close to that of conventional salt-in-PEO electrolytes which exhibit t_{Li^+} of about 0.2 because of stronger interaction of Li$^+$ with the ether oxygen.[9] This might be a consequence of the ordered microstructure which also influences the microstructure in the PEO-rich domains and thus modulates the interaction with the lithium cations.[36,48]

Hence, as Table 2 shows, more than 50% of the (still low) total conductivity of the ISO-7k sample (Li/EO = 0.22:1) is due to Li$^+$ conduction. Even higher t_{Li^+} values of 0.58 and 0.70 were found for ISO-5k and ISO-2k together with high total conductivities. This indicates a considerable decoupling of the ion transport from the polymer dynamics, in particular with respect to the lithium ions in ISO-2k. It leads to the observed high partial Li$^+$ conductivities of 0.03 and 2.56 mS cm^{-1} in ISO-5k (1.33:1) and ISO-2k (4.30:1), respectively. Note that these values are an average over the cross-section of the electrolyte. Taking into account that the conducting lamellar domains enriched with PEO and lithium salt are only a small fraction of the cross-section, one can assume that the local lithium conductivity is even higher, probably by up to one decade.[49]

3.2. Phase Composition and Microstructural Order.

The amount of lithium salt added to the various ISO samples affects the equilibrium morphology formed upon self-assembly, as discussed above.[37] To correlate the strong changes of the partial Li$^+$ conductivities with the ISO compositions, we characterized the polymer electrolytes with SAXS. Figure 2A
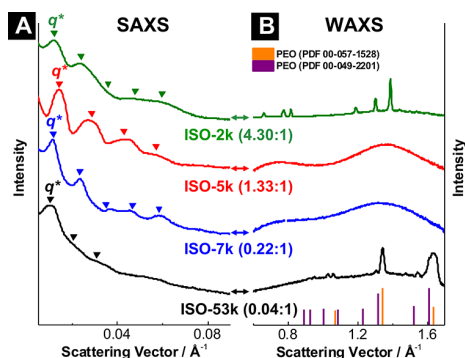
Figure 2. Typical X-ray scattering data: (A) SAXS and (B) WAXS at room temperature for ISO-53k (0.04:1), ISO-7k (0.22:1), ISO-5k (1.33:1), and ISO-2k (4.30:1) electrolytes. Triangles in panel (A) denote the theoretically predicted diffraction positions of a lamellar structure calculated from the first diffraction peak (q^*). Crystalline PEO library data (PDF 00-057-1528 and PDF 00-049-2201) are given in panel (B).

shows the scattering of the most conductive ISO/LiTFSI hybrids (all others are shown in Figure S2). We identified the microstructure of the polymer electrolytes by comparing the scattering vector (q) of high order diffraction peaks with the theoretically expected peak positions (marked with triangles in Figure 2A) as calculated from the first diffraction peak (q^*) of typical ISO microstructures. The experimental peak positions agreed well with those predicted for a lamellar microstructure.[50] The periodicity (d) of the lamellar, LiTFSI-blended PEO domains was calculated as $d = 2\pi/q^*$ to 61.1, 55.1, 43.9, and 52.5 nm for ISO-53k (0.04:1), ISO-7k (0.22:1), ISO-5k (1.33:1), and ISO-2k (4.30:1). The periodicity decreased for lower PEO block size; an exception was ISO-2k (4.30:1) which was dominated by an extended swelling of the PEO domain because of the much higher relative LiTFSI content.

Any crystallinity of PEO strongly influences the Li$^+$ conductivity as shown in several publications by Bruce et al. who investigated the conductivity of crystalline salt-in-PEO materials over a broad temperature range.[51] In this work, we performed WAXS to search for partially crystalline domains in the most conductive electrolytes for each of our ISO-based electrolytes and found clear evidence for ordering from the reflexes as shown in Figure 2B. ISO-53k (0.04:1) exhibited peaks at 14.6°, 15.1°, 19.1°, 22.1°, and 23.4° that we identified as Bragg diffraction from (021), (110), (120), (112), and (032) planes of PEO.[52] However, there was no crystalline phase identified for the samples derived from ISO-7k and ISO-5k as already expected from EIS and DSC results. Temperature-dependent in situ WAXS revealed that the initial crystallinity of the pristine electrolytes as seen immediately after solvent evaporation in ISO-7k (0.22:1) irreversibly vanished after thermal annealing above the melting temperature of PEO (Figure S3). A particular case was the sample ISO-2k (4.30:1), which exhibited strong crystallinity that did not vanish even at 120 °C and hence cannot originate from the PEO-rich domain. Additionally, the

characteristic diffraction pattern was different from that of our pristine LiTFSI as well as different from library data of crystalline LiTFSI (Figure S4). We also dissolved LiTFSI in THF and dried that solution following our synthetic protocol as used for the electrolyte preparation (i.e., EISA process in dry environment). A different scattering pattern compared to the pristine salt was obtained (Figure S4). We believe that the signal in ISO-2k (4.30:1) was caused by lithium with considerable additional THF coordination and the PEO ether oxygen.[29] Yet, any attempt to introduce comparably high amounts of salt into pure PEO (2000 g mol^{-1}) using THF to mimic the chemical environment in our BCE resulted in a honeylike mixture that did not show appreciable scattering .

In summary, the combined results from EIS, DSC, SAXS, WAXS, and the determination of t_{Li^+} revealed the following key features: (i) PEO chain stretching within the BCEs correlated with an improved ionic mobility. (ii) The highest total conductivity was always obtained for a two-dimensional (2D) lamellar microstructure; other morphologies (as reported in the Supporting Information, Figure S2) consistently revealed lower conductivities (Figure 1). (iii) The partial conductivity due to Li$^+$ generally increased with decreasing PEO block size. (iv) Large PEO blocks partially crystallized, accompanied by decreasing conductivity, especially at low temperatures. (v) Low $M_{W,PEO}$ provided less ether oxygen and higher Li/EO ratios, enabled by THF insertion as in ISO-2k (4.30:1).

We found electrolytes from BCE with $M_{W,PEO} \leq 5$ kg mol^{-1} and high Li concentrations most promising and continued with their evaluation in further detail.

3.3. Thermal, Electrochemical, and Mechanical Stabilities.

We evaluated the mechanical integrity of ISO-5k- and ISO-2k-derived BCE with applied potentials and at different temperatures. Our results suggests that residual THF (nonvolatile in vacuum <10^{-3} bar at 90 °C) complexes Li at Li/EO ratios >1 for ISO-5k and ISO-2k. The solvent may affect long-term thermal and electrochemical stability, act as a plasticizer, electropolymerize at the cathode at higher positive potentials, or simply evaporate on heating. We used TGA−MS to elucidate a possible thermal degradation of the BCEs, to quantify the remaining THF, and to determine a thermal stability window (Figure 3). The spectra indicate mass losses starting at 140 °C that were similar for both, ISO-5k (1.33:1) and ISO-2k (4.30:1) electrolytes, with leaving decomposition fragments including C$_2$H$_3^+$ ($m/z = 27$), C$_2$H$_5^+$/CO$^+$ ($m/z = 29$), C$_3$H$_5^+$ ($m/z = 41$), C$_3$H$_6^+$/C$_2$H$_2$O$^+$ ($m/z = 42$), and C$_3$H$_8^+$/C$_2$H$_4$O$^+$/CO$_2^+$ ($m/z = 44$). Only for ISO-5k (1.33:1), we found C$_4$H$_8$O$^+$ ($m/z = 72$). All these fragments are consistent with (decomposed) THF leaving the sample, with two main differences between our BCEs: (i) The fragment $m/z = 72$ that corresponds to an intact, ionized C$_4$H$_8$O ring was not detected for ISO-2k (4.30:1), probably because of stronger THF interaction in the electrolytes. (ii) We estimate an initial THF content of ~8% for ISO-5k (1.33:1) and ~5% for ISO-2k (4.30:1) from the total mass loss at 300 °C. This is surprising given the higher Li/EO ratio of ISO-2k (4.30:1) and its greater salt content that should require more THF to achieve sufficient Li$^+$ coordination. A possible explanation assumes different roles of THF within the PEO domain: in ISO-2k (4.30:1), THF may form clusters with Li$^+$ (and TFSI$^-$) that cause the observed strong crystalline scattering in WAXS, as discussed above. The clusters are strongly bound to the PEO domain and remain intact below 140 °C, in agreement with the temperature-dependent WAXS results that indicated crystallinity up to 120 °C. In ISO-5k
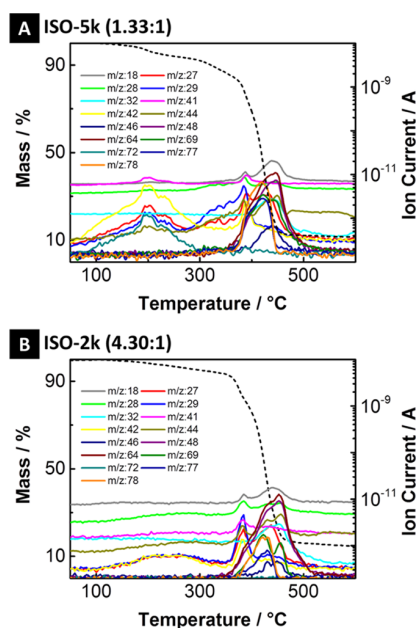
Figure 3. TGA−MS of (A) ISO-5k (1.33:1) and (B) ISO-2k (4.30:1) vs temperature. Mass loss is given as black dotted line; the most abundant fragments are shown together with their *m/z*.

(1.33:1), one Li$^+$ can interact with an EO repeating unit of PEO and a THF molecule. Such coordination cannot cause crystalline WAXS scattering, again consistent with our results. The THF in ISO-5k (1.33:1) is only partially coordinated and can thus soften the BCE as a plasticizer.[53]

The desired stability windows for electrolytes in LIBs and LMBs have to be at least 4 V.[54] We evaluated whether the ESWs of the investigated BCEs provides such an electrochemical stability range. Cyclic voltammetry (CV) was applied in the potential range from −0.6 to 7.0 V versus a Li/Li$^+$ pseudoreference electrode (Figure 4). The oxidative stability was tested at a Pt working electrode in a Pt|BCE|stainless steel

cell, the reductive stability at a Cu working electrode in a Cu| BCE|stainless steel cell. Note that the different starting potentials are due to the open-circuit potential that varies from every individual cell.

Measurements on the ISO-5k (1.33:1) electrolytes indicated an excellent oxidative stability up to 4.5 V versus Li/Li$^+$ but was limited by THF electropolymerization at higher potentials.[55−57] The THF oxidation was independently verified in voltammetry measurements on a 1 M solution of LiTFSI in THF (Figure S5). In addition, PEO oxidation is well known to start at roughly 4.5 V versus Li/Li$^+$.[58] Hence, the stability of the BCE studied here is restricted to potentials below 4.5 V. A second increase of current density above 5 V versus Li/Li$^+$ probably indicates the electrochemical oxidation and degradation of non-PEO blocks. Apart from that, ISO-2k (4.30:1) electrolytes showed limited stability above 4 V (vs Li/Li$^+$) with strong peaks [one decade higher than for ISO-5k (1.33:1)] in the first two cycles. We cannot attribute the peaks to specific reactions so far. On the low potential side, both membranes were stable against reduction down to −0.6 V versus Li/Li$^+$.

Both electrolytes seem to be sufficient for tests with state-of-the-art cathode materials such as lithium iron phosphate (Li intercalation at ∼3.5 V vs Li/Li$^+$)[59] or lithium cobalt oxide (Li intercalation at ∼4.0 V vs Li/Li$^+$).[59]

The mechanical strength of ISO-5k (1.33:1) and ISO-2k (4.30:1) was measured in oscillatory shear experiments at a constant frequency of 1 Hz and a constant force of 5 N. Figure 5 shows both storage (G') and loss (G'') moduli during heating and subsequent cooling. The values for ISO-2k (4.30:1) with G' = 10^7 Pa were one decade higher than for ISO-5k (1.33:1); both showed no detectable glass transitions (i.e., no intersection of G' and G'') within the test range. The lower G' for ISO-5k (1.33:1) additionally supports our assumption that THF acts as a plasticizer. In both systems, G' was restored on cooling. Examples in the literature showed that polymer-based electrolytes with comparable G' can successfully suppress dendritic growth.[15,16] The long-term stability of the electrode materials versus Li metal was examined by Li stripping/plating experiments in a symmetric Li|BCE|Li pouchbag cell (Figure S6). Cells
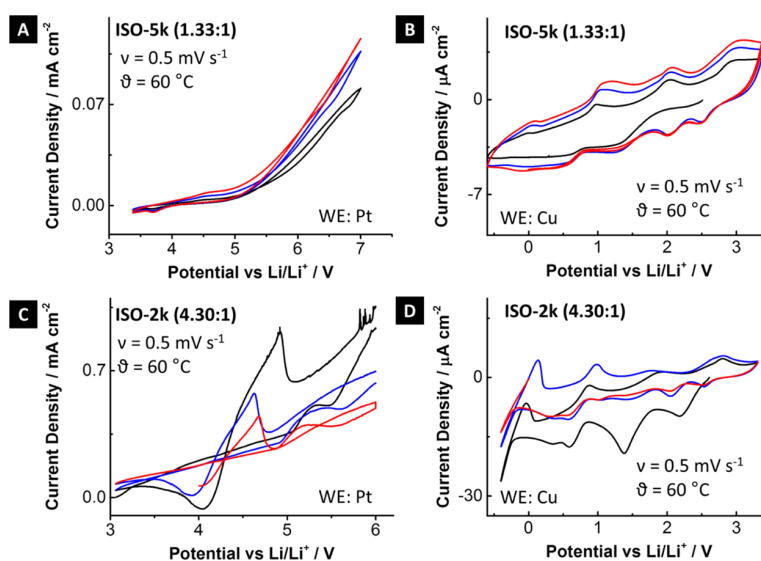
Figure 4. ESWs from CV in a 1st (black), 2nd (blue), and 3rd (red) cycle for ISO-5k (1.33:1) (A + B) and ISO-2k (4.30:1) (C + D). Oxidative stability was measured vs a Pt electrode and reductive stability vs a Cu electrode.
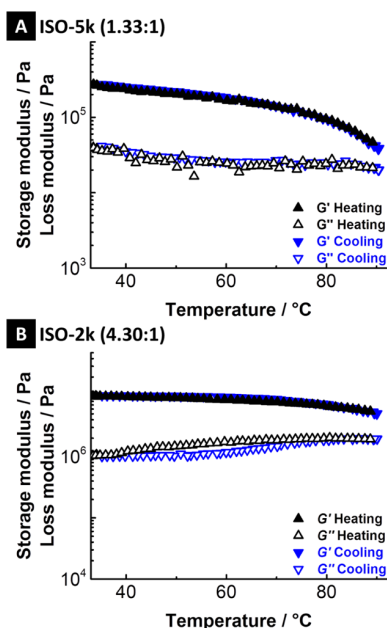
Figure 5. Rheological measurement of (A) ISO-5k (1.33:1) and (B) ISO-2k (4.30:1) on heating (black) and subsequent cooling (blue) of the storage modulus (G') and the loss modulus (G'').

with ISO-5k (1.33:1) and ISO-2k (4.30:1), respectively, run 100 cycles at 60 °C with a rate of 0.1 mA cm^{-2} without a safety shutdown. Accordingly, we believe that the BCP-based materials found here may be suitable to improve the lifetime and safety of lithium cells.

4. CONCLUSIONS AND OUTLOOK

This study demonstrates the versatility of multiblock copolymers and shows that it is possible to create polymer electrolytes with much higher local lithium conductivities than previously found in conventional salt-in-polymer electrolytes. This required a high local lithium salt concentration, a small concentration of donor atoms that coordinate the lithium ions, and an ordered triblock microstructure with preferential 2D lamellar, ion-conducting planes containing the conductive salt. The basic triblock copolymer system chosen in this work consisted of PI, PS, and PEO blocks with variable sizes. A large range of ordered microstructures in the parent phase diagram and the capability for self-assembly after dissolving high amounts of lithium salt make this material promising as BCEs.

The volume ratio PS/PI was kept constant as 1:2 to support the composition close to the optimum probability of 2D lamellar ordering of planes. The polar PEO blocks formed stable, salt-rich lamellar domains that exhibited superior ionic conductivities over a wide temperature range and remarkable high lithium transference numbers. The samples with the smallest PEO block sizes, that is ISO-5k (1.30:1) and ISO-2k (4.30:1) reached ionic conductivities around 1 mS cm^{-1}, thermal stability up to 140 °C, and electrochemical stability in the potential range 0−4.5 V versus Li/Li$^+$ reference.

Preliminary tests with lithium metal contact (potentiostatic polarization and Li stripping/plating experiments) indicated good stability: no preferred lithium dendrite growth or contact loss was observed. We were surprised to consistently find a small quantity of remaining, nonvolatile THF (as originally used as solvent for BCE preparation) in the stable samples. It will be interesting to investigate whether THF takes part in stabilizing an ordered salt-rich structure of the conducting domains. We plan to study the effect of modifying additives within BCP-based electrolytes in the near future, to be combined with cell-level studies with a special focus on cycling with Li metal anodes and typical LIB cathodes.

■ ASSOCIATED CONTENT

Ⓢ Supporting Information

The Supporting Information is available free of charge on the ACS Publications website at DOI: 10.1021/acs.chemmater.8b04686.

ISO/LiTFSI formulation for all different ISOs and resulting Li:EO ratios, results obtained from DSC, SAXS, temperature-dependent WAXS, WAXS of different LiTFSI reference samples, and oxidative electrochemical stability from linear sweep voltammetry (PDF)

■ AUTHOR INFORMATION

Corresponding Author
*E-mail: tobias.kraus@leibniz-inm.de (T.K.).

ORCID ⊙
Tobias Sebastian Dörr: 0000-0001-8164-3152
Peng Zhang: 0000-0003-1695-360X
Tobias Kraus: 0000-0003-2951-1704

Author Contributions
#A.P. and T.S.D. contributed equally to this work.

Notes
The authors declare no competing financial interest.

■ REFERENCES

(1) Schmuch, R.; Wagner, R.; Hörpel, G.; Placke, T.; Winter, M. Performance and cost of materials for lithium-based rechargeable automotive batteries. *Nat. Energy* **2018**, *3*, 267−278.
(2) Xu, W.; Wang, J.; Ding, F.; Chen, X.; Nasybulin, E.; Zhang, Y.; Zhang, J.-G. Lithium metal anodes for rechargeable batteries. *Energy Environ. Sci.* **2014**, *7*, 513−537.
(3) Placke, T.; Kloepsch, R.; Dühnen, S.; Winter, M. Lithium ion, lithium metal, and alternative rechargeable battery technologies: the odyssey for high energy density. *J. Solid State Electrochem.* **2017**, *21*, 1939−1964.
(4) Meister, P.; Jia, H.; Li, J.; Kloepsch, R.; Winter, M.; Placke, T. Best Practice: Performance and Cost Evaluation of Lithium Ion Battery Active Materials with Special Emphasis on Energy Efficiency. *Chem. Mater.* **2016**, *28*, 7203−7217.
(5) Wagner, R.; Preschitschek, N.; Passerini, S.; Leker, J.; Winter, M. Current research trends and prospects among the various materials and designs used in lithium-based batteries. *J. Appl. Electrochem.* **2013**, *43*, 481−496.
(6) Lin, D.; Liu, Y.; Cui, Y. Reviving the Lithium Metal Anode for High-Energy Batteries. *Nat. Nanotechnol.* **2017**, *12*, 194−206.
(7) Ryou, M.-H.; Lee, Y. M.; Lee, Y.; Winter, M.; Bieker, P. Mechanical Surface Modification of Lithium Metal: Towards Improved

Li Metal Anode Performance by Directed Li Plating. *Adv. Funct. Mater.* **2015**, *25*, 834−841.

(8) Aurbach, D.; Zinigrad, E.; Cohen, Y.; Teller, H. A short review of failure mechanisms of lithium metal and lithiated graphite anodes in liquid electrolyte solutions. *Solid State Ionics* **2002**, *148*, 405−416.

(9) Hiller, M. M.; Joost, M.; Gores, H. J.; Passerini, S.; Wiemhöfer, H.-D. The influence of interface polarization on the determination of lithium transference numbers of salt in polyethylene oxide electrolytes. *Electrochim. Acta* **2013**, *114*, 21−29.

(10) Doyle, M.; Fuller, T. F.; Newman, J. The importance of the lithium ion transference number in lithium/polymer cells. *Electrochim. Acta* **1994**, *39*, 2073−2081.

(11) Bieker, G.; Winter, M.; Bieker, P. Electrochemical in situ investigations of SEI and dendrite formation on the lithium metal anode. *Phys. Chem. Chem. Phys.* **2015**, *17*, 8670−8679.

(12) Winter, M. The Solid Electrolyte Interphase - The Most Important and the Least Understood Solid Electrolyte in Rechargeable Li Batteries. *Z. Phys. Chem.* **2009**, *223*, 1395−1406.

(13) Gao, Y.; Dahn, J. R. Correlation between the growth of the 3.3 V discharge plateau and capacity fading in Li1+xMn2−xO4 materials. *Solid State Ionics* **1996**, *84*, 33−40.

(14) Vetter, J.; Novák, P.; Wagner, M. R.; Veit, C.; Möller, K.-C.; Besenhard, J. O.; Winter, M.; Wohlfahrt-Mehrens, M.; Vogler, C.; Hammouche, A. Ageing mechanisms in lithium-ion batteries. *J. Power Sources* **2005**, *147*, 269−281.

(15) Stone, G. M.; Mullin, S. A.; Teran, A. A.; Hallinan, D. T.; Minor, A. M.; Hexemer, A.; Balsara, N. P. Resolution of the Modulus versus Adhesion Dilemma in Solid Polymer Electrolytes for Rechargeable Lithium Metal Batteries. *J. Electrochem. Soc.* **2012**, *159*, A222−A227.

(16) Khurana, R.; Schaefer, J. L.; Archer, L. A.; Coates, G. W. Suppression of Lithium Dendrite Growth Using Cross-Linked Polyethylene/Poly(ethylene oxide) Electrolytes: A New Approach for Practical Lithium-Metal Polymer Batteries. *J. Am. Chem. Soc.* **2014**, *136*, 7395−7402.

(17) Barai, P.; Higa, K.; Srinivasan, V. Impact of External Pressure and Electrolyte Transport Properties on Lithium Dendrite Growth. *J. Electrochem. Soc.* **2018**, *165*, A2654−A2666.

(18) Armand, M. B. Polymer Electrolytes. *Annu. Rev. Mater. Sci.* **1986**, *16*, 245−261.

(19) Bamford, D.; Reiche, A.; Dlubek, G.; Alloin, F.; Sanchez, J.-Y.; Alam, M. A. Ionic Conductivity, Glass Transition, and Local Free Volume in Poly(ethylene oxide) Electrolytes: Single and Mixed Ion Conductors. *J. Chem. Phys.* **2003**, *118*, 9420−9432.

(20) Weston, J.; Steele, B. Thermal history - conductivity relationship in lithium salt-poly (ethylene oxide) complex polymer electrolytes. *Solid State Ionics* **1981**, *2*, 347−354.

(21) Berthier, C.; Gorecki, W.; Minier, M.; Armand, M. B.; Chabagno, J. M.; Rigaud, P. Microscopic investigation of ionic conductivity in alkali metal salts-poly(ethylene oxide) adducts. *Solid State Ionics* **1983**, *11*, 91−95.

(22) Diddens, D.; Heuer, A.; Borodin, O. Understanding the Lithium Transport within a Rouse-Based Model for a PEO/LiTFSI Polymer Electrolyte. *Macromolecules* **2010**, *43*, 2028−2036.

(23) Rupp, B.; Schmuck, M.; Balducci, A.; Winter, M.; Kern, W. Polymer electrolyte for lithium batteries based on photochemically crosslinked poly(ethylene oxide) and ionic liquid. *Eur. Polym. J.* **2008**, *44*, 2986−2990.

(24) Teran, A. A.; Tang, M. H.; Mullin, S. A.; Balsara, N. P. Effect of molecular weight on conductivity of polymer electrolytes. *Solid State Ionics* **2011**, *203*, 18−21.

(25) Hallinan, D. T.; Mullin, S. A.; Stone, G. M.; Balsara, N. P. Lithium Metal Stability in Batteries with Block Copolymer Electrolytes. *J. Electrochem. Soc.* **2013**, *160*, A464−A470.

(26) Young, W.-S.; Kuan, W.-F.; Epps, T. H. Block Copolymer Electrolytes for Rechargeable Lithium Batteries. *J. Polym. Sci., Part B: Polym. Phys.* **2013**, *52*, 1−16.

(27) Young, W.-S.; Albert, J. N. L.; Schantz, A. B.; Epps, T. H. Mixed-Salt Effects on the Ionic Conductivity of Lithium-Doped PEO-Containing Block Copolymers. *Macromolecules* **2011**, *44*, 8116−8123.

(28) Epps, T. H.; Bailey, T. S.; Pham, H. D.; Bates, F. S. Phase Behavior of Lithium Perchlorate-Doped Poly(styrene-b-isoprene-b-ethylene oxide) Triblock Copolymers. *Chem. Mater.* **2002**, *14*, 1706−1714.

(29) Dörr, T. S.; Pelz, A.; Zhang, P.; Kraus, T.; Winter, M.; Wiemhöfer, H.-D. An Ambient Temperature Electrolyte with Superior Lithium Ion Conductivity based on a Self-Assembled Block Copolymer. *Chem.—Eur. J.* **2018**, *24*, 8061−8065.

(30) Timachova, K.; Villaluenga, I.; Cirrincione, L.; Gobet, M.; Bhattacharya, R.; Jiang, X.; Newman, J.; Madsen, L. A.; Greenbaum, S. G.; Balsara, N. P. Anisotropic Ion Diffusion and Electrochemically Driven Transport in Nanostructured Block Copolymer Electrolytes. *J. Phys. Chem. B* **2018**, *122*, 1537−1544.

(31) Mai, Y.; Eisenberg, A. Self-assembly of block copolymers. *Chem. Soc. Rev.* **2012**, *41*, 5969−5985.

(32) Orilall, M. C.; Wiesner, U. Block Copolymer based Composition and Morphology Control in Nanostructured Hybrid Materials for Energy Conversion and Storage: Solar Cells, Batteries, and Fuel Cells. *Chem. Soc. Rev.* **2011**, *40*, 520−535.

(33) Matsen, M. W.; Bates, F. S. Unifying Weak- and Strong-Segregation Block Copolymer Theories. *Macromolecules* **1996**, *29*, 1091−1098.

(34) Chatterjee, J.; Jain, S.; Bates, F. S. Comprehensive phase behavior of poly(isoprene-b-styrene-b-ethylene oxide) triblock copolymers. *Macromolecules* **2007**, *40*, 2882−2896.

(35) Hillmyer, M. A.; Bates, F. S. Synthesis and Characterization of Model Polyalkane−Poly(ethylene oxide) Block Copolymers. *Macromolecules* **1996**, *29*, 6994−7002.

(36) Gomez, E. D.; Panday, A.; Feng, E. H.; Chen, V.; Stone, G. M.; Minor, A. M.; Kisielowski, C.; Downing, K. H.; Borodin, O.; Smith, G. D.; Balsara, N. P. Effect of Ion Distribution on Conductivity of Block Copolymer Electrolytes. *Nano Lett.* **2009**, *9*, 1212−1216.

(37) Stefik, M.; Guldin, S.; Vignolini, S.; Wiesner, U.; Steiner, U. Block copolymer self-assembly for nanophotonics. *Chem. Soc. Rev.* **2015**, *44*, 5076−5091.

(38) Tyler, C. A.; Qin, J.; Bates, F. S.; Morse, D. C. SCFT Study of Nonfrustrated ABC Triblock Copolymer Melts. *Macromolecules* **2007**, *40*, 4654−4668.

(39) Chupp, J.; Shellikeri, A.; Palui, G.; Chatterjee, J. Chitosan-based gel film electrolytes containing ionic liquid and lithium salt for energy storage applications. *J. Appl. Polym. Sci.* **2015**, *132*, 42143 .

(40) Marzantowicz, M.; Dygas, J. R.; Krok, F.; Florjańczyk, Z.; Zygadło-Monikowska, E. Influence of crystalline complexes on electrical properties of PEO:LiTFSI electrolyte. *Electrochim. Acta* **2007**, *53*, 1518−1526.

(41) Mullin, S. A.; Stone, G. M.; Panday, A.; Balsara, N. P. Salt Diffusion Coefficients in Block Copolymer Electrolytes. *J. Electrochem. Soc.* **2011**, *158*, A619−A627.

(42) Chopade, S. A.; Au, J. G.; Li, Z.; Schmidt, P. W.; Hillmyer, M. A.; Lodge, T. P. Robust Polymer Electrolyte Membranes with High Ambient-Temperature Lithium-Ion Conductivity via Polymerization-Induced Microphase Separation. *ACS Appl. Mater. Interfaces* **2017**, *9*, 14561−14565.

(43) Morris, M. A.; An, H.; Lutkenhaus, J. L.; Epps, T. H. Harnessing the Power of Plastics: Nanostructured Polymer Systems in Lithium-Ion Batteries. *ACS Energy Lett.* **2017**, *2*, 1919−1936.

(44) Song, J. Y.; Wang, Y. Y.; Wan, C. C. Review of gel-type polymer electrolytes for lithium-ion batteries. *J. Power Sources* **1999**, *77*, 183−197.

(45) Stephan, A. M. Review on gel polymer electrolytes for lithium batteries. *Eur. Polym. J.* **2006**, *42*, 21−42.

(46) Bruce, P. G.; Vincent, C. A. Steady state current flow in solid binary electrolyte cells. *J. Electroanal. Chem. Interfacial Electrochem.* **1987**, *225*, 1−17.

(47) Bruce, P. G.; Hardgrave, M. T.; Vincent, C. A. Steady state current flow in solid binary electrolyte cells. *J. Electroanal. Chem. Interfacial Electrochem.* **1989**, *271*, 27−34.

(48) Singh, M.; Odusanya, O.; Wilmes, G. M.; Eitouni, H. B.; Gomez, E. D.; Patel, A. J.; Chen, V. L.; Park, M. J.; Fragouli, P.; Iatrou, H.;

Hadjichristidis, N.; Cookson, D.; Balsara, N. P. Effect of molecular weight on the mechanical and electrical properties of block copolymer electrolytes. *Macromolecules* **2007**, *40*, 4578−4585.

(49) Korte, C.; Peters, A.; Janek, J.; Hesse, D.; Zakharov, N. Ionic conductivity and activation energy for oxygen ion transport in superlattices - the semicoherent multilayer system YSZ (ZrO(2)+9.5 mol% Y(2)O(3))/Y(2)O(3). *Phys. Chem. Chem. Phys.* **2008**, *10*, 4623−4635.

(50) Epps, T. H.; Cochran, E. W.; Hardy, C. M.; Bailey, T. S.; Waletzko, R. S.; Bates, F. S. Network Phases in ABC Triblock Copolymers. *Macromolecules* **2004**, *37*, 7085−7088.

(51) Lilley, S. J.; Andreev, Y. G.; Bruce, P. G. Ionic Conductivity in Crystalline PEO6:Li(AsF6)1-x(SbF6)x. *J. Am. Chem. Soc.* **2006**, *128*, 12036−12037.

(52) Zardalidis, G.; Mars, J.; Allgaier, J.; Mezger, M.; Richter, D.; Floudas, G. Influence of chain topology on polymer crystallization: poly(ethylene oxide) (PEO) rings vs. linear chains. *Soft Matter* **2016**, *12*, 8124−8134.

(53) Cameron, G. G.; Ingram, M. D.; Sarmouk, K. Conductivity and Viscosity of Liquid Polymer Electrolytes Plasticized by Propylene Carbonate and Tetrahydrofuran. *Eur. Polym. J.* **1990**, *26*, 1097−1101.

(54) Kasnatscheew, J.; Streipert, B.; Röser, S.; Wagner, R.; Laskovic, I. C.; Winter, M. Determining oxidative stability of battery electrolytes: validity of common electrochemical stability window (ESW) data and alternative strategies. *Phys. Chem. Chem. Phys.* **2017**, *19*, 16078−16086.

(55) Dey, A. N.; Rudd, E. J. Electroinitiated Polymerization of Tetrahydrofuran. *J. Electrochem. Soc.* **1974**, *121*, 1294−1298.

(56) Campbell, S. A.; Bowes, C.; McMillan, R. S. The electrochemical behaviour of tetrahydrofuran and propylene carbonate without added electrolyte. *J. Electroanal. Chem. Interfacial Electrochem.* **1990**, *284*, 195−204.

(57) Ossola, F.; Pistoia, G.; Seeber, R.; Ugo, P. Oxidation potentials of electrolyte solutions for lithium cells. *Electrochim. Acta* **1988**, *33*, 47−50.

(58) Richardson, T. J.; Ross, P. N. Overcharge protection for rechargeable lithium polymer electrolyte batteries. *J. Electrochem. Soc.* **1996**, *143*, 3992−3996.

(59) Nitta, N.; Wu, F.; Lee, J. T.; Yushin, G. Li-ion battery materials: present and future. *Mater. Today* **2015**, *18*, 252−264.

Supporting Information

Self-assembled block copolymer electrolytes: enabling superior ambient cationic conductivity and electrochemical stability

Alexander Pelz,[a,b],* Tobias Sebastian Dörr,[c],* Peng Zhang,[c] Peter William de Oliveira,[c] Martin Winter,[a,d] Hans-Dieter Wiemhöfer,[a,b] Tobias Kraus[c,e,+]

[a]Helmholtz-Institute Münster, IEK-12, Forschungszentrum Jülich GmbH, Corrensstraße 46, 48149 Münster, Germany

[b]Institute of Inorganic and Analytical Chemistry, University of Münster, Corrensstraße 28/30, 48149 Münster, Germany

[c]INM - Leibniz Institute for New Materials, Campus D2 2, 66123 Saarbrücken, Germany

[d]MEET Battery Research Center, University of Münster, Corrensstraße 46, 48149 Münster, Germany

[e]Colloid and Interface Chemistry, Saarland University, Campus D2 2, 66123 Saarbrücken, Germany

*These authors contributed equally to this work.   a.pelz@fz-juelich.de

tobias.doerr@leibniz-inm.de

+Corresponding author's email address: tobias.kraus@leibniz-inm.de

The block copolymer electrolyte formulations used in this work are given within **Table S1**. We successively increased the content of conductive salt until segregation was observed and inhomogeneous membranes were obtained that we did not consider.

Table S1. ISO/LiTFSI formulation for all different ISOs and resulting Li:EO ratios in brackets below, calculated considering the ether oxygen provided by the particular PEO block.

			12.5 mass% LiTFSI in THF						
			200 µL	400 µL	600 µL	800 µL	1000 µL	1200 µL	1400 µL
			↓	↓	↓	↓	↓	↓	↓
	ISO-2k	4 mL →	ISO-2k (0.71:1)	ISO-2k (1.43:1)	ISO-2k (2.14:1)	ISO-2k (2.85:1)	ISO-2k (3.54:1)	ISO-2k (4.30:1)	ISO-2k (5.10:1)
4.0 mass% BCP in THF	ISO-5k	4 mL →	ISO-5k (0.33:1)	ISO-5k (0.67:1)	ISO-5k (1.00:1)	ISO-5k (1.41:1)	-	-	-
	ISO-7k	4 mL →	ISO-7k (0.22:1)	ISO-7k (0.44:1)	ISO-7k (0.66:1)	ISO-7k (0.89:1)	ISO-7k (1.12:1)	-	-
	ISO-53k	4 mL →	ISO-53k (0.04:1)	ISO-53k (0.08:1)	ISO-53k (0.12:1)	ISO-53k (0.17:1)	ISO-53k (0.20:1)	-	-

ISO/LiTFSI BCE hybrids were investigated with differential scanning calorimetry (DSC) to identify phase transitions between – 30°C and 100°C (**Figure S1**).
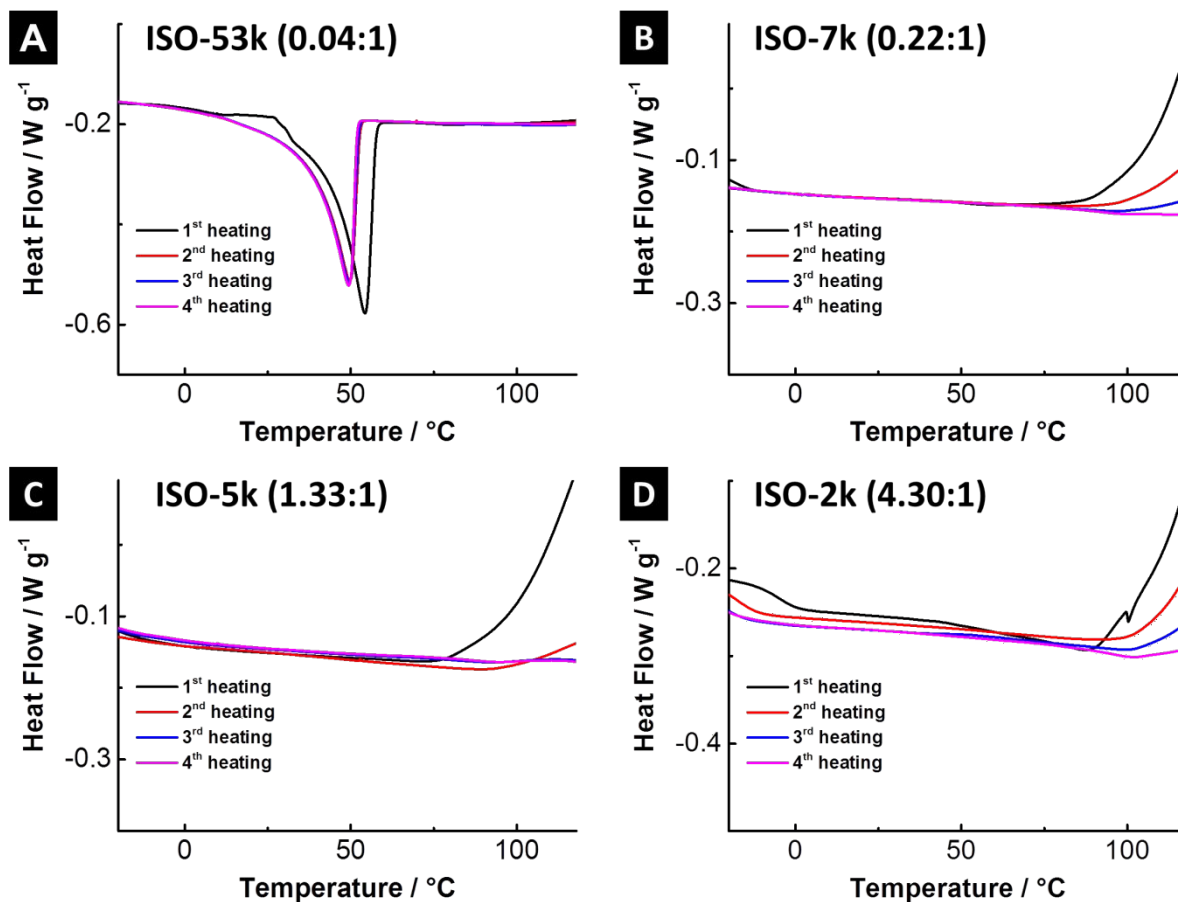
Figure S1. DSC in four consecutive heating cycles of the most conductive BCEs (a) ISO-53k (0.04:1), (b) ISO-7k (0.22:1), (c) ISO-5k (1.33:1) and (d) ISO-2k (4.30:1).

The energetically favorable microstructure that forms through evaporation induced self-assembly of ISO/LiTFSI BCE hybrids depends on the overall relative volume fractions was identified using Small-Angle X-ray Scattering (SAXS). **Figure S2** summarizes the 1D integrated SAXS pattern recorded at room temperature for selected sample compositions.
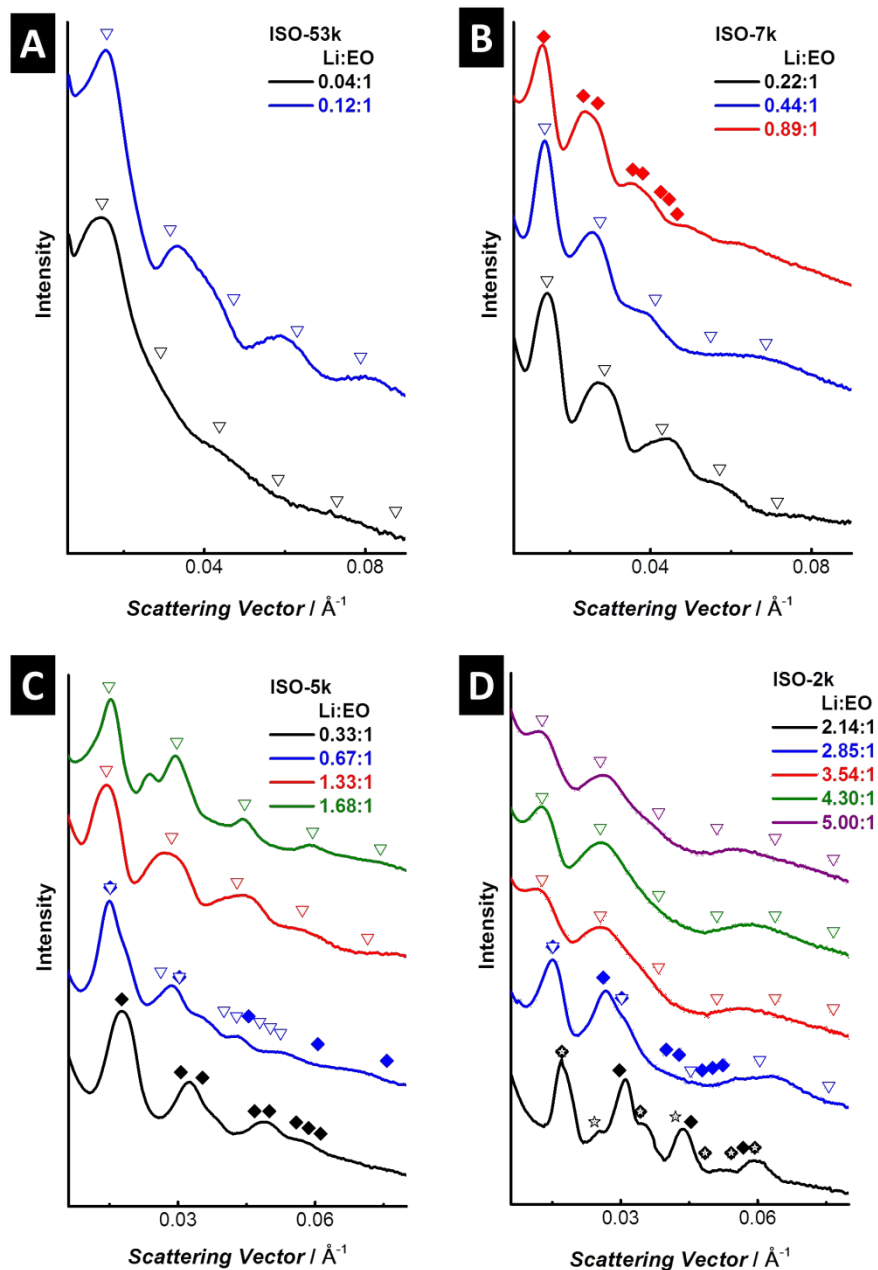
Figure S2. Radially integrated SAXS pattern at room temperature for all in EIS evaluable ISO/LiTFSI hybrids made from (a) ISO-53k, (b) ISO-7k, (c) ISO-5k and (d) ISO-2k. Theoretically predicted diffraction positions are calculated from the first diffraction peak (q*): triangles (lamellar, LAM), diamonds (gyroid, G^A) and stars (spherical micelle packing, BCC).

In situ Wide-Angle X-ray Scattering (WAXS) data recorded during heating of the pristine BCEs is shown in **Figure S3** to highlight the importance of a thermal treatment during synthesis. Representative traces are

shown at temperatures where phase transitions of crystalline PEO are expected together with data recoded after cooling (dark blue).
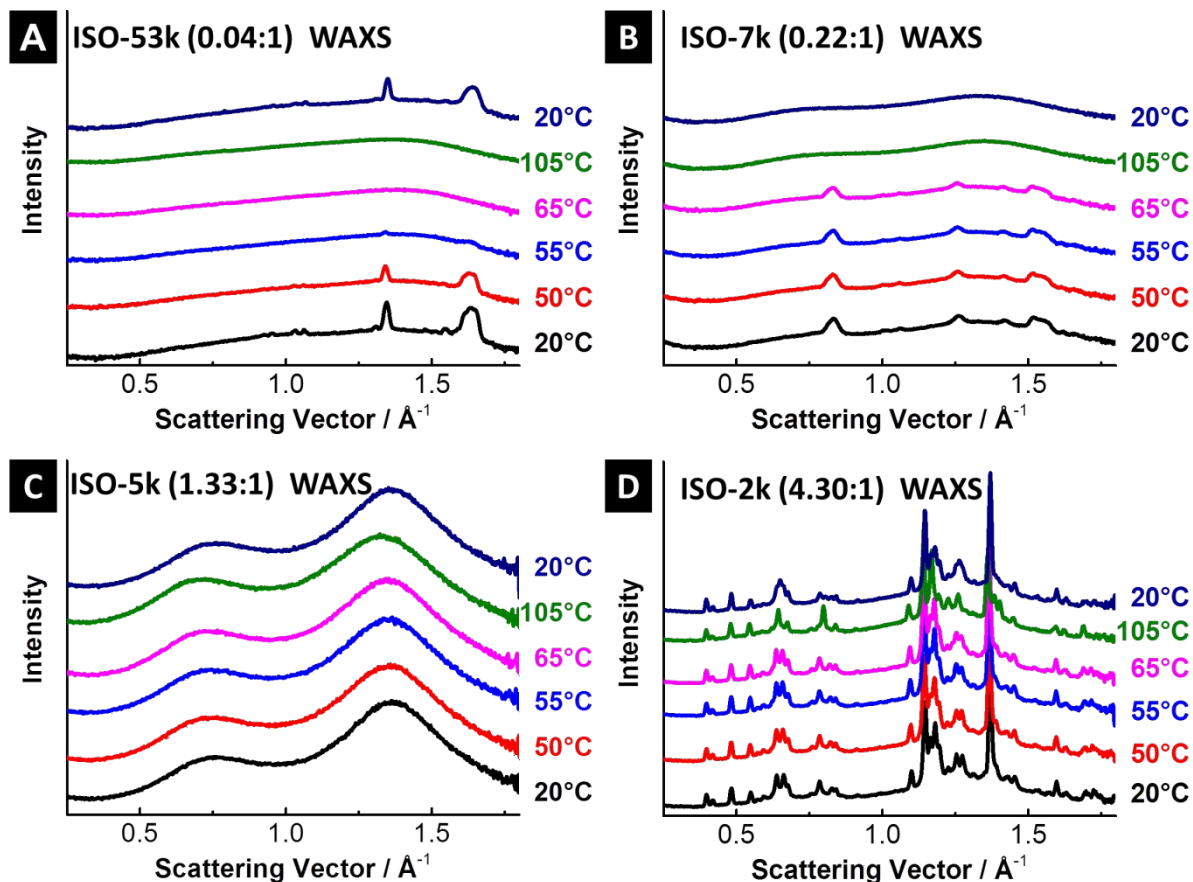
Figure S3. Temperature dependent *in-situ* WAXS for temperatures close to the expected phase transition temperature of PEO and after subsequent cooling (dark blue) of the most conductive BCEs (a) ISO-53k (0.04:1), (b) ISO-7k (0.22:1), (c) ISO-5k (1.33:1) and (d) ISO-2k (4.30:1).

Wide-Angle X-ray Scattering (WAXS) data for pristine LiTFSI, LiTFSI that was dissolved in THF and slowly dried (denoted as: LiTFSI-THF), ISO-2k (4.30:1) and the neat ISO-2k are shown in **Figure S4**. Crystalline triclinic P-1 LiTFSI data are included (PDF: 01-082-2341).
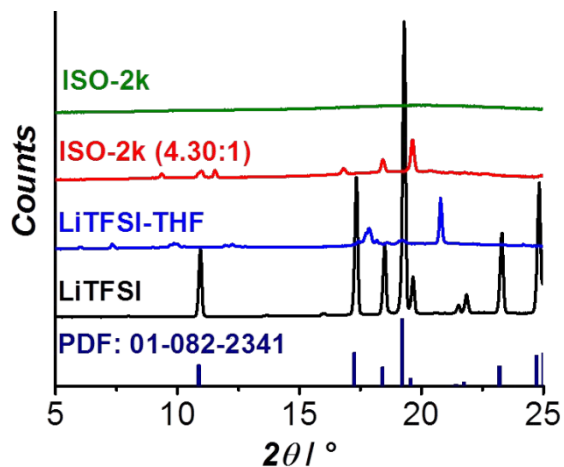
Figure S4. WAXS data of pristine LiTFSI (black), LiTFSI-THF (blue), ISO-2k (4.30:1) (red) and the neat ISO-2k (green). Crystalline LiTFSI library data (PDF:01-082-2341) are given (dark blue).

Linear sweep voltammetry (LSV) measurement on a 1M LiTFSI solution in THF in **Figure S5** demonstrates that oxidative degradation occurs at 4.5 V via THF electro-polymerization.
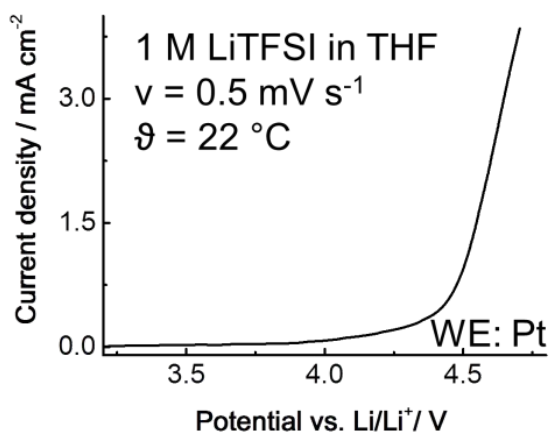
Figure S5. Oxidative electrochemical stability from linear sweep voltammetry (LSV) on a 1M LiTFSI in THF solution at 22 °C measured versus Li/Li+. The working electrode was Pt.

The long term stability of the electrode materials versus Li metal was examined with Li stripping/plating experiments in a symmetric Li|BCE|Li pouchbag cell. **Figure S6** shows the results for (a) ISO-5 (1.33:1) and (b) ISO-2k (4.30:1). Cycles were performed under constant conditions at 60°C, with an applied current density of 0.1 mA cm^{-2} (typical rate for liquid electrolytes) for a period of 1 h on one electrode, followed by the same procedure at the opposite electrode per cycle. We observed a continuous increase in overpotential, most likely due to an increasing surface roughness at the lithium electrodes. Despite of the harsh testing conditions, both cells ran 100 cycles without safety shutdown due to impending short circuit. Note also that the sheet resistance of the cell used here was on the order of $R_{sheet} = 2\ \Omega\ cm^2$ (overvoltage divided by the current density). Neglecting the interface resistance and ($L = 0.07$ cm), the steady state lithium ion conductivity of ISO-5k (1.33:1) and ISO-2k (4.30:1) can be estimated for cycles 25 to 45 as

$\sigma_{Li+} = L/R_{sheet} \approx 0.04 \pm 0.01$ S cm^{-1} at 60 °C, in very good agreement with the conductivity from impedance results.
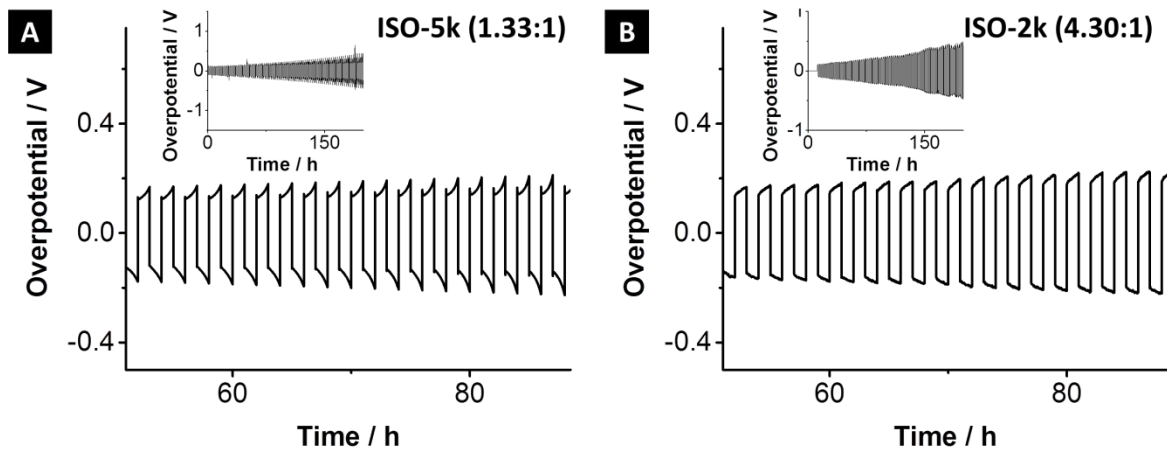
Figure S6. Li stripping/plating experiment performed at 60 °C and a current density of 0.1 mA cm^{-2} on (a) ISO-5k (1.33:1) and (b) ISO-2k (4.30:1); sample thickness ~700 μm. The results for the cycles 25 (50 h) to 45 (90 h) are shown in the main plot, the full 100 cycles (200 h) are shown in the inset.

Figure°S7 shows an exemplary potential scheme of the special function of THF within ISO-5k (1.33:1) and ISO-2k (4.30:1), based on the calculated Li:EO ratios. As suggested from TGA-MS, we assume THF either being partially coordinated to Li$^+$ (ISO-5k (1.33:1)) or forms clusters (ISO-2k (4.30:1)).
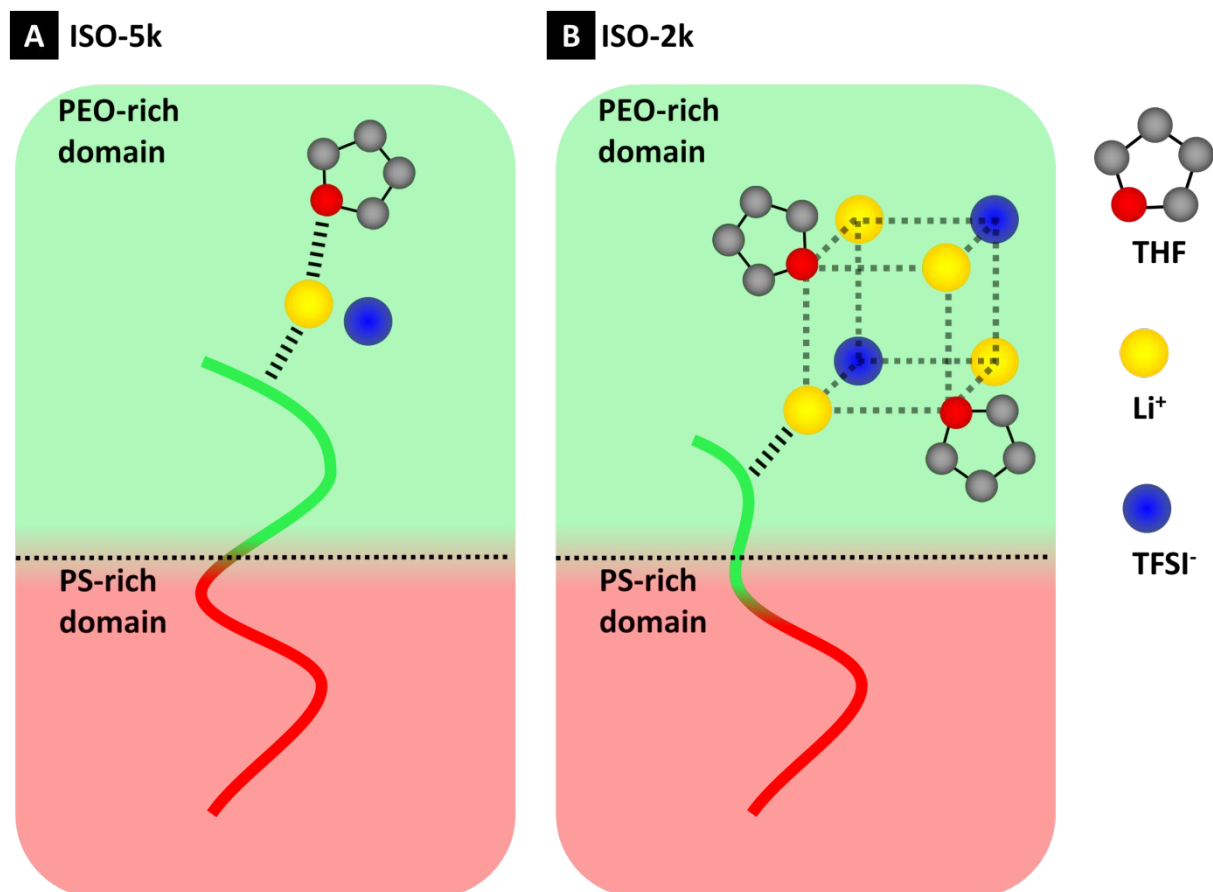
Figure S7. Exemplary schemes of the potential coordination of THF within (A) ISO-5k (1.33:1) and (B) ISO-2k (4.30:1), based on the calculated Li:EO ratios.

Chapter 4.4

Ordered Mesoporous TiO2-gyroids: Effects of Pore Architecture and Nb-doping on Photocatalytic Hydrogen Evolution under UV and VIS irradiation

Tobias Sebastian Dörr,[a] Leonie Deilmann,[b] Greta Haselmann,[b] Alexey Cherevan,[b] Peng Zhang,[a] Peter Blaha,[b] Peter W. de Oliveira,[a] Tobias Kraus,[a] and Dominik Eder[b,*]

[a]INM-Leibniz Institut für Neue Materialien, Campus D2 2, 66123 Saarbrücken, Germany
[b]Technische Universität Wien, Getreidemarkt 9, 1060 Wien, Austria

Abstract

We synthesize pure and Nb-doped TiO$_2$ photocatalysts with highly ordered alternating gyroid architecture and well-controllable mesopore size of 15 nm via co-

assembly of a poly(isoprene)-block-poly(styrene)-block-poly(ethylene oxide) block copolymer. A combined effort by electron microscopy, X-ray scattering, PL, XPS, Raman spectroscopy, and DFT simulations reveal that the addition of small amounts of Nb result in the substitution of Ti^{4+} with isolated Nb^{5+} species that introduces inter-bandgap states, while at high concentrations, Nb prefers to cluster forming shallow trap-states within the CBM of TiO$_2$. The gyroidal photocatalysts are remarkably active towards hydrogen evolution under UV and VIS light due to the open 3D network, where large mesopores ensure efficient pore diffusion and high photon harvesting. The gyroids yield unprecedented high evolution rates beyond 1000 µmol h^{-1} (per 10 mg catalyst), outperforming even the benchmark P25-TiO$_2$ more than 5-fold. Under UV light, the Nb-doping reduces the activity due to the introduction of charge recombination centers, while the activity in
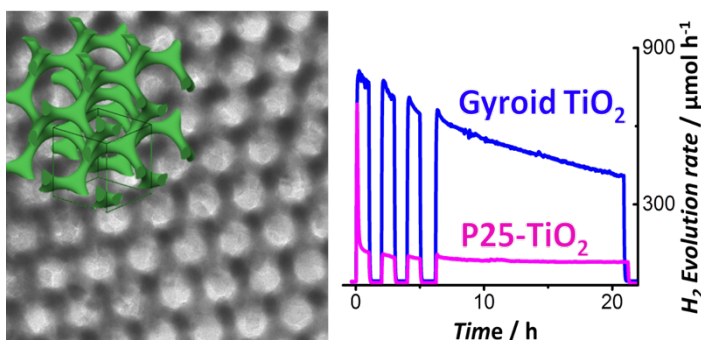
the VIS triple upon incorporation owing to a more efficient absorption of the inter-bandgap sites. This unique pore architecture may further offer hitherto undiscovered optical benefits to photocatalysis, related to chiral and metamaterial-like behavior, which will stimulate further studies focusing on novel light-structure interactions.

Ordered Mesoporous TiO₂ Gyroids: Effects of Pore Architecture and Nb-Doping on Photocatalytic Hydrogen Evolution under UV and Visible Irradiation

Tobias Sebastian Dörr, Leonie Deilmann, Greta Haselmann, Alexey Cherevan, Peng Zhang, Peter Blaha, Peter William de Oliveira, Tobias Kraus, and Dominik Eder*

Pure and Nb-doped TiO₂ photocatalysts with highly ordered alternating gyroid architecture and well-controllable mesopore size of 15 nm via co-assembly of a poly(isoprene)-*block*-poly(styrene)-*block*-poly(ethylene oxide) block copolymer are synthesized. A combined effort by electron microscopy, X-ray scattering, photoluminescence, X-ray photoelectron spectroscopy, Raman spectroscopy, and density functional theory simulations reveals that the addition of small amounts of Nb results in the substitution of Ti⁴⁺ with isolated Nb⁵⁺ species that introduces inter-bandgap states, while at high concentrations, Nb prefers to cluster forming shallow trap states within the conduction band minimum of TiO₂. The gyroidal photocatalysts are remarkably active toward hydrogen evolution under UV and visible light due to the open 3D network, where large mesopores ensure efficient pore diffusion and high photon harvesting. The gyroids yield unprecedented high evolution rates beyond 1000 μmol h⁻¹ (per 10 mg catalyst), outperforming even the benchmark P25-TiO₂ more than fivefold. Under UV light, the Nb-doping reduces the activity due to the introduction of charge recombination centers, while the activity in the visible triple upon incorporation is owed to a more efficient absorption due to inter-bandgap states. This unique pore architecture may further offer hitherto undiscovered optical benefits to photocatalysis, related to chiral and metamaterial-like behavior, which will stimulate further studies focusing on novel light–matter interactions.

1. Introduction

Hydrogen is considered as the green energy source of the future. One of the most promising routes to obtain this resource is the photoassisted production from water using solar energy.[1] Typically, a semiconductor material with a suitable bandgap (E_G), such as the most thoroughly studied titanium dioxide (TiO₂), converts photon energy into an electron–hole pair (i.e., exciton), which, after separation, migrates to the materials surface, eventually splitting water to O₂ and H₂.[1b,2] Despite considerable advances in recent research on photocatalysis, efforts remain devoted toward designing efficient catalysts capable of operating under solar light with high quantum efficiency, stability, durability, nontoxicity, and low cost.[3] Therefore, the community explores a wide range of materials design concepts.[4] One popular approach to improve the catalytic activity is to nanostructure the catalyst to achieve large surface areas, extended porosity, and, ideally, to control the exposed crystalline facets.[5] Typically, nanostructured materials come in a wide range of shapes and morphologies, such as quantum dots,[6] tubes,[7] rods,[8] sheets,[9] and wires.[10] Those nanoparticulate systems, however, often experience agglomeration/aggregation in liquid environments, consequently limiting reactant access to their active surface area (typically measured by Brunnauer–Emmett–Teller (BET) or density functional theory (DFT)).[11] This limits their validity as model systems in heterogeneous liquid catalysis.

Ordered porous catalysts have recently emerged as promising model catalysts and electrodes, due to their homogeneous pore distribution and tunable pore sizes.[12] A common approach is based on block copolymers (BCPs) as structure-directing agents using an evaporation-induced self-assembly (EISA) process.[13] Most researchers have used commercial polymers (e.g., Pluronic), which typically yield 2D pore arrangements with pore diameters below 10 nm.[14] However, recent advances have demonstrated that such small pores are not sufficiently large to eliminate kinetic limitations imposed by reaction diffusion through the pores in liquid environments.[12e,15] Moreover, we could recently show that a 3D-interconnected pore network (such as alternating or double gyroids) greatly facilitates reactant diffusion and can thus provide ready access to the entire interior surface, consequently enhancing the photocatalytic performance to a large extent.[16] For example,

T. S. Dörr, Dr. P. Zhang, Dr. P. W. de Oliveira, Prof. T. Kraus
INM-Leibniz Institut für Neue Materialien
Campus D2 2, 66123 Saarbrücken, Germany
L. Deilmann, G. Haselmann, Dr. A. Cherevan, Prof. P. Blaha,
Prof. D. Eder
Technische Universität Wien
Getreidemarkt 9, 1060 Wien, Austria
E-mail: dominik.eder@tuwien.ac.at

The ORCID identification number(s) for the author(s) of this article can be found under https://doi.org/10.1002/aenm.201802566.

**ADVANCED
SCIENCE NEWS**
www.advancedsciencenews.com

**ADVANCED
ENERGY
MATERIALS**
www.advenergymat.de

we demonstrated for photocatalytic hydrogen evolution that ordered mesoporous $CsTaWO_6$ catalysts with 40 nm pore sizes and a gyroidal architecture greatly outperformed those derived from the commercial Pluronic P-123 with 1D pores and 5 nm pore diameters.[14b,17]

The synthesis of ordered mesoporous metal oxide networks using BCP directed coassembly with a metal organic precursor through evaporation induced self-assembly has been pioneered by Wiesner and co-workers[18] and Stucky and co-workers[19] for silica (SiO_2) and aluminosilicates. TiO_2 was the first ordered mesoporous transition metal oxide and primarily synthesized for use in dye-sensitized solar cells (DSSCs).[20] In contrast to, for instance, tantalum oxide (Ta_2O_5), where extended crystalline domains have been reported (>25 nm),[21] mesoporous anatase TiO_2 typically comprises of distinctly smaller crystallites ($\approx 10 \pm 5$ nm) within the walls.[22] This compartmentalization is highly interesting, considering that the materials resistivity, and thus charge mobility, notably depends on the crystalline nature (i.e., size, topology, degree).[23] In photocatalysis, small crystallites can offer short diffusion ways for the excitons and lower recombination rates due to charge transfer in-between the grains.

Another approach toward advancing photocatalysts involves the tuning of the bandgap,[24] which has often been attempted via substitutional doping to prepare visible light photon harvesting catalysts.[1b,25] An example is the substitution on the Ti^{4+} sites by Nb^{5+} at low oxygen activity which includes the formation of Ti^{3+} defect states within the original bandgap of TiO_2 near its conduction band minimum (CBM).[26] This typically gives rise to an extended absorption range (e.g., bluish samples) and thus allows solar driven catalysis. Yet, it also lowers the redox potential of the separated excitons and, crucially, favors the formation of recombination centers, which considerably reduces the catalyst's activity.[1b,27] As a result, the activity of catalysts with visible light response often suffers under UV irradiation. In contrast, oxygen-rich environments upon synthesis are expected to favor the formation of Ti^{4+} vacancies and O^{2-} interstitials (O''_i), thus reducing the aforementioned limitations.[27] However, prediction of the materials response to light and its activity is not easy, in particular since the amount of doping significantly affects the electronic structure, crystallinity, and even morphology of the catalyst.[28]

In this work, we designed a model system comprising of pure and Nb-doped TiO_2 catalysts with a highly ordered mesoporous network of alternating gyroids and uniform pore diameters of 15 nm, via modified co-assembly of metal–organic precursors and an optimized poly(isoprene)-*block*-poly(styrene)-*block*-poly(ethylene oxide) (ISO) BCP (Section 2.1). The samples were characterized with a wide range of techniques, including X-ray powder diffraction (XRD), small-angle X-ray scattering (SAXS), X-ray photoelectron spectroscopy (XPS), transmission electron microscopy (TEM), energy-dispersive X-ray spectroscopy (EDX), diffuse reflectance spectroscopy (DRS), photoluminescence (PL), Raman spectroscopy, and inductively coupled plasma optical emission spectrometry (ICP-OES) toward their phase composition (Section 2.2) and morphology (Section 2.3) that is further supported by computational simulations using density functional theory. A crucial difference of lattice incorporation for Nb-doping has been found: small amounts of Nb resulted in preferential anisotropic incorporation, while lager amounts of Nb led to spatial clustering (Section 2.4). Finally, we evaluated and compared the photocatalytic performance of the samples toward hydrogen evolution under both, UV and visible illumination, benchmarked against similarly prepared nanoparticle (NP) references and a commercial P25-TiO_2 (Section 2.5).

2. Results and Discussions

2.1. Synthesis of Mesoporous Catalysts

The synthesis route for ordered mesoporous alternating gyroidal (G^A) TiO_2 is based on a macromolecular coassembly process and summarized in **Figure 1**. We first prepared an ISO terpolymer by sequential anionic polymerization, comprising of 30, 60, and 10 vol% of poly(isoprene) (PI), poly(styrene) (PS), and poly(ethylene oxide) (PEO), respectively, with a molecular weight (M_W) of 61 000 g mol^{-1} and a narrow polydispersity (D_P) of 1.09. The ISO was dissolved in tetrahydrofuran (THF) and mixed with a precursor solution containing either pure $Ti(^iProp)_4$ or a mixture of $Ti(^iProp)_4$ and $Nb(OEt)_5$, which selectively swelled the PEO block. The final structure of the catalyst material was defined by the relative volume fractions of the
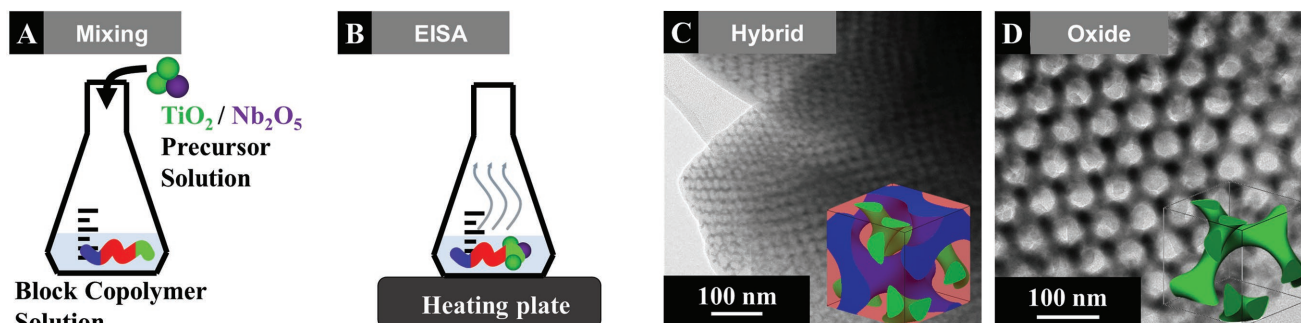
Figure 1. Illustration of the evaporation-induced self-assembly (EISA) based on the preparation of ordered mesoporous pure and Nb-doped TiO_2. A) A solution of the block copolymer is mixed with an adjusted amount of a precursor containing solution. B) Evaporation of the solvent induces self-assembly of the polymer, while the inorganic precursor selectively swells the PEO block. C) TEM image of the resulting polymer–inorganic hybrid with the expected arrangement (schematics in inset) before calcination and D) TEM image of the freestanding porous oxide after calcination with the expected gyroidal architecture (schematics in inset).

**ADVANCED
SCIENCE NEWS**

www.advancedsciencenews.com

**ADVANCED
ENERGY
MATERIALS**

www.advenergymat.de

polymer blocks after swelling and optimized by adjusting the ISO composition and amount of precursor solution.[29] The solutions were subjected to an EISA process to achieve gyroidal polymer–inorganic assemblies (further named as ISO/G^A-TiO2, ISO/G^A-TNO1, and ISO/G^A-TNO3). These solid hybrids were then calcined at 400 °C to remove the polymer and crystallize the inorganic gels to yield the respective porous gyroidal metal oxides, that is, the pure titania (sample: G^A-TiO2), and the 1 or 3 at% Nb-doped titania (sample: G^A-TNO1 and G^A-TNO3, respectively).

2.2. Phase Composition

XRD (**Figure 2**A) revealed that all calcined samples consisted nearly exclusively of the anatase phase (PDF No. 03-065-5714). This corresponds well with literature, where it is known that low process temperatures typically form the kinetically favored anatase rather than thermodynamic-stable rutile.[30] Yet, structural refinement showed that the pure TiO_2 sample contained a tiny amount (i.e., 3.2 mass%) of rutile. The amount decreased to 1.7 mass% upon doping, independent of the Nb concentration (Table S1, Supporting Information). It is further important to highlight the absence of any impurity phases, such as niobium oxides or mixed oxide solutions.

This is in line with Raman spectroscopy (Figure 2B), where all samples showed the typical modes associated with the anatase phase: a sharp $E_g(1)$ mode at 144 cm^{-1}, the characteristic $E_g(2)$ (196 cm^{-1}), B_{1g} (394 cm^{-1}), $E_g(3)$ (636 cm^{-1}) bands, and the combined B_{1g}/A_{1g} mode (centered at 514 cm^{-1}).[31] Any possible rutile modes were likely below the detection limit. Also, we did not observe any impurity phases (e.g., Nb_2O_5), in line with XRD. The incorporation of Nb slightly broadened the B_{1g} mode and caused a tiny shift toward lower Raman shift, which is consistent with previous works.[32] The center of the most intense $E_g(1)$ mode shifted from 144 to 146 cm^{-1} with increased Nb content.

Importantly, we did not observe any residual carbon in the calcined samples. This was in line with the thermogravimetric analysis (TGA, Figure S1A, Supporting Information) data of solid hybrids without calcination, which revealed the typical weight losses, induced by residual solvent evaporation (below 200 °C), the combustion of the precursor ligands (250–330 °C), and the oxidation of the polymer (above 350 °C). Crucially, when holding the calcination temperature at 400 °C for 4 h to simulate the calcination conditions for our sample, no additional weight loss was detected, hence confirming complete polymer removal. In addition, we did not observe any sp^2/sp^3 carbon-related peaks in Raman spectroscopy up to 2500 cm^{-1} (Figure S1B, Supporting Information).[16] This is in line with TEM, which shows no carbon layer on the materials' surfaces (**Figure 3**D–I). The absence of carbon in other forms can also be excluded by ICP-OES (Table S2, Supporting Information). All results thus confirm the complete removal of the structure-directing polymer upon calcination.
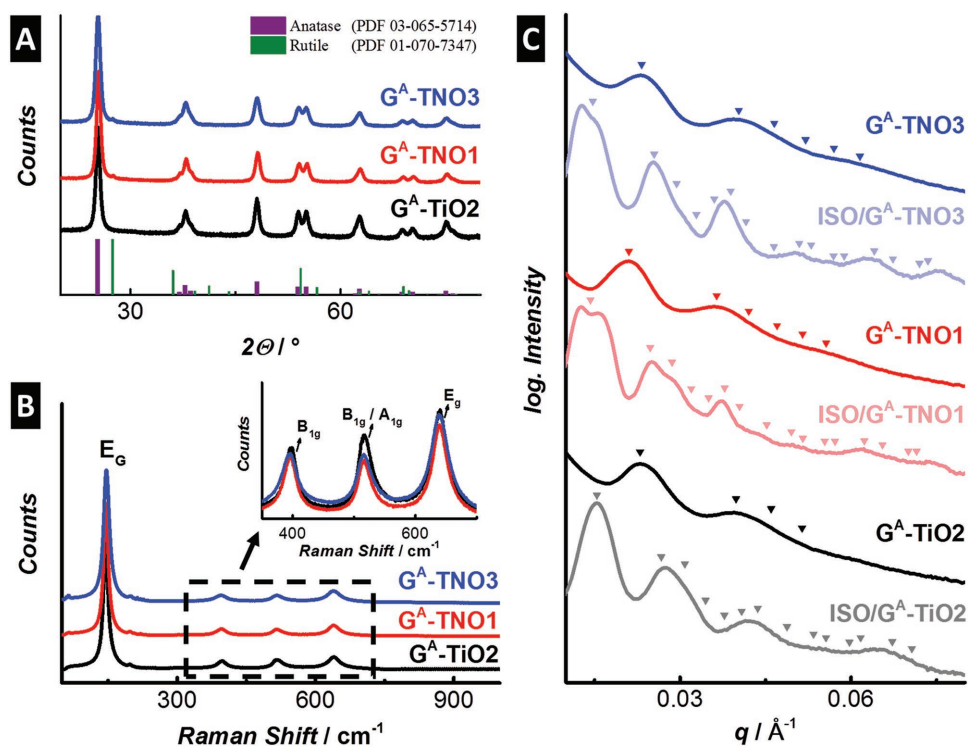
Figure 2. A) X-ray diffraction data for G^A-TiO2, G^A-TNO1, and G^A-TNO3, respectively, with reference data for anatase and rutile TiO_2 crystalline peaks marked in the curve. B) Raman spectra for the three samples with B_{1g}, B_{1g}/A_{1g}, and E_g peaks shown in the inset. C) Small-angle X-ray scattering data of the ISO/precursor hybrids and calcined samples. The theoretically predicted scattering positions corresponding to an alternating gyroid (G^A) structure are marked with triangles. For clarity reasons, the curves are shifted proportionally along the y-axis. The first peak center is set as q^*.

**ADVANCED
SCIENCE NEWS**
www.advancedsciencenews.com

**ADVANCED
ENERGY
MATERIALS**
www.advenergymat.de
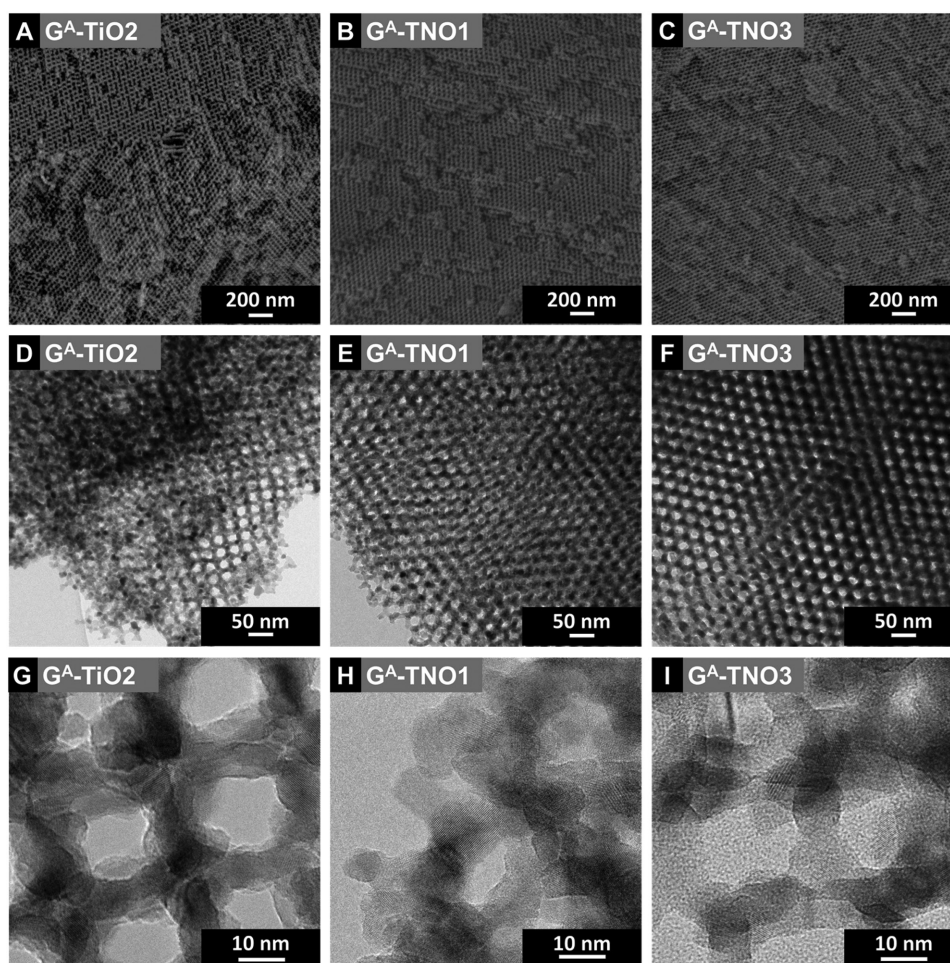
Figure 3. A–C) Scanning electron microscopy images and D–F) low- and G–I) high-magnification transmission electron microscopy images of the calcined G^A-TiO2, G^A-TNO1, and G^A-TNO3.

2.3. Pore Structure

Scanning electron microscopy (SEM) and TEM (Figure 3) data revealed that all calcined samples consisted of well-ordered mesopores with remarkably uniform pore diameters of around 15 nm. There was no noteworthy effect of the introduction of Nb on the pore architecture or pore diameter. The walls of the pores were composed of randomly oriented nanocrystals of around 10 nm, as estimated from TEM in Figure 3G–I.[22] Again, the addition of Nb did not significantly alter the compartmentalization of the pore walls or the size of the nanocrystals.

The porosity of the samples was investigated by nitrogen physisorption (BET, Figure S1C, Supporting Information). All nitrogen isotherms were largely identical in shape and show type IVa hysteresis, which is typical for a mesoporous material.[33] The specific surface areas (SSA$_{BET}$) were measured as 82, 95, and 100 m^2 g^{-1} for G^A-TiO2, G^A-TNO1, and G^A-TNO3, respectively, and the total pore volume was calculated to be 0.81 cm^3 g^{-1} (G^A-TiO2), 0.84 cm^3 g^{-1} (G^A-TNO1), and 0.89 cm^3 g^{-1} (G^A-TNO3).

SAXS provided in-depth information on the pore ordering, derived from the first scattering peak (q^*) and the respective ratios with the higher order peaks (q). Figure 2C reveals a clear periodicity in ISO/G^A-TiO2, with the calculated q/q^* ratios correlating well with the theoretical scattering pattern of a typical alternating gyroid (G^A) morphology ($q/q^* = 1$, $\sqrt{3}$, $\sqrt{4}$, $\sqrt{5}$,...).[34] Crucially, the G^A structure was largely preserved upon calcination, which is in line with the aforementioned SEM/TEM results. Note that the domain real-space spacing (d), calculated by $d = 2\pi q^{-1}$ had decreased from 41 to 27 nm, corresponding to a decrease of 32%, as indicated by the shift of q^* toward higher q-values.[12c] This is attributed to shrinkage of the Ti-containing domains upon calcination. Both, G^A-TNO1 and G^A-TNO3, show a comparable gyroid structure and a similar shrinkage extent of around 35%. Interestingly, we observed a significant split in the first scattering peak, which is indicative of structural complexity, as seen in the nonsymmetric 2D radial scattering for q^* (Figure S2, Supporting Information).

2.4. Incorporation of Niobium

The respective amounts of Nb in the samples were quantified by ICP-OES (Table S2, Supporting Information) and agreed well

ADVANCED
SCIENCE NEWS
www.advancedsciencenews.com

ADVANCED
ENERGY
MATERIALS
www.advenergymat.de
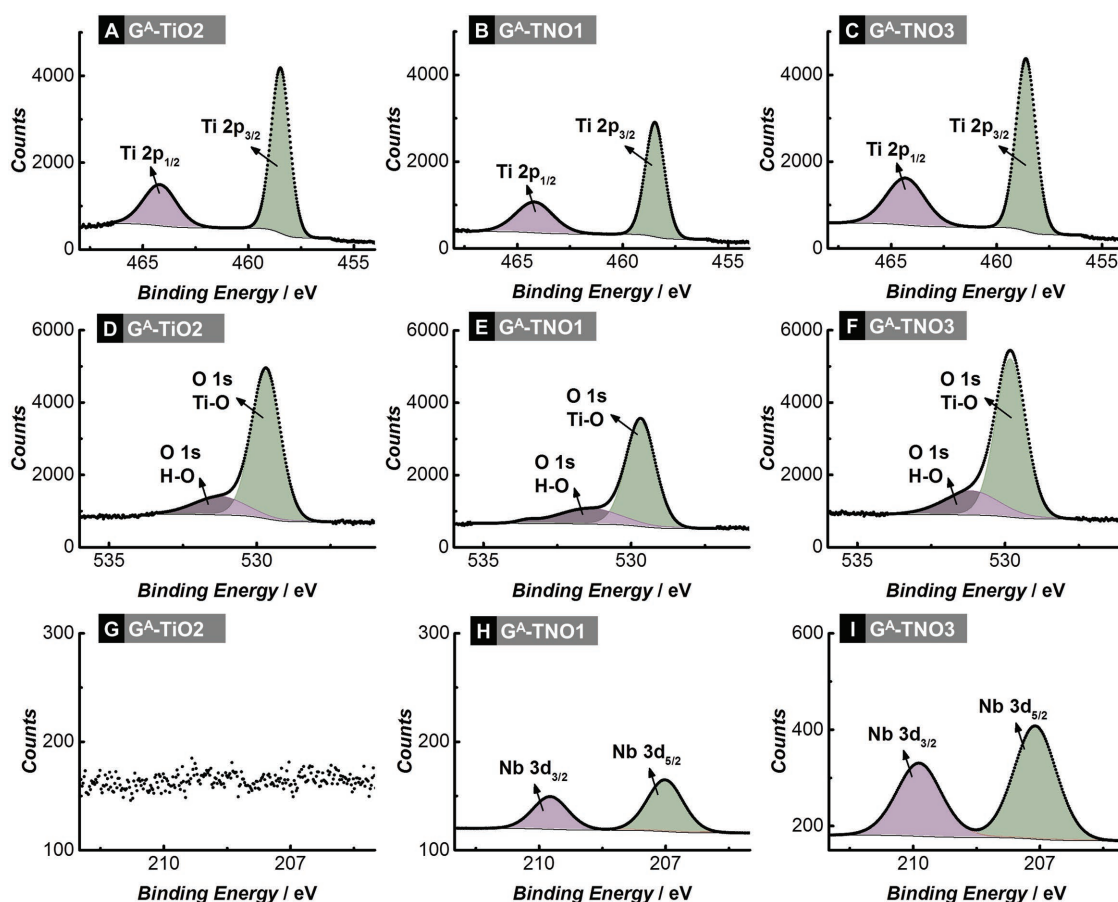
Figure 4. X-ray photoelectron spectroscopy data: A–C) Ti 2p spectra, D,E) O 1s spectra, and G–I) Nb 3d spectra of G^A-TiO2, G^A-TNO1, and G^A-TNO3, respectively.

with the expected values of 1.15 and 2.78 at%, for G^A-TNO1 and G^A-TNO3, respectively. A qualitative distribution can be derived from TEM-EDX analysis of the structured doped samples (Figure S3, Supporting Information). Rietfeld analysis of the XRD pattern revealed that the unit cells in both Nb-containing samples were larger than in the pure TiO$_2$, which suggests a substitutional doping of Ti with Nb (Table S1, Supporting Information). It is intriguing, however, that the expansion of the unit cell in G^A-TNO1 along the c-direction was considerably more pronounced (increase of c by 0.006 Å) than in a, b-direction (no apparent increase). This contrasts with G^A-TNO3, which showed a purely isotropic lattice widening.

The surprising anisotropic lattice increase in G^A-TNO1 was investigated further by DFT based simulations. Since DFT calculations do not have the accuracy to calculate lattice parameters on an absolute scale with the required precision, we quantified the changes of the nearest-neighbor Nb−O and Nb−Ti distances along the z (equals c) or x,y (equals a,b) directions when we relaxed the atomic positions until the forces were below 1 mRy bohr^{-1}. We found that the six nearest neighbor O atoms relaxed on average by 0.015 Å away from Nb, but there was marked anisotropy, and the largest increase of 0.020 Å was found in the z-direction. Similarly, the four nearest Ti atoms (which are above/below the x,y-plane) relaxed by 0.05 Å, while the four next nearest neighbors (all in the same x,y-plane)

increased their distance only by 0.03 Å. This is in accord with the measured 0.006 Å larger c lattice parameter of Nb-doped anatase and confirms an anisotropic substitutional doping.

XPS was used to analyze the oxidation state of the dopant and to clarify the nature of charge compensation, shown in **Figure 4**. It is important to note that all samples exclusively showed Ti^{4+} in the Ti 2p photoemission spectrum independent of doping.[35] A typical oxide splitting value of 5.7 eV between Ti 2p$_{1/2}$ and Ti 2p$_{3/2}$ was found. Although the full-width at half maximum (FWHM) for each spin–orbital component is expected to be the same, in the case of Ti 2p, the Ti 2p$_{1/2}$ is much more short living, broadened, and less distinct than expected (Coster–Kronig effect).[36] The O 1s spectrum was similar over all samples with no noticeable effect of material doping. Typical binding values for lattice oxygen (green, 529 eV) were found, but they tended to broaden toward higher binding energies (BEs) due to hydroxide surface groups (violet, centered ≈531 eV). In contrast, the Nb 3d spectra differed strongly between the pure and doped samples. As expected, no Nb was found for G^A-TiO2, while both, G^A-TNO1 and G^A-TNO3, contained the characteristic Nb 3d$_{5/2}$ and Nb 3d$_{3/2}$ peaks with their intensity increasing with higher Nb content. The Nb 3d signal splits in a ratio of 2:3 with 2.78 eV and symmetric FWHM (Table S3, Supporting Information), in line with literature.[37] However, G^A-TNO3 showed a significant decrease in binding
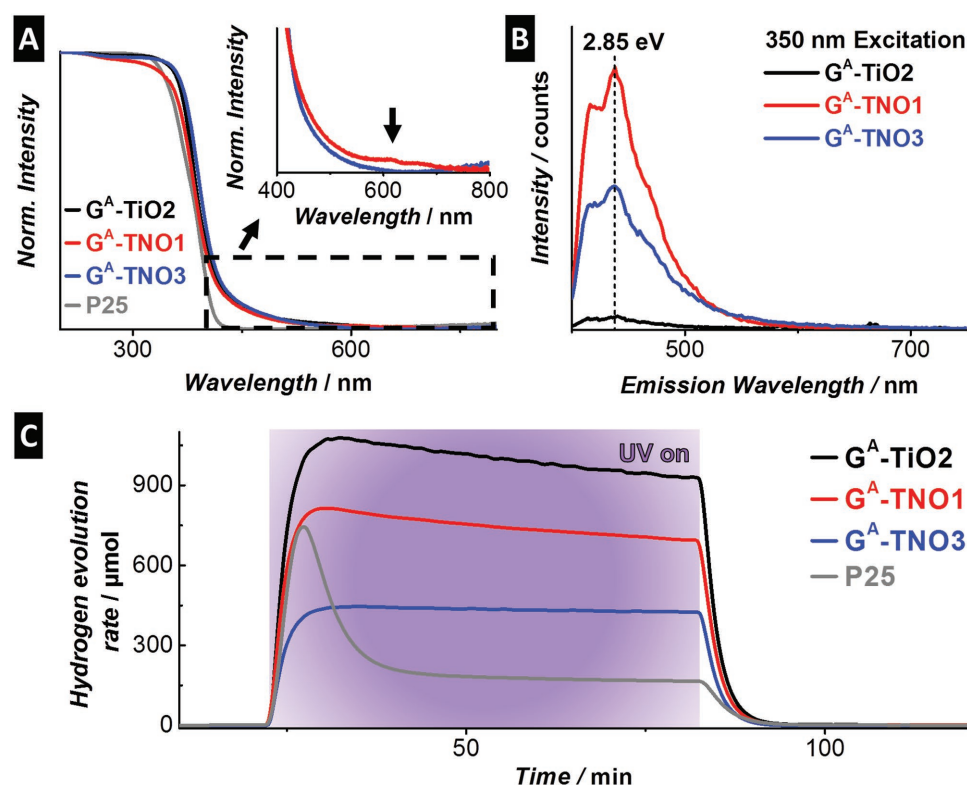
Figure 5. A) Diffuse reflectance spectroscopy of gyroidal samples and the commercial P25 reference with magnification of visible light range (400–800 nm). B) Photoluminescence spectra for gyroidal samples, excited with 350 nm laser. C) Evolution profiles of UV-driven hydrogen evolution (λ = 240–400 nm) for G^A-TiO2, G^A-TNO1, G^A-TNO3, and the commercial P25 reference.

energy of the Nb 3d by around 0.7 eV with respect to an identically prepared gyroidal Nb_2O_5 reference (Table S3, Supporting Information). A lower binding energy corresponds to a lower oxidation state of Nb due to a higher local electron density, such as provided by interstitial O''_i species, which may be present to charge compensate for Nb^{5+} doping.[38]

The presence of Nb is expected to affect the optical properties of TiO_2,[27] which we investigated with DRS (**Figure 5**A) as well as solid-state PL (Figure 5B). The absorption edge was almost identical for all gyroidal samples; the bandgap was calculated as 3.0 eV, which is in line with literature.[39] The absence of an extended absorption feature below 500 nm confirms that no Ti^{3+} defect states were formed within the TiO_2 bandgap, in line with XPS results.[40] Interestingly, G^A-TNO1 additionally exhibited weak absorption peaks at around 600 nm, which can be assigned to discrete intra-bandgap states formed by Nb within the minority rutile phase.[26d] The absence of this absorption features in G^A-TNO3 may well be explained by the tendency of Nb to form clusters, which instead favors the formation of shallow trap states within the TiO_2 CBM.[28] This hypothesis was tested by DFT simulations. Indeed, it appears that at higher Nb contents, the tendency of Nb atoms to cluster around the additional interstitial O''_i atom (i.e., when two Nb atoms are direct neighbors of the O-interstitial) is energetically more favorable by about 0.4 eV than the formation of isolated sites (i.e., when one Nb is close, but the other one is as far away as possible).

The doping and its effect on charge carrier trapping and transfer was further analyzed by PL with 350 nm excitation

(Figure 5b). The observed weak photoluminescence of G^A-TiO2 is in line with literature and has been attributed to a reduced recombination rate due to mobile charge carriers, charge transfer, or radiative quenching by surface groups.[41] Due to the high oxygen activity upon material's synthesis, we cannot exclude additional O''_i species as origin of the PL response, yet, only small amounts might be present as stabilizing higher valent metal atoms are not present in pure G^A-TiO2. However, the addition of Nb has significantly increased these defects causing a stronger emission response. In contrast, the Nb-containing samples showed a strong peak centered at around 440 nm (≈2.8 eV), with the highest photoluminescence intensity found for G^A-TNO1. Again, this can be explained by the presence of O''_i species, which may act as electron sinks and facilitate radiative recombination. Consequently, the more Nb species, the faster the recombination would be expected. However, in the case of G^A-TNO3, the comparative decrease in PL intensity can be attributed to the aforementioned Nb clustering, which favors non-radiative d-d transitions of the excited electrons within the shallow trap states.[26d,28,42]

In summary, the combined results from XPS, SAXS/XRD, DRS/PL/Raman spectroscopy, and DFT studies revealed several key features of our gyroidal photocatalysts. First, we found an absence of Ti^{3+}, which typically broadens the Ti 2p peaks in XPS toward lower binding energies.[43] Based on the downshift of the Nb 3d peak, we assume that the electron deficiency in our doped materials is charge compensated mainly by O^{2-} interstitials (O''_i), although a contribution by Ti^{4+} vacancies (V''''_{Ti}), as

**ADVANCED
SCIENCE NEWS**

www.advancedsciencenews.com

**ADVANCED
ENERGY
MATERIALS**

www.advenergymat.de

previously reported for high oxygen activity upon synthesis[26b–d] and polymer derived mesoporous materials,[44] is additionally possible. The results further suggest that, at low concentrations, Nb incorporates preferably as isolated species, introducing inter-bandgap states, while at higher concentrations, it prefers to cluster and form shallow states near the TiO_2 CBM. Both, the nature of Nb incorporation and charge compensation species, are expected to affect the photocatalytic performance of our catalysts.

2.5. Photocatalytic Evaluation

The photocatalytic performance of the samples was evaluated toward hydrogen evolution for both, UV ($\lambda = 240–400$ nm) and visible light ($\lambda = 400–800$ nm). As reference materials, we used (i) NPs, which were prepared under identical conditions as the gyroids, but without BCP (sample: NP-TiO2, NP-TNO1, and NP-TNO3 for the pure, 1 and 3 at% doped sample, respectively), and (ii) commercial P25-TiO_2 (sample: P25). The first references enabled us to investigate the influence of our 3D ordered mesoporous structure, while P25 allowed a setup-independent comparison with literature. Characterization of the reference materials can be found in Figure S4 (Supporting Information). For the photocatalytic test reaction a dispersion of 10 mg in a 1:1 H_2O:MeOH model solution was used with in situ photodeposited Pt as cocatalyst (≈0.5 mass%). The actual amount of Pt was 0.43 mass%, as quantitatively confirmed by post-mortem ICP-OES (Table S2, Supporting Information). The particles were of uniform size (≈2 nm) and well distributed on the surface of the catalysts (the visual representation of the Pt NPs with TEM can be found in Figure S5, Supporting Information).

2.5.1. UV Irradiation

The hydrogen evolution profiles are shown in Figure 5C, while the steady-state hydrogen evolution rates (HER) are summarized in **Figure 6**A. We observed three key features:

(1) Pore structure: The gyroids clearly outperformed the nanoparticulate counterparts to a large extent. For example, G^A-TiO2 and the corresponding NP-TiO2 showed activities of

1001 ± 76 µmol h^{-1} (mass-correlated: 0.1 mol g^{-1} h^{-1}) and 194 ± 7 µmol h^{-1} (mass-correlated: 0.02 mol g^{-1} h^{-1}), respectively. The effect was even more pronounced when comparing to P25, where the activity of G^A-TiO2 was increased by 5.5 times. The HER of G^A-TiO2 corresponds to a photonic efficiency of ≈12% (calculation can be found in the Supporting Information) and is currently among the highest values reported for pure TiO_2 photocatalysts (**Table 1**). The reasons for the superior activity of the gyroidal structures are manifold. The gyroidal samples exhibit larger specific surface areas than the nanoparticulate references, yet, this only accounts for a 60% increase of the rates, at maximum. Another contribution may arise from the large mesopores and the 3D open network, which allows direct access to the interior surface without kinetic limitations from pore diffusion. Furthermore, the size of the nanocrystals (around 10 nm) that build the walls of the gyroids is considered ideal to ensure short diffusion ways for the photoexcited charge carriers to the active surface sites, while permitting charge transfer in-between the grains thus lowering the recombination tendency.[22] At last, the excellent long-range ordering of the gyroidal pore structure may induce beneficial optical effects, possibly related to the reported negative refractive index (RI)[52] and metamaterial-like behavior[53] in gyroidal materials, whose impact on photoinduced energy conversation has yet to be investigated.

(2) Stability: The commercial P25 showed a steady-state activity of 173 ± 12 µmol h^{-1}, which is in line with literature under comparable process conditions and underlines the viability of our setup. Note that the initial activity for P25 was considerably higher but had dropped after minutes, leading to the values reported in literature. This recently discovered early-stage deactivation is supposed to originate from a complex interplay of UV-induced oxygen vacancies and the Pt cocatalyst active sites, which induces a change in reaction mechanism associated with CO formation.[54] Importantly, a calcination treatment prior to the reaction to anneal oxygen vacancies can minimize this deactivation process, thus highlighting the impact of defects. Crucially, our gyroidal samples did not show this early-stage deactivation, owing to the fact that they had already been exposed to high temperatures in oxygen-rich atmosphere during the template removal and crystallization. We further conducted cycling and duration experiments (up to 20 h), which revealed a slow deactivation process that is typically assigned
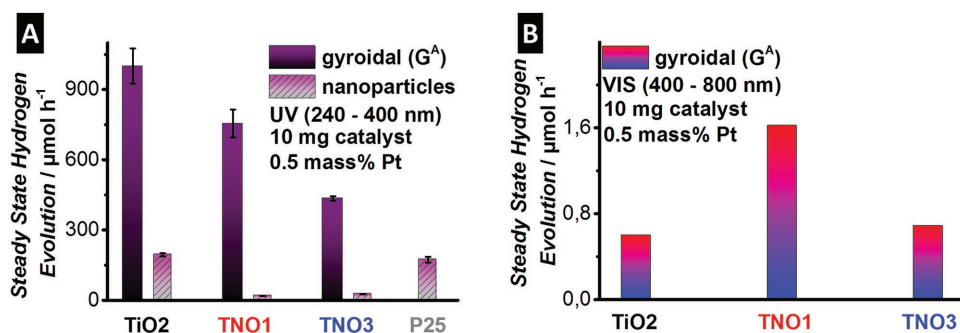
Figure 6. A) Steady-state evolution rates of UV-driven hydrogen evolution ($\lambda = 240–400$ nm) for G^A-TiO2, G^A-TNO1, G^A-TNO3, their nanoparticulate counterparts, and the commercial P25 reference. B) Steady-state evolution rates of visible-driven hydrogen evolution ($\lambda = 400–800$ nm) for G^A-TiO2, G^A-TNO1, G^A-TNO3; the values for the nanoparticle references (not shown) were below the detection limit.

Table 1. Exemplary results from UV-driven photocatalytic hydrogen evolution using pure TiO_2 taken from literature.

Crystal structure	Cocatalyst [mass%]	Setup		H_2 evolution rate		
		Light source	Reactant medium	Per hour (catalyst mass)	Mass-specific	Reference
Anatase	Pt (0.5)	Hg lamp 240–400 nm	H_2O:MeOH 1:1	1001 µmol h^{-1} (10 mg)	100.10 mmol h^{-1} g^{-1}	this work
Rutile	Pt (1)	Xe lamp 320–400 nm	H_2O:MeOH 9:1	2470 µmol h$^{-1a)}$ (100 mg)	24.70 mmol h^{-1} g^{-1}	[6a]
Anatase/rutile 67/33 mass%	Pt (0.5)	Xe lamp	H_2O:gylcerol 9:1	1026 µmol h^{-1} (100 mg)	10.26 mmol h^{-1} g$^{-1a)}$	[30]
Anatase	Pt (0.5)	Xe lamp 300–800 nm	H_2O:MeOH 22:5	405.2 µmol h^{-1} (60 mg)	6.75 mmol h^{-1} g$^{-1a)}$	[45]
Anatase/rutile	Pt (2.0)	LED 380 nm	H_2O:EtOH 1:1	385.0 µmol h^{-1} (50 mg)	7.70 mmol h^{-1} g$^{-1a)}$	[46]
Anatase/rutile 80/20 mass%	1:10 Ni:Pd (1) 10:1 Ni:Pd (0.5)	Hg lamp	H_2O:MeOH 1:1	≈220 µmol h^{-1} ≈130 µmol h^{-1} (50 mg)	4.40 mmol h^{-1} g$^{-1a)}$ 2.60 mmol h^{-1} g$^{-1a)}$	[47]
Anatase	Cu (1.5) Pd (1) Au (2)	Hg lamp	H_2O:MeOH 10:1	350 µmol h^{-1} 420 µmol h^{-1} 557 µmol h^{-1} (200 mg)	1.75 mmol h^{-1} g$^{-1a)}$ 2.10 mmol h^{-1} g$^{-1a)}$ 2.78 mmol h^{-1} g$^{-1a)}$	[48]
Anatase	Pt (0.2)	LED 365 nm	H_2O:MeOH 8:2	90.6 µmol h$^{-1a)}$ (50 mg)	1.81 mmol h^{-1} g$^{-1a)}$	[49]
Anatase	Rh (2) Pt (2)	Hg lamp 250–400 nm	Water vapor (10 mass% NaOH coated)	449 µmol h^{-1} 284 µmol h^{-1} (300 mg)	1.50 mmol h^{-1} g$^{-1a)}$ 0.95 mmol h^{-1} g$^{-1a)}$	[50]
Anatase	Pt (1)	Xe lamp 365 nm	H_2O:MeOH 8:2	68 µmol h^{-1} (100 mg)	0.68 mmol h^{-1} g$^{-1a)}$	[51]

a)Calculated from given values.

to surface poisoning and active site blocking (Figure S6, Supporting Information).[55] Still, the overall performance of the gyroidal samples remained superior, even after 20 h.

(3) Nb-doping: The activity decreased considerably upon Nb incorporation, that is, from 755 ± 60 to 435 ± 9 µmol h^{-1} for G^A-TNO1 and G^A-TNO3, respectively. Similarly, the corresponding values for the nanoparticulate references decreased to 26 µmol h^{-1}. From PL we expect for both doped gyroidal samples an increased charge recombination rate by radiative relaxation compared to G^A-TiO2. The lower activity of G^A-TNO3 despite lower PL intensity is likely caused by d-d transition within the shallow trap states followed by nonradiative relaxation, for example, via thermalization.[26a]

2.5.2. Visible Irradiation

We tested our materials under visible light (400–800 nm) using the same experimental conditions as for UV-driven catalysis (Figure 6B). Not surprisingly, the nanoparticle references exhibited no detectable H_2 evolution, although DRS suggests a pronounced bathochromic shift. In contrast, the gyroids showed remarkably high activities of 0.60, 1.62, and 0.68 µmol h^{-1}, for G^A-TiO2, G^A-TNO1, and G^A-TNO3, respectively. Normalized to weight, these values amount to

60, 162, and 68 µmol h^{-1} g^{-1}, respectively. These high values demonstrate that the aforementioned characteristics of the gyroidal structure also dramatically benefit the performance under visible light that is also comparable to advanced state-of-the-art materials (selection is given within Table S5, Supporting Information).

In contrast to the UV-based results, the activities under visible increased with the incorporation of Nb. In fact, G^A-TNO1 exhibited an activity that was almost three times higher than of G^A-TiO2 and G^A-TNO3. We attribute this enhancement to the presence of isolates Nb species, whose intra-bandgap states can offer additional absorption sites for a more efficient light harvesting. In comparison, the decrease of HER in G^A-TNO3 is attributed to the formation of clusters and the charge compensation with oxygen interstitials, where shallow trap states within the TiO_2 CBM replace the intra-bandgap states, in line with DFT simulations. Finally, the anisotropic substitution of Nb may additionally affect the photocatalytic performance, which has yet to be investigated in more detail.

3. Conclusion

In this work, we report on the preparation of BCP-derived mesoporous pure and Nb-doped TiO_2 with alternating gyroid architecture. The pores were remarkably well-ordered and uniform in diameter (≈15 nm). All samples consisted mainly of the

**ADVANCED
SCIENCE NEWS**

www.advancedsciencenews.com

**ADVANCED
ENERGY
MATERIALS**

www.advenergymat.de

anatase phase and did not contain any carbon residues or impurity phases, as confirmed by XRD, Raman spectroscopy, TEM, TGA, and ICP-OES. The high oxygen activity applied upon calcination prevented the formation of Ti^{3+} defects. Instead, XPS and DFT studies suggested the formation of interstitial O″$_i$ charge compensate for Nb^{5+} electron deficiency. The addition of small amounts of Nb resulted in the substitution of Ti^{4+} with isolated Nb^{5+} species causing an anisotropic lattice widening, as confirmed by XRD and DFT studies. DRS and PL revealed that these species introduced inter-bandgap states, which offer additional absorption sites in the visible region and facilitate charge recombination. In contrast, at high concentrations, Nb preferred to form clusters with shallow trap states within the CBM of TiO$_2$.

The performance of the gyroidal photocatalysts toward hydrogen evolution under both, UV and visible light conditions was among the highest reported in literature for pure TiO$_2$ photocatalysts. Interestingly, while the activity under UV light decreased by Nb doping due to the addition of charge recombination centers, the activity in the visible increased more than threefold upon the incorporation of 1 at% Nb. This enhancement was attributed to a more efficient absorption due to inter-bandgap sites. However, the activity dropped with increased Nb content, owing to the formation Nb clusters, which limited the absorption properties.

We further ascribe the superior activity of our gyroids to their beneficial porosity, large pore size, and 3D interconnectivity, which reduced kinetic limitations by pore diffusion, as well as to the compartmentalization of the narrow pore walls that allowed for short diffusion ways for photoexcited excitons. We believe that this unique pore architecture holds hitherto undiscovered optical benefits to photocatalysis, possibly related to the reported chiral and metamaterial-like behavior of the chiral alternating gyroid structure, which will stimulate further interest and future studies focusing on novel light–structure interactions.

4. Experimental Section

Materials: Benzene (99%, Alfa Aesar), THF (99%, <1000 ppm stabilizer, Alfa Aesar), chloroform (CHCl$_3$, 99,8+%, ACS, Alfa Aesar), methanol (99%, Alfa Aesar), *n*-butyllithium (*n*BuLi, 2.5 M in hexane, Alfa Aesar), *sec*-butyllithium (*sec*BuLi, 1.4 M in cyclohexane, Sigma Aldrich), 1,1-diphenylethylene (DPE, 98%, Alfa Aesar), isoprene (99%, <1000 ppm *p-tert*-butylcatechol, Sigma Aldrich), styrene (ReagentPlus, stabilized, Sigma Aldrich), ethylene oxide (EO, 99.8%, Praxair), calcium hydride (CaH$_2$, 1–20 mm granules, 88–98%, Alfa Aesar), potassium (98%, pieces in mineral oil, Fisher Scientific), naphthalene (99%, Fisher Scientific), titan(IV)isopropoxide (Ti(ⁱProp)$_4$, 99.999%, Sigma Aldrich), niobium(V)ethoxide (Nb(OEt)$_5$, 99.95% trace metals basis, Sigma Aldrich), P25-TiO$_2$ (Aeroxide TiO$_2$ P25, Evonik), hydrochloric acid (HCl, reagent grade, 37%, Sigma Aldrich), and absolute tetrahydrofuran (THF$_{abs}$, 99.85%, extra dry, unstabilized, Acros Organics) were directly used as received or purified as described below.

Polymer Synthesis: The polymeric template ISO was synthesized via living sequential anionic polymerization.[56] In short, all chemicals were cleaned with either *n*BuLi (using DPE as indicator) or CaH$_2$ (stirred overnight). The synthesized poly(isoprene)-*block*-poly(styrene) was endcapped by double-distilled EO using benzene as solvent, and the lithium counter ion was exchanged by potassium. The PEO block was finally prepared in THF and the final ISO was precipitated from CHCl$_3$ in an aliquot of MeOH, filtrated, and further stored at 6 °C.

Synthesis of G^A-TiO2 and G^A-TNO1/3: The mesoporous TiO$_2$ samples were synthesized using EISA as already described in literature for related inorganic materials.[12a,c,21] In summary, a 4.5 mass% ISO in THF$_{abs}$ solution was combined with a certain amount of a precursor solution containing THF$_{abs}$, HCl, and Ti(ⁱProp)$_4$ — for the preparation of TNO1/3 Nb(OEt)$_5$ partially replaces the Ti(ⁱProp)$_4$. The mixture was stirred for 3 h at room temperature, transferred into 5 mL PTFE beakers and placed on a hotplate (35 °C) covered with a glass dome. After 24 h the rubber-like polymer/precursor disc was further aged under reduced atmosphere (90 °C/24 h) and calcined at 400 °C/3 h using a ramp of 1 °C min⁻¹.

Synthesis of NP-TiO$_2$ and NP-TNO1/3: Nanoparticle references were prepared similar to their gyroidal counterparts, except there was no BCP present. Although no self-assembly was expected, the samples were placed in PTFE beakers on a hotplate under a glass dome, and further identically aged and calcined.

Material Characterization: The ISO polymer was characterized using combined proton nuclear magnetic resonance (^{1}H-NMR) and gel permeation chromatography (GPC). A sample of PI was taken during the preparation of ISO and analyzed on a Waters ambient-temperature GPC system equipped with a Waters 2410 differential RI detector. A concentration of 1 mg mL⁻¹ was used and characterized using PSS PI standards. The final composition and molecular weight (M_W) were determined by normalizing the ^{1}H-NMR signals, measured on a Bruker Avance III HD Nanobay equipped with a SampleXpress autosampler and a BBFO probe for 5 mm tubes at 300 MHz, to the PI GPC results. The final polydispersity ($Ð_P$) was further analyzed by GPC.

The mesoporous structure was investigated using a high-resolution field emission SEM JSM 7500F from JEOL. The electron microscopy images were measured with an accelerating voltage of 1.0–1.5 kV on a gold-sputtered powdered sample placed on a carbon tape. TEM was carried out using a JEOL 2100F microscope. The powdered samples were dispersed in isopropanol, drop-casted on a copper grid with a lacey carbon film from Gatan and measured with an accelerating voltage of 200 kV.

TGA was used to determine the mass loss during calcination of the ISO/precursor hybrids and to search for residual carbon after successful template removal. A TG 209 F1 Libra system from Netzsch with an automatic sample changer was used and the samples were placed in alumina crucible. In a typical experiment, 10 mg of sample were heated in synthetic air with 20 °C min⁻¹.

XRD patterns were recorded on a Bruker Discover D8 powder diffraction unit, equipped with a Cu-Kα ($\lambda = 0.154$ nm) source, operating in reflection mode at 40 kV and 40 mA, using a sapphire single-crystal sample holder. Data were acquired using a Bruker area AXS detector VANTEC 500 (resolution: 2048 pixel). In the applied configuration, the angle subtended by the detector was 33° and integration was performed in a 2θ angle range between 16° and 100° with a step size of 0.02°.

SAXS measurements were performed on a Xenocs XEUSS 2.0 setup equipped with a Dectris Pilatus 1M detector and a Cu-kα source ($\lambda = 0.154$ nm). The sample-to-detector size was 2512 mm, calibrated with a silver behenate standard. Either a piece of the rubber-like polymer/precursor disc or a piece of the calcined, freestanding oxide sample was placed on a Kapton tape and measured without further modification. For 1D patterns, the primary beam was masked and total radial integration was performed. The scattering of pure Kapton tape was measured; no scattering was found in the q range of 0.02–0.08 Å⁻¹.

XPS measurements were carried out on a custom-built SPECS XPS spectrometer equipped with a monochromated Al-Kα X-ray source (μFocus 350) and a hemispherical WAL-150 analyser (acceptance angle: 60°). All samples were mounted onto the sample holder using double-sided carbon tape. Pass energies of 100 and 30 eV and energy resolutions of 1 eV and 100 meV were used for survey and detail spectra, respectively (excitation energy: 1486.6 eV, beam energy and spot size: 70 W onto 400 μm, angle: 51° to sample surface normal, base pressure: 5 × 10⁻¹⁰ mbar, pressure during measurements: 2 × 10⁻⁹ mbar). Data analysis was performed using CASA XPS software, employing transmission corrections (as per the instrument vendor's specifications), Shirley/Tougaard backgrounds,[57] and Scofield sensitivity factors.[58] Charge

correction was applied so the adventitious carbon peak (C—C peak) was shifted to 284.8 BE. All content values shown are in units of relative atomic percent (at%), where the detection limit in survey measurements usually lies around 0.1–1 at%, depending on the element. The accuracy of XPS measurements is around 10–20% of the values shown. Assignment of different components was primarily done using ref. [59].

Raman spectra (RAMAN) were measured with a LabRAM Aramis from Horiba Jobin Yvon, using a 633 nm helium-neon laser with an 1800 gr mm^{-1} grating (0.75 cm^{-1} pixel^{-1}) in a range from 50 to 1000 cm^{-1}. The acquisition time was 10 s with a fourfold accumulation. Calibration was done with a Si wafer and TiO$_2$ spectra were normalized in intensity to either E$_g$ (144 cm^{-1}) or combined mode of B$_{1g}$/A$_{1g}$ (centered at 514 cm^{-1}) for full spectra or zoomed inset, respectively.

A Quantachrome Autosorb-6B was used for nitrogen gas sorption. Samples were degassed at 100 °C for 3 d and a total of 19 points for the adsorption and the desorption, respectively, were collected. The BET equation[60] was applied for the calculation of the specific surface area (SSA$_{BET}$).

DRS was measured on an Agilent Cary 5000 UV–visible–NIR high-performance spectrophotometer, equipped with an Agilent diffuse reflectance accessory (DRAs). Powdered samples were filled in a sample holder and measured through a quartz window with an acquisition time of 0.1 s with a resolution of 1 nm (scan rate: 600 nm min^{-1}). Calibration was done with 100% reflectance PTFE reference plate and a zero-reflectance background by blocking the beam.

For the fluorescence spectroscopic (PL) measurements, an Edinburgh Instruments FPS920 photoluminescence spectroscopy setup was used. This setup contains a XE900 Xenon Arc Lamp (500 W) as an illumination source, double Czerny–Turner monochromators (type TMS300) at both excitation and emission arms as well as a S900 single-photon photomultiplier (type R928) as the detector. In a single measurement, a powdered photocatalyst was squeezed between two quartz plates and put into the excitation light beam, while the reflected light was measured. UV and visible light excitation wavelengths were set to 350 ± 5 and 420 ± 5 nm, respectively. The signal was acquired in the range between 400 and 800 nm. To filter out excitation wavelength, cutoff filters of 395 and 455 nm were used for UV and visible excitations, respectively.

In order to support some of the experimental results and their interpretation, DFT calculations on the electronic structure of Nb impurities in Anatase using the WIEN2k code were performed.[61] The calculations employed the generalized gradient approximation[62] and a Hubbard-U term[63] with an U value of 7 eV. It was shown earlier[64] that U values above ≈5 eV lead to localization of Ti-3d electrons and a spin-polarized solution can be found; a larger U value also leads to a more credible bandgap of anatase.[65] To simulate the impurities, $4 \times 4 \times 2$ face-centered supercells (96 atoms/cell) were employed and convergence with body-centered cells (192 atoms/cell) was verified. The results for a single Nb impurity are similar to previous reports in literature.[26d,64-66]

Photocatalytic H$_2$ evolution was quantified in a closed home-built flow reactor, which was top-irradiated with a 200 W super pressure Hg lamp (UV: λ = 220–400 nm, visible: λ = 400–700 nm, Lumatec). During the reaction, the reactor was constantly purged with argon 5.0 as a carrier gas (flow rate: 30 mL min^{-1}, controlled with a mass flow controller, MCC Instruments). The amounts of generated hydrogen in the flow were quantified by a gas analyzer (X-Stream, Emerson) equipped with a thermal conductivity detector (TCD). 10 mg of each powdered photocatalyst were dispersed in a 10 mL aqueous methanol solution (50 vol%) by ultrasonication for 1 min. The reaction mixture was degassed by bubbling argon for 5 min and a certain amount of an aqueous H$_2$PtCl$_6$ solution was added to the mixture before closing the top lid to allow for in situ photodeposition of 0.5 mass% of platinum nanoparticles used as a cocatalyst.

Supporting Information

Supporting Information is available from the Wiley Online Library or from the author.

[1] a) A. Fujishima, K. Honda, *Nature* **1972**, *238*, 37; b) A. Kudo, Y. Miseki, *Chem. Soc. Rev.* **2009**, *38*, 253; c) K. Maeda, K. Domen, *J. Phys. Chem. Lett.* **2010**, *1*, 2655.

[2] K. Hashimoto, H. Irie, A. Fujishima, *Jpn. J. Appl. Phys.* **2005**, *44*, 8269.

[3] K. Maeda, K. Domen, *Bull. Chem. Soc. Jpn.* **2016**, *89*, 627.

[4] a) S. J. A. Moniz, S. A. Shevlin, D. J. Martin, Z.-X. Guo, J. Tang, *Energy Environ. Sci.* **2015**, *8*, 731; b) J. Ran, J. Zhang, J. Yu, M. Jaroniec, S. Z. Qiao, *Chem. Soc. Rev.* **2014**, *43*, 7787; c) X. Zou, Y. Zhang, *Chem. Soc. Rev.* **2015**, *44*, 5148.

[5] a) F. Bosc, A. Ayral, P. A. Albouy, C. Guizard, *Chem. Mater.* **2003**, *15*, 2463; b) J. Zhang, Q. Xu, Z. Feng, M. Li, C. Li, *Angew. Chem., Int. Ed.* **2008**, *47*, 1766; c) E. Baldini, L. Chiodo, A. Dominguez, M. Palummo, S. Moser, M. Yazdi-Rizi, G. Auböck, B. P. P. Mallett, H. Berger, A. Magrez, C. Bernhard, M. Grioni, A. Rubio, M. Chergui, *Nat. Commun.* **2017**, *8*, 13.

[6] a) L. D. Li, J. Q. Yan, T. Wang, Z. J. Zhao, J. Zhang, J. L. Gong, N. J. Guan, *Nat. Commun.* **2015**, *6*, 5881; b) A.-W. Xu, Y. Gao, H.-Q. Liu, *J. Catal.* **2002**, *207*, 151.

[7] a) N. Bouazza, M. Ouzzine, M. A. Lillo-Rodenas, D. Eder, A. Linares-Solano, *Appl. Catal., B* **2009**, *92*, 377; b) D. Eder, *Chem. Rev.* **2010**, *110*, 1348.

[8] L. Miao, S. Tanemura, S. Toh, K. Kaneko, M. Tanemura, *Appl. Surf. Sci.* **2004**, *238*, 175.

[9] J. Yu, L. Qi, M. Jaroniec, *J. Phys. Chem. C* **2010**, *114*, 13118.

[10] a) G. Wang, H. Wang, Y. Ling, Y. Tang, X. Yang, R. C. Fitzmorris, C. Wang, J. Z. Zhang, Y. Li, *Nano Lett.* **2011**, *11*, 3026; b) H. B. Wu, H. H. Hng, X. W. Lou, *Adv. Mater.* **2012**, *24*, 2567.

[11] a) Y. Noda, B. Lee, K. Domen, J. N. Kondo, *Chem. Mater.* **2008**, *20*, 5361; b) Y. Takahara, J. N. Kondo, T. Takata, D. Lu, K. Domen, *Chem. Mater.* **2001**, *13*, 1194.

[12] a) M. Stefik, S. Guldin, S. Vignolini, U. Wiesner, U. Steiner, *Chem. Soc. Rev.* **2015**, *44*, 5076; b) J. G. Werner, T. N. Hoheisel, U. Wiesner, *ACS Nano* **2014**, *8*, 731; c) S. W. Robbins, P. A. Beaucage, H. Sai, K. W. Tan, J. G. Werner, J. P. Sethna, F. J. DiSalvo, S. M. Gruner, R. B. Van Dover, U. Wiesner, *Sci. Adv.* **2016**, *2*, e1501119; d) Z. Wei, S. Fanfei, P. Kai, T. Guohui, J. Baojiang, T. Rhiyu, T. Chungui, F. Honggang, *Adv. Funct. Mater.* **2011**, *21*, 4193; e) A. Cherevan, L. Deilmann, T. Weller, D. Eder, R. Marschall, *ACS Appl. Energy Mater.*, https://doi.org/10.1021/acsaem.8b01123.

[13] a) T. S. Dörr, A. Pelz, P. Zhang, T. Kraus, M. Winter, H.-D. Wiemhöfer, *Chem. - Eur. J.* **2018**, *24*, 8061; b) J. G. Werner, G. G. Rodriguez-Calero, H. D. Abruna, U. Wiesner, *Energy Environ. Sci.* **2018**, *11*, 1261.

[14] a) R. Liu, Y. Ren, Y. Shi, F. Zhang, L. Zhang, B. Tu, D. Zhao, *Chem. Mater.* **2008**, *20*, 1140; b) T. Weller, J. Sann, R. Marschall, *Adv. Energy Mater.* **2016**, *6*, 1600208.

[15] L. Li, M. Krissanasaeranee, S. W. Pattinson, M. Stefik, U. Wiesner, U. Steiner, D. Eder, *Chem. Commun.* **2010**, *46*, 7620.

[16] T. S. Dörr, S. Fleischmann, M. Zeiger, I. Grobelsek, P. W. de Oliveira, V. Presser, *Chem. - Eur. J.* **2018**, *24*, 6358.

[17] T. Weller, L. Deilmann, J. Timm, T. S. Dörr, P. A. Beaucage, A. S. Cherevan, U. B. Wiesner, D. Eder, R. Marschall, *Nanoscale* **2018**, *10*, 3225.

[18] M. Templin, A. Franck, A. Du Chesne, H. Leist, Y. Zhang, R. Ulrich, V. Schädler, U. Wiesner, *Science* **1997**, *278*, 1795.

[19] D. Zhao, J. Feng, Q. Huo, N. Melosh, G. H. Fredrickson, B. F. Chmelka, G. D. Stucky, *Science* **1998**, *279*, 548.

[20] P. Docampo, M. Stefik, S. Guldin, R. Gunning, N. A. Yufa, N. Cai, P. Wang, U. Steiner, U. Wiesner, H. J. Snaith, *Adv. Energy Mater.* **2012**, *2*, 676.

[21] A. S. Cherevan, S. Robbins, D. Dieterle, P. Gebhardt, U. Wiesner, D. Eder, *Nanoscale* **2016**, *8*, 16694.

[22] S. Guldin, S. Huttner, P. Tiwana, M. C. Orilall, B. Ulgut, M. Stefik, P. Docampo, M. Kolle, G. Divitini, C. Ducati, S. A. T. Redfern, H. J. Snaith, U. Wiesner, D. Eder, U. Steiner, *Energy Environ. Sci.* **2011**, *4*, 225.

[23] a) T. Dittrich, *Phys. Status Solidi A* **2000**, *182*, 447; b) T. Dittrich, J. Weidmann, F. Koch, I. Uhlendorf, I. Lauermann, *Appl. Phys. Lett.* **1999**, *75*, 3980.

[24] K. Lalitha, G. Sadanandam, V. D. Kumari, M. Subrahmanyam, B. Sreedhar, N. Y. Hebalkar, *J. Phys. Chem. C* **2010**, *114*, 22181.

[25] A. Kubacka, G. Colon, M. Fernandez-Garcia, *Catal. Today* **2009**, *143*, 286.

[26] a) D. D. Mulmi, T. Sekiya, N. Kamiya, S. Kurita, Y. Murakami, T. Kodaira, *J. Phys. Chem. Solids* **2004**, *65*, 1181; b) L. R. Sheppard, T. Bak, J. Nowotny, *J. Phys. Chem. B* **2006**, *110*, 22447; c) M. Valigi, D. Cordischi, G. Minelli, P. Natale, P. Porta, C. P. Keijzers, *J. Solid State Chem.* **1988**, *77*, 255; d) H.-Y. Lee, J. Robertson, *J. Appl. Phys.* **2013**, *113*, 213706.

[27] L. N. Kong, C. H. Wang, H. Zheng, X. T. Zhang, Y. C. Liu, *J. Phys. Chem. C* **2015**, *119*, 16623.

[28] T. Nikolay, L. Larina, O. Shevaleevskiy, B. T. Ahn, *Energy Environ. Sci.* **2011**, *4*, 1480.

[29] M. C. Orilall, U. Wiesner, *Chem. Soc. Rev.* **2011**, *40*, 520.

[30] Y. Qiu, F. Ouyang, R. Zhu, *Int. J. Hydrogen Energy* **2017**, *42*, 11364.

[31] W. F. Zhang, Y. L. He, M. S. Zhang, Z. Yin, Q. Chen, *J. Phys. D: Appl. Phys.* **2000**, *33*, 912.

[32] A. M. Ruiz, G. Dezanneau, J. Arbiol, A. Cornet, J. R. Morante, *Chem. Mater.* **2004**, *16*, 862.

[33] M. Thommes, K. Kaneko, A. V. Neimark, J. P. Olivier, F. Rodriguez-Reinoso, J. Rouquerol, K. S. Sing, *Pure Appl. Chem.* **2015**, *87*, 1051.

[34] T. H. Epps, E. W. Cochran, C. M. Hardy, T. S. Bailey, R. S. Waletzko, F. S. Bates, *Macromolecules* **2004**, *37*, 7085.

[35] A. J. Gardecka, G. K. L. Goh, G. Sankar, I. P. Parkin, *J. Mater. Chem. A* **2015**, *3*, 17755.

[36] P. Le Fèvre, J. Danger, H. Magnan, D. Chandesris, J. Jupille, S. Bourgeois, M. A. Arrio, R. Gotter, A. Verdini, A. Morgante, *Phys. Rev. B* **2004**, *69*, 155421.

[37] a) M. Z. Atashbar, H. T. Sun, B. Gong, W. Wlodarski, R. Lamb, *Thin Solid Films* **1998**, *326*, 238; b) M. Kim, C. Kwon, K. Eom, J. Kim, E. Cho, *Sci. Rep.* **2017**, *7*, 44411.

[38] J. Wang, X. Wang, Z. Cui, B. Liu, M. Cao, *Phys. Chem. Chem. Phys.* **2015**, *17*, 14185.

[39] T. M. Breault, B. M. Bartlett, *J. Phys. Chem. C* **2012**, *116*, 5986.

[40] F. Zuo, L. Wang, T. Wu, Z. Zhang, D. Borchardt, P. Feng, *J. Am. Chem. Soc.* **2010**, *132*, 11856.

[41] a) J. Yang, X. Zhang, C. Wang, P. Sun, L. Wang, B. Xia, Y. Liu, *Solid State Sci.* **2012**, *14*, 139; b) B.-X. Chen, H.-S. Rao, W.-G. Li, Y.-F. Xu, H.-Y. Chen, D.-B. Kuang, C.-Y. Su, *J. Mater. Chem. A* **2016**, *4*, 5647.

[42] B. Roose, K. C. Gödel, S. Pathak, A. Sadhanala, J. P. C. Baena, B. D. Wilts, H. J. Snaith, U. Wiesner, M. Grätzel, U. Steiner, A. Abate, *Adv. Energy Mater.* **2016**, *6*, 1501868.

[43] M. S. J. Marshall, D. T. Newell, D. J. Payne, R. G. Egdell, M. R. Castell, *Phys. Rev. B* **2011**, *83*, 035410.

[44] Y. D. Wang, B. M. Smarsly, I. Djerdj, *Chem. Mater.* **2010**, *22*, 6624.

[45] H. Xu, P. Reunchan, S. Ouyang, H. Tong, N. Umezawa, T. Kako, J. Ye, *Chem. Mater.* **2013**, *25*, 405.

[46] F. Amano, M. Nakata, A. Yamamoto, T. Tanaka, *Catal. Sci. Technol.* **2016**, *6*, 5693.

[47] A. L. Luna, D. Dragoe, K. Wang, P. Beaunier, E. Kowalska, B. Ohtani, D. B. Uribe, M. A. Valenzuela, H. Remita, C. Colbeau-Justin, *J. Phys. Chem. C* **2017**, *121*, 14302.

[48] T. Sreethawong, S. Yoshikawa, *Catal. Commun.* **2005**, *6*, 661.

[49] Z. Lian, W. Wang, G. Li, F. Tian, K. S. Schanze, H. Li, *ACS Appl. Mater. Interfaces* **2017**, *9*, 16959.

[50] K. Yamaguti, S. Sato, *J. Chem. Soc., Faraday Trans. 1* **1985**, *81*, 1237.

[51] W. Zhou, W. Li, J.-Q. Wang, Y. Qu, Y. Yang, Y. Xie, K. Zhang, L. Wang, H. Fu, D. Zhao, *J. Am. Chem. Soc.* **2014**, *136*, 9280.

[52] K. Hur, Y. Francescato, V. Giannini, S. A. Maier, R. G. Hennig, U. Wiesner, *Angew. Chem., Int. Ed.* **2011**, *50*, 11985.

[53] S. Vignolini, N. A. Yufa, P. S. Cunha, S. Guldin, I. Rushkin, M. Stefik, K. Hur, U. Wiesner, J. J. Baumberg, U. Steiner, *Adv. Mater.* **2012**, *24*, OP23.

[54] G. M. Haselmann, D. Eder, *ACS Catal.* **2017**, *7*, 4668.

[55] M. L. Sauer, D. F. Ollis, *J. Catal.* **1996**, *163*, 215.

[56] a) M. A. Hillmyer, F. S. Bates, *Macromolecules* **1996**, *29*, 6994; b) J. Chatterjee, S. Jain, F. S. Bates, *Macromolecules* **2007**, *40*, 2882.

[57] a) S. Tougaard, *Surf. Interface Anal.* **1997**, *25*, 137; b) D. A. Shirley, *Phys. Rev. B* **1972**, *5*, 4709.

[58] J. H. Scofield, *J. Electron Spectrosc. Relat. Phenom.* **1976**, *8*, 129.

[59] a) C. D. Wagner, A. V. Naumkin, A. Kraut-Vass, J. W. Allison, C. J. Powell, J. R. Rumble, *NIST X-ray Photoelectron Spectroscopy Database, NIST Standard Reference Database Number 20,* National Institute of Standards and Technology, Gaithersburg, MD **2000**; b) G. Beamson, D. Briggs, *High Resolution XPS of Organic Polymers: The Scienta ESCA300 Database*, Wiley, New York **1992**.

[60] S. Brunauer, P. H. Emmett, E. Teller, *J. Am. Chem. Soc.* **1938**, *60*, 309.

[61] P. Blaha, K. Schwarz, G. K. H. Madsen, D. Kvasnicka, J. Luitz, R. Laskowski, F. Tran, L. D. Marks, *WIEN2k, An Augmented Plane Wave + Local Orbitals Program for Calculating Crystal Properties*, Karlheinz Schwarz, Vienna University of Technology, Vienna, Austria **2018**.

[62] J. P. Perdew, K. Burke, M. Ernzerhof, *Phys. Rev. Lett.* **1996**, *77*, 3865.

[63] S. L. Dudarev, G. A. Botton, S. Y. Savrasov, C. J. Humphreys, A. P. Sutton, *Phys. Rev. B* **1998**, *57*, 1505.

[64] Y. Kesong, D. Ying, H. Baibiao, F. Yuan Ping, *J. Phys. D: Appl. Phys.* **2014**, *47*, 275101.

[65] X. Han, K. Song, L. Lu, Q. Deng, X. Xia, G. Shao, *J. Mater. Chem. C* **2013**, *1*, 3736.

[66] a) B. J. Morgan, D. O. Scanlon, G. W. Watson, *J. Mater. Chem.* **2009**, *19*, 5175; b) S. Khan, H. Cho, D. Kim, S. S. Han, K. H. Lee, S.-H. Cho, T. Song, H. Choi, *Appl. Catal., B* **2017**, *206*, 520.

**ADVANCED
ENERGY
MATERIALS**

Supporting Information

Ordered Mesoporous TiO$_2$ Gyroids: Effects of Pore Architecture and Nb-Doping on Photocatalytic Hydrogen Evolution under UV and Visible Irradiation

Tobias Sebastian Dörr, Leonie Deilmann, Greta Haselmann, Alexey Cherevan, Peng Zhang, Peter Blaha, Peter Williamde Oliveira, Tobias Kraus, and Dominik Eder*

Supporting Information

Ordered Mesoporous TiO₂-gyroids: Effects of Pore Architecture and Nb-doping on Photocatalytic Hydrogen Evolution under UV and VIS irradiation

Tobias Sebastian Dörr, Leonie Deilmann, Greta Haselmann, Alexey Cherevan, Peng Zhang, Peter Blaha, Peter William de Oliveira, Tobias Kraus, and Dominik Eder*

Figure S1. (A) Thermogravimetric analysis of inorganic/polymer hybrid (ISO/G^A-TiO2) and the corresponding oxide after thermal removal of the polymer template (G^A-TiO2). Applied Temperature profile for ISO/G^A-TiO2 is inciated by blue dotted line. (B) RAMAN spectroscopy with extended range and magnification of 1000 – 2500 cm^{-1} and (C) nitrogen gas sorption isotherme for gyroidal samples.
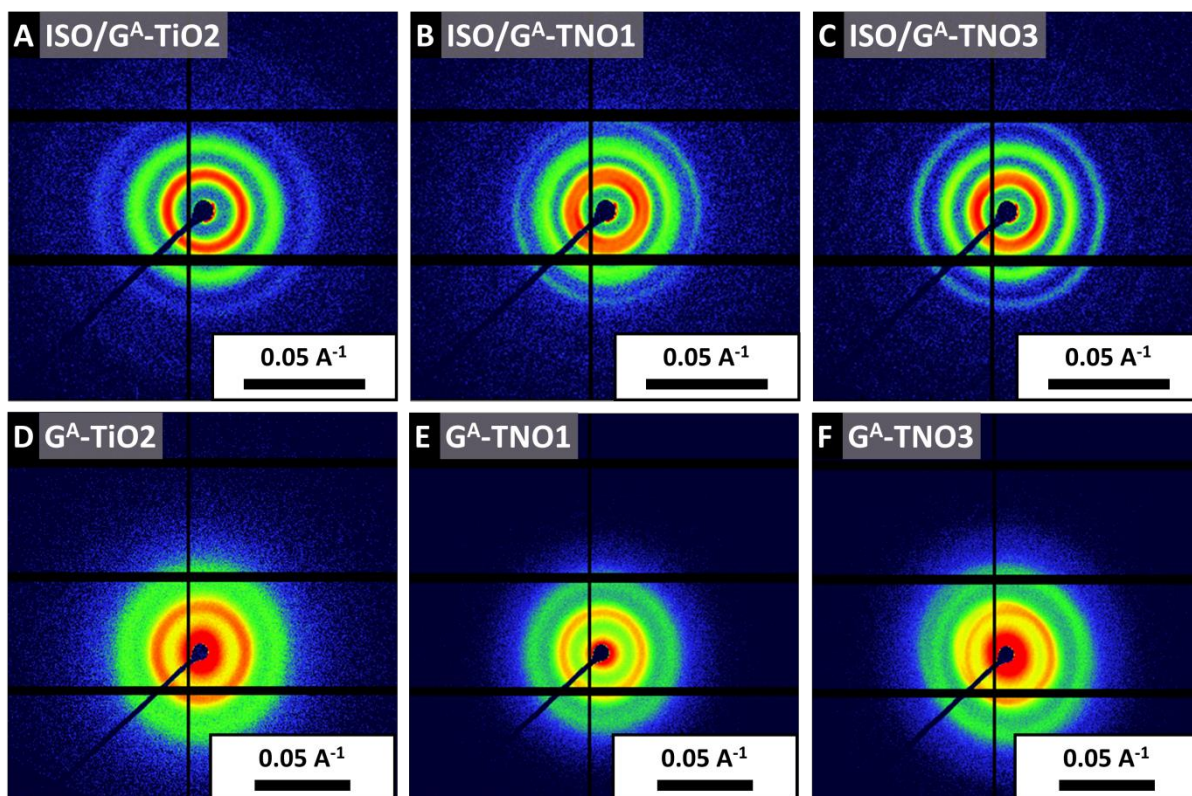
Figure S2. 2D small-angle X-ray scattering patterns of the (A-C) inorganic/polymer hybrids and (D-F) the corresponding calcined samples after template removal. The black strikes are due to beam stop and modular gaps of the Pilatus detector.
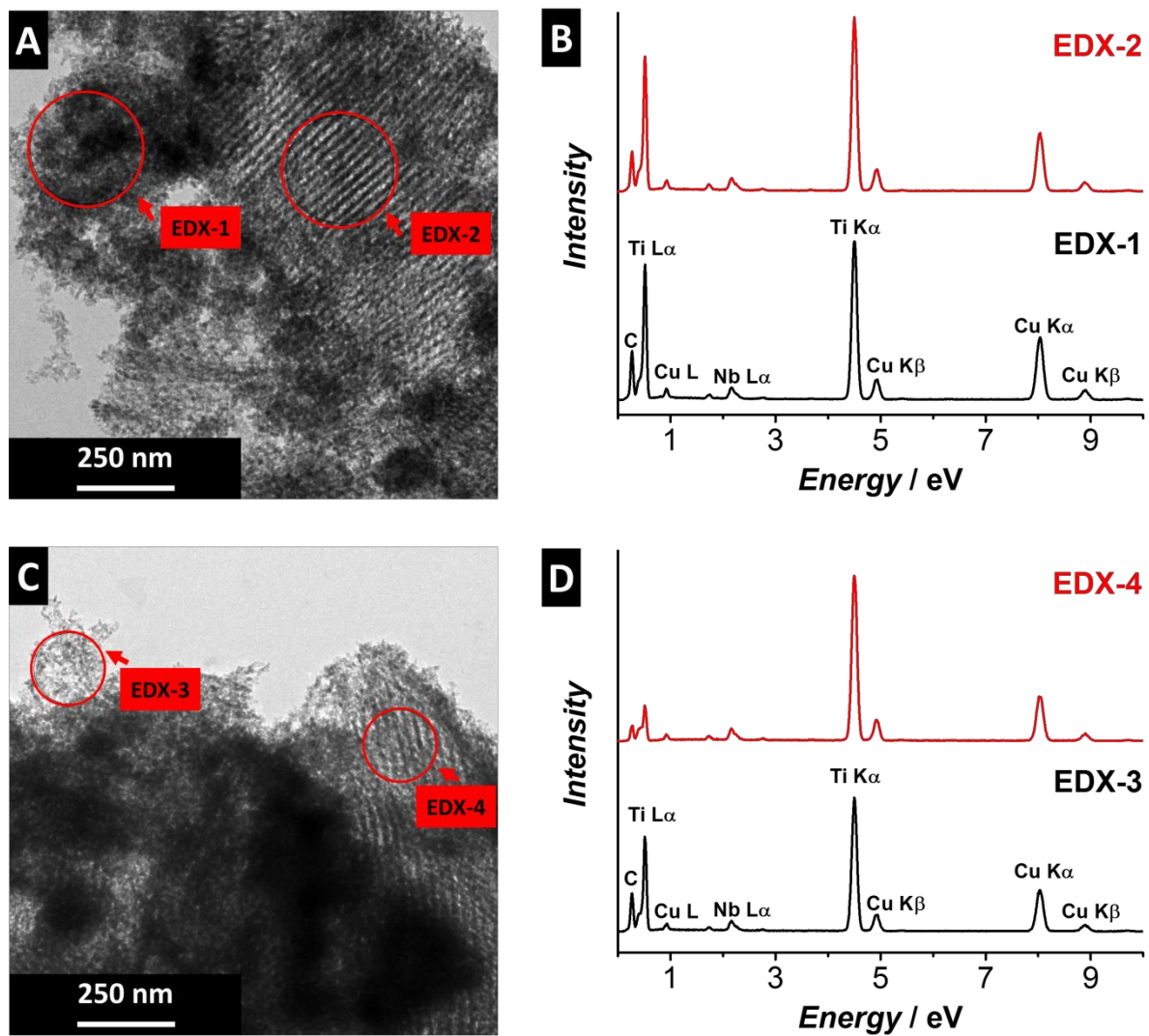
Figure S3. TEM images of (A + B) G^A-TNO3 with (B + D) corresponding qualitative EDX analysis.
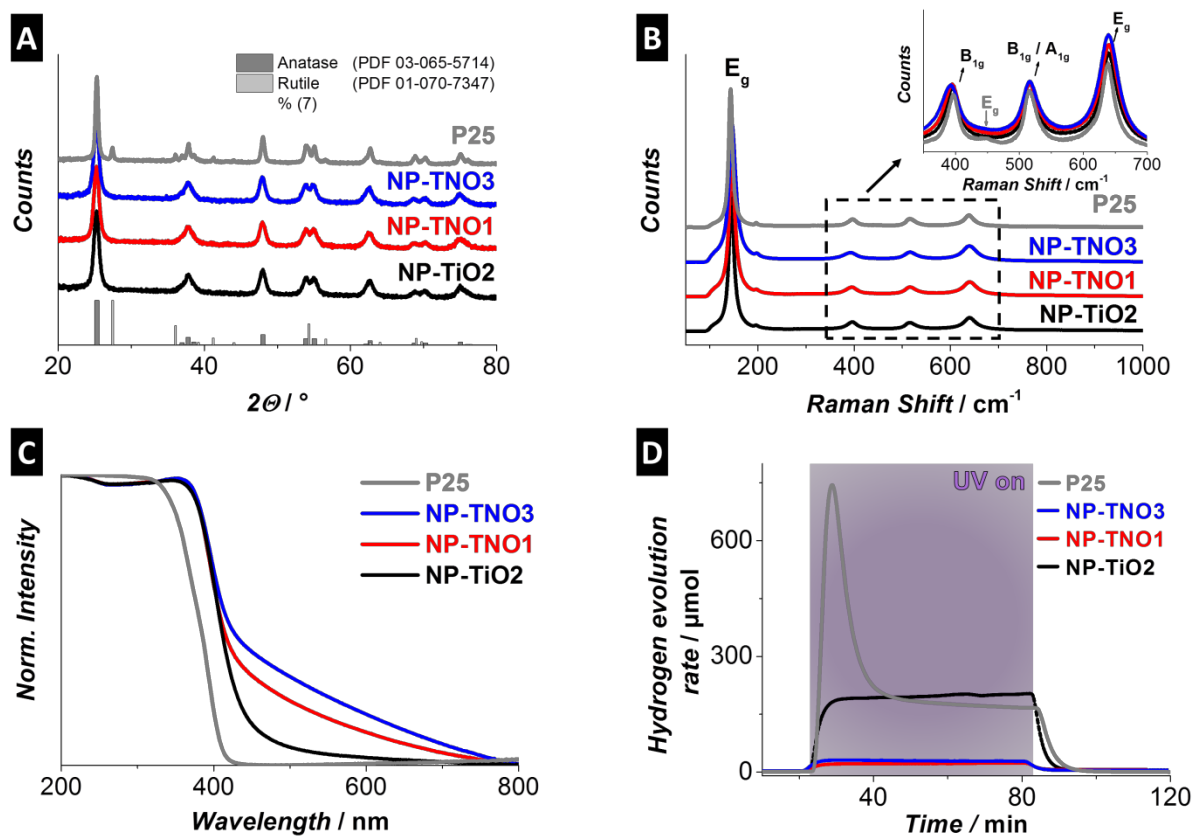
Figure S4. Characterization of the nanoparticulate references. (A) X-ray powder diffraction (XRD) including bibliographic data for anatase (PDF 03-065-5714) and rutile (PDF 01-070-7347). (B) RAMAN and (C) diffuse reflectance (DRS) spectroscopy. (D) Hydrogen evolution profiles under UV light.
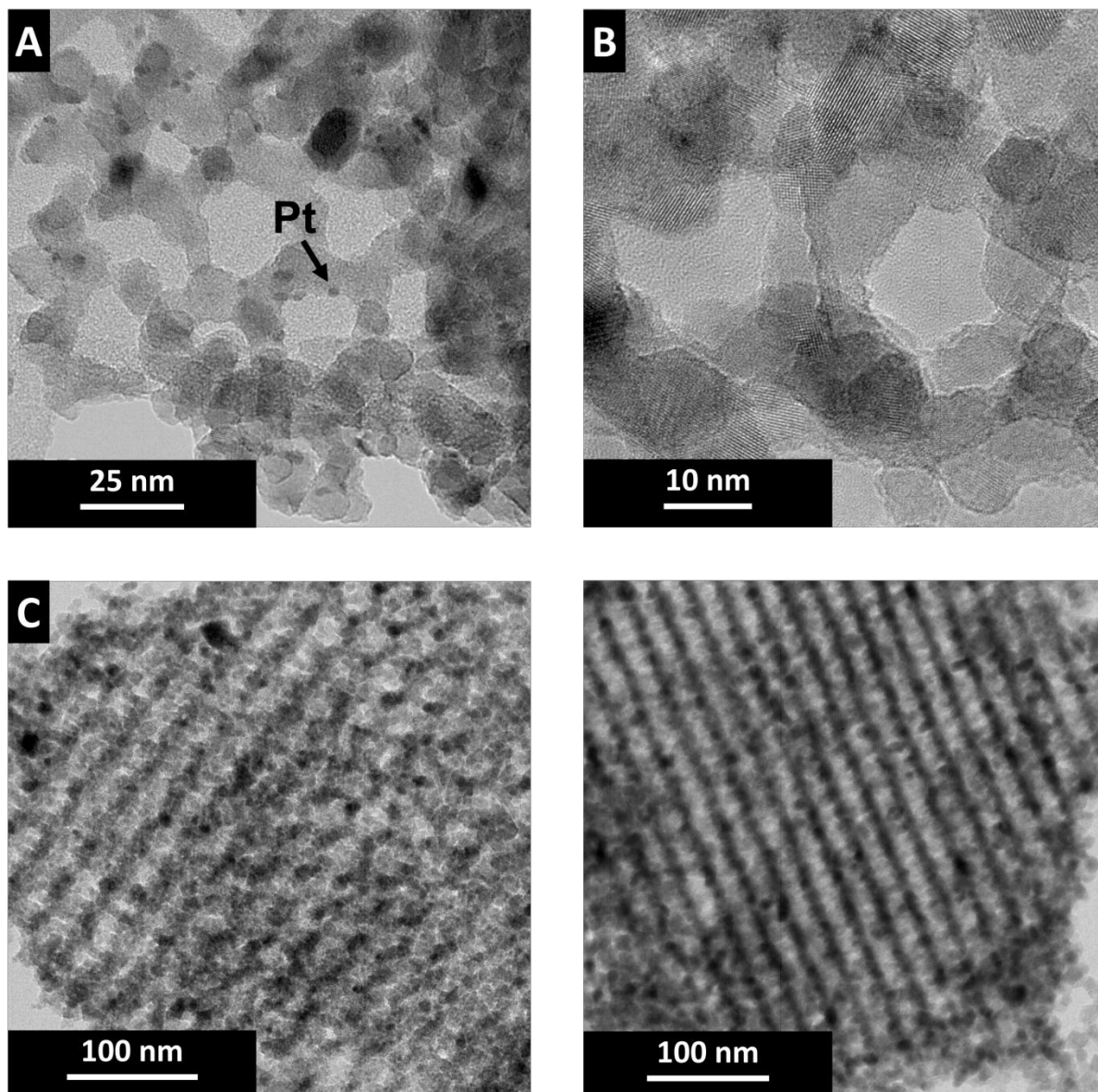
Figure S5. Post-mortem TEM anaysis of G^A-TiO2. Darker spots represent photodeposited Pt nanoparticles as indicated in (A).
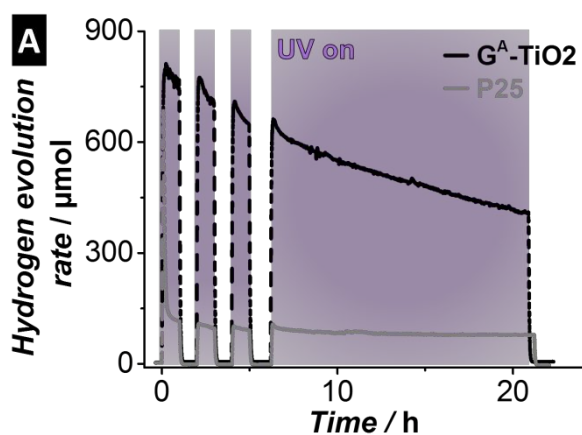
Figure S6. Cylcic and long time hydrogen evolution profiles under UV light for G^A-TiO2 and P25.

5

Table S1. Results from Rietveld refinement.

	G^A-TiO2		G^A-TNO1		G^A-TNO3	
Phase	anatase	rutile	anatase	rutile	anatase	rutile
Mass%	96.812	3.188	98.369	1.631	98.345	1.655
Crystallite size	12.1 nm	24.6 nm	15.6 nm	35.9 nm	13.7 nm	29.4 nm
Space Group	I41/amdZ	P42/mnm	I41/amdZ	P42/mnm	I41/amdZ	P42/mnm
Lattice constant	a = 3.78697 Å c = 9.50578 Å	a = 4.59190 Å c = 2.95567 Å	a = 3.78680 Å c = 9.51132 Å	a = 4.59414 Å c = 2.95640 Å	a = 3.78879 Å c = 9.51234 Å	a = 4.59440 Å c = 2.95890 Å
Cell volume	136.32392 Å^3	62.32181 Å^3	136.39049 Å^3	62.39821 Å^3	136.54878 Å^3	62.45797 Å^3

Table S2. Results from ICP-OES.

Sample	Mass / mg	Ti / mg l^{-1}	Nb / mg l^{-1}	Pt / mg l^{-1}	Mass% Ti	Mass% Nb	Mass% Pt
G^A-TiO2	28.75	3.31 ± 0.05	--	--	57.57 ± 0.78	--	--
G^A-TNO1	59.59	6.53 ± 0.14	13.76 ± 0.36	--	54.45 ± 0.01	1.15 ± 0.03	--
G^A-TNO3	64.18	7.13 ± 0.08	39.80 ± 0.82	--	55.58 ± 0.60	3.10 ± 0.06	--
G^A-TNO3†	13.61	1.41 ± 0.02	8.63 ± 0.08	1.18 ± 0.05	51.76 ± 0.77	3.17 ± 0.03	0.43 ± 0.02

†recovered sample after H$_2$ evolution experiment

Table S3. Results from XPS spectra deconvolution of Nb 3d signal.

	Position / eV		Area [%]		FWHM‡ / eV	
Sample	Nb 3d$_{5/2}$	Nb 3d$_{3/2}$	Nb 3d$_{5/2}$	Nb 3d$_{3/2}$	Nb 3d	ΔE_B / eV
G^A-TNO1	206.97	209.75	60.02	39.98	1.17	2.78
G^A-TNO3	206.32	209.10	60.15	39.85	1.19	2.78
NP-TNO1	208.05	210.83	57.95	42.05	1.24	2.78
NP-TNO3	208.13	210.91	59.18	40.82	1.38	2.78
Nb$_2$O$_5$ Reference	207.05	209.63	60.54	39.46	1.11	2.78

‡FWHM was set to be identical.

Calculation of the photonic efficiency of the photocatalytic reaction has been performed based on the following equation:[S1]

$$Photonic\ efficiency\ (\%) = \frac{\#\ of\ H_2\ molecules\ produced \times 2}{\#\ of\ incident\ light\ photons} \times 100$$

Number of H$_2$ molecules has been derived from the value of HER activity after 30 min of light exposure using the following equation:

$$\#\ of\ H_2\ molecules\ produced\ per\ second = \frac{activity\ (\mu mol/h) \times N_A\ (molecules/mol)}{3600\ (s/h) \times 1000000 (\mu mol/mol)}$$

Number (#) of incident photons has been calculated using power energy meter PM100D (Thorlabs) and amounted for 2.77×10^{18} photons/sec assuming that all useful photons had the same energy of 5.67×10^{-17} J (corresponding to a wavelength of 350 nm, which represents an intensity-weighted average of Hg lamp spectrum output in the region between 240 and 400 nm).

Table S4. Calculated photonic efficiency values in sacrificial water splitting towards H$_2$ evolution for the tested samples.

Sample	H$_2$ evolution rate / μmol h^{-1}	Photonic efficiency / %
G^A-TiO2	1001	12.1
G^A-TNO1	755	9.1
G^A-TNO3	435	5.2
TiO$_2$-P25	174	2.1

Table S5. Selection of recent progresses in photocatalytic hydrogen evolution from literature.

Material	Co-catalyst (mass%)	Setup		H$_2$ Evolution rate		Reference (year)
		Light source	Reactant medium	Per hour (catalyst mass)	Mass-specific	
N-doped reduced graphene oxide-MoS$_2$	-	Halogen lamp	H$_2$O:TEOA 10:1.5 (+ 0.15 mM EOSIN Y)	[a)]84 mmol h^{-1} (2 mg)	42 mmol h^{-1} g^{-1}	[S2] (2013)
N deficient graphitic C$_3$N$_4$	Pt (1)	Xe-lamp > 420nm	H$_2$O:lactic acid 4:1	69 µmol h^{-1} (10 mg)	6.9 mmol h^{-1} g^{-1}	[S3] (2017)
WS$_2$-CdS	-	Xe-lamp > 420nm	H$_2$O:lactic acid 10:1	[a)]19.8 µmol h^{-1} (10 mg)	1984 µmol h^{-1}g^{-1}	[S4] (2015)
MoS$_2$-CdS	-	Xe-lamp > 420nm	H$_2$O:lactic acid 10:1	[a)]14.7 µmol h^{-1} (10 mg)	1472 µmol h^{-1}g^{-1}	[S4] (2015)
GaN:ZnO	Ni (1.25)	Hg-lamp > 300nm	H$_2$O	126 µmol h^{-1} (300 mg)	[a)]420 µmol h^{-1} g^{-1}	[S5] (2006)
ONHL (Oxygen and Nitrogen co-linked heptazine)	Pt (5)	Xe-lamp > 420nm	H$_2$O:TEOA 10:1	10.2 µmol h^{-1} (100 mg)	[a)]102 µmol h^{-1}g^{-1}	[S6] (2017)
CdS	MoS$_2$-graphene (0.5)	Xe-lamp > 400nm	H$_2$O:lactic acid 5:1	2.32 mmol h^{-1} (100 mg)	[a)]23.2 µmol h^{-1}g^{-1}	[S7] (2014)
ZrO$_2$/TaON	Pt (0.5)	Xe-lamp > 420nm	H$_2$O (1 mM NaI)	[a)]3.5 µmol h^{-1} (200 mg)	[a)]17.5 µmol h^{-1}g^{-1}	[S8] (2008)
TaON	Pt (0.5)	Xe-lamp > 420nm	H$_2$O (1 mM NaI)	[a)]2 µmol h^{-1}	[a)]10 µmol h^1 g^{-1}	[S8] (2008)

[a)]calculated from given values

References

[S1]   a) E. Braslavsky Silvia, M. Braun André, E. Cassano Alberto, V. Emeline Alexei, I. Litter Marta, L. Palmisano, N. Parmon Valentin, N. Serpone, *Pure Appl. Chem., Vol. 83*, **2011**, p. 931; b) M. Qureshi, K. Takanabe, *Chem. Mater.* **2017**, *29*, 158-167.
[S2]   U. Maitra, U. Gupta, M. De, R. Datta, A. Govindaraj, C. N. R. Rao, *Angew. Chem.* **2013**, *125*, 13295-13299.
[S3]   H. Yu, R. Shi, Y. Zhao, T. Bian, Y. Zhao, C. Zhou, G. I. N. Waterhouse, L.-Z. Wu, C.-H. Tung, T. Zhang, *Adv. Mater.* **2017**, *29*, 1605148.
[S4]   J. Chen, X.-J. Wu, L. Yin, B. Li, X. Hong, Z. Fan, B. Chen, C. Xue, H. Zhang, *Angew. Chem.* **2015**, *127*, 1226-1230.
[S5]   K. Maeda, K. Teramura, N. Saito, Y. Inoue, K. Domen, *J. Catal.* **2006**, *243*, 303-308.
[S6]   Y. Wang, M. K. Bayazit, S. J. A. Moniz, Q. Ruan, C. C. Lau, N. Martsinovich, J. Tang, *Energy Environ. Sci.* **2017**, *10*, 1643-1651.
[S7]   M. Liu, F. Li, Z. Sun, L. Ma, L. Xu, Y. Wang, *Chem Commun* **2014**, *50*, 11004-11007.
[S8]   M. Kazuhiko, T. Hiroaki, K. Kentaro, H. Masanobu, T. Masashi, D. Kazunari, *Bull. Chem. Soc. Jpn.* **2008**, *81*, 927-937.

5. CONCLUSION

In this thesis, block copolymer derived three-dimensional ordered hybrid materials have been employed for their device application in energy storage and conversion. By preparing tailored ISOs and their use as structure directing agent, I could precisely prepare functional nanostructures. Including lamellar, alternating gyroid, and perforated lamellar of inorganic and hybrid materials that led to improved performance in contemporary energy storage and conversion application.

First, a TiO_2/carbon hybrid was prepared for its application as anode material in LIBs. A combined effort of self-assembly and *in-situ* carbonization of the structure directing template enabled ultrathick (300 µm) and dense (0.88 g cm^{-3}), freestanding monoliths. The thin carbon layer after carbonization compensated for the general low electronic conductivity of oxides that are preferred for anodes due to their superior intercalation kinetics over commonly used graphite. The mass loading (i.e. volumetric energy density) of our monoliths were at least one decade above commonly used electrodes and outperformed similarly thick powdered mesoporous TiO_2 casted reference (i.e. 60 % higher volumetric capacity). The results are of particular interest for industrial applications, where dense materials are required for downsizing (e.g. mobile energy storage). The high mass loading thus compensates for the additional cell components. A critical summary of the most important key features of the material prepared here is given within **Table 2**.

Table 2. Critical review of **Chapter 4.1**.

	TiO₂/C –Hybrid Monoliths as LIB Anode	
	Opportunities	**Challenges**
Material aspect Mesoporous TiO₂ as Anode	▪ High rate performance ▪ Safer operation potential ▪ No exfoliation ▪ Abundant and non-toxic materials ▪ High chemical stability ▪ Reduced diffusion limitation ▪ Large electrode|electrolyte interface ▪ *In-situ* conductive carbon layer formation	▪ Lower specific capacity than commonly used graphite ▪ Low intrinsic conductivity ▪ Brittle nature ▪ Comparably costly ▪ Limited scalability of electrode size
Key feature Ultrathick and dense monoliths	▪ High volumetric and areal capacity ▪ Percolating structure ensures beneficial charge transport ▪ High mass loading enables downsizing ▪ Reduced inactive additives ▪ Reduced costs, i.e. Cu and Au current collectors[‡]	▪ Lack of flexibility ▪ May cause contact problems during cell assembly

Next, different ISO/LiTFSI electrolytes have been prepared for their use in LMBs, which are generally considered as the "next-generation" of batteries due to the superior capacity of Li metal (3862 mAh g⁻¹). The smallest $M_{W,PEO}$ ISOs with 2 kg mol⁻¹ and 5 kg mol⁻¹ greatly outperformed those with larger $M_{W,PEO}$ in terms of cationic conductivities in a relevant temperature range of -20 °C to 90 °C. Unprecedented high Li:EO ratios up to 5:1 resulted in altered Li coordination that deviated from classical strong two ether oxygen coordination. As a result, stable conductivity up to 1 mS cm⁻¹ over the entire temperature range was achieved, which suggested an ionic mobility decoupled from slow polymer relaxation. These cationic conductivities are in a range of state of the art liquid and gel-type electrolytes and several orders of magnitude above recently reported polymer electrolytes. Those promising BCEs additionally provided high mechanical integrity,

---

[‡] Common electrodes are usually thin casted on large areas of current collectors and coiled; thick electrodes mitigate this need for large areas to provide comparable storage capacity.

extended thermal stability and electrochemical resistance versus lithium. The critical summary of the progress presented in **Chapter 4.2** and **4.3** is depicted in **Table 3**.

Table 3. Critical review of **Chapter 4.2** and **4.3**.

<table>
<tr><th colspan="3">ISO/LiTFSI hybrids as BCE</th></tr>
<tr><th></th><th>Opportunities</th><th>Challenges</th></tr>
<tr>
<td>Material aspect
Nanostructured BCP as electrolyte</td>
<td>

Enables self-assembly
Mechanical flexibility
Triblock allows for 2D lamellar PEO as minor component
High compatibility with common (hydrophilic) Li salts
Oriented "pathways" for ions
Chains stretching increases mobility
Phase pure domain mitigates "defects" that may decrease mobility

</td>
<td>

Aromatic ring (PS) and double bond (PI) potentially degrade above 4.5 V
Requires organic solvents for EISA process (i.e. THF)
Only with $M_{W,PEO} \leq 5$ kg mol^{-1} reasonable to use
Limited scalability
Thick electrolyte membranes (~700 µm)

</td>
</tr>
<tr>
<td>Key feature
Ultra-small conductive block</td>
<td>

Conductivity comparable to state of the art liquid and gel electrolytes
Superior Li contribution to overall conductivity
Enables high Li:EO ratios that decouple ionic and polymer mobility
Smaller PEO enables larger PI and PS blocks (increased mechanical integrity)
ESW enables a plethora of common cathode materials vs. lithium metal

</td>
<td>

Non-removable THF that compensates for lack of ether oxygen coordination may electro-polymerize above 4.5 V
Decreased electrochemical stability along decreased $M_{W,PEO}$

</td>
</tr>
</table>

Last, G^A Nb-doped and pure TiO_2 has been prepared for its use in heterogeneous catalysis. The performance in H_2 evolution was investigated under UV and VIS irradiation. Highly uniform pores with a diameter of ~15 nm enabled high pore diffusion with sufficiently high surface areas of ~80 - 100 m^2 g^{-1}. Combined X-ray diffraction, photoluminescence and density functional theory based calculations indicated two regimes for the mechanism of doping: at low Nb amounts (i.e. 1 at.%), isolated Nb species introduced mid-gap states that enabled VIS absorption. In

contrast, Nb tended to cluster at higher amounts, creating shallow trap states that vanished activity under both, UV and VIS irradiation. Crucially, a superior activity was found for the pure mesoporous TiO_2 under UV, which was among the highest values reported and outperformed even the benchmark P25-TiO_2 more than 5-fold. We ascribed that activity to an enhanced electron transport due to the percolating network with wall thicknesses in the range of exciton diffusion range, enhanced inter-grain charge transfer, and high accessibility of the mesoporous networked material by the reactants. **Table 4** depicted the critical review of the results.

Table 4. Critical review of **Chapter 4.4**.

Nb-doped and pure TiO_2 photocatalysts		
	Opportunities	**Challenges**
Material aspect Mesoporous Nb-doped and pure TiO_2	▪ High reduction potential ▪ Abundant and non-toxic material ▪ High chemical stability ▪ Reduced diffusion limitation ▪ Wall-thickness in the range of exciton diffusibility ▪ 3D network structure may offer optical effects ▪ Reduces arbitrary surface loss due to agglomeration/aggregation ▪ Partial exchange of precursor allows for doping; coordination to PEO during self-assembly prevents for segregation	▪ Wide-band gap semiconductor ▪ Nb tends to cluster ▪ Co-catalyst (i.e. Pt) required ▪ Limited scalability
Key feature Structure-activity correlation	▪ UV activity among the highest reported in literature ▪ High VIS activity at optimized Nb-doping concentration ▪ Elucidating of mechanism of Nb incorporation correlated to doping concentration	▪ VIS activity far lower than UV activity (usually a problem in photocatalysis) ▪ Typical deactivation in long-term experiment due to poisoning (active site blocking)

6. OUTLOOK

The concept of TiO_2/C hybrid monoliths clearly shows the benefits of freestanding, nanostructured electrodes that reduce inactive materials and enable downsizing. Future storage solutions will include applications, where space is the limiting factor, rather than the mass of the cell (e.g. mobile energy storages). The concept presented can easily be extended to advanced materials via reasonable substitution by a metallic dopant. Non-structured vanadium doped TiO_2 (sample: V-doped TiO_2) already showed superior performance compared to pure TiO_2 (**Figure 11**). In the long-term, the procedure has to be transferred to state of the art electrode materials such as $LiCoO_2$ or $LiFePO_4$.
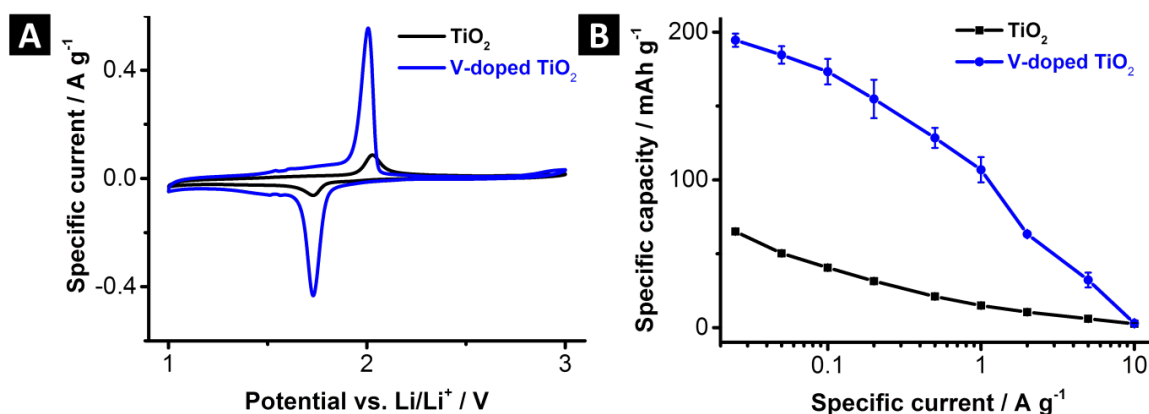
Figure 11. (**A**) Cyclic voltammograms and (**B**) gravimetric discharge capacity with variable rates between 0.025 to 10 A g^{-1} of pure and vanadium-doped TiO_2 at 0.1 mV s^{-1}.

BCEs that have been prepared from BCP co-assembly with LiTFSI indicate that ISO is a suitable candidate for its use in LMBs. Their chemical, electrochemical and thermal stabilities are sufficient to withstand the harsh environment using lithium metal under applied voltage. Although the measured mechanical integrity suggests a distinct stability versus Li dendrite growth, its direct investigation is not yet reported. **Figure 12** shows first data from stripping/plating experiments of pristine membranes. It is still an open question, whether this mechanical dendrite growth retention of the ISOs with $M_{W,PEO}$ of 2 kg mol^{-1} (sample: ISO-2k) and 5 kg mol^{-1} (sample: ISO-5k) can be improved by: (i) thermal annealing (i.e. 90 °C) or (ii) further M_W variation of individual blocks

or the total M_W of the ISO with persistent volume fraction ratios. LiTFSI was initially chosen due to its safe operation and good compatibility with typical solvents used in our EISA process and the PEO block, yet, other salts (e.g. $LiPF_6$ or $Li(C_2O_4)_2$) may improve the performance metrics.
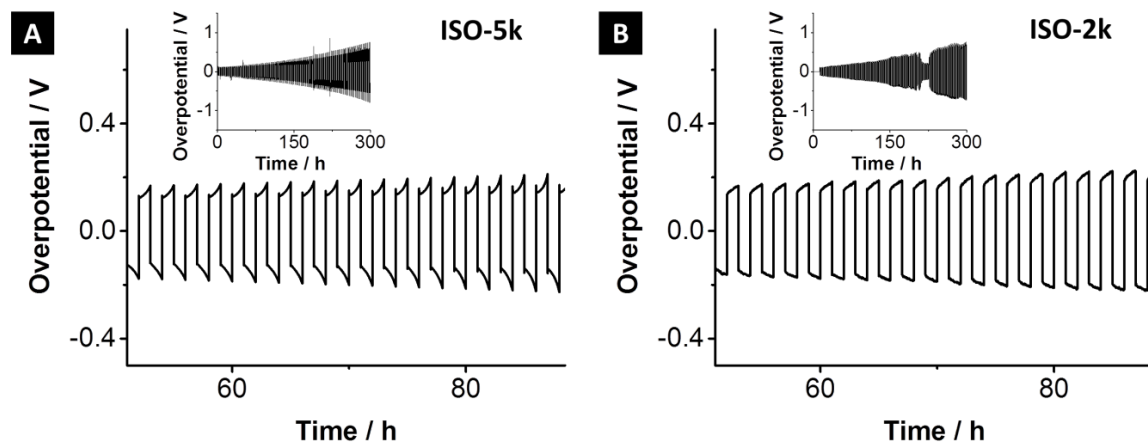
Figure 12. Lithium stripping/plating results for 40 hours (20 completed cycles) for (A) ISO-5k and (B) ISO-2k derived electrolytes as discussed in **chapter 4.3**. The inset shows a 300 hours long-term measurement (150 completed cycles).

The model system comprising gyroidal pure and Nb-doped TiO_2 already exhibited superior H_2 evolution rates under UV and VIS irradiation compared to related materials. This work presents a viable method to increase the materials activity by simple optimization of the nanostructure. Next steps will include the expansion towards advanced photocatalyst materials that enable overall water splitting,[105] for instance perovskites like $La_4CaTi_5O_{17}$.[106] It was already demonstrated that multi-component systems can be structured into alternating gyroids using ISO block copolymers, i.e. $CsTaWO_6$.[56b] Last, I believe that the unique pore architecture of the G^A morphology holds hitherto undiscovered optical benefits to photocatalysis, possibly related to the recently reported metamaterial-like[107] and chiral behavior.[102a] Once this correlation has been fully understood, optimization may offer dramatically increased performance metrics that paves the way for a sustainable future energy economy.

7. REFERENCES

[1] J. Cot-Gores, A. Castell, L. F. Cabeza, *Renewable and Sustainable Energy Rev.* **2012**, *16*, 5207-5224.

[2] H. Lund, *Energy* **2007**, *32*, 912-919.

[3] I. Dincer, *Renewable and Sustainable Energy Rev.* **2000**, *4*, 157-175.

[4] P. M. Cox, R. A. Betts, C. D. Jones, S. A. Spall, I. J. Totterdell, *Nature* **2000**, *408*, 184.

[5] T. L. Root, J. T. Price, K. R. Hall, S. H. Schneider, C. Rosenzweig, J. A. Pounds, *Nature* **2003**, *421*, 57.

[6] Eurostat, "Consumption of energy" can be found under https://ec.europa.eu/eurostat/statistics-explained/index.php?title=Archive:Consumptio n_of_energy, **2017**.

[7] EAFO, "PEV (M1) market share in the European Union" can be found under http://www.eafo.eu/eu, **2018**.

[8] Z. Yang, J. Zhang, M. C. W. Kintner-Meyer, X. Lu, D. Choi, J. P. Lemmon, J. Liu, *Chem. Rev.* **2011**, *111*, 3577-3613.

[9] a) J. Xu, S. Dou, H. Liu, L. Dai, *Nano Energy* **2013**, *2*, 439-442; b) J. M. Tarascon, M. Armand, *Nature* **2001**, *414*, 359-367.

[10] K. Ozawa, *Solid State Ionics* **1994**, *69*, 212-221.

[11] a) F. Jiao, J. L. Bao, A. H. Hill, P. G. Bruce, *Angew. Chem., Int. Ed.* **2008**, *47*, 9711-9716; b) D. K. Kim, P. Muralidharan, H.-W. Lee, R. Ruffo, Y. Yang, C. K. Chan, H. Peng, R. A. Huggins, Y. Cui, *Nano Lett.* **2008**, *8*, 3948-3952; c) E. Hosono, T. Kudo, I. Honma, H. Matsuda, H. Zhou, *Nano Lett.* **2009**, *9*, 1045-1051.

[12] a) A. Yamada, S. C. Chung, K. Hinokuma *J. Electrochem. Soc.* **2001**, *148*, A224-A229; b) H. Huang, S.-C. Yin, L. F. Nazar, *Electrochem. and Solid-State Lett.* **2001**, *4*, A170-A172.

[13] R. Fong, U. von Sacken, J. R. Dahn, *J. Electrochem. Soc.* **1990**, *137*, 2009-2013.

[14] D. Aurbach, Y. Talyosef, B. Markovsky, E. Markevich, E. Zinigrad, L. Asraf, J. S. Gnanaraj, H.-J. Kim, *Electrochim.Acta* **2004**, *50*, 247-254.

[15] K. Mizushima, P. C. Jones, P. J. Wiseman, J. B. Goodenough, *Mater. Res. Bull.* **1980**, *15*, 783-789.

[16] B. Scrosati, *J. Electrochem. Soc.* **1992**, *139*, 2776-2781.

[17] E. Kang, Y. S. Jung, G. H. Kim, J. Chun, U. Wiesner, A. C. Dillon, J. K. Kim, J. Lee, *Adv. Funct. Mater.* **2011**, *21*, 4349-4357.

[18] M. Winter, *Z. Phys. Chem.* **2009**, *223*, 1395-1406.

[19] A. Tolosa, B. Krüner, S. Fleischmann, N. Jäckel, M. Zeiger, M. Aslan, I. Grobelsek, V. Presser, *J. Mater. Chem. A* **2016**, *4*, 16003-16016.

[20] A. Tolosa, S. Fleischmann, I. Grobelsek, A. Quade, E. Lim, V. Presser, *ChemSusChem* **2018**, *11*, 159-170.

[21] a) L. David, R. Bhandavat, U. Barrera, G. Singh, *Nat. Commun.* **2016**, *7*, 10998; b) X. Zhao, C. M. Hayner, M. C. Kung, H. H. Kung, *ACS Nano* **2011**, *5*, 8739-8749; c) N. Bouazza, M. Ouzzine, M. A. Lillo-Rodenas, D. Eder, A. Linares-Solano, *Appl. Catal., B* **2009**, *92*, 377-383.

[22] T. S. Dörr, S. Fleischmann, M. Zeiger, I. Grobelsek, P. W. de Oliveira, V. Presser, *Chem. - Eur. J.* **2018**, *24*, 6358-6363.

[23] a) M. G. Fischer, X. Hua, B. D. Wilts, I. Gunkel, T. M. Bennett, U. Steiner, *ACS Appl. Mater. Inter.* **2017**, *9*, 22388-22397; b) J. Lee, Y. S. Jung, S. C. Warren, M. Kamperman, S. M. Oh, F. J. DiSalvo, U. Wiesner, *Macromol. Chem. Phys.* **2011**, *212*, 383-390.

[24] M. C. Orilall, U. Wiesner, *Chem. Soc. Rev.* **2011**, *40*, 520-535.

[25] P. G. Bruce, B. Scrosati, J. M. Tarascon, *Angew. Chem., Int. Ed.* **2008**, *47*, 2930-2946.

[26] a) R. Schmuch, R. Wagner, G. Horpel, T. Placke, M. Winter, *Nat. Energy* **2018**, *3*, 267-278; b) W. Xu, J. L. Wang, F. Ding, X. L. Chen, E. Nasybutin, Y. H. Zhang, J. G. Zhang, *Energy*

Environ. Sci. **2014**, *7*, 513-537; c) T. Placke, R. Kloepsch, S. Duhnen, M. Winter, *J. Solid State Electrochem.* **2017**, *21*, 1939-1964; d) M. H. Ryou, Y. M. Lee, Y. J. Lee, M. Winter, P. Bieker, *Adv. Funct. Mater.* **2015**, *25*, 834-841.

[27]   D. Aurbach, E. Zinigrad, Y. Cohen, H. Teller, *Solid State Ionics* **2002**, *148*, 405-416.

[28]   a) M. M. Hiller, M. Joost, H. J. Gores, S. Passerini, H. D. Wiemhofer, *Electrochim. Acta* **2013**, *114*, 21-29; b) M. Doyle, T. F. Fuller, J. Newman, *Electrochim. Acta* **1994**, *39*, 2073-2081; c) G. Bieker, M. Winter, P. Bieker, *Phys. Chem. Chem. Phys.* **2015**, *17*, 8670-8679; d) G. M. Stone, S. A. Mullin, A. A. Teran, D. T. Hallinan, A. M. Minor, A. Hexemer, N. P. Balsara, *J. Electrochem. Soc.* **2012**, *159*, A222-A227.

[29]   a) M. B. Armand, *Annu. Rev. Mater. Sci.* **1986**, *16*, 245-261; b) D. Bamford, A. Reiche, G. Dlubek, F. Alloin, J. Y. Sanchez, M. A. Alam, *J. Chem. Phys.* **2003**, *118*, 9420-9432; c) J. E. Weston, B. C. H. Steele, *Solid State Ionics* **1981**, *2*, 347-354.

[30]   A. A. Teran, M. H. Tang, S. A. Mullin, N. P. Balsara, *Solid State Ionics* **2011**, *203*, 18-21.

[31]   a) T. H. Epps, T. S. Bailey, H. D. Pham, F. S. Bates, *Chem. Mater.* **2002**, *14*, 1706-1714; b) W. S. Young, W. F. Kuan, T. H. Epps, *J. Polym. Sci. Pol. Phys.* **2014**, *52*, 1-16.

[32]   T. S. Dörr, A. Pelz, P. Zhang, T. Kraus, M. Winter, H.-D. Wiemhofer, *Chem. - Eur. J.* **2018**, *24*, 8061-8065.

[33]   a) E. D. Gomez, A. Panday, E. H. Feng, V. Chen, G. M. Stone, A. M. Minor, C. Kisielowski, K. H. Downing, O. Borodin, G. D. Smith, N. P. Balsara, *Nano Lett.* **2009**, *9*, 1212-1216; b) M. Singh, O. Odusanya, G. M. Wilmes, H. B. Eitouni, E. D. Gomez, A. J. Patel, V. L. Chen, M. J. Park, P. Fragouli, H. Iatrou, N. Hadjichristidis, D. Cookson, N. P. Balsara, *Macromolecules* **2007**, *40*, 4578-4585.

[34]   K. C. Divya, J. Østergaard, *Electr. Power Syst. Res.* **2009**, *79*, 511-520.

[35]   S. J. Hurst, E. K. Payne, L. Qin, C. A. Mirkin, *Angew. Chem., Int. Ed.* **2006**, *45*, 2672-2692.

[36]   a) A. Kudo, Y. Miseki, *Chem. Soc. Rev.* **2009**, *38*, 253-278; b) S. J. A. Moniz, S. A. Shevlin, D. J. Martin, Z.-X. Guo, J. Tang, *Energy Environ. Sci.* **2015**, *8*, 731-759; c) F. E. Osterloh, *Chem. Mater.* **2008**, *20*, 35-54.

[37]   a) S. Sato, J. M. White, *Chem. Phys. Lett.* **1980**, *72*; b) K. Yamaguti, S. Sato, *J. Chem. Soc., Faraday Trans. I* **1985**, *81*, 1237-1246; c) A. Fujishima, K. Honda, *Nature* **1972**, *238*, 37-38.

[38]   K. Maeda, K. Domen, *J. Phys. Chem. Lett.* **2010**, *1*, 2655-2661.

[39]   A. L. Linsebigler, G. Lu, J. T. Yates, *Chem. Rev.* **1995**, *95*, 735-758.

[40]   K. Maeda, *J. Photochem. Photobiol., C* **2011**, *12*, 237-268.

[41]   K. Maeda, K. Domen, *J. Phys. Chem. C* **2007**, *111*, 7851-7861.

[42]   M. Ni, M. K. H. Leung, D. Y. C. Leung, K. Sumathy, *Renewable and Sustainable Energy Rev.* **2007**, *11*, 401-425.

[43]   a) L. Miao, S. Tanemura, S. Toh, K. Kaneko, M. Tanemura, *Appl. Surf. Sci.* **2004**, *238*, 175-179; b) J. Yu, L. Qi, M. Jaroniec, *J. Phys. Chem. C* **2010**, *114*, 13118-13125; c) G. Wang, H. Wang, Y. Ling, Y. Tang, X. Yang, R. C. Fitzmorris, C. Wang, J. Z. Zhang, Y. Li, *Nano Lett.* **2011**, *11*, 3026-3033; d) Z. Wei, S. Fanfei, P. Kai, T. Guohui, J. Baojiang, R. Zhiyu, T. Chungui, F. Honggang, *Adv. Funct. Mater.* **2011**, *21*, 1922-1930.

[44]   a) F. Bosc, A. Ayral, P. A. Albouy, C. Guizard, *Chem. Mater.* **2003**, *15*, 2463-2468; b) J. Zhang, Q. Xu, Z. Feng, M. Li, C. Li, *Angew. Chem., Int. Ed.* **2008**, *47*, 1766-1769; c) E. Baldini, L. Chiodo, A. Dominguez, M. Palummo, S. Moser, M. Yazdi-Rizi, G. Auböck, B. P. P. Mallett, H. Berger, A. Magrez, C. Bernhard, M. Grioni, A. Rubio, M. Chergui, *Nat. Commun.* **2017**, *8*, 13.

[45]   a) L. D. Li, J. Q. Yan, T. Wang, Z. J. Zhao, J. Zhang, J. L. Gong, N. J. Guan, *Nat. Commun.* **2015**, *6*; b) F. Amano, M. Nakata, A. Yamamoto, T. Tanaka, *Catal. Sci. Technol.* **2016**, *6*, 5693-5699.

[46]   a) S. G. Kumar, L. G. Devi, *J. Phys. Chem. A* **2011**, *115*, 13211-13241; b) D. C. Hurum, A. G. Agrios, K. A. Gray, T. Rajh, M. C. Thurnauer, *J. Phys. Chem. B* **2003**, *107*, 4545-4549.

[47]   a) J. C. Yu, X. C. Wang, X. Z. Fu, *Chem. Mater.* **2004**, *16*, 1523-1530; b) S. Y. Choi, M. Mamak, N. Coombs, N. Chopra, G. A. Ozin, *Adv. Funct. Mater.* **2004**, *14*, 335-344; c) K. Hashimoto, H. Irie, A. Fujishima, *Jpn. J. Appl. Phys.* **2005**, *44*, 8269; d) M. Alvaro, C. Aprile, M. Benitez, E. Carbonell, H. Garcia, *J. Phys. Chem. B* **2006**, *110*, 6661-6665.

[48]   A. Zaleska, *Recent Pat. Eng.* **2008**, *2*, 157-164.

[49]   R. Asahi, T. Morikawa, T. Ohwaki, K. Aoki, Y. Taga, *Science* **2001**, *293*, 269-271.

[50]   H. Irie, Y. Watanabe, K. Hashimoto, *J. Phys. Chem. B* **2003**, *107*, 5483-5486.

[51]   T. Ihara, M. Miyoshi, Y. Iriyama, O. Matsumoto, S. Sugihara, *Appl. Catal., B* **2003**, *42*, 403-409.

[52]   Z. Zongyan, L. Qingju, *J. Phys. D: Appl. Phys.* **2008**, *41*, 025105.

[53]   S. Na Phattalung, S. Limpijumnong, J. Yu, *Appl. Catal., B* **2017**, *200*, 1-9.

[54]   a) L. N. Kong, C. H. Wang, H. Zheng, X. T. Zhang, Y. C. Liu, *J. Phys. Chem. C* **2015**, *119*, 16623-16632; b) S. Khan, H. Cho, D. Kim, S. S. Han, K. H. Lee, S.-H. Cho, T. Song, H. Choi, *Appl. Catal., B* **2017**, *206*, 520-530; c) Q. Sun, D. Cortie, S. Zhang, T. J. Frankcombe, G. She, J. Gao, L. R. Sheppard, W. Hu, H. Chen, S. Zhuo, D. Chen, R. L. Withers, G. McIntyre, D. Yu, W. Shi, Y. Liu, *Adv. Mater.* **2017**, *29*, 1605123; d) A. L. Castro, M. R. Nunes, M. D. Carvalho, L. P. Ferreira, J. C. Jumas, F. M. Costa, M. H. Florêncio, *J. Solid State Chem.* **2009**, *182*, 1838-1845.

[55]   a) H.-Y. Lee, J. Robertson, *J. Appl. Phys.* **2013**, *113*, 213706; b) T. Nikolay, L. Larina, O. Shevaleevskiy, B. T. Ahn, *Energy Environ. Sci.* **2011**, *4*, 1480-1486 c) T. S. Dörr, L. Deilmann, G. Haselmann, A. Cherevan, P. Zhang, P. Blaha, P. W. de Oliveira, T. Kraus, D. Eder, *Adv. Energy Mater.* **2018**, 1802566.

[56]   a) T. Weller, J. Sann, R. Marschall, *Adv. Energy Mater.* **2016**, *6*, 1600208; b) T. Weller, L. Deilmann, J. Timm, T. S. Dörr, P. A. Beaucage, A. S. Cherevan, U. B. Wiesner, D. Eder, R. Marschall, *Nanoscale* **2018**, *10*, 3225-3234.

[57]   A. S. Cherevan, S. Robbins, D. Dieterle, P. Gebhardt, U. Wiesner, D. Eder, *Nanoscale* **2016**, *8*, 16694-16701.

[58]   Y. Xia, J. A. Rogers, K. E. Paul, G. M. Whitesides, *Chem. Rev.* **1999**, *99*, 1823-1848.

[59]   M. Terrones, *Annu. Rev. Mater.Res.* **2003**, *33*, 419-501.

[60]   A. P. Alivisatos, *Science* **1996**, *271*, 933-937.

[61]   V. V. Pokropivny, V. V. Skorokhod, *Mater. Sci. Eng.,C* **2007**, *27*, 990-993.

[62]   X. Younan, W. G. M., *Angew. Chem., Int. Ed.* **1998**, *37*, 550-575.

[63]   S. Y. Chou, P. R. Krauss, P. J. Renstrom, *Science* **1996**, *272*, 85-87.

[64]   D. Eder, *Chem. Rev.* **2010**, *110*, 1348-1385.

[65]   W. Guo, M. Zhang, A. Banerjee, P. Bhattacharya, *Nano Lett.* **2010**, *10*, 3355-3359.

[66]   L. David, G. Singh, *J. Phys. Chem. C* **2014**, *118*, 28401-28408.

[67]   Y. Xia, G. M. Whitesides, *Langmuir* **1997**, *13*, 2059-2067.

[68]   Y. Wenbo, R. Chamnan, A. P. S., S. Zixue, I. J. T. S., Z. Wuzong, *Adv. Funct. Mater.* **2009**, *19*, 2826-2833.

[69]   M. Stefik, S. Guldin, S. Vignolini, U. Wiesner, U. Steiner, *Chem Soc Rev* **2015**, *44*, 5076-5091.

[70]   J. G. Werner, G. G. Rodriguez-Calero, H. D. Abruna, U. Wiesner, *Energy Environ. Sci.* **2018**, *11*, 1261-1270.

[71]   a) Z.-Y. Zhou, N. Tian, J.-T. Li, I. Broadwell, S.-G. Sun, *Chem. Soc. Rev.* **2011**, *40*, 4167-4185; b) Hurst, K. , Luther, J. M., Ban, C. and Christensen, S. (2017). Nanomaterials for Energy Applications. In: Metrology and Standardization of Nanotechnology (Eds E. Mansfield, D. L. Kaiser, D. Fujita and M. Van de Voorde), Wiley-VCH, Weinheim.

[72]   J. G. Werner, T. N. Hoheisel, U. Wiesner, *ACS Nano* **2014**, *8*, 731-743.

[73]   P. Docampo, M. Stefik, S. Guldin, R. Gunning, N. A. Yufa, N. Cai, P. Wang, U. Steiner, U. Wiesner, H. J. Snaith, *Adv. Energy Mater.* **2012**, *2*, 676-682.

[74] B. C. Garcia, M. Kamperman, R. Ulrich, A. Jain, S. M. Gruner, U. Wiesner, *Chem. Mater.* **2009**, *21*, 5397-5405.

[75] M. Berthelot, *Bull. Soc. Chim. Fr.* **1867**, *7*, 43.

[76] R. B. Seymour, *J. Chem. Educ.* **1988**, *65*, 327.

[77] a) Kaminsky W., Arndt M. (1997) Metallocenes for polymer catalysis. In: Polymer Synthesis/Polymer Catalysis. Advances in Polymer Science, vol 127, Springer, Berlin, Heidelberg; b) P. C. Möhring, N. J. Coville, *J. Organomet. Chem.* **1994**, *479*, 1-29.

[78] W. H. Carothers, *J. Am. Chem. Soc.* **1929**, *51*, 2548-2559.

[79] H. R. Kricheldorf, G. Schwarz, *Macromol. Rapid Commun.* **2003**, *24*, 359-381.

[80] D. A. Tomalia, H. Baker, J. Dewald, M. Hall, G. Kallos, S. Martin, J. Roeck, J. Ryder, P. Smith, *Polymer Journal* **1985**, *17*, 117.

[81] a) P. J. Flory, *J. Chem. Phys.* **1942**, *10*, 51-61; b) M. L. Huggins, *J. Chem. Phys.* **1941**, *9*, 440-440; c) M. L. Huggins, *J. Chem. Phys.* **1942**, *46*, 151-158.

[82] a) B. F. S., *J. Appl. Crystallogr.* **1988**, *21*, 681-691; b) R. Krishnamoorti, W. W. Graessley, N. P. Balsara, D. J. Lohse, *J. Chem. Phys.* **1994**, *100*, 3894-3904.

[83] Y. Mai, A. Eisenberg, *Chem. Soc. Rev.* **2012**, *41*, 5969-5985.

[84] D. E. Discher, F. Ahmed, *Annu. Rev. Biomed. Eng.* **2006**, *8*, 323-341.

[85] L. Leibler, *Macromolecules* **1980**, *13*, 1602-1617.

[86] A. N. Semenov, *Zh. Eksp. Teor. Fiz.* **1985**, *88*, 1242-1256.

[87] a) E. Helfand, Z. R. Wasserman, *Macromolecules* **1976**, *9*, 879-888; b) E. Helfand, Z. R.Wasserman, *Macromolecules* **1978**, *11*, 960-966; c) E. Helfand, Z. Wasserman, *Macromolecules* **1980**, *13*, 994-998.

[88] a) M. W. Matsen, F. S. Bates, *Macromolecules* **1996**, *29*, 1091-1098; b) M. W. Matsen, F. S. Bates, *J. Chem. Phys.* **1997**, *106*, 2436-2448; c) M. W. Matsen, *J. Phys.: Condens. Matter* **2002**, *14*, R21.

[89] a) F. S. Bates, G. H. Fredrickson, *Phys. Today* **1999**, *52*, 32-38; b) H.-C. Kim, S.-M. Park, W. D. Hinsberg, *Chem. Rev.* **2010**, *110*, 146-177.

[90] a) S. Ludwigs, A. Böker, A. Voronov, N. Rehse, R. Magerle, G. Krausch, *Nat. Mater.* **2003**, *2*, 744; b) A. Volker, S. Reimund, *Macromol. Symp.* **1997**, *113*, 19-26.

[91] a) J. Chatterjee, S. Jain, F. S. Bates, *Macromolecules* **2007**, *40*, 2882-2896; b) C. A. Tyler, J. Qin, F. S. Bates, D. C. Morse, *Macromolecules* **2007**, *40*, 4654-4668.

[92] F. S. Bates, M. A. Hillmyer, T. P. Lodge, C. M. Bates, K. T. Delaney, G. H. Fredrickson, *Science* **2012**, *336*, 434-440.

[93] O. W. Webster, *Science* **1991**, *251*, 887-893.

[94] M. A. Hillmyer, F. S. Bates, *Macromolecules* **1996**, *29*, 6994-7002.

[95] T. S. Bailey, H. D. Pham, F. S. Bates, *Macromolecules* **2001**, *34*, 6994-7008.

[96] a) Y. Tsuneo, S. Toshio, K. Kazuyuki, K. Chuzo, *Bull. Chem. Soc. Jpn.* **1990**, *63*, 988-992; b) C. T. Kresge, M. E. Leonowicz, W. J. Roth, J. C. Vartuli, J. S. Beck, *Nature* **1992**, *359*, 710.

[97] D. Zhao, J. Feng, Q. Huo, N. Melosh, G. H. Fredrickson, B. F. Chmelka, G. D. Stucky, *Science* **1998**, *279*, 548-552.

[98] S. A. Bagshaw, E. Prouzet, T. J. Pinnavaia, *Science* **1995**, *269*, 1242-1244.

[99] M. Templin, A. Franck, A. Du Chesne, H. Leist, Y. Zhang, R. Ulrich, V. Schädler, U. Wiesner, *Science* **1997**, *278*, 1795-1798.

[100] a) S. Guldin, S. Huttner, P. Tiwana, M. C. Orilall, B. Ulgut, M. Stefik, P. Docampo, M. Kolle, G. Divitini, C. Ducati, S. A. T. Redfern, H. J. Snaith, U. Wiesner, D. Eder, U. Steiner, *Energy Environ. Sci.* **2011**, *4*, 225-233; b) S. W. Robbins, P. A. Beaucage, H. Sai, K. W. Tan, J. G. Werner, J. P. Sethna, F. J. DiSalvo, S. M. Gruner, R. B. Van Dover, U. Wiesner, *Sci. Adv.* **2016**, *2*.

[101] J. G. Werner, S. S. Johnson, V. Vijay, U. Wiesner, *Chem. Mater.* **2015**, *27*, 3349-3357.

[102] a) S. Vignolini, N. A. Yufa, P. S. Cunha, S. Guldin, I. Rushkin, M. Stefik, K. Hur, U. Wiesner, J. J. Baumberg, U. Steiner, *Adv. Mater.* **2012**, *24*, Op23-Op27; b) S. C. Warren, L. C.

Messina, L. S. Slaughter, M. Kamperman, Q. Zhou, S. M. Gruner, F. J. DiSalvo, U. Wiesner, *Science* **2008**, *320*, 1748-1752.

[103]   M. R. Bockstaller, Y. Lapetnikov, S. Margel, E. L. Thomas, *J. Am. Chem. Soc.* **2003**, *125*, 5276-5277.

[104]   T. N. Hoheisel, K. Hur, U. B. Wiesner, *Prog. Polym. Sci.* **2015**, *40*, 3-32.

[105]   M. Hara, T. Kondo, M. Komoda, S. Ikeda, J. N. Kondo, K. Domen, M. Hara, K. Shinohara, A. Tanaka, *Chem. Commun.* **1998**, 357-358.

[106]   H. G. Kim, D. W. Hwang, J. Kim, Y. G. Kim, J. S. Lee, *Chem. Commun.* **1999**, 1077-1078.

[107]   H. Kahyun, F. Yan, G. Vincenzo, M. S. A., H. R. G., W. Ulrich, *Angew. Chem., Int. Ed.* **2011**, *50*, 11985-11989.

8. APPENDIX

8.1 List of abbreviations and symbols

$AgNO_3$	Silver nitrate
BCE	Block copolymer electrolyte
BCP	Block copolymer
C	Cylinders
CB	Conduction band
CBM	Conduction band minimum
D_P / PDI	(Poly)dispersity index
e^-	Electron
E_G	Band gap energy
EISA	Evaporation-induced self-assembly
G	Gyroidal
G^A	Alternating gyroid
h^+	Hole
H_2	Hydrogen
H_2O	Water
ISO	Poly(isoprene)-b-poly(styrene)-b-poly(ethylene oxide)
k_B	Boltzmann constant
LAM	Lamellar
Li	Lithium
LIB	Lithium ion battery
LiTFSI	lithium bis(trifluoromethane-sulfonyl)imidate
LMB	Lithium metal battery
M_i	Molecular Mass
M_W	Molecular weight average
N_A	Polymerization degree (here: of A)
Nb	Niobium
Nb_2O_5	Niobium pentoxide
n_i	Number of polymer chains at same molecular weight
O_2	Oxygen
ϕ_A	Volume fraction (of A)
PEO	Poly(ethylene oxide)
PET	Poly(ethylene terephthalate)
PI	Poly(isoprene)
PS	Poly(styrene)
R	Ideal gas constant
S	Spheres
SCF	Self-consistent field

SHE	Standard hydrogen electrode
SI	Poly(styrene)-b-poly(isoprene)
SSL	Strong segregation limit
T_G	Glass transition temperature
TiO_2	Titanium dioxide
T_{ODT}	Order-to-disorder transition temperature
UV	Ultra violet
VB	Valence band
VBM	Valence band maximum
WSL	Weak segregation limit
ΔG	Gibbs free Energy
ΔH	Enthalpy
ΔS	Entropy
ε_{AB}	Interaction energy per repeat unit (here: between A and B)
X_{AB}	Flory-Huggins interaction parameter (here: between A and B)
χN	Segregation product

8.2 Curriculum vitae

TOBIAS SEBASTIAN DÖRR

- Date of birth   06 April 1990
- Nationality   German

- Address   Wallerfanger Straße 162a
66740 Saarlouis

- Contact   +49 176 63384840
tobias.doerr90@gmail.com

PERSONAL CAREER

2015/08 - present	**PHD STUDENT** INM – Leibniz Institute for New Materials gGmbH & Saarland University (Kraus Group) University of Muenster / Technical University Vienna (Eder Group) Title: Block copolymer derived three-dimensional ordered hybrid materials for energy storage and conversion - Design of novel nanostructured materials - Research project organization and coordination, including third-party fund acquisition - Draft of scientific publication and nationally and internationally presentation of the results
2014/09 – 2014/11	**RESEARCH FELLOWSHIP** Cornell University, Ithaca (NY), USA
2013/11 – 2015/07	**UNDERGRADUATE ASSISTANT** University of Muenster - Research in the Eder Group / Tutor
2013/11 - 2015/07	**MASTER'S PROGRAM CHEMISTRY** University of Muenster - Degree: Master of Science (M. Sc.), Grade: 1.0 - Thesis: Gyroidal Mesoporous Transition Metal Oxides and Nitrides - Synthesis and Photocatalytical Evaluation (Grade 1.0)

2013/01 – 2013/10	**UNDERGRADUATE ASSISTANT** INM – Leibniz Institute for New Materials gGmbH
2010/10 - 2013/10	**BACHELOR'S PROGRAM CHEMISTRY** Saarland University - Degree: Bachelor of Science (B. Sc.), Grade: 2.1 - Thesis: Controlled Structuring of Surfaces as a Basis for Conductive Layers using Emulsions (Grade: 1.3)
2010/04 - 2010/09	**BACHELOR'S PROGRAM MICRO-TECHNOLOGY AND NANOSTRUCTURES** Saarland University
2009/07 – 2010/03	**MILITARY SERVICE** Horb am Neckar and Idar-Oberstein/Birkenfeld
2000/08 - 2009/06	**ABITUR** Illtalgymnasium Illingen

SKILLS

Languages	- German (native) - French (basic)	- English (fluent) - Spanish (basic)
Training	- Consulting Workshop - Sachkundenachweis nach §5 der ChemVerbsV - Diplôme d'études en langue française (DELF) – Niveau B1	
Fellowship	- e-fellows.net Stipendium (since 08/2016) - DAAD Stipendium zur akademischen Aus- und Fortbildung im Ausland	
IT-Skills	- MS Office (very good) - Origin (very good) - Databases/reference management (e.g. SciFinder, Endnote) (very good)	

8.3 List of publications

Patents

S-1   de Oliveira P. W., **Dörr T.**, Moh K. (2015). Verfahren zur Herstellung strukturierter

metallischer Beschichtungen

DE102013114572A1, EP3084039A2

Peer-reviewed publications

ORCID iD: 0000-0001-8164-3152

J-1   Weller T., Deilmann L., Timm J., **Dörr T. S.**, Beaucage P. A., Cherevan A. S., Wiesner U. B.,

Eder D., Marshall R., A crystalline and 3D periodically ordered mesoporous quaternary

semiconductor for photocatalytic hydrogen generation *Nanoscale* **2018**, 10, 3225-3234

J-2   **Dörr T. S.**, Fleischmann S., Zeiger M., Grobelsek I., de Oliveira P. W., Presser V., Ordered

Mesoporous Titania/Carbon Hybrid Monoliths for Lithium-ion Battery Anodes with High

Areal and Volumetric Capacity *Chem. - Eur. J.* **2018**, 24, 6358-6363 [**Hot Paper**]

J-3   **Dörr T. S.**, Pelz A., Zhang P., Kraus T., Winter M., Wiemhöfer H.-D., An Ambient Temperature

Electrolyte with Superior Lithium Ion Conductivity based on a Self-Assembled Block

Copolymer *Chem. - Eur. J.* **2018**, 24, 8061-8065 [**Hot Paper**] [**Inside Cover**]

J-4   Krüner B., **Dörr T. S.**, Shim H., Sann J., Janek J., Presser V., Gyroidal Porous Carbon

Activated with NH_3 or CO_2 as Lithium-Sulfur Battery Cathodes *Battery & Supercaps* **2018**,

1, 83-94

J-5   Imholt L., **Dörr T. S.**, Zhang P., Ibing L., Cekic-Laskovic I., Winter M., Brunklaus G., Grafted

polyrotaxanes as highly conductive electrolytes for lithium metal batteries *J. Power*

Sources **2018**, 409, 148-158

J-6   **Dörr, T. S.**, Deilmann L., Haselmann G., Cherevan A., Zhang P., Blaha P., de Oliveira P. W., Kraus T., Eder D., ORDERED MESOPOROUS TIO2 GYROIDS: EFFECTS OF PORE ARCHITECTURE AND NB-DOPING ON PHOTOCATALYTIC HYDROGEN EVOLUTION UNDER UV AND VIS IRRADIATION *Adv. Energy Mater.* **2018**, 1802566

J-7   Pelz A., **Dörr T. S.**, Zhang P., de Oliveira P. W., Winter M., Wiemhöfer H.-D., Kraus T., SELF-ASSEMBLED BLOCK COPOLYMER ELECTROLYTES: ENABLING SUPERIOR AMBIENT CATIONIC CONDUCTIVITY AND ELECTROCHEMICAL STABILITY *Chem. Mater.* **2018**, 31, 277-285

J-8   Fleischmann S., **Dörr T. S.**, Frank A., Hieke S. W., Doblas-Jimenez D., Scheu C., de Oliveira P. W., Kraus T., Presser V., GYROIDAL NIOBIUM SULFIDE / CARBON HYBRID MONOLITHS FOR ELECTROCHEMICAL ENERGY STORAGE, *in press*, DOI: 10.1002/batt.201900035

Posters

P-1   **Dörr T. S.**, de Oliveira P. W., Arzt E., ADVANCED PHOTOCATALYSTS THROUGH BLOCK COPOLYMER SELF-ASSEMBLY

INM – Leibniz Institute for New Materials (internal), 2016

P-2   Rogin P., Kampka J., **Dörr T. S**., de Oliveira P. W., PHOTOMETALLIZATION FOR TOUCH SCREENS

INM – Leibniz Institute for New Materials (internal), 2017

P-3   Deilmann L., **Dörr T. S.**, Cherevan A., Wiesner U., Eder D. GYROIDAL TRANSITION METAL OXIDES WITH LARGE PORES FOR PHOTOCATALYTIC HYDROGEN PRODUCTION

12th International conference on Materials Chemistry, York, UK; July 20th – 23rd 2015

P-4   Pelz A., Grünebaum M., **Dörr T. S.**, Wiemhöfer H.-D. NEW ELECTROLYTE SYSTEMS TOWARDS LITHIUM METAL ANODE

2nd Graz Battery Days, Graz, Austria, September 27th – 28th 2016

P-5   **Dörr T. S.**, Pelz A., Zhang P., Kraus T., Winter M., Wiemhöfer H.-D. Sᴇʟꜰ-ᴀssᴇᴍʙʟᴇᴅ BCP/Lɪ

ꜱᴀʟᴛ ʜʏʙʀɪᴅ ᴇʟᴇᴄᴛʀᴏʟʏᴛᴇ ᴡɪᴛʜ ʜɪɢʜ ʀᴏᴏᴍ-ᴛᴇᴍᴘᴇʀᴀᴛᴜʀᴇ ᴄᴏɴᴅᴜᴄᴛɪᴠɪᴛʏ

Material Research Society (MRS) Spring Meeting 2018, Phoenix (AZ), USA, April 1st – 6th

2018

P-6   Pelz A., **Dörr T. S.**, Winter M., Wiemhöfer H.-D. Tʀɪʙʟᴏᴄᴋ ᴄᴏᴘᴏʟʏᴍᴇʀᴇʟᴇᴄᴛʀᴏʟʏᴛᴇꜱ ᴡɪᴛʜ

ᴘᴏʟʏᴍᴇʀ-ɪɴ-ꜱᴀʟᴛ ʟɪᴋᴇ ʟɪᴛʜɪᴜᴍ ᴛᴏ ᴏxʏɢᴇɴ ʀᴀᴛɪᴏꜱ

The 19th International Meeting on Lithium Battery (IMLB), June 17th – 22nd 2018